Resolving the signatures of the environmental quenching of star formation with SAMI

Adam L. Schaefer

Submitted in total fulfilment of the requirements
of the degree of Doctor of Philosophy

2018/02/24

School of Physics
Faculty of Science
The University of Sydney

Abstract

In this thesis we use spatially resolved spectroscopy from the SAMI Galaxy Survey to investigate the mechanisms that suppress, or quench, the star formation (SF) in galaxies in dense environments. We calculate integrated star formation rate (SFR) and quantify the distribution of SF in different ways, including the radial distribution of SF and the non-parametric $r_{50,\mathrm{H}\alpha}/r_{50,cont}$. These measurements are compared to various environment density metrics from the GAMA survey. The spatial signatures of environment quenching vary with the stellar mass of the galaxies. Massive galaxies in dense environments are quenched outside-in, while low mass galaxies do not appear to exhibit such behaviour.

We find that the signatures of environment quenching are most likely to be seen in galaxy groups more massive than $10^{12.5}\,\mathrm{M}_{\odot}$. Above this halo mass the fraction of galaxies that appear to be environmentally affected rises significantly. Within groups there is no correlation between the indicators of environment quenching and other measures of environment. From the projected phase-space distribution of the quenching galaxies in the groups, we speculate that the changes in the SF properties of these galaxies must occur over timescales longer than the group dynamical time.

Using a case study of 4 galaxies with centrally-concentrated SF and a mass-matched control sample, we study how the gradients in the stellar populations of galaxies change during quenching. We derive stellar population age profiles, and find that the quenching galaxies are$0.7 \pm 0.6\,\mathrm{Gyr}$ older at R_e than the controls.The kinematics for our galaxies rule out the accretion of misaligned gas as responsible for their SF morphology, and a toy model rules out starvation as a mechanism. Based on their residence in massive groups and their star-formation morphology, we suggest that the outer parts of these galaxies have been quenched by an event that rapidly stripped the gas in their discs, leaving the inner parts of the galaxy to quench by starvation.

Declaration

This is to certify that to the best of my knowledge, the content of this thesis is my own work. This thesis has not been submitted for any degree or other purposes.

It should be noted that the measurements of Lick Indices presented in Chapter 4 were made by Dr. Nicholas Scott. Ancillary data from the GAMA survey have been used throughout this thesis. I did not prepare these data and the relevant references to their sources have been added to the text. All other data analysis, unless otherwise noted, is my own work.

I certify that the intellectual content of this thesis is the product of my own work and that all the assistance received in preparing this thesis and sources have been acknowledged.

Adam Linus Schaefer

Acknowledgements

Throughout the course of my candidature I have received an immense amount of support from my academic supervisors, my colleagues, my friends, and my family. I wish to express my unlimited gratitude all the people who have eased my passage from a state of complete ignorance to one of slightly lesser ignorance.

My thanks to Professor Scott Croom for your unwavering support, your generosity with your time, and for putting up with my terrible jokes while observing. Professor Sarah Brough, for providing a great environment for research, and for making sure my thesis never lost its mojo. Dr. Nicholas Scott for your extreme patience and guidance. Your index measurements were absolutely stellar, and without them my final chapter would have been throughly Licked. Dr. James Allen for teaching me everything I know about coding and then introducing me to StackExchange for everything else. I could not have asked for a better team of supervisors. It has been an honour to be your student and a privilege to join you on this never-ending journey towards understanding the Universe.

I am also indebted to Dr. Jesse van de Sande for your higher-order advice on research, snorkelling, and the intricacies of the Dutch language; to Dr. Michael Pracy, for your royal advice and extremely useful discussion over the years; and to Dr. Julia Bryant for teaching me the anatomy of SAMI and keeping the observing runs on theme.

To my friends from office 335A, Rebecca McElroy, Jessica Bloom, Hamish Clark, Joe Callingham and others: What sanity that I have retained I owe to your friendship, fellowship, and your particular brand of humour. What sanity I have lost, I also owe to your friendship, fellowship, and your particular brand of humour. You have been a light to me in dark places, when all other lights went out. Thank you.

I would also like to acknowledge my colleagues from Radio Galaxy morning Tea: Dr. Vanessa Moss, Dr. Elizabeth Mahoney, Dr. James Allison, Marcin Glowacki, Professor Elaine Sadler, Professor Richard Hunstead, and Dr Helen Johnston for our extremely interesting and useful discussions on a broad range of topics.

I would like to thank my good friends Linda Ngo for teaching me what motivation is, Dr. Sarah Reeves for showing me what persistence looks like, Aina Musaeva for showing me the meaning of strength. You have been an inspiration.

And finally I would like to thank my father Dr. Nicholas Schaefer, my mother (soon to be Dr.) Dale Fallon, and my brother Alistair Schaefer. You have encouraged my passion for science and thirst for knowledge for my entire life, and it is your whole-hearted support that has brought me to where I am today.

Contents

List of Figures

List of Tables

Chapter 1

Introduction

1.1 Galaxies and their evolution

Galaxies are islands of stars and star formation in the endless ocean of the Universe. They represent the fundamental building blocks for structure on the largest of scales, and are themselves composed of stars. The construction of galaxies from between millions and trillions of individual stars, formed over billions of years of cosmic history, means they are necessarily very complicated systems. Understanding how galaxies were formed and have evolved over the past 13 billion years has become a primary focus for astronomers. Crucial to this endeavour is knowing where the stars in these galaxies came from, how they formed and under what circumstances this process can be halted.

1.1.1 Early observations of galaxies

The first recorded observation of galaxies comes from the Persian astronomer Abd al-Rahman al-Sufi, who noted the Andromeda Galaxy and the Large Magellanic Cloud circa 964 C.E. in his seminal *Book of Fixed Stars* (Abd al-Rahman al-Sufi, 964)[1].

Following the advent of large telescopes, the variety in the shapes and sizes of galaxies was noticed almost immediately, and a system of classification was soon required. William Herschel's catalogues of star clusters and nebulae included classifications of these objects based on their apparent brightness and morphology (Herschel, 1786, 1789, 1802). However, Lord Rosse's sketches of objects such as M51, made at the eyepiece of his 72-inch telescope, are the first known observations of the spiral structure of such objects (see Rosse, 1850, for the original sketches of this object).

Using large telescopes and photographic technology, astronomers such as Wolf (1908) and Lundmark (1926) began to look for patterns in the morphologies of these mysterious objects. These early classifications were built upon by Hubble (1926), who classified galaxies as spiral, barred spiral, or elliptical. The 'Hubble Tuning Fork' (see Figure 1.1) was first presented in *The Realm of the Nebulae* (Hubble, 1936), but was finalised by Sandage (1961). This scheme for the classification of galaxies is still in use today.

[1] A electronic copy of the *Book of Fixed Stars* can be accessed online at `https://www.wdl.org/en/item/2484/`.

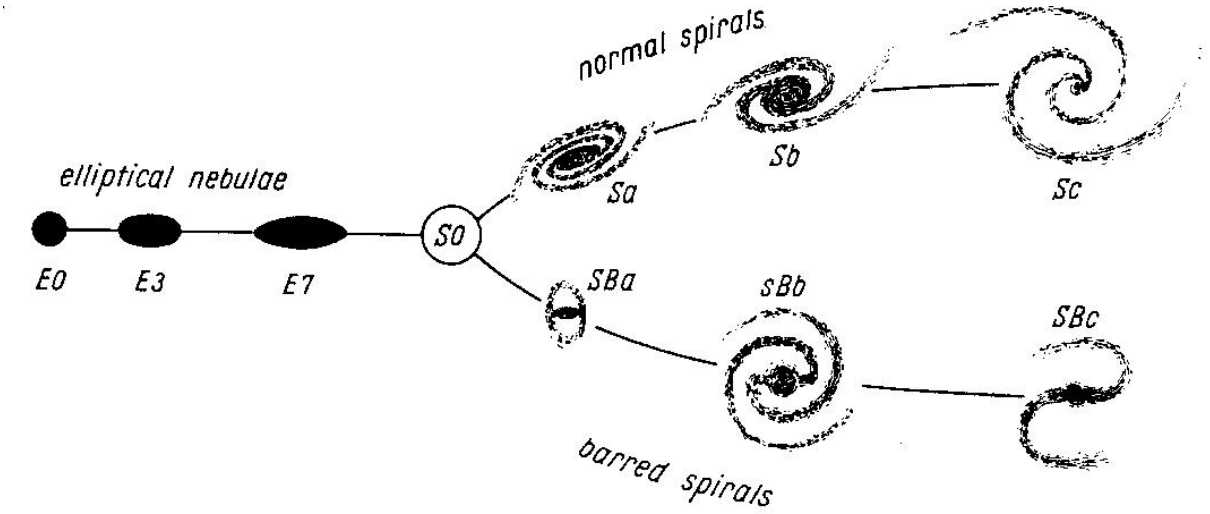

Figure 1.1: The 'tuning fork' diagram for the classification of galaxies from Hubble (1936), reproduced in Sandage et al. (1975).

As photographic techniques improved, the number of catalogued extended astronomical objects increased as well. However, it was not until nearly a millennium after Abd al-Rahman al-Sufi's observations, that our improved astronomical instrumentation and methodology enabled Hubble (1925) to understand these objects as systems of stars separate to our own Milky Way. The discovery of galaxies as 'island universes' directly analogous to our own, but located at enormous distances, opened up an entirely new avenue of astronomical research and forced astronomers to revise their understanding of the Universe at large.

1.1.2 The cosmic history of star formation

Edwin Hubble's original work focussed on a few hundred of the brightest galaxies, but we now know the observable Universe to contain some 2×10^{12} galaxies above a stellar mass of $10^6\,\mathrm{M}_\odot$ (Conselice et al., 2016). With modern instruments, these galaxies can be observed over a vast range of distances and therefore over a similarly vast range of lookback times. Observing these systems across cosmic time shows the galaxy population evolving in a number of striking ways.

The Universe reached a peak star formation rate density at $z \sim 1.9$, with the star formation declining ever since (e.g. Heavens et al., 2004; Hopkins & Beacom, 2006; Madau & Dickinson, 2014). Early studies of evolution of the cosmic star formation rate, such as those accomplished by Madau et al. (1996) and Madau et al. (1998), used photometric observations of Lyman absorbers across a range of redshifts to probe the evolution of neutral gas in the Universe. By studying the detectability of galaxies in the ultraviolet, the star formation rate density, and the chemical properties of the intergalactic medium could be studied out to beyond $z = 2.5$. Lilly et al. (1996) noted a decline in the ultraviolet luminosity density of the Universe, tracing star-formation, since $z = 1$. The evolution of the star formation rate density of the Universe is shown in Figure 1.2.

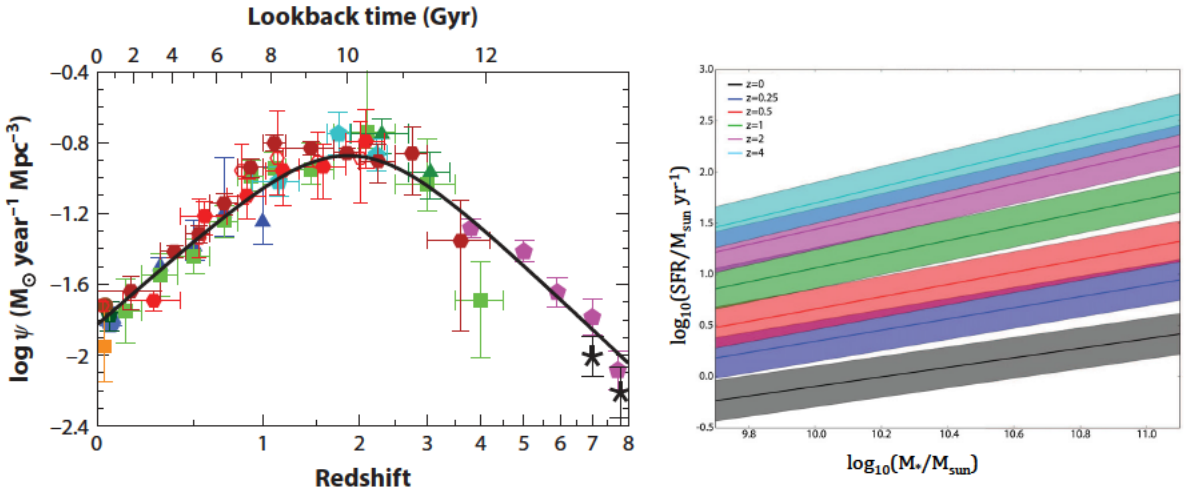

Figure 1.2: The star formation history of the Universe. (*Left*) This image, taken from Madau & Dickinson (2014), shows combined ultraviolet and infrared measurements of star formation density, ψ, from the present day back to redshift, $z = 8$. The Universe reached peak star formation density at $z \approx 1.9$. (*Right*) The evolution of the star formation rate - stellar mass (SFR-M_*) main sequence as compiled by Speagle et al. (2014) from multiple sources. As cosmic time progresses there is a reduction in the star formation rates of galaxies at all stellar masses, though dropping off faster at higher stellar mass.

There are two distinct ways in which the star formation rate density in the Universe could have been higher than today: a larger number of star-forming galaxies could have been present, or that individual galaxies had higher star formation rates for their stellar mass. Measurements of the so-called star formation rate main sequence, the tight correlation between the stellar mass and total star formation rate of galaxies, proved the first of these possibilities false. Observational studies of the star formation rates of individual galaxies across a range of redshifts showed that star formation rates in all star-forming galaxies at all stellar masses were higher up to $z \approx 2$. (Noeske et al., 2007; Whitaker et al., 2012). This result that has been confirmed by a number of subsequent studies, but see Speagle et al. (2014) for a compilation and review of the data, that are presented in the right panel of Figure 1.2. The peak star formation rate density is thought to be the result of the accretion rate of gas onto galaxies reaching a maximum at this time.

In the time following this peak, the accretion rate declined. At around the same time as this peak in star formation, the simulations presented by van de Voort et al. (2011) suggest that two important things happened. At $z = 3$ the rate at which gas fell into galaxies in a cold state (i.e. with temperature less than 3×10^5 K), a process called cold-mode accretion, reached a maximum. However, the rate at which gas entered galaxies above this temperature (hot-mode accretion) continued to increase until $z = 1$. In addition to the reduction in cold-mode accretion the role of active galactic nuclei (AGN) in heating gas and expelling it from galaxies also increased. As cold-mode accretion became less dominant, the resulting gas surface density in typical galaxies was reduced as well, meaning that star formation became less intense (Hopkins et al., 2008; Scoville et al.,

2017).

Studies of the quantitative morphology of galaxies over a large range of redshifts have shown that their structure has been evolving (e.g. Conselice et al., 2008; Conselice, 2014). At high redshifts ($z \sim 2$) the most massive spheroidal galaxies are observed to be extremely compact, up to a factor of five smaller than similar galaxies of the same stellar mass in the local Universe (Trujillo et al., 2007; Buitrago et al., 2008). These high redshift galaxies are thought to be the progenitors of the local elliptical population that will grow in size by merging with lower mass galaxies (Naab et al., 2009). In this way, massive galaxies are said to have formed inside-out, with their inner parts forming relatively soon after the Big Bang and their outer parts growing subsequently.

Of particular interest to us is that the way in which galaxies form stars has changed remarkably. Observations of star formation at high redshift have shown that star formation was more clumpy, with many stars forming in large knots and complexes (see e.g. Elmegreen et al., 2008; Wuyts et al., 2012). It has been proposed that these large clumps of star formation were made possible by high turbulence in the gas (Wisnioski et al., 2012), which reduced the impact of feedback processes that would otherwise destroy them. Under the relatively high gas densities that this afforded these galaxies, star formation was able to continue at a relatively high rate.

By $z = 1$, the star formation rates in galaxies had begun to decline. Nelson et al. (2013) showed that a sample of galaxies at this redshift have star formation rate radial distributions that decay exponentially with distance from the galaxy centres. However, they also showed that this star formation essentially follows the stars, ruling out central starbursts as the dominant mode of star formation at this redshift. Since this time, the total star formation in galaxies has declined gradually. Studying the reduction of star formation since $z = 0.7$, Buat et al. (2008) concluded that the conditions under which stars form in galaxies has not changed, and that only the overall rate has dropped to the levels that we see today.

1.2 The galaxy population today

By virtue of their relative brightness and size, galaxies at low redshift are more easily studied in detail than those at high redshift. The wealth of multi-wavelength data that have become available through numerous large surveys has enabled us to perform a rigorous census of the galaxy population today.

1.2.1 Colour-mass diagram

The surveys that provide data on the largest possible number of galaxies have been those that study the colours of galaxies. Galaxy colours are influenced by many factors, with redder galaxies generally found to be older, more metal-rich, more massive, contain more dust, or have a lower star formation rate per unit mass (specific star formation rate). Trends between galaxy colour and morphology have been noticed for several decades (e.g. de Vaucouleurs, 1961), with ‘early-type’ lenticular and elliptical galaxies having redder colours than ‘late-type’ spirals. With the larger samples available more recently Strateva

et al. (2001) was able to discern a bimodality in the galaxy population, with mostly star-forming galaxies falling into a 'blue cloud' and more passive galaxies comprising a 'red sequence', when the effects of dust are accounted for. Star-forming galaxies will contain a higher proportion of young, hot, and luminous blue stars than galaxies which are passive. As the proportion of these young stars diminishes, a galaxy will exhibit progressively redder colours. However, more massive galaxies have different star formation histories to less massive galaxies (Tinsley, 1968). At higher stellar mass, a more substantial old underlying stellar population exists. For this reason the red and blue sequences are not independent of stellar mass. More massive galaxies are seen to be redder for both subpopulations. The galaxy bimodality is shown in Figure 1.3.

Due to the relationship between the colours of galaxies and their specific star formation rates, these colours can also be an indicator of the properties of the emission lines in galaxies (Strateva et al., 2001). Galaxies in the blue cloud of the colour-mass diagram tend to exhibit emission lines in their spectra, with emission line ratios that are largely consistent with being excited by radiation from a young stellar population (e.g. Kauffmann et al., 2003c; Brinchmann et al., 2004). Most galaxies in the red sequence are not observed to form stars, however roughly 30% exhibit faint emission lines (Yan et al., 2006).

For galaxies in the blue cloud, as briefly mentioned above, there is a tight correlation between their stellar mass and star formation rate. This main sequence, seen across different redshifts in Figure 1.2, was first noted by Brinchmann et al. (2004). Galaxies on the main sequence occupy the blue cloud of the colour-mass diagram, if dust attenuation is corrected for. The existence of the stellar mass-star formation rate relation has been a focus in the study of galaxy evolution since its discovery. The low scatter (0.2 dex, Speagle et al., 2014) in the relation hints that various regulatory processes that must be at play to balance the replenishment of gas with its consumption through star formation and its expulsion through feedback (Lilly et al., 2013). The small scatter seen in the main sequence, and the agreement of its parameters between multiple star formation rate measurements (Speagle et al., 2014) mean that it can be used to test various models of galaxy evolution (e.g. Schaye et al., 2015). Furthermore, it can act as a useful benchmark for the expected star formation rates of galaxies under normal circumstances. It can therefore be used for comparison during observational tests of some astrophysical effect or galaxy property on their evolution.

The colour-mass diagram has become an indispensable tool for understanding how galaxies change over time. It has been interpreted as an evolutionary sequence, with galaxies moving to higher mass along the blue cloud as they either form new stars or accrete them through mergers. The galaxies may later transition through the sparsely populated green valley to the red sequence as their star formation stops. The cessation of star formation is termed 'quenching'. After quenching, galaxies can move up in mass along the red sequence by merging with other quenched galaxies (e.g. Baldry et al., 2004).

For the study of the quenching of galaxies, much attention has been paid to the green valley, the narrow region between the blue cloud and red sequence (e.g. Faber et al., 2007; Martin et al., 2007; Fang et al., 2012; Salim et al., 2012). Galaxies in this region of the colour-mass diagram may be in the process of quenching. Studying these galaxies could yield clues as to the nature of this important transition.

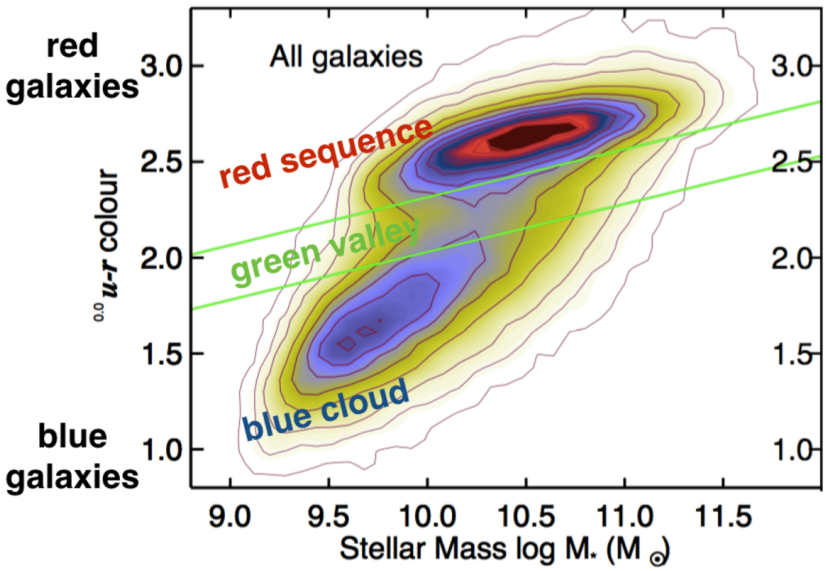

Figure 1.3: Colour as a function of stellar mass for galaxies in the Sloan Digital Sky Survey. The population is separated into two distinct clumps, the blue cloud and the red sequence, separated by the relatively sparse green valley. Image sourced from *theconversation.com*[2].

Active galactic nuclei (AGN), the energetic central regions of galaxies that result from the accretion of material onto a supermassive black hole, are thought to play an important role in the evolution of galaxies. Theorists have proposed AGN as a source of heating for the hot halo gas observed around nearby galaxies (Tabor & Binney, 1993). The simulations of Di Matteo et al. (2005) showed that luminous AGN, in particular those that are triggered by mergers, can release enough energy to drive outflows that strip a galaxy of its neutral gas. Further semi-analytic modelling by Bower et al. (2006) indicated that feedback from AGN was required to explain the observed luminosity distribution of galaxies. Without this feedback, the simulations predict a number of massive, star-forming galaxies that exceeds the number observed. Observationally, Nandra et al. (2007) studied the locations of a sample of X-ray-selected AGN in the colour-magnitude diagram, showing that they inhabit either the green valley or the red sequence. Their findings were consistent with the AGN either causing or maintaining the suppression of star formation in the AGN host galaxies.

In contrast, Fang et al. (2012) used resolved ultraviolet imaging to study galaxies in the FUV-r colour transition zone. They determined that a subpopulation of galaxies in their sample had extended low-level star formation that corresponded to a slow decline in star formation uniformly across their galaxies. This is at odds with the expected signatures of rapid quenching (on a timescale less than 500 Myr) due to an AGN-driven outflow.

While feedback from an AGN may be responsible for some fraction of the red sequence of galaxies, there is mounting evidence that star formation can be regulated by external processes.

1.3 Galaxy Environments Quench Star Formation

Hubble & Humason (1931) were among the first to report that galaxy properties depend on environment. They noted, in passing, an excess of red, early type galaxies in clusters compared to the population of more isolated systems. This was followed up by numerous studies, including Morgan (1961), who observed that the brightest galaxies in clusters tend to be elliptical in morphology and have colours consistent with a lack of recent star formation. The findings of these studies were summarised in a review by Abell (1965). The morphological variation of galaxies between the richly populated clusters and the sparsely populated field was quantified by Dressler (1980), where the highly influential morphology-density relation was first laid out. The original Dressler paper dealt only with very rich galaxy clusters, but the morphology-density relation was extended to less extreme group environments by Postman & Geller (1984). While the morphology density relation was strongly suggestive of an evolutionary transition between star-forming late-type galaxies and passive early-type galaxies in dense environments, the mechanism that produces this trend is not obvious. In particular, it was not clear how the variation in morphology relates to the change in star formation rate. Does a galaxy in a dense environment change its morphology and then subsequently lower its star formation rate? Or does the reduction in star formation precede the morphological transformation? The answer to these questions depends on the way in which galaxies interact with their environment.

1.3.1 Environmental mechanisms for quenching star formation

The rate at which stars can form in a galaxy depends on the amount of gas present and the thermodynamic state of the gas. While galaxies with a higher density of gas will form stars more rapidly (Schmidt, 1959), the collapse of these clouds is only possible if certain criteria are met. For individual gas clouds, the Jeans criteria must be satisfied (Jeans, 1902). That is, for a given density of gas and the size of the gas cloud, the temperature must be low enough so that gas pressure does not exceed the gravitational force. Furthermore, if the gas is undergoing differential rotation, such as in the disc of a galaxy, the shear velocity between adjacent elements of gas must also be overcome to enable star formation (Safronov, 1960; Toomre, 1964). Thus, in galaxies, there are two main ways to reduce star formation: remove the gas, depriving the galaxy of fuel for further star formation, or stabilise the gas against gravitational collapse either through heating or dynamical effects.

[2]This image first appeared in Schawinski et al. (2014), but was modified to this form by Kevin Schawinski for an article that appeared online at http://theconversation.com/is-our-milky-way-galaxy-a-zombie-already-dead-and-we-dont-know-it-52732 accessed

Ram pressure stripping

One of the first methods proposed for removing the gas from a galaxy is called ram pressure stripping. The theoretical framework for this method of gas removal from a galaxy was put in place by Gunn & Gott (1972). They showed that a galaxy moving with velocity v through a hot intergalactic medium with density ρ_e would experience a ram pressure,

$$P_{ram} = \rho_e v^2. \tag{1.1}$$

The gas in this galaxy is kept in place by the gravitational potential of the disc, and so experiences a restoring force per unit area of

$$F_{rest} = 2\pi G \Sigma_* \Sigma_g, \tag{1.2}$$

where G is the universal gravitational constant, Σ_* is the stellar surface density, and Σ_g is the gas surface density. This calculation assumes that the stellar component dominates the mass budget in the galaxy disc. If the ram pressure exceeds this restoring force, then the gas will be stripped from the disc. Since the stellar surface density drops with radius, the gas towards the outer parts of a galaxy is removed most easily. The rate at which gas is lost due to ram pressure depends on the density in the intracluster medium, the velocity of the galaxy through the intergalactic medium and also the angle between the plane of the galaxy disc and its trajectory through the cluster. Simulations show that galaxies moving face-on into the cluster can lose a large fraction of their gas in 10^7 to 10^8 yr (e.g. Abadi et al., 1999; Quilis et al., 2000). In galaxies moving edge-on into the cluster, or on orbits that do not take them through the cluster core, the timescale for the removal of gas can be much longer. Furthermore, the mass of the galaxy and its morphology can play a part in the extent to which a galaxy can be stripped by ram-pressure (Hester, 2006). Galaxies with a more massive bulge component for example, will have a higher stellar mass density and therefore be more difficult to strip. Dwarf irregular galaxies, on the other hand, have a relatively shallow gravitational potential well, and should be most susceptible to ram pressure stripping.

Ram pressure stripping has been observed to take place in galaxy clusters. In Figure 1.4, we show a broadband optical image of the galaxy NGC 4522, located in the Virgo cluster. On this image, Kenney et al. (2004) overlaid the contours of HI column density. The distribution of the cool, neutral gas shows how it is swept back under the influence of the 'wind' imposed by the motion of the galaxy through the intracluster medium. Another manifestation of this process are the so-called 'jellyfish galaxies' (Fumagalli et al., 2014; Poggianti et al., 2016). These are systems that show knots of star-formation in the turbulent wake behind the ram pressure-stripped galaxy.

The identification of several spectacular examples of ram-pressure stripped galaxies in clusters from the morphology of their neutral gas and star formation has been supplemented by larger studies of the neutral gas content of cluster galaxies. Cortese et al. (2012) showed that the relative sizes of the UV discs of 273 Virgo cluster galaxies in comparison to the i band disc sizes are related to their neutral gas content. That is, as the amount of neutral gas in cluster galaxies is reduced, the scale size of their star-forming disc is reduced as well in an outside-in fashion. The original relation from Cortese et al. (2012)

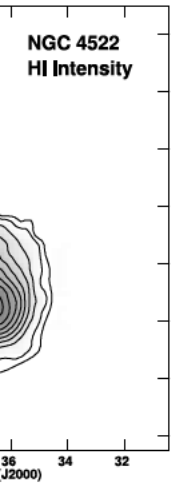

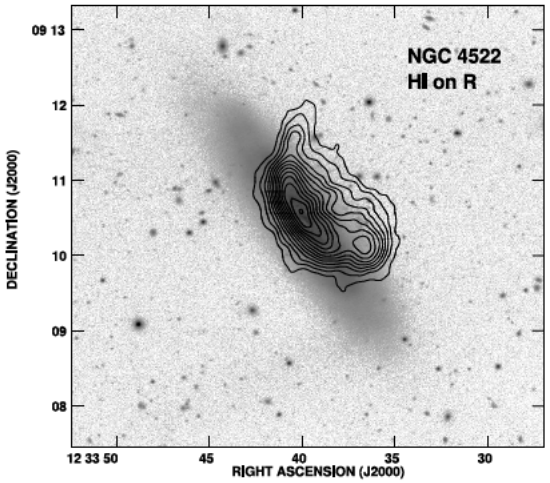

FIG. 3.—H I moment 0 contour map of NGC 4522 on *R*-band gray-scale image from the WIYN telescope from Kenney & Koopmann (1999). The lowest H I contour level and contour increments are 50 mJy beam $^{-1}$ km s $^{-1}$. The optical image is shown with logarithmic stretch. Note the distorted outer stellar disk.

cross marks H I kinematic
the northeast of nucleus,
our is 25 mJy beam $^{-1}$ km
cm $^{-2}$. The contour incre-
4.4, 16.0, 17.6, 19.2, and

made tapered images
t the interferometer

e free channels are

own in Figure 2. This
images that showed
alues below 2 σ after
o superposed on an
3 shows that H I is
e stars in the central
e plane of the stellar
ond R $0.4R_{25}$. Be
bove the disk plane,
xtends 60″ 4.5 kpc

thin 20″ to +11″ of
+11″ to +50″ above
, although this is an
+11″ to +25″ con
We have also made
1″ region as a disk
Ve show the 20″ to
des more flux. The
utlined in Figure 4,
ed by 57° so that the

en estimated by as
tric about the major
from regions to the
lanar H I comprises

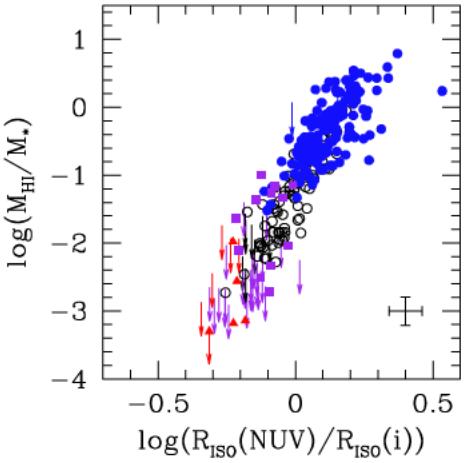

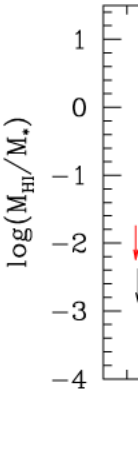

Figure 1.5: The HI gas fraction vs. the NUV-to-*i* (*le*
ratio as a function of the near UV disc
size relative to the *i* band disc size, pre-
sented by Cortese et al. (2012). Galax-
ies with more extended UV discs have a
higher gas mass, and those with smaller
UV disc sizes have lower gas masses.
Open circles are HI deficient galaxies,
filled circles are HI normal, and arrows
are non-detections.

Notes. The best linear fitting parameters are pro
two variables are correlated.

Figure 4.—The impact of ram pressure on the distribution of gas in the galaxy NGC 4522, in the Virgo cluster. The greyscale image is taken in the optical R band, while the contours show the column density of HI. The neutral gas is being swept back by ram pressure, while the stars are undisturbed. This image was taken from Kenney et al. (2004).

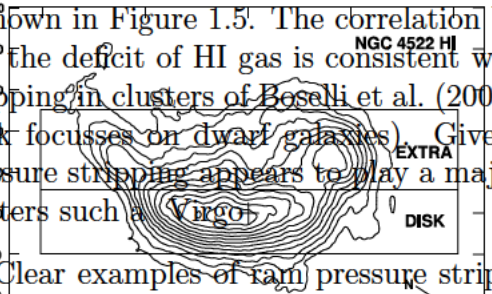

FIG. 4.—H I moment 0 map of NGC 4522, rotated by 57° so that the major axis is oriented horizontally. The inset boxes identify the regions sampled in the associated position-velocity plots in Figs. 9 and 10, which are from cuts parallel to the major axis of the galaxy.

is shown in Figure 1.5. The correlation between the scale length of the star-forming disc and the deficit of HI gas is consistent with the predictions for the effect of ram pressure stripping in clusters of Boselli et al. (2006) and Boselli et al. (2008, though this particular work focusses on dwarf galaxies). Given the sample size of Cortese et al. (2012), ram pressure stripping appears to play a major role in building up the red sequence in galaxy clusters such a Virgo.

Clear examples of ram pressure stripping in action, such as in NGC 4522, are easily identified in clusters. Evidence is now mounting that this process is able to affect galaxies in groups. Hester (2006) devised analytic models to show that galaxies in groups of mass as low as 10^{13}M$_\odot$ could be quenched by ram pressure stripping. The closer a galaxy's orbit takes it to the centre of the group, the higher the mass at which it is able to be stripped of its gas. In these models, it is possible that more massive galaxies are only partially stripped, while less massive galaxies may be fully stripped. Observationally, Brown et al. (2017) showed that the integrated HI content of galaxies that are satellites in more massive group haloes declines with increasing halo mass at fixed stellar mass and star formation rate. A comparison of this observation to semianalytic models and hydrodynamic simulations showed that some kind of fast-acting process, like ram pressure stripping, was required to explain the observations.

7. The effect of the Virgo cluster on morphology

The results presented in the previous sectio
dence of the strong connection between HI
the UV star-forming disk. Since HI remov
dramatic effects of the environment on clu
et al. 1990; Cortese et al. 2008, 2011; Chun
teresting to investigate what happens to the
when the HI is gradually removed from the
ready suggests that the UV disk should shr
ies, and this is clearly visible in Fig. 7, w
tio of the *g*-to-*i*, NUV-to-*i* and FUV-to-*i* ef
isophotal radii (bottom row) as a function
quantity in the *y*-axis is sometimes referre

Viscous stripping

Ram pressure stripping of the cold gas in a galaxy disc represents the most extreme kind of stripping event that will quench star formation. However, other processes exist that are able to remove gas from galaxies. Nulsen (1982) suggested a process called viscous stripping as a viable method of liberating the gas from the discs of galaxies. When a galaxy with a cold and dense interstellar medium moves through a hot, tenuous intergalactic medium, the gas at the boundary can experience a momentum transfer due to the viscosity. Depending on whether the flow of the gas is turbulent or laminar, this process can strip gas at different rates. The momentum transfer between the interstellar and intergalactic media occurs regardless of the orientation of the galaxy disc to its velocity through space. Simulations of galaxies in clusters that allowed galaxies to run over a long period of time showed that ram pressure stripping will tend to act promptly if the intergalactic medium is inhomogeneous. However, this prompt stripping event can be followed by a more protracted stripping of the remaining gas by its viscous interaction with the surrounding hot gas (Quilis et al., 2000; Roediger & Hensler, 2004). Rasmussen et al. (2006) made detailed observations of the gas loss occurring in NGC 2276 as it moves through its group environment. Their combined X-ray and HI observations of the galaxy and the stripped gas implicated viscous stripping in a significant fraction of the mass loss from this galaxy. At the current rate of mass loss, this process could quench the galaxy within approximately 1 Gyr.

Simulations of the viscous stripping of gas are relatively rare in the literature, which means that the qualitative impact that this process will have on the gas in galaxies is difficult to define. The simulations of Quilis et al. (2000) demonstrated that the outer parts of a galaxy are the first to be removed under the influence of both viscous stripping and ram pressure stripping. Roediger et al. (2015) simulated the case of M 89, an elliptical galaxy in the Virgo cluster, demonstrating that gas is preferentially removed from the outer parts first. To find galaxies that are currently undergoing viscous stripping, we would need to observe the state of the gas trailing behind the galaxy, and know the details of the surrounding intergalactic medium.

Strangulation

The stripping of gas from a galaxy need not directly impact the gas in the star-forming disc to affect quenching. Larson et al. (1980) proposed the mechanism of strangulation, occasionally called starvation, for shutting down star formation in galaxy clusters.

Galaxies in the field are commonly surrounded by extended discs or halos of neutral gas, as shown in Figure 1.6. The gas in these surrounding envelopes will slowly fall towards the stellar disc and replenish the fuel for star formation. However, in dense environments, such as clusters, Larson et al. (1980) proposed that this surrounding gas reservoir can be swept away by ram pressure, viscous, or tidal stripping, while leaving the gas in the star forming disc undisturbed. Under these circumstances, star formation will persist in the galaxy until all the remaining fuel has been exhausted. This mechanism is called strangulation. Larson et al. (1980) calculated the cessation of star formation by strangulation should take place over several Gyr, which is relatively protracted in

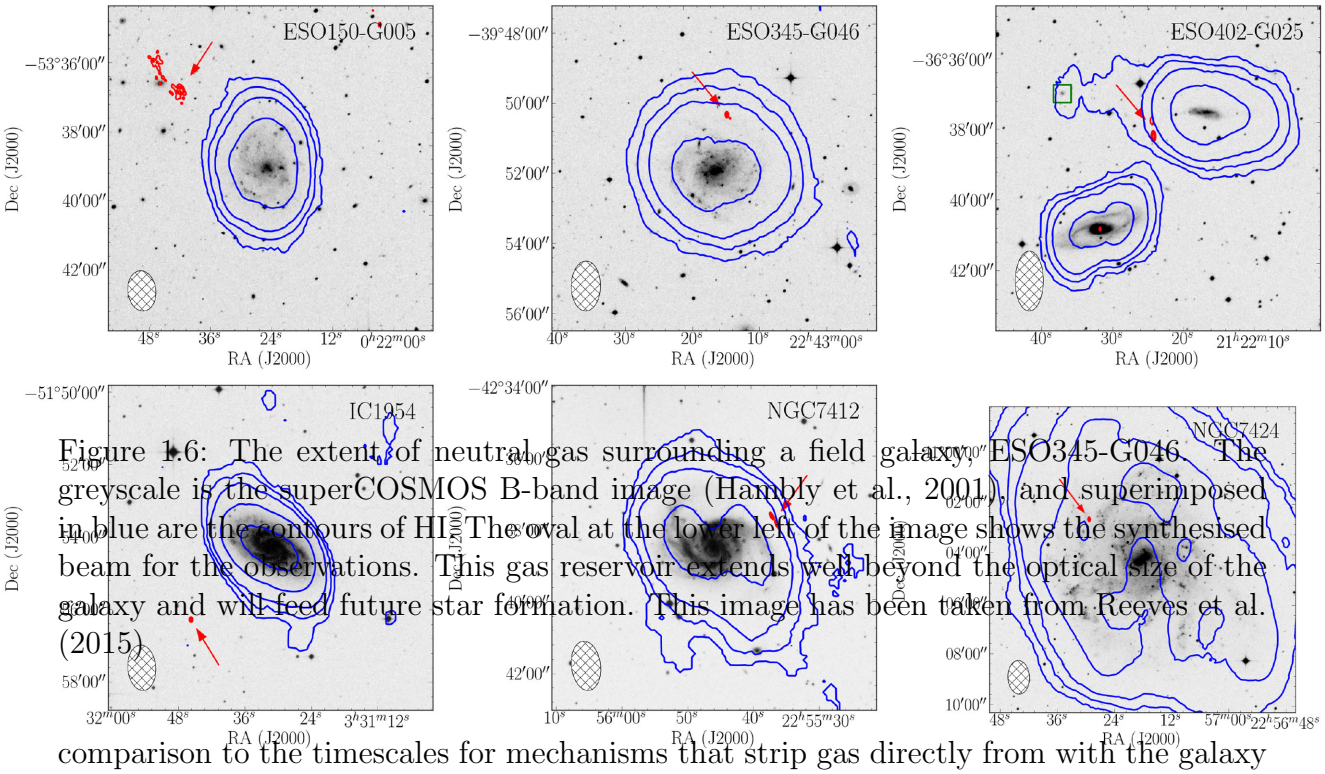

Figure 1.6: The extent of neutral gas surrounding a field galaxy, ESO345-G046. The greyscale is the superCOSMOS B-band image (Hambly et al., 2001), and superimposed in blue are the contours of HI. The oval at the lower left of the image shows the synthesised beam for the observations. This gas reservoir extends well beyond the optical size of the galaxy and will feed future star formation. This image has been taken from Reeves et al. (2015).

comparison to the timescales for mechanisms that strip gas directly from with the galaxy optical disc.

Simulations by Kawata & Mulchaey (2008) showed that even in groups with mass as low as $8 \times 10^{12}\,M_{\odot}$, strangulation is able to take place, with ram pressure stripping the hot gas that would otherwise cool and fall into the galaxy disc. Bekki et al. (2002) argued that the formation of S0 galaxies in the outer parts of clusters could be explained by the gradual decline in star formation resulting from strangulation. These studies have been backed up by a large number of simulations, many of which claim that direct stripping of the gas from galaxy discs may not be as important as was predicted by some of the original papers (e.g. Font et al., 2008; McCarthy et al., 2008). However, the vast majority of these simulations do not treat the strangulation in a spatially resolved way, and if they do the simulation resolution is too low to adequately model the resulting star formation distribution.

There have been many observational studies that suggest strangulation is an important mechanism for quenching star formation in galaxies at low redshift. Peng et al. (2015) argued that the total metal content of galaxies in the red sequence was consistent with the slow subsidence star formation during strangulation. von der Linden et al. (2010) observed a slow decline in the star formation rates of galaxies at fixed stellar mass at smaller cluster centric radii, and suggested that strangulation must be acting over the cluster crossing time (several Gyr) and begin before galaxies enter the cluster cores. A similar line of reasoning was employed by Eales et al. (2017) for galaxies outside of clusters. They posited that the steady reduction in specific star formation rates of star-forming galaxies with stellar mass implies a gradual movement from the blue cloud to the red sequence, and favours strangulation as the mechanism.

Sweeping away the gaseous halo of a galaxy is not the only way that strangulation

can be initiated. Recently, Aragon-Calvo et al. (2016) suggested the mechanism of cosmic web detachment for initiating strangulation. In low-density field environments, galaxies maintain their supply of gas by being fed fresh fuel from coherent streams of gas, the so-called cosmic web, that are related to large-scale filamentary structures. Cosmic web detachment can happen in several ways. When a galaxy enters a cluster or group it can become detached from these filaments, leading to the ultimate starvation of their gas supply. The gas content and star formation rates of galaxies in pairs and groups was studied by Janowiecki et al. (2017). They observed that the central galaxies with stellar masses below $10^{10.2}\,\mathrm{M}_{\odot}$ of low-mass groups had higher gas contents and star formation rates than equivalent isolated galaxies or galaxies in higher mass groups. Their results lend credibility to the idea that the feeding of gas from the cosmic web is crucial to the evolution of galaxies and to the onset of strangulation.

Tidal interactions

Not all methods of quenching require an interaction with the intergalactic medium. The distribution and total rate of star formation in a galaxy can be modified by gravitational interactions with its companions. Hernquist (1989) presented one of the first simulations of the tidal interactions of galaxies that traced the motion of both stars and gas simultaneously and with sufficient resolution. During the simulated interaction, the stars and gas were both perturbed, but dissipative shocks robbed the gas of angular momentum, causing it to fall towards the galaxy centres. The resulting gas density in the centre is capable of triggering a nuclear starburst (Heckman, 1990). If this starburst consumes a large fraction of the gas in the galaxy, then star formation will subsequently be reduced and the interaction will have initiated the passage of that galaxy towards the red sequence. In this way, absent further accretion of gas from the surroundings, tidal interactions are able to quench star formation. In addition to this mechanism, a close encounter between two galaxies may result in tidal stripping of gas from the outer parts of one of the galaxies. Generally the larger of the two galaxies will accrete material from the smaller of the two, thus reducing the gas reservoir of the smaller, and its ability to form stars in the long term.

The strength of a tidal interaction by a companion system on a galaxy is dependent on the mass ratio, and the difference in the gravitational field strength of the companion across the galaxy. Dahari (1984) introduced a measure of the tidal interaction strength that encapsulates these dependencies,

$$P_{gc} = \left(\frac{M_c}{M_g}\right) \times \left(\frac{r_g}{d_{gc}}\right)^3, \tag{1.3}$$

where M_c is the mass of the companion, M_g is the mass of the perturbed galaxy, d_{gc} is their separation and r_g is the radius of that galaxy. Byrd & Valtonen (1990) showed that if $P_{gc} \gtrsim 0.006 - 0.1$, then the infall of gas towards the centre is possible, though the precise value depends on the ratio of the total halo mass to the disc. However, the amount of work done on a galaxy by the tidal effect depends on the time over which the interaction occurs. Systems that spend a longer time interacting will experience a greater overall

tidal perturbation. The implication of this is that galaxies in clusters, where the galaxy velocity dispersion is very high, are less likely to experience a tidally induced starburst than galaxies in groups.

The effect of tidal interactions on the galaxy population as a whole is difficult to quantify. Astronomers will often search for morphological features that may suggest the gravitational interaction between two galaxies. These features include tidal tails (Toomre & Toomre, 1972), photometric asymmetries (e.g. Coziol & Plauchu-Frayn, 2007) and bridges of material between galaxies (e.g. Irwin, 1994). In clusters, the remnants of a tidal interactions may be short-lived. Adams et al. (2012) reported a deficiency of tidal features near the cores of galaxy clusters, though they note that the trend could also mean an excess of tidal features far from the cluster core due to the longer interaction timescales there. In less extreme environments outside of clusters, the tidal features can survive for much longer, of order a Gyr (Tal et al., 2009).

There have been a number of studies that have implicated tidal interactions in the suppression of star formation in clusters and groups. Moss et al. (1998) found that galaxies with compact, circumnuclear star formation are predominantly morphologically disturbed. This work was extended by Moss & Whittle (2000) where they showed that within clusters, galaxies with circumnuclear star formation are more common in regions of higher local galaxy density. Similarly in groups, Rasmussen et al. (2012) observed that at fixed group mass, the local density of galaxies was correlated with the reduction in star formation, implicating tidal interactions in the suppression of star formation. However, at fixed galaxy density, Rasmussen et al. (2012) also noted a reduction in the star formation rate with group mass, suggesting that the global group environment must also play a role. The timescale for quenching suggested by their analysis was $\sim 2\,\mathrm{Gyr}$, and the authors argued that both tidal interactions and strangulation must both be playing a role in quenching star formation.

While the gas can be strongly affected, these tidal interactions are also capable of altering the stellar distribution, including increasing the dispersion of the stars in the vertical direction to generate lenticular galaxies. This leaves tidal interactions as an attractive prospect for at least partly explaining the morphology-density relation.

The prevalence of different quenching mechanisms

As we have seen, there are a multitude of different potential environmental mechanisms that are able to suppress star formation, and there is observational evidence to support the fact that they all occur. Based on what we know about how these processes act, we can hypothesise what types of environment will be most conducive to particular mechanisms. For example, very large clusters with hot, dense intergalactic media will strip gas from fast-moving galaxies by ram pressure, while groups where the relative velocity between galaxies is lower will be more efficient at producing tidal interactions between galaxies.

To some extent the apparently contradictory results must be due to each mechanism occurring more readily in different environments. This point was argued by Smethurst et al. (2017) who, using optical colours, UV detections, and detailed morphological classifications, found that no single quenching mechanism dominates in galaxy groups. Only in the most extreme environments does one particular mechanism begin to dominate. To

understand how each mechanism contributes to the population of quenched galaxies at low redshift, large, representative samples are crucial.

1.4 Quenching in large surveys

Much of the original work on environment quenching targeted relatively small samples of galaxies in clusters (e.g. Oemler, 1974; Sullivan et al., 1981; Nulsen, 1982; Giovanelli & Haynes, 1983). In recent years, large-scale galaxy surveys have provided valuable insight into the nature of star formation and quenching under a variety of circumstances. Modern surveys of large areas of the sky generally consist of multi-band imaging, from which photometric measurements are derived, and single-fibre spectroscopy of a large number of targets. The most influential of these surveys at low redshift have been the Sloan Digital Sky Survey (SDSS; York et al., 2000), the 2 degree Field Galaxy Redshift Survey (2dFGRS; Colless et al., 2001) and the Galaxy And Mass Assembly survey (GAMA; Driver et al., 2009, 2011; Liske et al., 2015), but many surveys have been done of galaxies at high redshift as well (e.g. Scoville et al., 2007; Newman et al., 2013).

1.4.1 Stellar Mass

Modern surveys have discerned two primary modes of star formation quenching. The strongest mode appears to be related to the stellar mass of galaxies. This was first shown rigorously by Kauffmann et al. (2003b), who showed that the fraction of galaxies that are no longer forming stars rises sharply above a critical stellar mass of $3 \times 10^{10}\,\mathrm{M}_{\odot}$. This result was verified by Baldry et al. (2006) and numerous other studies (e.g. Peng et al., 2010; Geha et al., 2012; Darvish et al., 2016). Recently, some authors have divided the quenching into two distinct modes, mass quenching and environment quenching (e.g. Balogh et al., 2004; Peng et al., 2010).

While mass quenching appears to be one of the dominant methods of reducing star formation, it is an empirical classification only, and a number of mechanisms have been invoked to explain the phenomenon.

Dekel & Birnboim (2006) and Cattaneo et al. (2006) proposed that galaxies above the critical stellar mass will tend to inhabit more massive dark matter halos. They argued that if these halos exceed $10^{12}\,\mathrm{M}_{\odot}$ at $z < 2$, then any cold gas that is accreted onto them will be shock heated to the virial temperature and become dispersed throughout the halo. At $z \geq 2$, these authors suggested that dense, cold streams of gas were able to penetrate the host gas, fuelling starbursts. Following the shock heating of gas as it is accreted onto a halo in the low-redshift Universe, this gas can be prevented from cooling by energy injection from an active galactic nucleus (though an AGN may not be required in very massive halos where the cooling time is large). The heating of the galactic halo by an AGN is termed radio-mode feedback. With a large sample of galaxies assembled from the SDSS, Bluck et al. (2014) showed that the total bulge mass appears to be the best predictor for whether a galaxy is quenched or not. They argued that since the mass of the supermassive black hole in the centre of the galaxy is tightly correlated with the mass of the bulge, and based on the energetics of such a black hole heating the surrounding gas,

that radio mode AGN feedback is likely to be responsible for the observed population of passive galaxies.

Alternatively, Davis et al. (2014) put forward evidence for a dynamical mechanism by which the suppression of star formation may occur. In their study of early type galaxies, they observed a reduced star formation efficiency in galaxies with large bulges. They proposed that in regions of a galaxy where the gravitational potential is steep, shear forces may stabilise the gas against further collapse, preventing star formation (See also Martig et al., 2013). Further morphological quenching can also be enacted by bars in galaxies. Gavazzi et al. (2015) studied the specific star formation rates of galaxies from $z = 0.3$ to now, and showed that systems with strong bars often have star formation in their centres that is well below the expected star formation rate for galaxies of their mass. While the centres of the galaxies can be rendered passive by the galactic bars, Gavazzi et al. (2015) noted that an additional quenching mechanism is required to shut down star formation in their outskirts.

Many surveys of the star-formation in galaxies have noted that the stellar surface density in galaxies is a good predictor for the star-forming properties of massive galaxies, with high stellar surface densities increasing the probability that a particular galaxy is quenched (e.g. Franx et al., 2008). Following on from this, Conroy et al. (2015), proposed that stellar winds and other ejecta from an evolved stellar population in a spheroidal galaxy may be sufficient to heat the surrounding interstellar medium, and thus prevent the collapse of molecular clouds to form new stars. In this situation the heating of the interstellar medium is enhanced by the random motions of the evolving stars through their host galaxy, leading to heating that scales with the stellar velocity dispersion in galaxies.

The phenomenology of mass quenching as presented by Peng et al. (2010) shows that whatever process may be responsible, it is independent of environment. As we saw in Section 1.3.1, the rate at which some environmental quenching mechanisms can influence a galaxy varies with the stellar mass of the galaxy. For example lower mass galaxies will be more easily stripped of their gas by ram pressure than a more massive galaxy. For this reason, most studies aimed at understanding environment quenching will control for the stellar mass in their sample.

1.4.2 Environment

In large galaxy surveys, the problem of discerning the environment quenching mechanism was approached from the perspectives of the timescale over which it is expected to act, and the measure of the local environment in which particular mechanisms would be most efficient. Lewis et al. (2002), observed the suppression of star formation in star-forming galaxies even in the outskirts of large clusters. This observation ruled out very rapid mechanisms such as ram pressure stripping as being the only cause of environment quenching. A similar conclusion was reached by the early work on the SDSS data by Gómez et al. (2003). In their sample of 8598 galaxies, they found that the star formation rates of star-forming galaxies is reduced above a critical projected galaxy surface density of $1\,\mathrm{Mpc}^{-2}$, even in the outer regions of clusters. With an even larger sample of 521 galaxy clusters,

von der Linden et al. (2010) solidified this result, concluding that strangulation must be the dominant environmental mechanism producing the red sequence in galaxy clusters.

There are some subtleties in the interpretation of the radial dependence of the suppression of star formation seen in galaxy clusters. The hierarchical picture of structure formation predicts that clusters will be surrounded by infalling galaxy groups (Frenk & White, 2012). If environmental effects in galaxy groups are efficient, then 'pre-processing', where environment-driven evolutionary effects are seen in galaxies prior to their accretion into a cluster, may occur (Zabludoff et al., 1996; Fujita & Goto, 2004). The enhanced signatures of environment quenching in infalling groups has been noted in several studies (e.g. Cortese et al., 2006; Wetzel et al., 2013; Haines et al., 2015; Bianconi et al., 2018), and may explain the radial trends mentioned above. The issue of contamination diminishes with the increasing depth and completeness of the spectroscopic surveys used to define the cluster and group environment.

The slow mode of was quenching was called into question by a study using GAMA data (Wijesinghe et al., 2012). This paper looked at the specific star formation rates of star-forming galaxies as a function of the local galaxy density, not including galaxies in clusters. Their analysis showed no change in the star formation rates of star forming galaxies with increasing environment density, but did notice a rise in the fraction of passive, non-star-forming, systems. This observation leads to the conclusion that any trend between the star formation rates of galaxies and their surrounding environment must be the product of an extremely rapid quenching process, or the result of a quenching process that occurred a long time ago.

A substantial effort has been made on GAMA data to improve their star formation rate estimates and incorporate a diverse suite of environment measures into their studies. The nearest-neighbour surface density measures used by Wijesinghe et al. (2012) have been used to great effect in a number of studies (e.g. Brough et al., 2013), and Chapter 2 of this thesis. These surface densities have the advantage of being valid across a wide dynamic range of environment densities. Moreover, this kind of measurement was noted by Muldrew et al. (2012) to be an excellent tracer of substructure within large-scale environmental overdensities such as clusters. The high level of spectroscopic completeness in GAMA has allowed some other measures of environment to be made as well. These include dark matter halo mass and group membership (Robotham et al., 2011), and the location of galaxies in filaments (Alpaslan et al., 2014), sheets and voids (Eardley et al., 2015).

These measurements have revealed a complicated picture of the evolution of galaxies in dense environments. For example, Davies et al. (2015) presented evidence that the interaction between galaxies in close pairs can both enhance and suppress star formation, with the more massive of the pair typically enhanced and the less massive of the pair quenched. The variation in star formation in their data appeared to be more prominent for Hα, a short-timescale star formation rate indicator, suggesting that close-pair interactions may play a significant role in the evolution of these galaxies. Davies et al. (2016a) showed that passive galaxies with stellar masses less than $10^{9.5}\,\mathrm{M}_{\odot}$ only exist in pairs. Simulation of the dynamical friction between merging galaxies by Boylan-Kolchin et al. (2008) predict that galaxies in this low mass range can have merging timescales in excess of 8 Gyr. Based

on this, Davies et al. (2016a) argue that strangulation is the most likely mechanism for producing passive galaxies in pairs. It should be noted that this analysis included very few galaxies in clusters.

For more massive galaxies with stellar mass above $10^{9.5}\,M_{\odot}$, Grootes et al. (2017) modelled the relationship between star formation rates of GAMA spiral galaxies and the rate at which they accrete gas from their surroundings. They found that aside from a minority of strongly quenched spirals, galaxies in groups appear to continue to accrete gas from their surroundings at approximately the same rate as non-group galaxies. The relationship between the colour of galaxies and their local environment density, they argue, is primarily due to the changing prevalence of galaxies with larger bulge components. The authors note that this conclusion is clearly in tension with the results of other studies that implicate strangulation as a major contributor to the red sequence outside of clusters.

1.5 Integral field spectroscopy: The resolution revolution

One way to break the stalemate between fast and slow-acting modes of quenching is to directly observe how that mechanism is affecting star formation in galaxies. Spectroscopy provides a wealth of information about the nature of the ionised gas and stellar components of a galaxy, from star formation rates and metallicities to stellar populations properties and dynamics. Unfortunately single fibre surveys such as 2dFGRS, GAMA, and SDSS require an aperture correction to estimate integrated quantities for galaxies and don't directly measure star formation rates in the outer parts of galaxies. In recent years the technique of integral field spectroscopy has been making progress in addressing these shortcomings.

1.5.1 Techniques of integral field spectroscopy

Integral field spectroscopy (IFS) is a technique that involves dividing the image plane up into smaller elements, called spatial pixels (spaxels), and then extracting a spectrum from each of these elements. There are several methods of achieving the segmentation of the image of a galaxy that can be used to construct an integral field spectrogram.

Image slicing

One method of dividing the image of a galaxy up is to use the technique of image slicing. This can be achieved by several means, but is commonly performed with a Bowen (1938) image slicer. This is an instrument constructed from several glass prisms placed at the focus of a telescope and located so as to direct different parts of the image to different parts of a spectral slit (Pierce, 1965). Image slicing can also be implemented by an array of slicing mirrors oriented at different angles. Image slicer spectrographs have been widely deployed in telescopes around the world (e.g. Content, 2006; Dopita et al., 2007). The basic principle of an image slicer is set out in Figure 1.7.

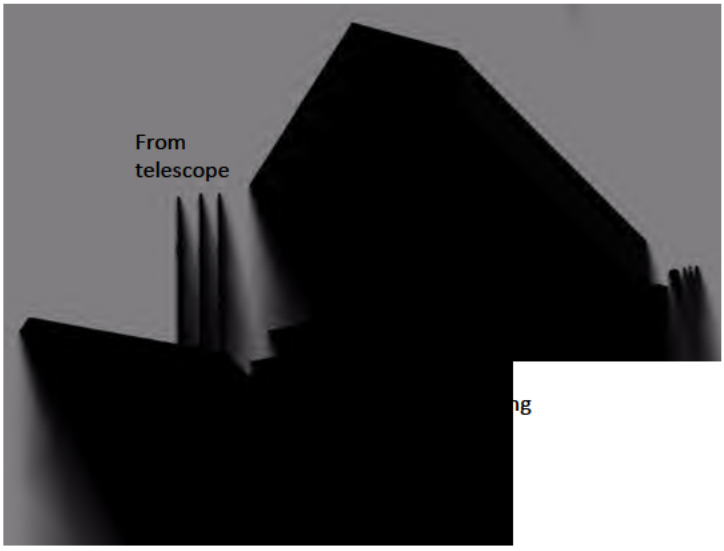

Figure 1.7: The basic layout for a Bowen image slicer. This image was taken from Pierce (1965) and shows the path of adjacent light rays through the apparatus. Light that falls onto different parts of the image plane are directed to different prisms (or mirrors in other designs) and therefore enter the spectrograph along different parts of the slit.

Lenslet arrays

A different approach to the problem of dividing an image up into spaxels involves the use of an array of micro lenses. In this scheme a closely packed array of very small lenses, called lenslets, focuses the light from the flat, uniformly filled image plane, to a sparsely filled regular grid of focussed points of light. These points of light are passed through a rotated grism, giving an array of spectra that can then be mapped back to the image plane, producing a spectral image of the target. Lenslet array integral field units (IFUs), like image slicers, have the advantage of completely covering the image plane in their field of view with minimal gaps. This style of instrument has been used by a number of telescopes including the Spectrographic Areal Unit for Research on Optical Nebulae (SAURON; Bacon et al., 2001), SINgle Faint Object Near-IR Investigation integral field spectrograph (SINFONI; Eisenhauer et al., 2003), and the Kyoto tridimensional spectrograph (Sugai et al., 2010). See Figure 1.8 for an example of a lenslet array.

Fibre-based IFS

Fibre-based integral field spectroscopy is a natural extension of single-fibre spectroscopy that allows the observer to sample multiple parts of a galaxy simultaneously. Optical fibre cores are combined to form a single IFU, and this structure, seen face-on in the example in Figure 1.9, is mounted at the focal plane of a telescope. The fibre cores receive the focussed light and transport it to a spectrograph, where it is dispersed for spectral analysis. The optical fibres that comprise the IFU are often circular in cross-section, which means that they do not completely fill the focal plane. During an observation the

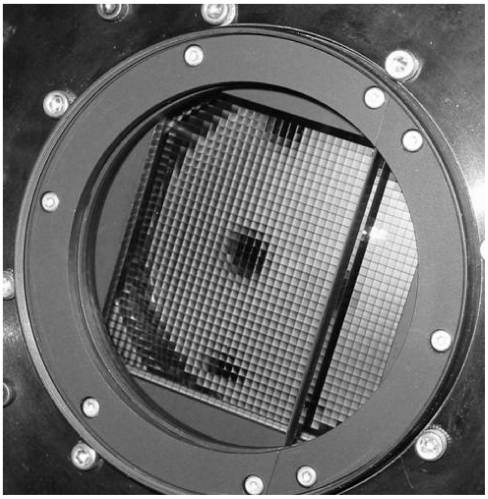

Figure 1.8: The lenslet array of the Kyoto tridimensional spectrograph, as shown by Sugai et al. (2010). Each lenslet in the grid focuses the light from their respective part of the image plane onto a grism, allowing the spectral decomposition of the target image at every point.

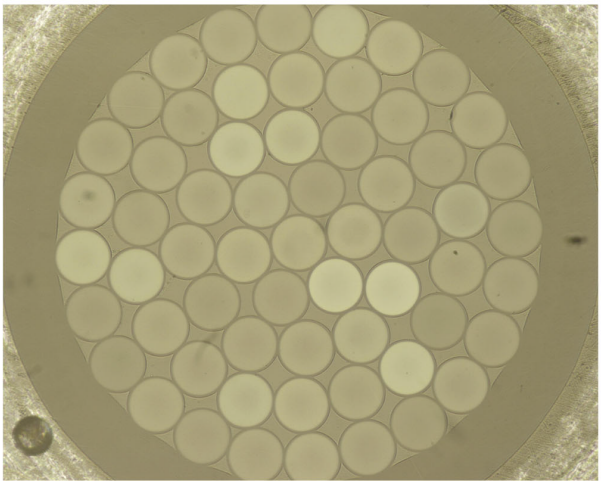

Figure 1.9: The face of one of thirteen SAMI hexabundles as imaged by Bryant et al. (2015). This hexabundle is composed of 61 fused fibre cores, which are fed into a spectrograph that disperses the light as desired.

Figure 1. Top: new design for the magnetic connector which attaches hexabundle to the field plate. The diameter of the footprint of the connecto is 12.5 mm on the field plate, requiring a separation of at least 15 mm between galaxies in any one tiled field. A rectangular protrusion or 'key' in the outer ring slots into a smaller hole in the plate beside a larger hol for the central hexabundle ferrule. The key secures the rotation of the bundl relative to the plate as desired. of the 61-core hexabundles manufacture at the University of Sydney. The diameter of the hexabundle is <1 mm an is mounted in the centre of the smallest tube in the top image, inset in th black cylinder which protects the face of the fibres.

pointing of the telescope can be dithered to fill in the gaps and achieve an even coverage of the target object. Fibre integral field units have adopted by many observatories around the world, and influential surveys such as the Calar Alto Legacy Integral Field Area Survey (CALIFA; Roth et al., 2005; Kelz et al., 2006; Sánchez et al., 2012), Mapping Galaxies at Apache Point Observatory (MaNGA; Bundy et al., 2015) and the Sydney-Australian Astronomical Observatory Multi-object Integral Field Spectrograph Galaxy Survey (SAMI; Croom et al., 2012; Allen et al., 2015; Sharp et al., 2015; Bryant et al., 2015). Fibre integral field spectrographs are preferred for large surveys because they are easily scalable and can include multiple IFUs in the same instrument without the need for additional spectrographs.

Table 1. Throughput of the upgraded SAMI fibre cable using WF105/125 fibre with slit blocks attached, compared to both bare fibre of the same type (WF105/125), and to the previous SAMI fibre type (AFS105/125). Throughputs were measured through *B* and *R* Bessel filters, centred at 457 nm (width 27 nm) and 596 nm (asymmetric profile of width 60 nm), respectively.

Fibre type (all 40+/−1 m long)	Percent blue throughput	Percent red throughput
AFS105/125	55	81
Bare WF105/125	83	91
WF105/125 fibre cable with slit block	82	91.5

1.5.2 The Sydney-Australian Astronomical Observatory Multi-object Integral Field Spectrograph

The SAMI instrument is a multi-object integral field spectrograph mounted at the prime-focus of the 3.9 m Anglo-Australian Telescope at Siding Spring Observatory, in New South Wales, Australia. It was commissioned in the year 2011, and upgraded to its current form in February 2013. SAMI comprises 13 hexabundle integral field units (Bland-Hawthorn et al., 2011), each with a total of 61 circularly-packed 100 μm fibre cores, that sample the image of a galaxy with a 73% fill-factor. Each fibre core subtends 1.″6 on the sky, giving the hexabundles a 15″ field of view. An additional 26 100 μm single fibres are deployed

has a throughput that is similar to bare WF105/125 fibre, and clearly much better than the AFS105/125 fibre used in the original SAMI instrument. In the blue, the fibre replacement gives a 30 per cent gain in throughput for the fibre component of the SAMI system.

simultaneously and are dedicated to night-sky calibration. All 819 fibres are fed into the AAOmega spectrograph (Sharp et al., 2006). The hexabundles and sky fibres are deployed over a 1 degree field of view.

1.5.3 The SAMI Galaxy Survey

SAMI was built for the purpose of complementing large galaxy surveys, with the SAMI Galaxy Survey taking most of the instrument's time on the telescope. This survey aims to observe approximately 3600 galaxies in total. The 2700 galaxies that make up the main sample have been selected from the GAMA spectroscopic survey. This main sample is supplemented with an additional 900 galaxies from specifically targeted galaxy clusters, that come from the 2dFGRS and SDSS (Owers et al., 2017). In this thesis we shall focus our attention on the non-cluster sample of galaxies. This main sample is selected from the equatorial regions of the GAMA survey in their 9, 12, and 15 hour right ascension fields. GAMA was selected as the parent catalogue for the SAMI Galaxy Survey because of its high level of spectroscopic completeness (98.5% down to a limiting magnitude of $r = 19.8\,\mathrm{mag}$; Liske et al., 2015).

The galaxies observed for the SGS have a selection function that covers a wide range in stellar mass ($10^7 < M_*/\mathrm{M}_\odot < 10^{12}$). The galaxy selection as a function of stellar mass is stepped in redshift between $z = 0.004$ and $z = 0.095$ to give four volume-limited samples that result in an approximately even distribution of stellar masses in the total sample. The final sample covers a large volume of space, meaning that the survey covers a representative sample of galaxies and environments in the local Universe. A full description of the SAMI Galaxy Survey Target selection is given by Bryant et al. (2015).

The combination of the SAMI multi-object integral field unit with the AAOmega spectrograph means that there is a lot of flexibility in the way that observations can be made. AAOmega is a dual-beam spectrograph that allows a large wavelength coverage at appreciable spectral resolution. For the SAMI Galaxy Survey a dichroic mirror is employed that passes light with wavelength, λ, above 5700 Å to the red arm of the spectrograph and reflects light with shorter wavelengths to the blue arm. In the red arm of the spectrograph, the light is passed through a grating with a resolution of $R = \lambda/\Delta\lambda = 4260$ at $\lambda = 6850$ Å, giving an approximately Gaussian line-spread function with a Full Width at Half Maximum (FWHM) of 1.61 Å. The red arm is configured to provide a wavelength coverage between $\lambda 6300 - 7400$ Å. The blue arm of the spectrograph is passed through a grating that yields $R = \lambda/\Delta\lambda = 1810$ at $\lambda = 4800$ Å for a line spread function with 2.65 Å FWHM. With this setup, the blue arm covers wavelengths between $3700 - 5800$ Å. See van de Sande et al. (2017) for the full details of how the spectral resolution was measured.

The SAMI Galaxy Survey uses the 13 hexabundles to simultaneously collect data on 12 galaxies, with the final hexabundle targeting a secondary standard star for calibration. While the filling factor of fibre cores in the SAMI hexabundles is higher than many other fibre integral field units, there is still some light lost between the cores during a single observation. To achieve 100% spatial coverage of the target galaxies, a hexagonal dither pattern is employed. This strategy involves offsetting the telescope between 0.″4 and 0.″7 and maintaining that pointing for a single exposure. Each pointing is maintained for

approximately 1800 s, though sometimes as low as 1500 s. Each set of galaxies is observed in up to 7 positions, giving a total integration time of 12600 s per galaxy.

The raw data are reduced using the 2 degree Field data reduction pipeline (2dFDR Croom et al., 2004). This process includes bias frame subtraction, dark current subtraction, wavelength calibration, extraction of the fibre image from the raw frames, and flat fielding. The resulting row-stacked spectra are then combined using the custom PYTHON SAMI software package to give the final, flux-calibrated three dimensional data cubes.

The volume of information that can be extracted from the SAMI data cubes is large in comparison to many other techniques such as narrow-band imaging, multi-band photometry, or single-fibre spectroscopy. Resolved spectroscopy allows us to extract kinematics and metallicity from both the stars and ionised gas, as well as calculate dust extinction and correct for its effects locally within a galaxy. The SAMI Galaxy Survey will therefore be an excellent resource for enhancing our understanding of galaxies and their evolution in the low-redshift Universe. In particular, the integral field capabilities of SAMI allows us to study star formation on a galactic scale in great detail. Coupled with the depth and completeness of the GAMA galaxy survey, the SAMI sample will provide an excellent testbed for different mechanisms of star formation quenching across a range of environments.

1.6 This Thesis

In this thesis we aim to address the question of what mechanisms act to quench star formation in galaxy groups. We utilise the spatially resolved measurements of Hα and Hβ emission made available through the SAMI Galaxy Survey to quantify the distribution of star formation within a carefully selected sample of galaxies. These data will allow us to look inside galaxies as they drop off the main sequence in dense environments, providing additional information about the nature of these quenching mechanisms. Combined with the GAMA survey data, which includes some of the best environment measures available, we quantify the changing distribution of star formation and attempt to relate this to how environment quenching proceeds in galaxy groups.

In Chapter 2 we present work that was published in the Monthly Notices of the Royal Astronomical Society. This paper includes a sample of 201 dust-corrected star formation rate radial profiles, integrated star formation rates and star formation concentration measurements. These values are compared to the fifth-nearest neighbour galaxy surface density environment measure (Σ_5), and the galaxy stellar mass.

In Chapter 3, which has been submitted for publication to Monthly Notices of the Royal Astronomical Society, we use an expanded sample of 325 star-forming galaxies to explore the types of environment that are likely to initiate quenching. Taking the specific star formation rate and the scale-radius ratio as as good indicators of quenching, we explore how these parameters vary with group halo mass, the estimated instantaneous tidal perturbation between galaxies, group-centric distance and velocity relative to the systemic velocity.

In Chapter 4 we focus on a sample of 4 galaxies with $10^{10.2} < M_*/\mathrm{M}_\odot < 10^{10.5}$ that appear to be undergoing environment quenching in massive groups. These are compared to a mass-matched sample of galaxies that are not in groups, and their properties are

compared. For this chapter we have performed a more comprehensive analysis of the galaxies, that takes advantage of the integral field spectroscopic nature of the data.

Finally, in Chapter 5 we briefly summarise our main results and conclusions. We go on to outline further work that will be done on this topic that will allow us to expand upon the results presented here.

Chapter 2

The SAMI Galaxy Survey: spatially resolving the environmental quenching of star formation in GAMA galaxies

The content of this chapter was published in the Monthly Notices of the Royal Astronomical Society in issue 464, pages 121–142, under the title '*The SAMI Galaxy Survey: spatially resolving the environmental quenching of star formation in GAMA galaxies*'. It was written by Schaefer, A. L.; Croom, S. M.; Allen, J. T.; Brough, S.; Medling, A. M.; Ho, I.-T.; Scott, N.; Richards, S. N.; Pracy, M. B.; Gunawardhana, M. L. P.; Norberg, P.; Alpaslan, M.; Bauer, A. E.; Bekki, K.; Bland-Hawthorn, J.; Bloom, J. V.; Bryant, J. J.; Couch, W. J.; Driver, S. P.; Fogarty, L. M. R.; Foster, C.; Goldstein, G.; Green, A. W.; Hopkins, A. M.; Konstantopoulos, I. S.; Lawrence, J. S.; López-Sánchez, A. R.; Lorente, N. P. F.; Owers, M. S.; Sharp, R.; Sweet, S. M.; Taylor, E. N.; van de Sande, J.; Walcher, C. J.; Wong, O. I.

All text was written by A. L. Schaefer as was all analysis of the reduced data. S. M. Croom, J. T. Allen, S. Brough, and N. Scott acted in a supervisory role, assisting with the direction of the project and the interpretation of the results. Spectral fitting was done using the LZIFU software, written by Ho et al. (2016a), though this software was been modified by A. L. Schaefer for this work. All data from the GAMA Galaxy Survey, including stellar mass estimates, Sérsic fit parameters, and were taken from catalogues without modification by the author. Figures in this chapter have not been modified form their published form, but some have been rescaled to fit the page.

Abstract

We use data from the Sydney-AAO Multi-Object Integral Field Spectrograph (SAMI) Galaxy Survey and the Galaxy And Mass Assembly (GAMA) survey to investigate the spatially-resolved signatures of the environmental quenching of star formation in galaxies. Using dust-corrected measurements of the distribution of Hα emission we measure the radial profiles of star formation in a sample of 201star-forming galaxies covering three orders of magnitude in stellar mass (M_*; $10^{8.1}$-$10^{10.95}\,M_\odot$) and in 5^{th} nearest neighbour local environment density (Σ_5; $10^{-1.3}$- $10^{2.1}\,\mathrm{Mpc}^{-2}$). We show that star formation rate gradients in galaxies are steeper in dense ($\log_{10}(\Sigma_5/\mathrm{Mpc}^2) > 0.5$) environments by $0.58 \pm 0.29\,\mathrm{dex}\,{r_e}^{-1}$ in galaxies with stellar masses in the range $10^{10} < M_*/M_\odot < 10^{11}$ and that this steepening is accompanied by a reduction in the integrated star formation rate. However, for any given stellar mass or environment density the star-formation morphology of galaxies shows large scatter. We also measure the degree to which the star formation is centrally concentrated using the unitless scale-radius ratio ($r_{50,H\alpha}/r_{50,cont}$), which compares the extent of ongoing star formation to previous star formation. With this metric we find that the fraction of galaxies with centrally concentrated star formation increases with environment density, from $\sim 5 \pm 4\%$ in low-density environments ($\log_{10}(\Sigma_5/\mathrm{Mpc}^2) < 0.0$) to $30 \pm 15\%$ in the highest density environments ($\log_{10}(\Sigma_5/\mathrm{Mpc}^2) > 1.0$). These lines of evidence strongly suggest that with increasing local environment density the star formation in galaxies is suppressed, and that this starts in their outskirts such that quenching occurs in an outside-in fashion in dense environments and is not instantaneous.

2.1 Introduction

The process of star formation is critical to the evolution of galaxies. The rate of star formation past and present has a significant effect on the optical colours and morphology of a given galaxy (Dressler & Gunn, 1992). It has become apparent that the environment within which a galaxy is situated plays an important role in that galaxy's development (e.g. Hubble & Humason, 1931; Oemler, 1974; Dressler, 1980). The presence of a relationship between galaxy environment and star-forming properties suggests that the transformation from star-forming to quiescent, a process called quenching, could be affected by the environment.

A number of mechanisms have been proposed that could cause quenching to occur. These mechanisms generally involve the removal of the gas supply that fuels star formation. Ram pressure stripping has been identified as a potential method for reducing the amount of available gas in a galaxy disc (Gunn & Gott, 1972) and in the surrounding halo (McCarthy et al., 2008). The role of ram pressure stripping in quenching star formation in cluster galaxies has been well established. The best evidence for ram pressure stripping acting to quench star formation within clusters comes from unresolved measurements of neutral hydrogen in cluster galaxies (e.g. Giovanelli & Haynes, 1985; Solanes et al., 2001; Cortese et al., 2011). The signatures of ram pressure stripping include the confinement of star formation to the central regions of the galaxy (Koopmann & Kenney, 2004a; Cortese et al., 2012), and the presence of a tail visible in Hα, neutral hydrogen, or both (Balsara

et al., 1994). Boselli et al. (2006) utilised multiwavelength imaging to constrain the stellar population gradients within a galaxy to confirm that ram pressure stripping acts on late type galaxies in clusters. This process is also capable of acting in compact groups (Rasmussen et al., 2008a) as well as in less concentrated environments (Bekki, 2009; Merluzzi et al., 2013). Nichols & Bland-Hawthorn (2011) successfully explain the gas fractions of dwarfs in the Milky Way + M31 system by modelling gas removal by ram pressure from these objects analytically. However, Rasmussen et al. (2008a) find that ram pressure stripping alone cannot explain the gas deficiencies in more massive group galaxies, with masses of approximately $4 \times 10^{10}\,\mathrm{M}_{\odot}$ or greater.

It has been pointed out that other transport processes could be responsible for the removal of gas from galaxy discs in dense environments. In particular, turbulent viscous and inviscid stripping have been suggested to be significant mechanisms for gas removal in dense environments (Nulsen, 1982; Roediger et al., 2013). When the velocity of the galaxy through the intergalactic medium is subsonic, viscous and turbulent mixing between the two media can become important in liberating gas from galaxies. The timescale for removing the gas from galaxies undergoing viscous stripping is shorter than for ram-pressure stripping (Nulsen, 1982). Modelling has shown that the morphological signatures of these mechanisms may be similar to those of ram-pressure stripping (e.g. Boselli & Gavazzi, 2006; Roediger et al., 2015).

The timescale on which a disc galaxy would deplete its gas through ordinary star formation is on the order of a few Gyr (Miller & Scalo, 1979; Tinsley & Danly, 1980). In order to explain the existence of gas-rich disc galaxies in the Universe today, it is necessary to suppose that the gas within their discs has been replenished by infall from the intergalactic medium (e.g. Larson, 1972). If this supply is cut off, then quenching will occur in a process called strangulation. This is most likely to transpire when the gas envelope surrounding spiral galaxies is swept away as the galaxy and its halo enter a cluster or group and fall through the denser intergalactic medium of these environments (Larson et al., 1980). Strangulation is likely to quench star formation over a period of several Gyrs (McCarthy et al., 2008) once the gas in the disc ceases to be replenished. Peng et al. (2015) estimate that strangulation is responsible for quenching approximately 50% of the passive galaxy population today, though they do not investigate the dependence of this fraction on environment density. Strangulation is predicted to occur in galaxy groups by Kawata & Mulchaey (2008). Some simulations (e.g. Bekki et al., 2002) suggest that the formation of anaemic spirals, systems with uniformly suppressed star formation (van den Bergh, 1991; Elmegreen et al., 2002), can be explained by strangulation. This process is not expected to produce the same spatial distribution of star formation as other processes such as ram-pressure stripping while quenching is taking place.

Galaxies in high-density environments such as clusters or galaxy groups may also experience tidal interactions with their nearest neighbours, or the group or cluster gravitational potential. These tidal interactions often have the effect of driving gas towards the centre of the galaxy and triggering circumnuclear starbursts (e.g. Heckman, 1990). These starburst episodes can deplete the gas reservoir of the galaxy, causing it to become quenched. Simulations (e.g. Hernquist, 1989; Moreno et al., 2015) have shown that gravitational instabilities driven by tidal interactions will drive a large fraction of the gas in a

galaxy towards the centre and enhance star formation on short timescales. This will have the effect of producing galaxies with centrally-concentrated star formation shortly after an interaction.

Faber et al. (2007) argued that gas-rich major mergers between blue-sequence galaxies can induce a period of starburst, which rapidly depletes the interstellar gas within these systems. Following this merger, the remnant moves to the red sequence. However, Blanton (2006) notes that between $z = 1$ and $z = 0$ the number of blue-sequence galaxies is reduced by less than 10%. This implies that major-merger-driven quenching cannot have been the dominant mechanism for decreasing star formation in the second half of the Universe's history.

Recently, large-scale spectroscopic and photometric surveys have been able to make significant progress in understanding the relationship between galaxy environment and star formation. Modern multi-object spectroscopic surveys such as the 2 Degree Field Galaxy Redshift Survey (2dFGRS; Colless et al., 2001), the Sloan Digital Sky Survey (SDSS; York et al., 2000) and the Galaxy and Mass Assembly survey (GAMA; Driver et al., 2011; Hopkins et al., 2013) have allowed the determination of star formation rates in several hundred thousand galaxies. However, the gain in sample size afforded by these single-fibre spectroscopic surveys is offset by the fact that the star formation in each galaxy is reduced to an estimate of the integrated total, which can be affected by aperture bias. Consequently, this observational technique has been unable to identify galaxies that are in the process of quenching, and arguments involving the timing and frequency of quenching must be invoked to determine which mechanisms are producing the observed trends.

A spectroscopic study of 521 clusters in the SDSS by von der Linden et al. (2010) indicated that the star formation rates of galaxies decline slowly during the infall into a cluster, with the most rapid quenching only occurring at the centres of clusters. The inferred quenching timescales were therefore long, roughly a few Gyrs, which is comparable to the cluster crossing time. This conclusion is in agreement with Lewis et al. (2002) and Gómez et al. (2003) who note the existence of galaxies with low specific star formation rates at large distances from the centres of clusters and conclude that rapid environmental quenching alone cannot explain the population of galaxies seen in the local Universe.

This picture appears to be inconsistent with the results of other work. Using the optical colours of galaxies, Balogh et al. (2004) argue that once galaxy luminosity is controlled for, the dominant environmental trend is the changing ratio of red to blue galaxies, with very little change in the average colour of the blue galaxies. Similarly a spectroscopic investigation by Wijesinghe et al. (2012) using GAMA data showed no correlation between the star formation rates of star-forming galaxies and the local environment density. In this sample, the trend was visible only when the passive galaxy population was included in the analysis, suggesting that it is the changing fraction of passive galaxies that is responsible for the observed environmental trends, and that quenching must therefore be either a rapid process or no longer proceeding in the local Universe.

The ambiguity between fast and slow-mode quenching may in part arise from the different definitions of passive and star forming used by various teams (see e.g. Taylor et al., 2015), as well as the different methods of quantifying environment density employed. Moreover, these large-scale surveys are not able to investigate the spatial distribution of

star formation in galaxies that are in the process of being quenched.

The spatial properties of star formation in dense environments have been studied using narrow-band imaging of the Hα distribution within galaxies (e.g. Koopmann & Kenney, 2004b,a; Gavazzi et al., 2006; Bretherton et al., 2013). In the Virgo cluster, Koopmann & Kenney (2004a) note that approximately half of 84 observed spiral galaxies have spatially-truncated star formation while less than 10% are anaemic (have globally reduced star formation). Welikala et al. (2008) and Welikala et al. (2009), using spatially-resolved photometry from SDSS, suggested that the suppression of star formation in dense environments occurs predominantly in the centres of galaxies. Welikala et al. (2009) observed that the integrated star formation rates in star-forming galaxies decline with density, implying that the observed environmental trends cannot be completely explained by the morphology-density relation. In lower density group and field environments, Brough et al. (2013) used optical integral field spectroscopy to examine the radial distribution of star formation for 18 $10^{10}\,\mathrm{M}_{\odot}$ galaxies and found no correlation between the star formation rate gradient and the local density.

Several studies have also suggested that the stellar mass, bulge mass or other internal properties of a galaxy have a greater influence on whether it is quenched than does the environment (e.g. Peng et al., 2010; Bluck et al., 2014; Pan et al., 2016, among others). Peng et al. (2010) argued that quenching can be explained by two separable processes that depend on mass and environment. Mass quenching could be achieved by several mechanisms including AGN feedback, which either removes gas from the galaxy disc directly or prevents it accreting from the halo, or by feedback that is related to star-formation such as supernova winds.

While it is likely that all quenching mechanisms operate to some extent, it remains uncertain how dominant each mode is at a given environment density and galaxy mass. In this paper we investigate the radial distribution of star formation in galaxies observed as part of the Sydney-AAO Multi-object Integral Field Spectrograph (SAMI) Galaxy Survey (Croom et al., 2012; Allen et al., 2015; Bryant et al., 2015; Sharp et al., 2015). The application of spatially-resolved spectroscopy to this problem represents an important step towards a better understanding of the quenching processes in galaxies. With this technique applied to a large sample of galaxies, the spatial distribution of star formation in galaxies can be resolved and the direct results of the various quenching mechanisms can be observed. The broad range of stellar masses and environments targeted by SAMI make it an excellent survey for studying the spatial signatures of environmental quenching processes.

In Section 2.2 we introduce the data used, our target selection and important ancillary data. Section 2.3 details the data reduction techniques employed by SAMI and the subsequent analysis of the flux-calibrated spectra. Results are presented in Section 2.4 with a discussion and conclusion given in Sections 2.5 and 2.6 respectively. Throughout this paper we assume a flat ΛCDM cosmology with $H_0 = 70$ km s^{-1} Mpc^{-1}, $\Omega_M = 0.27$ and $\Omega_\Lambda = 0.73$ and adopt a Chabrier (2003) stellar initial mass function.

2.2 Data and Target Selection

SAMI is a fibre-based integral field spectrograph capable of observing 12 galaxies simultaneously (Croom et al., 2012). Below we describe the full SAMI Galaxy Survey, which will include ~ 3400 objects.

2.2.1 Target Selection

SAMI Galaxy Survey targets were chosen from the parent GAMA survey. GAMA provides a high level of spectroscopic completeness (98.5% in the regions from which SAMI targets were drawn; Liske et al., 2015), providing spectroscopy of targets 2 magnitudes deeper than the SDSS. Within the GAMA survey regions there is a large volume of complementary multi-wavelength data available, including radio continuum (NVSS; Condon et al., 1998, FIRST; Becker et al., 1995) and emission line data (HIPASS; Barnes et al., 2001), infrared (UKIDSS; Lawrence et al., 2007) and ultraviolet (*GALEX*; Liske et al., 2015) photometry, in addition to the SDSS and GAMA optical imaging, photometry and spectroscopy. The SAMI targets were selected from a number of pseudo volume-limited samples, with each volume based on a spectroscopic redshift corrected for local flow effects (Tonry et al., 2000) and galaxy stellar mass estimates of Taylor et al. (2011). Each volume is selected to be well above the sensitivity limits of the GAMA spectroscopic survey. SAMI will collect data for ~ 3400 galaxies in the redshift range $0.001 < z < 0.1$.

The full SAMI survey also includes a complementary cluster sample of ~ 600 galaxies selected from eight clusters. High mass clusters are not well-represented in the GAMA survey and as such the SAMI cluster galaxies have been selected in a different way to the main sample. To ensure homogeneity for our sample, we do not include the cluster galaxies in this study. The target selection for the SAMI survey is discussed in detail by Bryant et al. (2015).

2.2.2 SAMI Data

The data used in the present study were obtained between 2013 and 2015 as part of the SAMI Galaxy Survey. Each of the 808 galaxies comprising our input sample were observed with an offset dither pattern of approximately 7 pointings to achieve uniform coverage, with each pointing being exposed for 1800 s and a total integration time of 12600 s for each galaxy.

The raw data were reduced with the 2dFDR pipeline (Croom et al., 2004). This process resulted in row-stacked spectra that have been wavelength calibrated and subtracted of night sky continuum and emission line features. These spectra are combined into data cubes using a PYTHON pipeline[1] designed specifically for the construction of SAMI data cubes. The process of constructing the data cubes includes a correction for atmospheric dispersion, flux calibration and the removal of telluric absorption features. The data reduction is described in detail by Allen et al. (2015) and Sharp et al. (2015). The data

[1] Astrophysics Source Code Library, ascl:1407.006 `ascl.net/1407.006`

for each galaxy observed are divided between two cubes corresponding to the blue and red arms of the AAOmega spectrograph (Sharp et al., 2006). These spectral cubes cover wavelengths $\lambda\lambda$3700–5800 Å with a spectral resolution of R = 1810 (at λ = 4800 Å) for the blue and $\lambda\lambda$6300–7400 Å in the red at R = 4260 (at λ = 6850 Å)[2]. The data from each of the dithered pointings were regridded onto a 50×50 array of $0\farcs5$ square spatial picture elements (spaxels), each containing the spectrum of the target galaxy at that point. For a full discussion of the cubing process, see Sharp et al. (2015).

2.2.3 Environment Density

From an observational perspective it is difficult to define a single metric which fully describes the local environment of a galaxy. The metric used must be guided by the available data and the environmental processes of interest. For example, the effects of the gaseous intracluster medium on galaxy evolution are best quantified by using the X-ray properties of the cluster (see e.g. Owers et al., 2012), while galaxy merger or interaction rates can be studied using analysis of galaxy close pairs (e.g. Patton et al., 2000; Robotham et al., 2014). It is not clear what physical mechanism causes the environmental quenching of star formation, so there is no obvious choice as to which metric is appropriate to identify the various processes, although it is appropriate to select a measurement that is sensitive over a variety of density ranges. Muldrew et al. (2012) constructed mock observational catalogues from cosmological simulations to examine the relationship between various environment density metrics and the underlying dark-matter distribution. They found that n^{th} nearest neighbour estimators, defined as $\Sigma_n = \frac{n}{\pi \times r_n^2}$, where r_n is the projected distance to the galaxy's n^{th} nearest neighbour above some absolute magnitude limit, performed well at recovering the local density of dark matter.

We use the fifth-nearest-neighbour local surface density measurement, Σ_5, to quantify the local environment around galaxies that have been targeted by SAMI. The high level of spectroscopic completeness of the GAMA survey means that it is well suited to calculating Σ_5. These environment measurements are performed on a density defining pseudo-volume-limited population of galaxies that have been observed spectroscopically by GAMA. This population includes all galaxies in the GAMA-II catalogue with reliable redshifts and K-corrected SDSS r-band absolute magnitudes, $M_r(z_{ref} = 0, Q = 1.03) < -18.5$, where $Q = 1.03$ models the expected redshift evolution of M_r (Loveday et al., 2015). Only objects within 1000 km s^{-1} of a target galaxy contribute to the estimate of its local surface density and the observed surface density is scaled by the reciprocal of the survey completeness in that vicinity[3] (Brough et al., 2013).

In practice the measurement of Σ_5 can be difficult. In GAMA, galaxies for which the fifth nearest neighbour is more distant than the nearest survey boundary may have

[2]These spectral resolutions differ from the values quoted in previous SAMI papers. The latest resolution values are derived empirically from CuAr arc spectra by Van de Sande et al. *in prep.*

[3]The GAMA spectroscopic completeness, defined as the ratio of the number of objects with measured redshifts to the number of potential spectroscopic targets in a survey region, is extremely high. For the 808 input SAMI galaxies the mean GAMA completeness in the surrounding region is 0.976 with a standard deviation of 0.038. As such, the reciprocal weighting of the Σ_5 measurements will not bias the results presented here.

erroneous environment density measurements, and the true value of Σ_5 is probably higher than the value measured. Galaxies for which this is a problem are more likely to be situated in the lowest density environments. We have rejected 188 galaxies for which Σ_5 was not able to be reliably measured.

The GAMA catalogue also includes two other environment density estimates: A Counts In Cylinder measurement, which counts the number of galaxies in a cylinder of radius 1 h^{-1} Mpc and depth of 1000 km s^{-1}, and an Adaptive Gaussian Ellipsoid (AGE) density measurement following Schawinski et al. (2007).

Given that the results of Muldrew et al. (2012) indicate that the adaptively-defined Σ_5 measurement will recover the underlying density field in small-scale dense environments better than the aperture-based density measurements we will use this as the metric for environment density for the majority of our analysis. We shall use the term "local density" to refer to Σ_5 and unless otherwise stated all environment density measurements will be 5^{th} nearest neighbour densities. This choice of environment density metric is the same as has been used in previous studies of environmental quenching using the GAMA survey (Wijesinghe et al., 2012; Brough et al., 2013).

2.2.4 Stellar masses

We make use of the GAMA photometric estimates of the galaxy stellar masses derived by Taylor et al. (2011). Stellar masses were calculated using stellar population synthesis modelling of the GAMA *ugriz* spectral energy distributions and assuming a Chabrier (2003) stellar initial mass function. These calculations are used to produce a four-parameter fit which includes the e-folding timescale for the star formation history, age, stellar metallicity, and dust extinction. Modelling the galaxy SEDs in this fashion produces estimates of the mass-to-light ratio with typical statistical uncertainties of approximately 0.1 dex for galaxies brighter than $r_{petro} = 19.6$ mag. These measurements were made using the total integrated light for each galaxy and as such estimate the integrated stellar mass for the entire galaxy, which is often larger than the SAMI aperture.

2.2.5 Sample selection

While the capabilities of integral field spectroscopy allow us to construct a more complete picture of the star formation morphology of a galaxy than single fibre or long-slit spectroscopy, the nature of a large-scale hexabundle IFS survey presents us with some limitations. In particular, the SAMI instrument consists of hexabundles (Bland-Hawthorn et al., 2011; Bryant et al., 2014) which subtend 15″ on the sky. The combined effect of the on-site seeing and the data cube construction process results in a point spread function (PSF) full width at half maximum (FWHM) distribution with median $\sim 2\farcs2$. Thus, we are faced with biases at both high and low redshifts. At low redshifts we encounter the problem that galaxies with higher stellar mass are not sampled out to large radii and we risk the interpretation of small-scale substructure within a galaxy as a true star formation rate gradient. Conversely, at higher redshifts galaxies will tend to have smaller angular sizes and the spatial structure can be dominated by beam smearing of the image intro-

duced by the seeing during observation. We reduce these issues by selecting only galaxies for which the SDSS r-band effective radius (r_e) satisfies $0.4r_e \leq 7''.5 \leq 3.0r_e$. That is, the SAMI hexabundle field-of-view, with projected radius of $7''.5$, must not sample a galaxy beyond $3.0r_e$ or encompass a region of the galaxy less than $0.4r_e$ in radius. A total of 55 galaxies from the original 808 are rejected under these criteria.

In addition to the constraints placed on this sample by the target selection of the SAMI Galaxy Survey, some further restrictions on the galaxies analysed were required to ensure the integrity of this work. Photoionisation of ambient gas within each galaxy from non-stellar sources or an old stellar population will contaminate the measurement of star formation. This will be the case for galaxies with an active galactic nucleus (AGN) or a Low Ionisation Nuclear Emission Region (LINER). To guarantee that the measured Balmer line flux was the result of gas excitation from a young stellar population, the spectrum from a central circular $2''$ aperture was extracted from each galaxy. Within this aperture the intensities of Hα, [N II] λ6583, [O III] λ5007 and Hβ were measured and compared (see Section 2.3.2 for a discussion of the emission line measurements).

We used the ionisation diagnostics of Kewley et al. (2001) and Kauffmann et al. (2003c) to classify each central-spectrum as either AGN/LINER, composite or star-forming. Systems with line ratios above both the Kauffmann and Kewley lines were identified as AGN/LINER and those between the two diagnostic curves were classified as composite. A total of 179 galaxies with AGN-like emission line ratios were found with this method, though the emission line signal-to-noise ratio in 76 of these were so low that this classification is uncertain. All of these galaxies were removed from the sample. A further 111 galaxies classified as composite were also rejected. Systems classified as either AGN or composite have not been included in the final sample. A Baldwin et al. (1981) diagnostic diagram is shown in Figure 2.1 for our data and shows the separation of the star-forming sample from galaxies that are not star-forming.

Given that our sample covers a range of redshifts, an aperture of fixed angular size will cover a larger area of a target galaxy that is at higher redshift. This may lead to a systematic mixing of the flux from an AGN with the flux from the surrounding galaxy, with the level of contamination increasing with redshift. However, given that the median point spread function in the reconstructed data cubes is $2''.2$, this contamination is already present, meaning that the contamination of the central spectrum by the surrounding galaxy is unavoidable. The mixing of the AGN and star-forming spectral components is discussed by Kauffmann et al. (2003c). We note that for galaxies that contain AGN, the effect of this mixing is to move their emission line ratios from the AGN region of the Baldwin et al. (1981) diagram, to the composite region. As we reject such galaxies from our sample, the contamination of star-formation in the most distant galaxies in our sample is likely to be minimal.

In the case of edge-on disc galaxies, the radial binning technique applied to our maps cannot give an accurate picture of the true radial profile of the star formation rate. 126 galaxies with ellipticities greater than 0.7 were classified as edge-on disc galaxies and were therefore also rejected. We discarded an additional 199 galaxies for which the PSF FWHM for the observation extends more than $0.75r_e$ or is greater than $4''$ to minimise the effect of beam smearing on our conclusions. Finally, given the range of emission

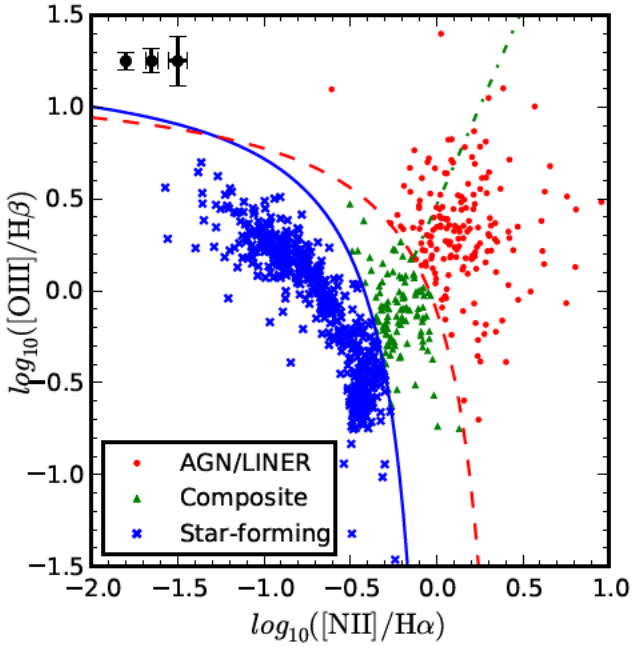

Figure 2.1: An ionisation diagnostic diagram (Baldwin et al., 1981) for the 808 galaxies in our input sample. The red dashed curve is the AGN cutoff of Kewley et al. (2001) and the solid blue curve is the star-forming limit as defined by Kauffmann et al. (2003c). The diagonal, green dot-dashed line separates AGN from LINERs. The emission line fluxes are extracted from the central circular 2″ of each galaxy. Galaxies classified as AGN/LINER (179) are represented by red points, those with composite spectra (111) are marked with green triangles, and galaxies with emission line ratios consistent with ionisation from a young stellar population are classified as star-forming (518) are marked with blue crosses. In the top left of this diagram we show, from left to right, the 25^{th}, 50^{th} and 75^{th} percentile error bars on each quantity in black.

line strengths in the sample, it was useful to split the galaxies into two groups based on their absorption-corrected Hα equivalent widths ($\mathrm{EW_{H\alpha}}$), with positive equivalent widths indicating emission. Equivalent widths were determined by summing the entire data cube over its spatial dimensions and deriving the EW from the resulting spectrum. For this purpose, the EW is defined as the continuum-corrected Hα flux divided by the continuum level at the Hα wavelength extrapolated over the absorption line. As the $\mathrm{EW_{H\alpha}}$ in star-forming systems is tightly correlated with their specific star formation rate, we define galaxies for which the integrated aperture spectrum has $\mathrm{EW_{H\alpha}} > 1$ Å in emission as star-forming and galaxies with $\mathrm{EW_{H\alpha}} \leq 1$ Å as quiescent. This distinction separates those galaxies in the star-forming "main sequence" from those which appear to be quenched. Cid Fernandes et al. (2011) recommend a 3 Å cut in $\mathrm{EW_{H\alpha}}$ to separate passive and star-forming galaxies. However, this recommendation was based on the use of SDSS single-fibre spectroscopy and is thus sensitive to the distribution of star formation within the system. Our summation over the entire SAMI aperture ensures that galaxies with, for example,

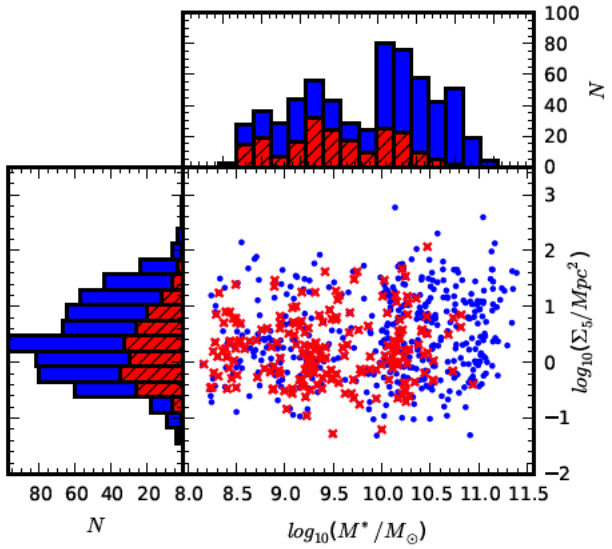

Figure 2.2: The distribution of galaxy stellar masses and fifth-nearest-neighbour surface densities for our sample. Blue and red points represent the entire sample of 808 observed SAMI galaxies and red indicates the sample after the application of the constraints outlined in Sections 2.2.1 and 2.2.3. The upper histograms show the distributions of $\log_{10}(M_*/M_\odot)$ and the histograms on the left are the distributions of $\log_{10}(\Sigma_5/\mathrm{Mpc}^2)$ with blue for the input sample and red hatched for the final star-forming sample. Note that the subsample retained for analysis has reduced coverage of the M_*-Σ_5 parameter space, with most galaxies lost at high stellar mass and in high density environments.

passive centres and star-forming edges are not selected against. The reduction of the $EW_{H\alpha}$ cut takes into account the contribution from the passive regions of the galaxy.

We find that the rejection of galaxies based on their central spectrum, $EW_{H\alpha}$ and ellipticity is sufficient to eliminate all significant non-central non-star-forming emission from our sample. Highly inclined galaxies that show extra-planar emission or shock-excited winds driven by star formation (see e.g. Ho et al., 2016b) are rejected. For those that are not inclined to our line of sight, the contribution to the total flux is generally low enough as to not be detected. Galaxies with spatially extended line emission excited by old stellar populations (Sarzi et al., 2010; Belfiore et al., 2016) do not satisfy the $EW_{H\alpha}$ criterion.

Our final star-forming sample comprises 201 galaxies. Note that a number of galaxies that were rejected failed on multiple criteria. The star-forming sample contains galaxies with stellar masses in the range $10^{8.2}$-$10^{10.9}$ $M_\odot$ and fifth nearest neighbour environment densities in the range $10^{-1.3}$-$10^{2.1}$ Mpc^{-2}. This range of environment densities incorporates galaxies from low-density field environments to groups of halo mass $10^{14.5}$ $M_\odot$ and between 2 and 104 members per group, though the current sample does not include all the galaxies within each group. The variation of the star-formation properties of galaxies in groups will be the subject of a future paper. The distributions of galaxy stellar masses

and local environment densities are displayed in Figure 2.2. In this figure, blue colours indicate the input sample of 808 galaxies and red indicates galaxies that remain after the above constraints are applied. There is a dearth of star-forming galaxies with stellar masses above $M_* = 10^{11}\,M_\odot$. This is consistent with mass and environment quenching as described by Peng et al. (2010). We also show the distributions of other relevant parameters in our final sample in Figure 2.3. This final sample covers a wide range of galaxy stellar masses, environment densities and morphologies.

2.3 Spectral fitting and analysis

2.3.1 Binning And The Balmer Decrement

Obtaining accurate measurements of emission line fluxes, especially Hβ, is essential to estimating and properly correcting for the presence of dust obscuration along the line of sight. This is particularly important when the lines are observed to be only weakly in emission. In order to properly account for the underlying stellar absorption features, a S/N of at least 10 per angstrom in the continuum is desirable. In regions of galaxies with low surface brightness, such as the outer edges of the disk, some level of spatial binning is often required to achieve this. An added complication is that dust attenuation along the line of sight is corrected for using a non-linear combination of Hα and Hβ fluxes. In each spatial bin, the observed Hα fluxes, $f_{\mathrm{H}\alpha}$, are corrected for dust attenuation along the line of sight according to the Cardelli et al. (1989) dust extinction law. This correction uses the deviation of the Balmer decrement (BD; the ratio $f_{\mathrm{H}\alpha}/f_{\mathrm{H}\beta}$) from the theoretical value of 2.86 for case B recombination to model the amount of intervening dust along the line of sight.

$$F_{\mathrm{H}\alpha} = f_{\mathrm{H}\alpha}\left(\frac{BD}{2.86}\right)^{2.36} \tag{2.1}$$

This extinction correction assumes the dust to be a foreground screen that is not cospatial with the emission nebulae (Calzetti, 2001), and the assumption of case B recombination assumes a temperature of 10000 K and an electron density of $100\,\mathrm{cm}^{-2}$. The intrinsic Balmer decrement for an HII region is dependent on the temperature of the gas (Dopita & Sutherland, 2003), and therefore has a dependence on the oxygen abundance in the gas. Star-forming galaxies are observed to have radial gradients in their metallicity abundances (Vila-Costas & Edmunds, 1992; Zaritsky et al., 1994), and are therefore likely to exhibit gradients in the average temperature of the gas in their HII regions (e.g. Churchwell & Walmsley, 1975; Quireza et al., 2006). Dopita & Sutherland (2003) calculate that the intrinsic Balmer decrement can be as high as 3.04 when the temperature is 5000 K and as low as 2.75 when the temperature is at 20000 K. At the low-temperature end of this scale, the deviation of the Balmer decrement from the assumed value will mean that the true corrected flux is $\sim 15\%$ lower than we estimate. If the true HII region temperature is at the upper end of this temperature range, the true dust-corrected flux will be $\sim 9\%$ higher than our estimate. In general the deviations from the assumed temperature of 10000 K will be smaller than this, and indeed it is common throughout the literature to assume a temperature of 10000 K.

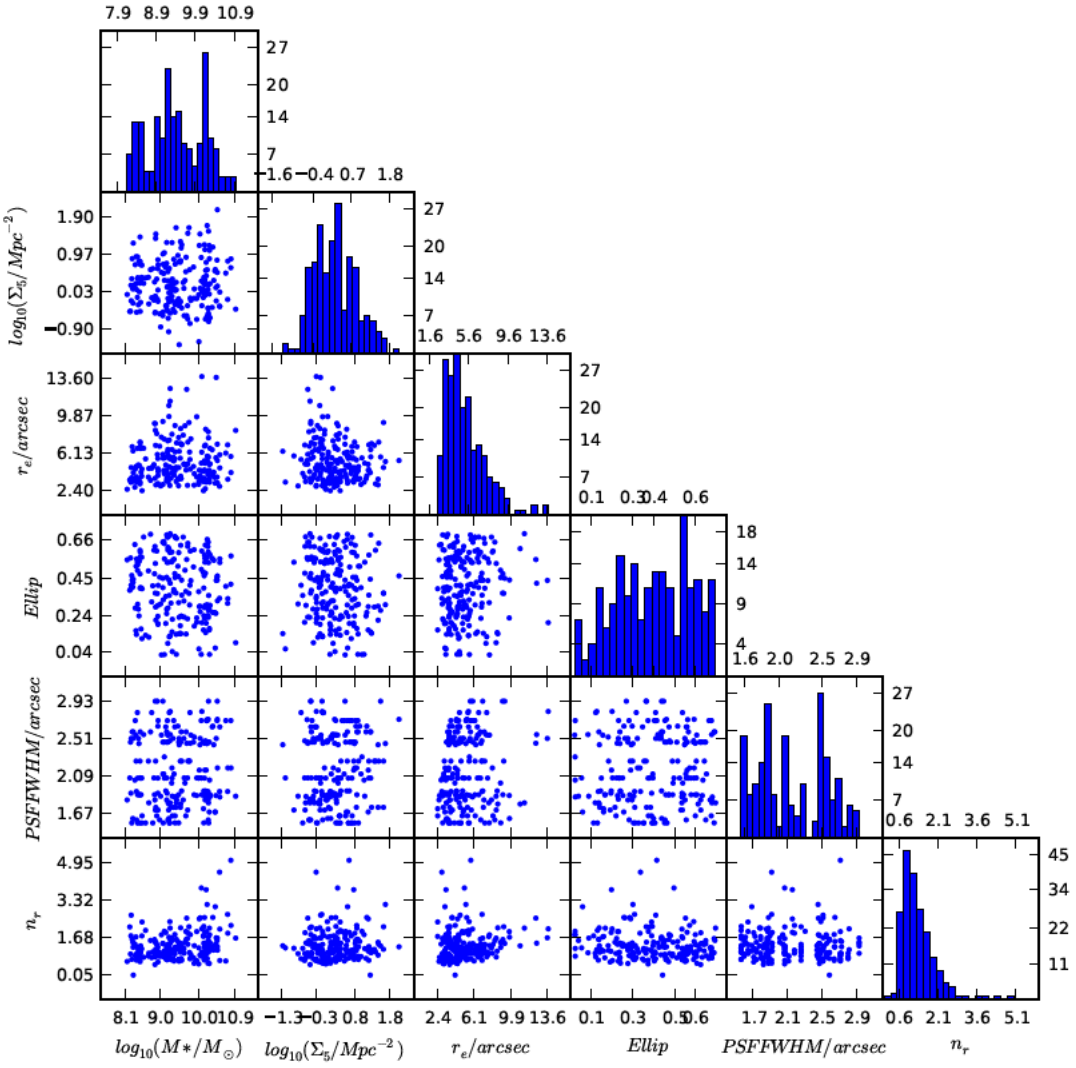

Figure 2.3: Global galaxy parameters for the final sample of 201 galaxies. We show the distributions of $\log_{10}(M_*/M_\odot)$, $\log_{10}(\Sigma_5/Mpc^{-2})$, r_e, ellipticity, PSF FWHM and the Sérsic n_r. Along the diagonal we show the histograms of each of these parameters while the off-diagonal diagrams show the relationship between the variables for each galaxy.

The addition of fluxes from spatially-distinct regions of a galaxy will result in an incorrect dust correction and an underestimation of the corrected Hα flux. Furthermore, summing the flux over large radial ranges in a data cube may have negative consequences for the interpretation of the radial gradients in galaxies. Averaging the Hα over a large radial bin will have theads note of flattening the radial profile, and providing a biased estimate of the star formation rate gradient. With these constraints in mind we have implemented a modified version of the adaptive binning algorithm of Cappellari & Copin (2003), which is based on the Voronoi tessellation of bins within an image to achieve a desired S/N. For this work we have performed what we term 'Annular-Voronoi binning'. In this scheme we define Voronoi bins within a series of concentric elliptical annuli with ellipticities and position angles defined by the r-band morphology of the target galaxy. Within each annulus a number of sub-bins are constructed to achieve a target S/N of 10 per Å in the continuum in a 200 Å-wide window around the redshifted wavelength of the Hβ line. The construction of each bin is subject to the constraint that the contributing spaxels must be contiguous. The determination of the variance value in each Voronoi bin takes into account the spatial covariance in the SAMI data described by Sharp et al. (2015). The binning is applied to both the blue and the red SAMI data cubes. This scheme has the advantage of improving the reliability of continuum subtraction, retaining the radial structure within galaxies and maintaining the locality of the dust corrections. An example of such an annular bin is shown in Figure 2.4.

The application of our annular Voronoi binning method has some advantages over other commonly used adaptive binning schemes. The standard Voronoi binning scheme as outlined by Cappellari & Copin (2003) works by taking an initial spaxel, and accreting adjacent spaxels to construct a roughly round bin with the desired S/N ratio. With this technique, large bins will often cover a large radial range within a galaxy, and may sum over significant changes in the emission line properties. An alternative technique explored by Cappellari & Copin (2003) is the quadtree adaptive binning method (Samet, 1984). This achieves a higher S/N in groups of spaxels by constructing a mesh of square bins that each achieves the required S/N ratio. The quadtree method suffers from the same problem as the Voronoi method, that is, bins the may cover a large radial range. Further to this, the circular geometry of the SAMI hexabundles means that the bins at larger radius will often not achieve the desired S/N ratio. If is for these reasons that we have elected to use the annular Voronoi method for our analysis.

We have calculated the Hα luminosity, L(Hα), of each galaxy using both a single global dust correction from the spatially integrated IFU (SFR_{glob}) and from summing locally dust corrected Hα within the annular Voronoi bins (SFR_{loc}). The star formation rate can be calculated from the total L(Hα) using the Kennicutt (1998) relation with a Chabrier (2003) IMF:

$$\mathrm{SFR} = \frac{L(H\alpha)}{2.16 \times 10^{34}\ \mathrm{W}}\ \mathrm{M}_{\odot}\ \mathrm{yr}^{-1} \tag{2.2}$$

It should be noted that we have not corrected the star formation rate for aperture effects. Despite the ability of integral field spectroscopy to sample a large area of a target source, we are often unable to observe Hα emission in the outer regions of galaxies. A correction for this aperture bias has been developed by Hopkins et al. (2003a) and

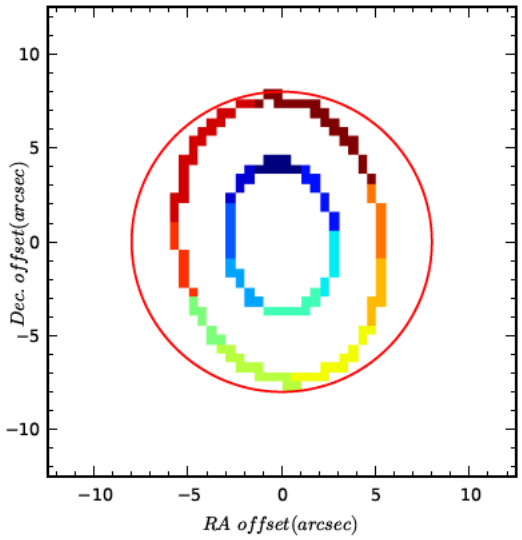

Figure 2.4: An example of Annular-Voronoi binning which has been applied to the SAMI data cubes. In this example, spaxels in two annuli with an ellipticity of 0.28 at a position angle of 98.8° and a width of one spaxel are grouped into contiguous sub-bins, represented here as groups of pixels with the same colour. Spectral fitting, emission line integration and dust corrections are performed independently within each sub-bin. The red circle represents the size of the SAMI aperture. For clarity, only two annular bins are shown, although the entire SAMI field is partitioned into bins.

Brinchmann et al. (2004) for single fibre spectroscopic observations of galaxies but an analogous correction has not been applied to this data (but see Richards et al., 2016, for a discussion of aperture corrections to star formation rates with SAMI). There is no systematic correlation between the projected sizes of the galaxies in our sample and other galaxy properties including M_* and Σ_5, meaning that aperture effects will not have a strong impact on the integrated specific star formation rates we present here. We compare the integrated star formation rates (SFRs) for the star-forming galaxies in our sample using the two different dust correction methods in the upper panel of Figure 2.5. A one-to-one relationship appears to hold for the star formation rates of galaxies in the star-forming sample. For quiescent galaxies neither measurement is very accurate as the relative errors become high. Furthermore, the lower panel of Figure 2.5 shows that above a SFR of 1 $M_\odot$ yr^{-1}, the global dust correction underestimates the SFR by approximately 8% on average. We note that this conclusion is based on a small number of galaxies, and that this figure is likely to be revised if a larger sample size is employed. This discrepancy is as expected and we thus use the locally dust corrected star formation rates for the remainder of this work.

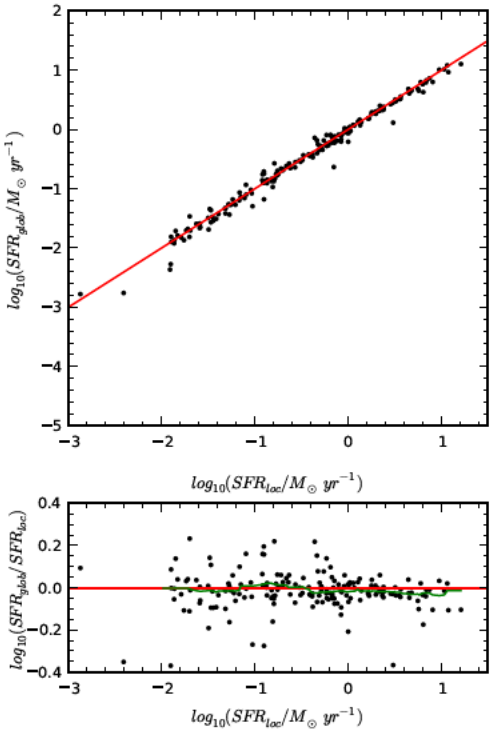

Figure 2.5: Comparison of integrated star formation rates for objects in the star-forming sample using local dust corrections within each Annular-Voronoi bin and with a single dust correction for the whole galaxy. Red lines indicate the line of equality. In the upper panel we compare these two methods. In the lower panel we show the log ratio of the star formation rate estimate for these two methods. The green line is the running median, calculated in a sliding window of width 0.5 dex. There is a shallow downward trend, indicating the global dust correction is underestimating the star formation rate for the most star-forming galaxies. For galaxies forming stars at a rate greater than 1 $M_\odot$ yr^{-1}, the average $SFR_{glob}/SFR_{loc} = 0.917 \pm 0.016$.

2.3.2 Emission line fluxes

Fluxes were extracted from each annular Voronoi bin using a modified version of LZIFU, a pipeline designed by Ho et al. (2014) and described in detail by Ho et al. (2016a). LZIFU incorporates stellar template fitting to the continuum using Penalized Pixel Fitting (pPXF; Cappellari & Emsellem, 2004) and returns a multiple component Gaussian fit to the emission lines using the MPFIT algorithm (Markwardt, 2009). The accuracy of the emission line flux measurements is ultimately tied to the accuracy with which we can fit and subtract the underlying stellar absorption features. The stellar continuum in each spectrum has been modelled using pPXF to fit a combination of simple stellar population models (SSP) from the MILES library (Vazdekis et al., 2010) as well as an 8^{th} degree multiplicative polynomial to account for any residual flux calibration errors and the reddening effect of dust. Strong emission lines were masked during the fitting process

and weaker emission lines were clipped by setting the CLEAN keyword when invoking pPXF. A 65 template subset of the full MILES SSP library was used to independently fit the stellar continua in each spatial bin. These templates span 5 stellar metallicities in the range $-1.71 \leq [Z/H] \leq 0.22$ and for each of these metallicities sample SSPs at 13 logarithmically spaced ages between 0.063 and 14 Gyrs. These models were formed at a spectral resolution of 2.5 Å FWHM. Note that this is higher than the spectral resolution of the 580V grating used in the blue arm of the SAMI instrument but lower than the spectral resolution of the 1000R grating used for the red arm of SAMI. This discrepancy in the resolutions will mean that a minimum stellar velocity dispersion can be measured from our data. At 6890.94 Å, the wavelength of the Hα absorption line at a redshift of 0.05, this corresponds to a minimum measurable stellar velocity dispersion of 37.8 km s^{-1}. This velocity dispersion is a reasonable lower limit on the measured dispersion of spectra in SAMI. The values for the velocity dispersion returned by the pPXF fit of the MILES templates to the red SAMI data cubes are unreliable, however, a good fit to the data is still obtained and the stellar absorption correction is valid. In any case, the emission line fitting is done after the continuum has been subtracted from the spectrum and the spectral resolution of the stellar templates has no effect on the emission line measurements. In each spaxel the wavelengths of the emission lines fit are allowed to float relative to the redshift of the stellar continuum, but are fixed with respect to each other. LZIFU outputs maps for the distribution of the strongest emission lines which have been corrected for absorption by the stellar continuum. An example of the resulting fit to a spectrum that shows all the relevant features is shown in Figure 2.6.

2.3.3 Radial Profiles

The radial profiles of star formation were calculated from the LZIFU outputs. Each galaxy was treated as a circular disc tilted at some angle to the line of sight. To take into account the effect of this projection onto the sky, the radial profiles of Hα were constructed by averaging the dust corrected fluxes over a series of concentric elliptical annuli. These annuli were centred on the centroid of the continuum flux of each galaxy, with their ellipticities and position angles based on the GAMA photometric model fits to reanalysed SDSS DR7 r-band images (Kelvin et al., 2012). Some examples of radial profiles, dust-corrected Hα maps and EW(Hα) maps are shown for galaxies with a range of stellar masses and star-forming morphologies in Figure 2.7. Taking the inclination of the galaxy to our line of sight improves our estimate of the radial distribution of Hα. However, in some cases the presence of strong morphological irregularities such as bars, and spiral arms can skew the photometric fit and yield erroneous parameters. A visual inspection of the GAMA Sérsic profile fits for the 201 star-forming galaxies in the sample resulted in the identification of 15 galaxies where the galaxy morphology skews the photometric fit and the measured ellipticity does not constrain the inclination to our line of sight well. The prevalence of these galaxies shows no trend with stellar mass or environment density. Moreover, this effect changes the measured average surface brightness at $1\,r_e$ typically by less than 0.2 dex and never more than 0.4 dex. We therefore conclude that such galaxies do not affect the results of this work.

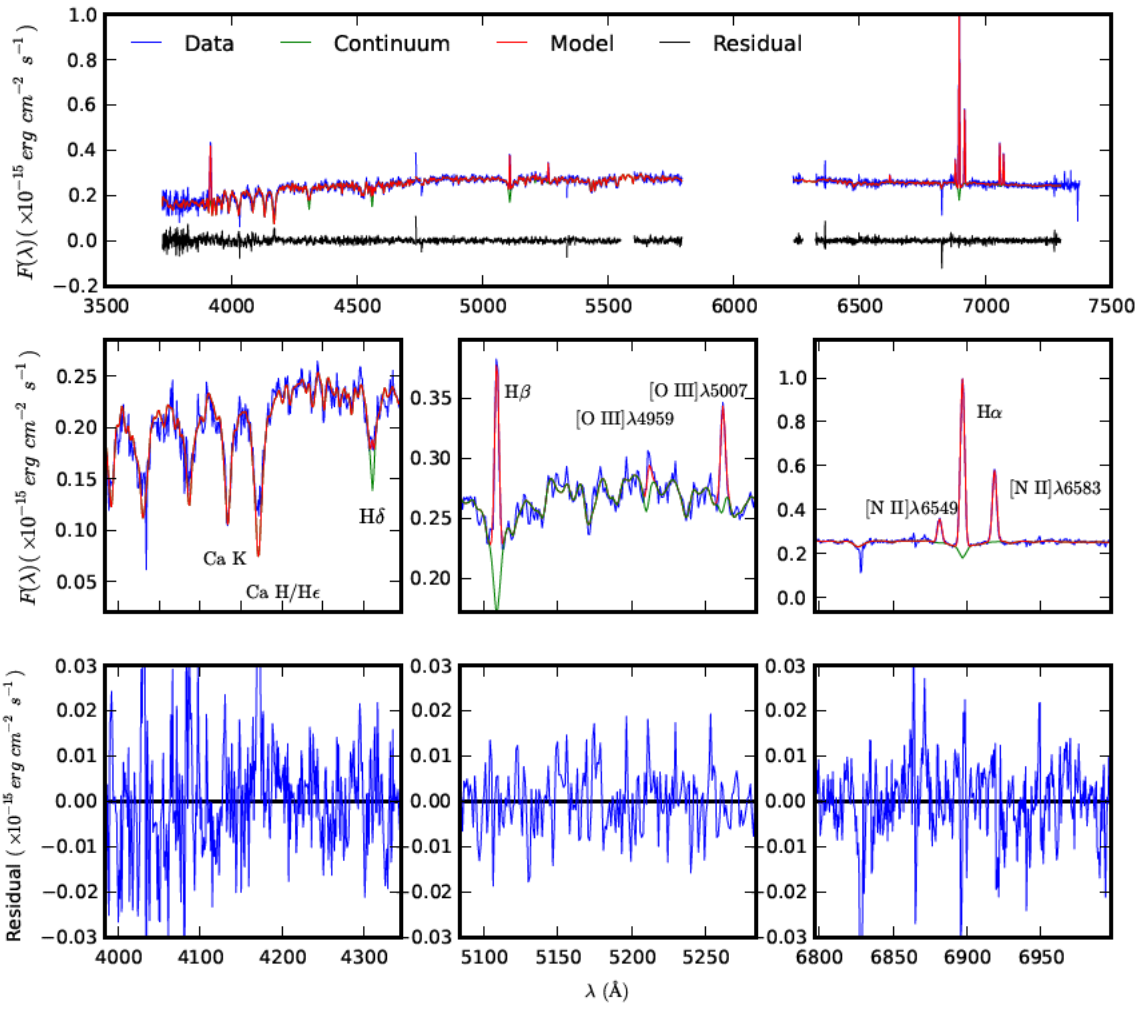

Figure 2.6: An example of spectral fitting using LZIFU for a single spaxel in a star-forming galaxy (GAMA catalogue ID: 517070). This is a typical star-forming galaxy and was chosen for illustrative purposes based on the intermediate S/N of the continuum and emission lines so that all the spectral features are easily visible within a single panel. The fitted model (shown in red) includes a linear combination of simple stellar population templates to fit the continuum and a series of Gaussians for the emission lines. The continuum model, which is composed of the combined stellar templates, is shown in green. In the upper row we show the spectrum, fit and residuals to the entire optical spectrum for the galaxy in a single spaxel. The central row shows the spectrum continuum and emission line fit around the D_n4000, Hβ and Hα spectral features. The lower row shows the residuals to the fit in the corresponding wavelength range. The horizontal black lines denote the zero point. Higher order Balmer emission lines have not been fitted, as only Hα, Hβ and Hδ were used for this work. The spikes in the residual spectrum in the first column are the result of these emission lines not being accounted for in the model.

For an ensemble of galaxies it will be useful to construct an average radial profile that is indicative of the radial behaviour of the star formation distribution for the group as a whole. We can construct a 'median profile' for a selection of galaxies by choosing the median value of log-flux in some radial bin. For this work we have rebinned each radial profile onto a grid with the radial axis in units of r_e, the r-band effective radius within which one half of the total r-band light is contained. Each radial bin has a size of $0.2\,r_e$, and in each bin we calculate the value of the median radial profile by simply extracting the median flux. At each point the errors on the measurement of the median are computed from the standard deviation of 1000 median values obtained by bootstrap resampling of radial profiles in the sample. The radial profiles of Hα for all the star-forming galaxies in our sample are shown in Figure 2.8. These profiles are split into three equally sized bins of $\log_{10}(\Sigma_5/\mathrm{Mpc}^2)$ and $\log_{10}(\mathrm{M}_*/\mathrm{M}_\odot)$. To quantify the changes in the star formation distribution in galaxies of different stellar masses and in different environments we fit each median profile in Figure 2.8 with an exponential of the form

$$\log_{10}(\Sigma_{L(\mathrm{H}\alpha)}) = a \times r/r_e + b. \tag{2.3}$$

The parameters of these fits are displayed in Figure 2.8 at the upper right of each panel. The errors on these parameters are obtained by bootstrap resampling the galaxies in each stellar mass and environment density bin, recalculating and refitting the median profiles.

2.3.4 D_n4000 and $\mathrm{H}\delta_A$ gradients

The strength of the D_n4000 index in a galaxy spectrum is indicative of the age of the stellar population. While the D_n4000 index alone is insufficient to determine the precise age of the stellar population, particularly where the most recent episode of star formation was more than 1 Gyr ago (Kauffmann et al., 2003a), gradients of its strength are indicative of underlying stellar population age gradients. However, caution must be taken with the interpretation of gradients in D_n4000, as this quantity is also sensitive to changes in the stellar metallicity. We have measured the D_n4000 index, as defined by Balogh et al. (1999), in concentric elliptical annuli around the centres of the galaxy. Gradients of the D_n4000 index are calculated from the values at the centre and within an ellipse with a semi-major axis length of $5''$. Due to the stochastic occurrence and short lifetimes of individual H II regions in galaxies, the D_n4000 gradients can be used to confirm that any radial trend in the Hα-derived star-forming properties of a galaxy can be explained as genuine quenching rather than as random, short-timescale fluctuations in the Hα distribution. In particular, positive D_n4000 gradients (i.e. D_n4000 stronger in the galaxy outskirts) are evidence for outside-in quenching acting or the recent enhancement of centrally located star formation in a formerly passive galaxy.

In addition to its dependence on the light-weighted age of a stellar population, the strength of D_n4000 is sensitive to the metallicity as well. In general, D_n4000 increases in strength with increasing metallicity (e.g. Bruzual, 1983; González Delgado et al., 2005). Therefore, radial variation in D_n4000 may correspond to either an age gradient or a metallicity gradient, or a combination of both. This degeneracy can be broken if the

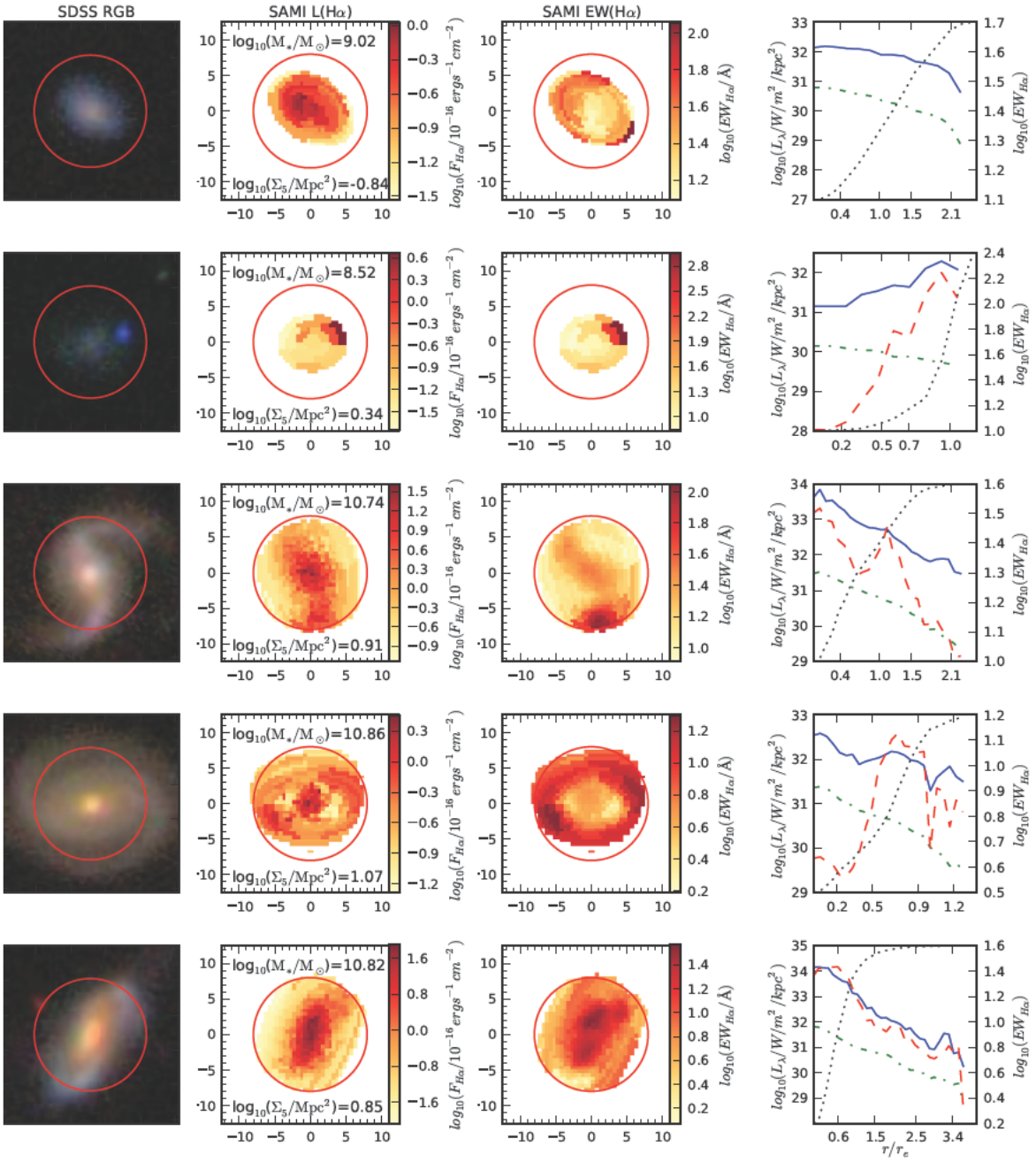

Figure 2.7: Example galaxies with a range of stellar masses, local environment densities and Hα morphologies. On the far left is a colour optical image from the SDSS *gri* photometry, left-of-centre is the extinction-corrected $\log_{10}$(Hα) flux map reconstructed from the annular-Voronoi bins and right-of-centre is the Hα equivalent width map, made from the annular-Voronoi bins. The SDSS image and each SAMI map are located in boxes that are 25″ on each side. In each image the red circle marks the 15″ SAMI field of view. On the far right we show the radial profiles for $\log_{10}(\mathrm{H}\alpha/W/kpc^2)$ luminosity surface density (blue solid), $\log_{10}(\mathrm{EW_{H\alpha}})$ (red dashed), the SAMI red arm integrated continuum (green dot-dashed) and the curve of growth for dust-corrected Hα (black dotted). Each curve of growth is scaled such that 0% of the flux from the galaxy is at the bottom of the panel and 100% of the flux is at the top.

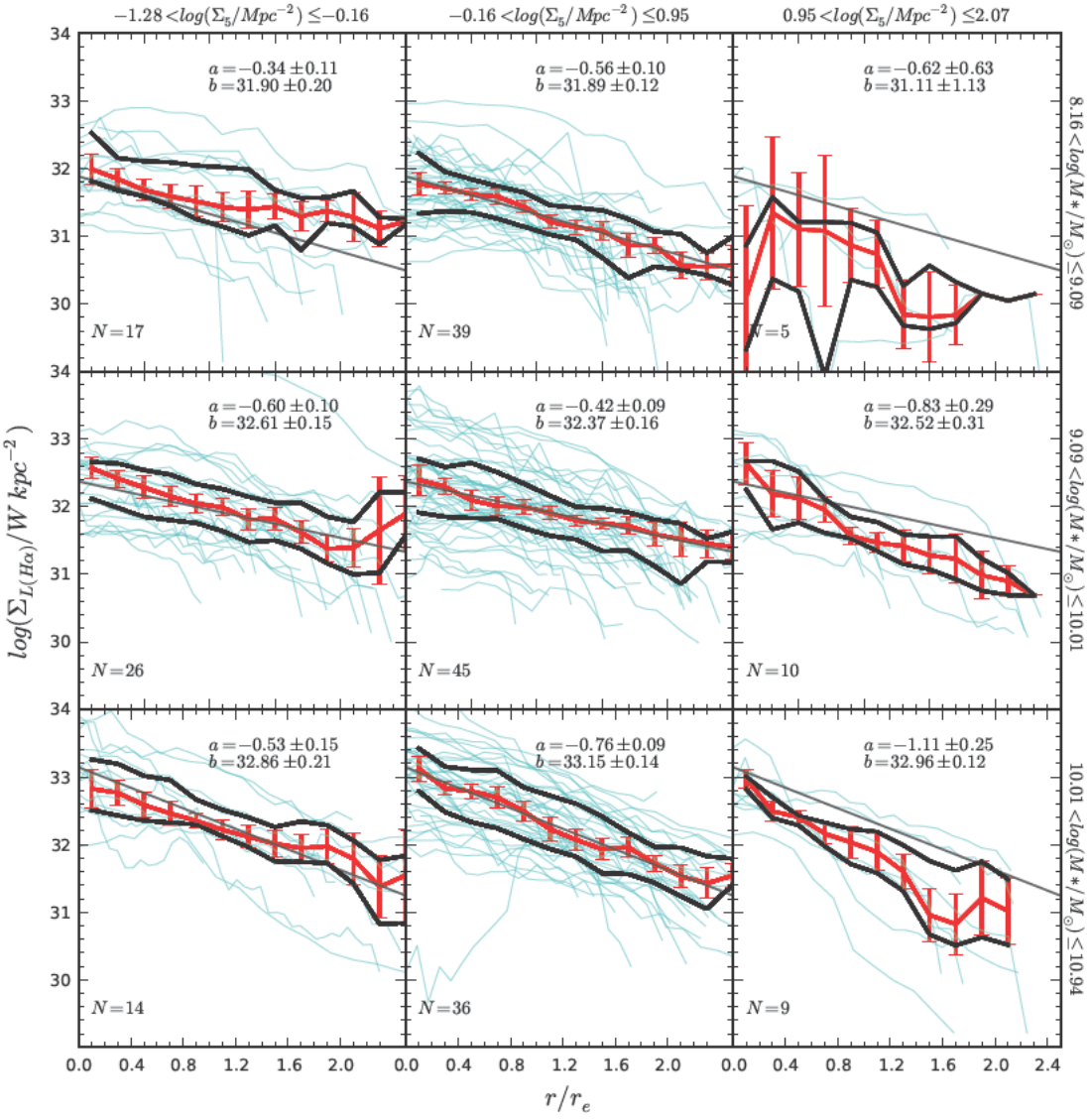

Figure 2.8: The radial profiles of Hα luminosity surface density for each of the star-forming galaxies in the sample, split into three bins of stellar mass (increasing from top to bottom) and environment density (increasing from left to right). Each bin covers one third of the total range in $\log_{10}(M_*/M_\odot)$ and $\log_{10}(\Sigma_5/\mathrm{Mpc}^2)$. The profile of each galaxy is shown in cyan, with the median profile of each bin shown in red. Bootstrapped errors on the median profile are plotted in $0.2R_e$ intervals. Thick black lines show the 25^{th} and 75^{th} percentiles of the radial profiles. For each stellar mass interval an exponential fit to the median profile of the central density bin is overplotted in black on each panel for comparison. In the upper right of each panel we show the best-fit parameters of the exponential fit (using Equation 2.3) to the median profile in that bin of stellar mass and environment density.

strengths of multiple features are measured. Alternatively, under the assumption of a constant metallicity gradient between galaxies, differences in the D_n4000 gradients within the sample can be interpreted as a variation in the recent star formation history.

The $H\delta_A$ absorption line equivalent width is also useful in estimating the age of a galaxy's stellar population, since Balmer absorption lines are strongest in relatively short lived B and A-type stars. We measure the strength of the $H\delta$ absorption from the spectrum after subtraction of the emission line fit using the index bands defined by Worthey & Ottaviani (1997). A gradient is then calculated as for D_n4000.

2.4 Results

In this section we present our analysis of the $H\alpha$ emission in the star-forming galaxies observed by SAMI. This includes both the integrated star formation rates and the spatial distribution of star formation in the galaxies as a function of their stellar mass and their local environment density.

2.4.1 Integrated Star Formation Rates

We investigate the effect of local environment density on the integrated star formation in galaxies and see in Figure 2.9 that the overall level of star formation in all galaxies (star-forming and passive) decreases for galaxies in higher density environments. This is in agreement with other surveys (e.g. Balogh et al., 2004; Wijesinghe et al., 2012).

The relationship between the specific star formation rates (SFR/M_*; sSFR) of star-forming galaxies and their local environment density and stellar mass can be seen in Figure 2.9. In the left panel of the upper row we compare sSFR to Σ_5. There is evidence for a correlation between the sSFR of star-forming galaxies and Σ_5 (Spearman's $\rho = -0.27$, $p = 1.3 \times 10^{-4}$) though again, a higher fraction of quiescent systems exist in high-density regions. The passive fraction of galaxies increases both with stellar mass and environment density, with a steady rise in the passive fraction above $\log_{10}(\Sigma_5/\mathrm{Mpc}^2) = 0.5$, corresponding to a fifth-nearest neighbour separation of 0.7 Mpc. In the right panel of the upper row in Figure 2.9 we compare the sSFR to the stellar mass of each galaxy. There is no correlation between the specific star formation rate and the stellar masses of star forming galaxies in our sample, with a Spearman rank correlation coefficient of $\rho = -0.016$ and $p = 0.83$. The quiescent fraction in galaxies appears to increase abruptly above $\sim 10^{10}$ $M_\odot$, in accordance with previous studies (e.g. Kauffmann et al., 2003b; Geha et al., 2012).

The quiescent fraction of galaxies as a function of mass and environment density given the data is displayed in the lower row of Figure 2.9. The fractions here are calculated as the 50^{th} percentile of the beta distribution defined by the total number of galaxies in each bin and the number of these that are quiescent, with the lower and upper error bars being the 15.9^{th} and 84.1^{th} percentiles of this distribution respectively. This approach is taken following Cameron (2011). We see that the passive fraction of galaxies increases above $\log_{10}(\Sigma_5/\mathrm{Mpc}^2) = 0.5$ and above masses of $\log_{10}(M_*/M_\odot) = 10$.

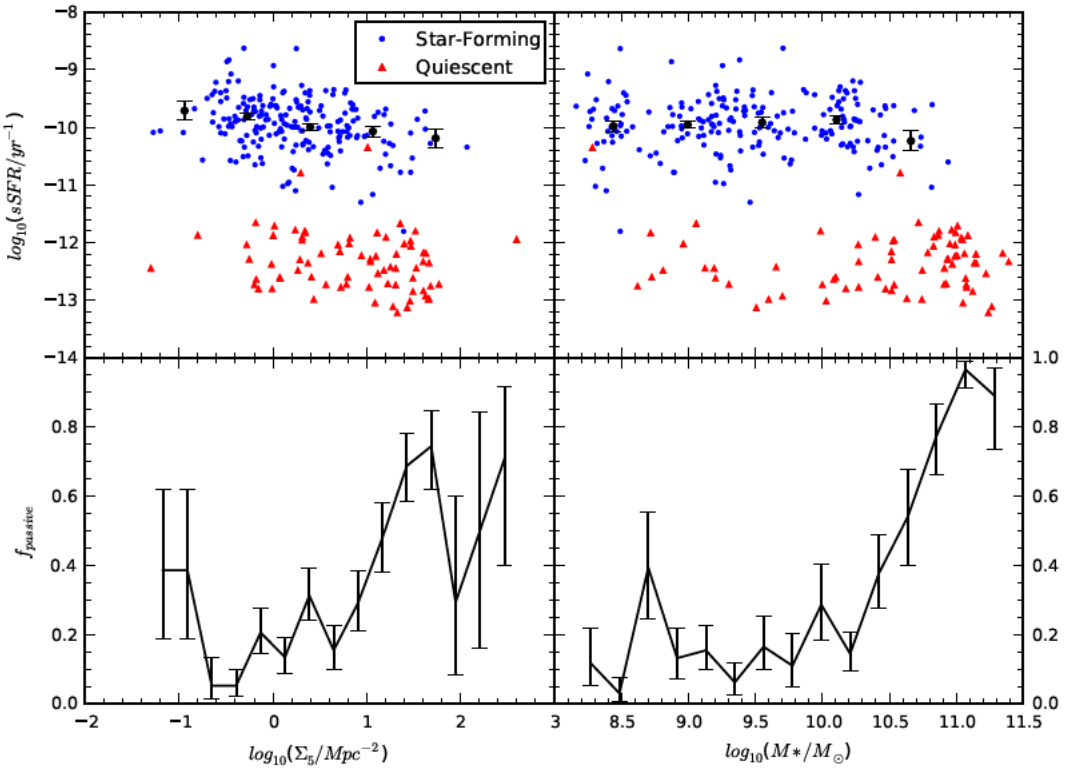

Figure 2.9: The upper row shows the specific star formation rates of galaxies as a function of their environment density (left) and stellar mass (right). Data for star-forming galaxies are shown with blue points, while the data for the passive galaxies are shown with red triangles. The black points are the median values of the specific star formation rates of star-forming galaxies in equally spaced bins of $log_{10}(\Sigma_5/\mathrm{Mpc}^2)$ or $log_{10}(M_*/\mathrm{M}_\odot)$. The errors are estimated as the standard deviation of the median in 1000 samples bootstrapped from each bin. The lower row shows the expectation value of the fraction of galaxies that we classify as quiescent as a function of Σ_5 and M_*. The passive fraction of galaxies increases above $\mathrm{M}_* = 10^{10}$ $\mathrm{M}_\odot$ and above $\log(\Sigma_5/\mathrm{Mpc}^2) = 0.5$.

The correlation between specific star formation rate and local environment density is weak but significant for all star-forming systems. The dominant trend appears to be the changing fraction of passive galaxies in higher density regions, particularly at higher stellar mass, though a weak trend may be evident for the star-forming galaxies. This conclusion is strongly dependent on the definition of a passive galaxy and our ability to measure star formation rates in systems with weak emission lines. This result is largely consistent with the results of Wijesinghe et al. (2012) who found that the changing fraction of passive galaxies dominates the environmental trend.

To control for the effect of the mass of a galaxy on its star formation rate, we have performed this analysis in two bins of restricted stellar mass. The upper panel of Figure 2.10 is constrained to stellar masses in the range 10^8 to 10^9 $M_\odot$, while the lower panel shows galaxies between 10^{10} and $10^{10.5}$ $M_\odot$. These mass bins were chosen from the peaks in the stellar mass distribution of our sample shown in Figure 2.2. Within each range of stellar mass we show the estimated specific star formation rate as a function of Σ_5. We test for the dependence of the specific star formation rate in galaxies on environment density with a Spearman rank correlation test. Star-forming galaxies in the higher mass sub-sample have a correlation coefficient of $\rho = -0.32$ with a p-value of $p = 0.022$. The correlation coefficient between $\log_{10}(\Sigma_5)$ and $\log_{10}(sSFR)$ in the lower mass subsample is $\rho = -0.31$ with $p = 0.021$.

The correlation within the star-forming galaxies in the low-mass subsample is consistent with the results of some studies, such as Rasmussen et al. (2012) who find that star-forming galaxies in groups have their star formation suppressed on average by 40% relative to the field and that the trends are more prominent in lower stellar mass galaxies. This is qualitatively similar to other studies on this topic (Welikala et al., 2009; Bai et al., 2010). A direct comparison between the current work and these previous results is difficult given that the environment density metrics differ between the two samples, as does the definition of a star-forming system. A future paper using SAMI data will examine the effect of group environments on the star formation distribution in galaxies and will allow a more direct comparison to other galaxy group studies.

2.4.2 Dust-Corrected Hα Radial Profiles

We have calculated the radial profiles of dust-corrected Hα emission for 201 star-forming galaxies in the SAMI Galaxy Survey. These do not include galaxies that have been classified as quiescent in Section 2.4.1. The profiles trace the star-formation rate surface density with radius. In contrast to the radial profiles of broadband images, which can often be well described by a Sérsic profile, the distribution of Hα is difficult to parametrise. The existence of spiral arms and asymmetric or clumpy structures in the ionised gas make the description of the radial distribution of gas with a single functional form problematic. These radial profiles are displayed in Figure 2.8, where we have separated the profiles based on their stellar mass and local environment density. There is significant variation in the shape of each radial profile, and the median profiles show some change with environment density in a given mass bin, tending to be steeper at higher densities. At constant environment density, the normalisation of the radial profiles changes with stel-

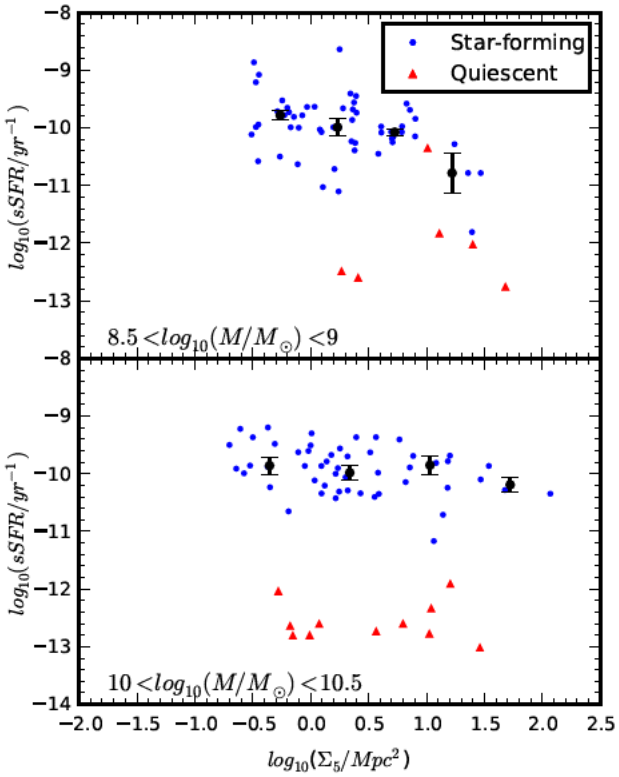

Figure 2.10: Specific star formation rates as a function of Σ_5 for star-forming (blue points) and quiescent (red triangles) galaxies in two bins of stellar mass. The upper panel shows 55 star-forming and 6 quiescent galaxies with stellar masses in the range $10^8 < M_* < 10^9$ $M_\odot$. A weak correlation between the specific star formation rates and local densities exists for galaxies in this mass range. The lower panel shows 51 star-forming and 11 quiescent galaxies with $10^{10} < M_* < 10^{10.5}$ $M_\odot$. There is a weak correlation between the specific star formation rate and local density in this mass bin. For both panels the black points show the median specific star formation rate for the star-forming galaxies in equally spaced bins of $\log_{10}(\Sigma_5)$, with error bars determined as the bootstrapped error on the median in each bin.

lar mass in accordance with the known SFR-M_* relationship (Brinchmann et al., 2004), albeit with significant scatter. There is also some evidence for a steepening of the radial profiles with environment density, especially above $M_* = 10^{10}\,M_\odot$, where the gradient of the median profile changes by $0.58 \pm 0.29\,dex\,r_e^{-1}$ over the full range of environment densities. The best-fit central star formation rate surface density for the median profiles shows no significant change over the range of environments in our sample.

Normalised Hα profiles

Within the relatively narrow bins of stellar mass and environment density in Figure 2.8 the normalisation of the star formation rate radial profiles vary by over a factor of one hundred. This is because of the stochastic nature of star formation and morphological variations between galaxies, or other factors that may not be attributable to the environment. These variations inhibit our ability to discern systematic differences in the star formation rate gradients across different environments. We correct for the effect of the normalisation of the star formation radial profiles by dividing each profile by its central value. In Figure 2.11 we show each normalised radial profile in the star-forming sample in three equally spaced, logarithmic bins of mass and environment density as in Figure 2.8. For each subset of galaxies we display the median profile and the 25^{th} and 75^{th} percentile profiles. The median profiles are approximately exponential, and we calculate slope parameters of the exponential fits in the same way as was done for Figure 2.8. These parameters are shown in Figure 2.11.

In the lowest mass bin there is no evidence for a change in the gradient between the lowest and highest density environments, though we note that the small numbers in these bins do not allow strong conclusions to be made. For galaxies with $10 < \log 10(M_*/M_\odot) < 11$ the median gradient of the normalised star-formation rate surface density radial profiles steepens from $0.54 \pm 0.18\,dex\,r_e^{-1}$ in the lowest density environments to $1.09 \pm 0.26\,dex\,r_e^{-1}$ in the highest density environments. The $0.55 \pm 0.32\,dex\,r_e^{-1}$ increase in the gradient is significant at the 1.7σ level.

2.4.3 A Non-parametric Gradient Estimate: Hα r_{50} vs. continuum r_{50}

The complexity of galaxy star formation morphology means that no single parametrisation will be sufficient to describe a galaxy's star-forming properties completely. We therefore turn to non-parametric methods of tracing the spatial signatures of star formation suppression in high-density environments. Non-parametric measurements of the star formation distribution in galaxies relative to the stellar light have been performed by a number of authors (e.g. Koopmann et al., 2006; Cortese et al., 2012; Bretherton et al., 2013). Following these previous studies, we can examine the possibility of outside-in quenching by measuring how concentrated current star formation is compared to previous episodes of star formation. We do this by comparing the half-light radius, r_{50}, of Hα to that of the continuum as seen by SAMI. This analysis is performed by summing light within concentric elliptical annuli determined from the GAMA photometry to obtain

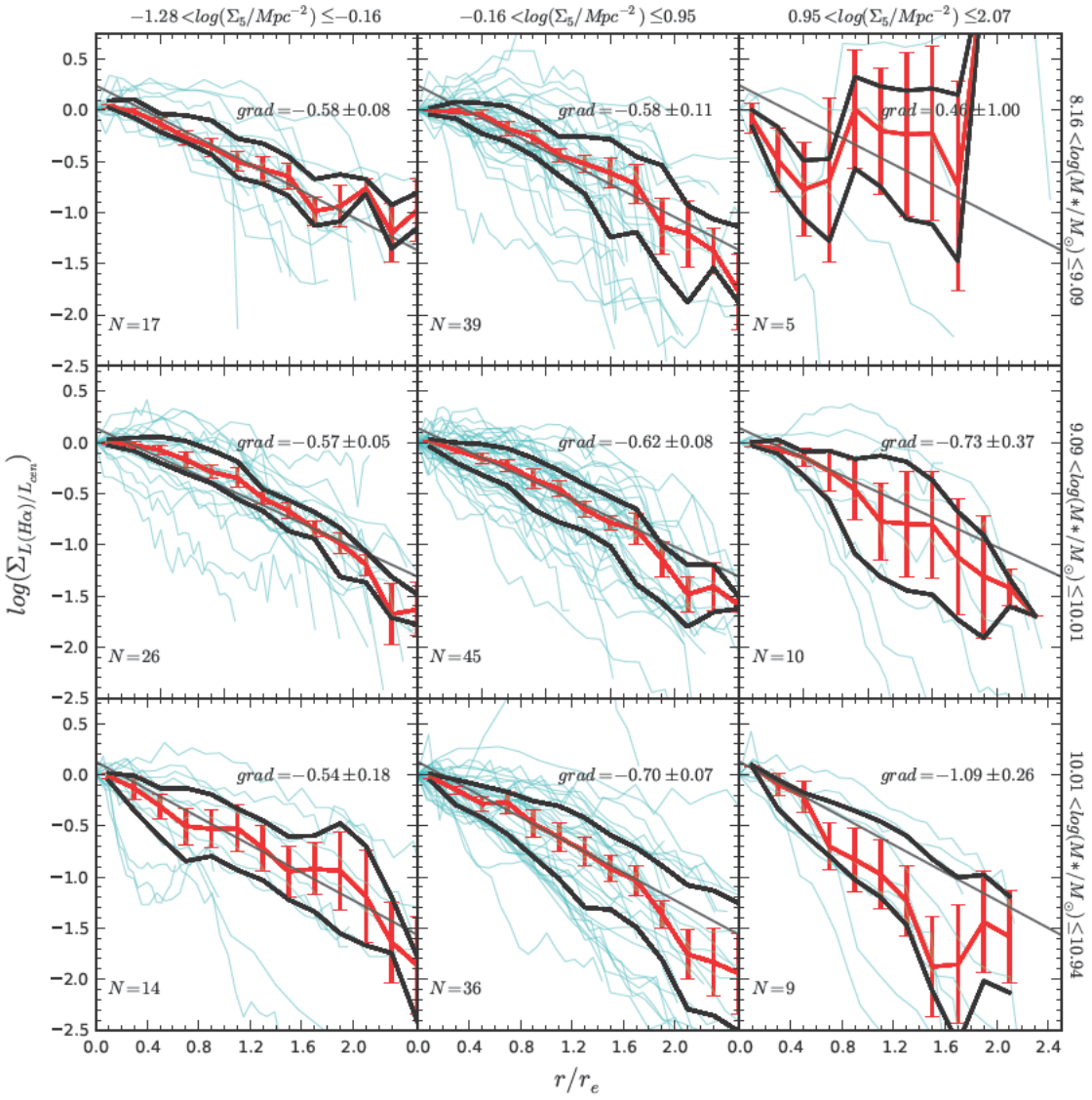

Figure 2.11: Radial profiles for each of the star-forming galaxies in bins of stellar mass and environment density normalised at the centre. Each cyan coloured profile is the radial distribution of star formation divided by the value at the centre of the galaxy. In red we display the median normalised profile and the black lines are the 25^{th} and 75^{th} percentile profiles. Each row of panels contains galaxies within the same stellar mass bin, and mass increases downwards. Each column contains galaxies drawn from the same bin of environment density, with environment density increasing towards the right. As in Figure 2.8, these bins cover one third of the total range in $\log_{10}(M_*/M_\odot)$ and $\log_{10}(\Sigma_5/\mathrm{Mpc}^2)$. The diagonal black lines are the exponential fit to the median profiles of the central environment density bin for each row. In the bottom left of each panel we show the number of galaxies in each bin, while in the top right we show the gradient of an exponential fit to the median profile, with a bootstrapped 1σ error.

curves of growth for extinction-corrected Hα and red continuum light within the SAMI aperture. Some examples of dust-corrected Hα curves of growth are displayed in the right hand column of Figure 2.7 in black. The radius at which these curves of growth reach 50% of their maximum is defined to be r_{50}. In Figure 2.12 we show the ratio $r_{50,H\alpha}/r_{50,cont}$ as a function of the local surface density and stellar mass. If $r_{50,H\alpha}/r_{50,cont} \gtrsim 1$, star formation is spatially extended and the current buildup of stellar mass in the galaxy is occurring in the outer parts. If $r_{50,H\alpha}/r_{50,cont} < 1$ then star formation is centrally concentrated and stellar mass in the galaxy is now predominantly accumulating in the inner region. This measurement provides a differential test to examine the relative spatial extent of star formation over a range of masses and environments. A discussion of some possible issues with this measurement can be found below in Section 2.4.3. In the star-forming sample $\log_{10}(r_{50,H\alpha}/r_{50,cont})$ has a median of -0.020 and a standard deviation of 0.099. The Spearman rank correlation coefficient between Σ_5 and $r_{50,H\alpha}/r_{50,cont}$ is $\rho = -0.10$ with $p = 0.14$.

Figure 2.12 shows that galaxies in higher density environments have a greater probability of having centrally concentrated star-formation than do galaxies in low-density environments. It is important to note that dense environments in this sample harbour both galaxies with extended star-formation, as seen in the low-density regions, as well as galaxies with a more compact star formation morphology. However, the distribution of scale-radius ratios changes with increasing environment density. In Figure 2.12 we see that the scatter in the distribution of $r_{50,\mathrm{H}\alpha}/r_{50,cont}$ increases significantly with environment density, and that this scatter is biased towards galaxies with more centrally concentrated star formation in dense environments.

We define galaxies with $\log_{10}(r_{50,H\alpha}/r_{50,cont}) < -0.2$ (i.e. further than two standard deviations below the median) as 'centrally concentrated'. The fraction of galaxies with centrally concentrated star formation, increases significantly with environment. We see in Figure 2.13 that below $\Sigma_5 = 10^{0.5}\,\mathrm{Mpc}^{-2}$ typically only $5 \pm 4\%$ of galaxies show this centrally concentrated star forming morphology, where the $1\,\sigma$ error on this fraction is estimated following Cameron (2011). In higher density environments the fraction of centrally-concentrated star-forming galaxies rises to $30 \pm 15\%$.

In Figure 2.13 the red and green points represent the fractions of star-forming galaxies with centrally-concentrated star formation for stellar masses below and above stellar masses of $10^{10}\,\mathrm{M}_\odot$ respectively. There is some evidence that galaxies with stellar masses greater than $10^{10}\,\mathrm{M}_\odot$ show centrally concentrated star formation more readily than do galaxies with stellar masses below $10^{10}\,\mathrm{M}_\odot$. The fraction of galaxies with centrally concentrated star formation is the same for both the high and low stellar mass subsamples over all environments except for in the second highest environment density bin. Here the high mass subsample shows a higher fraction of centrally concentrated star formation than the low mass subsample. This may imply that higher mass galaxies are more susceptible to environmental effects than lower mass galaxies. This seems unlikely given that the efficiency of environmental quenching mechanisms such as ram pressure stripping and tidal disruption of the star-forming disc is predicted to be reduced in higher mass galaxies. An alternative explanation for this may be that any process that causes star formation to be centrally concentrated occurs on much shorter timescales in lower mass

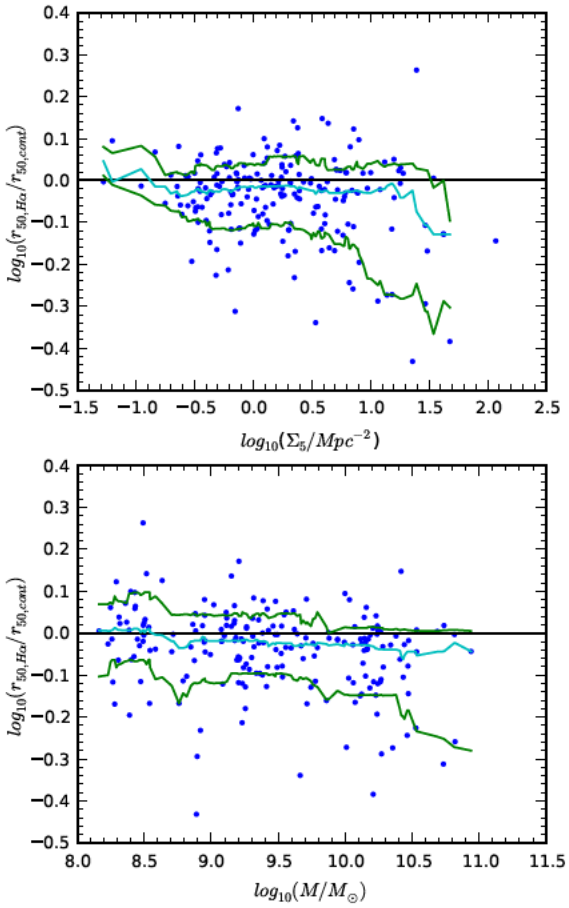

Figure 2.12: *Upper panel:* The scale radius ratio $r_{50,H\alpha}/r_{50,cont}$ for the star-forming galaxies in the sample as a function of the fifth-nearest neighbour local density. Higher values indicate more spatially-extended star formation while lower values are the signature of centrally-concentrated star formation. We show the 15^{th} (green), 50^{th} (blue) and 85^{th} (green) percentiles of $r_{50,\mathrm{H}\alpha}/r_{50,cont}$ calculated in a sliding bin of width 0.5 dex. While the 85^{th} percentile remains flat over the range of environments considered, the $15th$ percentile shows a sharp drop above $\log_{10}(\Sigma_5/Mpc^2) = 0.75$. *Lower panel:* The scale radius ratio as a function of stellar mass for the same sample. The percentiles of the scale-radius ratio distribution show no strong trend with the stellar masses in this sample.

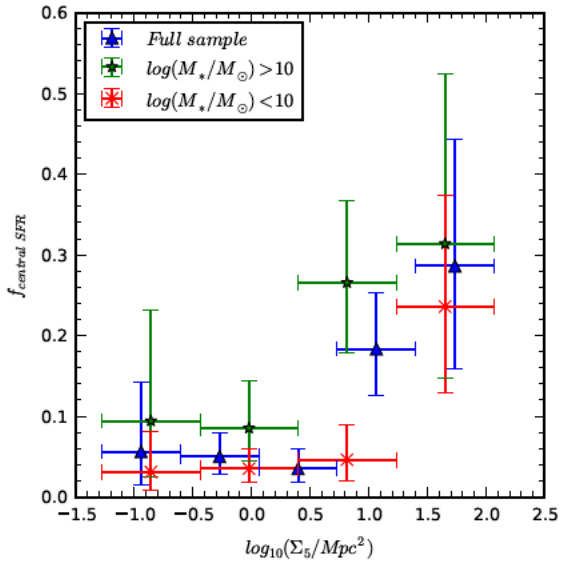

Figure 2.13: Fraction of galaxies with centrally concentrated star-formation as a function of local environment density. Blue triangles show the fractions for the full star-forming sample, red crosses are the fractions for star-forming galaxies with $log_{10}(M_*/M_\odot) < 10$, while green star symbols are the fractions for galaxies with $log_{10}(M_*/M_\odot) > 10$,. Fractions and vertical errors are calculated after Cameron (2011) while the horizontal error bars show the range in environment densities over which each fraction was computed.

galaxies or that low mass galaxies are quenched in a qualitatively different manner in all but the most dense environments.

Systematic biases and sources of error for the scale-radius ratio

Errors on the scale-radius ratio for each galaxy are extremely difficult to quantify. Small uncertainties in this quantity arise from random errors on the measured flux and photometric fits to the galaxy's ellipticity and position angle. These error terms are small in comparison to the uncertainties induced by observational effects.

Beam-smearing, which will force the scale-radius ratio towards 1, and aperture effects will have a larger contribution to the systematic biases in this measurement. We are only able to measure the scale-radius ratio from the parts of the galaxy which fall within the 15″ SAMI hexabundle. Given that the distribution of effective radii for the galaxies in our sample (see Figure 2.3) includes a number of galaxies which are large relative to the SAMI aperture, it is possible that aperture effects may introduce biases in our measurement of the scale-radius ratio. This bias is dependent on the distribution of star formation in each galaxy observed. If the star formation in a galaxy is radially extended, then the scale-radius ratio measurement will be lower than the true value. For systems with more centrally concentrated star formation, the scale-radius ratio measured within the IFU aperture will be higher than the true value. If the radius out to which we observe the

galaxies in the sample was randomly distributed across all environments, these aperture effects would add scatter to the $r_{50,H\alpha}/r_{50,cont}$ vs. Σ_5 relation, but would not induce a trend. Indeed, when we look for a correlation between $r_{50,H\alpha}/r_{50,cont}$ and $7.5/r_e$ (the effective radius coverage of the SAMI aperture), we find no significant correlation, with Spearman's $r = -0.03$ with a p-value of 0.61. When we control for the effects of galaxy mass and environment on the sample with a partial correlation analysis, this correlation coefficient is reduced in magnitude to -0.02 with a p-value of 0.71. Moreover, when the effect of radial coverage on the correlation between $r_{50,H\alpha}/r_{50,cont}$ vs. Σ_5 is controlled for, we see no reduction in its strength. We also see no correlation between Σ_5 and the radial coverage of galaxies within our sample. There is therefore no trend between Σ_5 and $r_{50,H\alpha}/r_{50,cont}$ imposed by our sample selection. We conclude that the effective radius coverage does not affect our ability to discern environmental trends, though it may affect the measured value of the ratio for individual galaxies. Since the dominant error terms for individual galaxies are unquantifiable with the current data, we do not include them in the figures.

Scale-radius ratio and the D_n4000 gradient

The lifetimes of H II regions are short relative to the evolutionary timescale of galaxies. To test for the possibility of short-timescale variability in the Hα distribution, we consider the scale radius ratio, $r_{50,H\alpha}/r_{50,cont}$ in conjunction with the radial gradient in the D_n4000 strength. This gradient has the additional advantage of being able to approximate age gradients in the stellar populations of these galaxies. In Figure 2.14 we present the relationship between the D_n4000 gradient, $r_{50,H\alpha}/r_{50,cont}$ and Σ_5 for galaxies with stellar mass exceeding 10^{10} $M_\odot$. This mass range is chosen because the continuum in these galaxies has sufficient S/N to make an accurate estimate of the D_n4000 break out to large radius.

We find that the D_n4000 gradient is anti-correlated with the scale-radius ratio. This implies that galaxies that are identified as being quenched in their outskirts by the scale-radius ratio also have older stellar populations toward their edges relative to those which show no evidence for Hα truncation. Galaxies with more radially extended star formation will have a higher proportion of young stars in their outskirts, and therefore exhibit younger stellar populations towards their edge. The observed relationship corroborates the evidence from the scale-radius ratios and Hα luminosity surface density profiles that increasing environment density reduces the star formation in the outskirts of galaxies. This correlation is illustrated in Figure 2.15, where we see two galaxies from different density environments with different Hα morphologies. The age gradients inferred from the D_n4000 and $H\delta_A$ measurements are opposite for these two systems, though we must note that we have made the assumption that there is no systematic difference in the metallicity gradient between galaxies with spatially-extended or centrally-concentrated star formation.

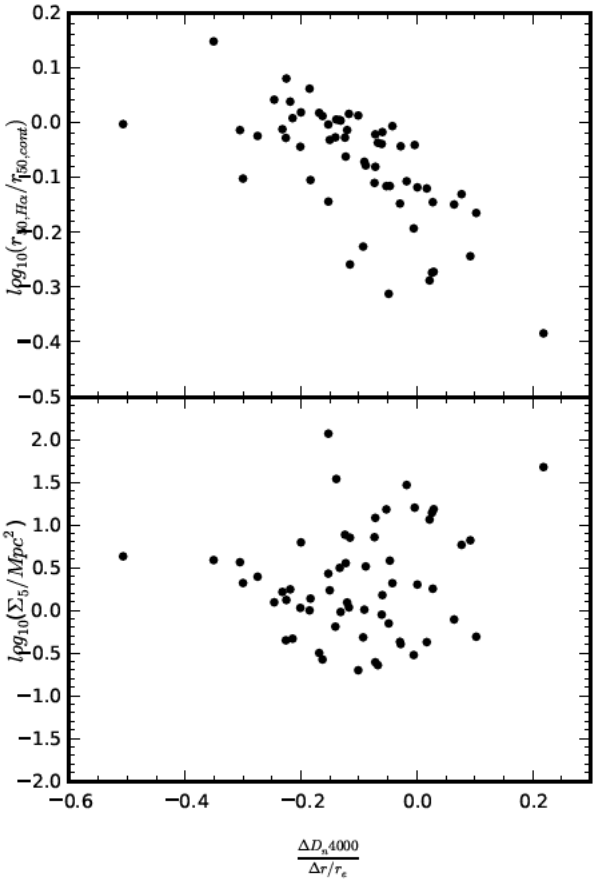

Figure 2.14: Relationship between Σ_5, $r_{50,H\alpha}/r_{50,cont}$ and the D_n4000 gradient for the 60 star-forming galaxies with $M_* > 10^{10}$ $M_\odot$. The upper panel illustrates the correlation between the scale-radius ratio and the D_n4000 gradient. Galaxies with positive D_n4000 gradients have either older stellar populations or higher stellar metallicities towards their edges and tend to have a centrally concentrated Hα distribution. The lower panel shows no significant correlation between the D_n4000 gradient and $\log_{10}(\Sigma_5/\mathrm{Mpc}^2)$.

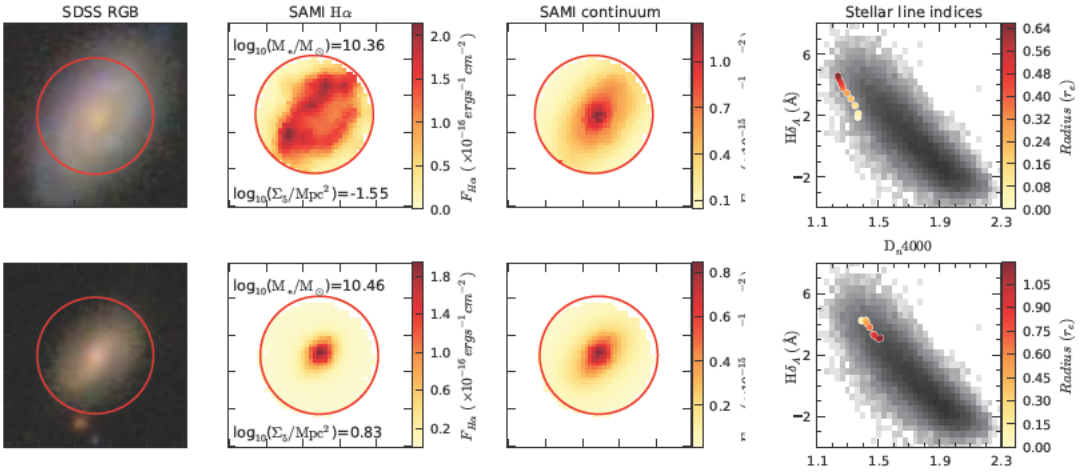

Figure 2.15: Examples of the relationship between the star formation morphology of a galaxy and the inferred age gradients in the underlying stellar populations. Each row shows (from left to right) the SDSS image, the SAMI Hα map, the SAMI continuum map and the radial distribution of the D_n4000 strength and the emission-subtracted Hδ absorption equivalent width index. The red circles in the three left columns are 15″ in diameter, encircling the SAMI field of view, and each box is 25″ in width and height. In the final column, the greyscale background traces the distribution of D_n4000 and $H\delta_A$ for a large sample of galaxies from the SDSS (Kauffmann et al., 2003c). The coloured points are measured values from the SAMI data cube, with yellow points extracted from the centre of the galaxy and red points from towards the edge. The upper row shows a galaxy (GAMA 41144) with an extended Hα morphology and an older stellar population in the centre, as evidenced by the higher D_n4000 and lower $H\delta_A$. The lower row presents a system (GAMA 492384) from a more dense environment with a concentrated star formation morphology and older stellar populations towards the edge of the galaxy disc.

Scale-radius ratio and the specific star formation rate

We adopt the definition of quenching that is the movement of a galaxy off the star formation main sequence to a lower specific star formation rate. By examining the spatial distribution of current star formation in galaxies as they make this transition we can better understand the mechanisms responsible for this evolution. While the current sample is the largest studied to date, it is still of insufficient size to make strong statements about the statistics of particular quenching mechanisms in different environments. We note that systems with specific star formation rates that are lower than the star-forming main sequence are located in a range of environments and have a variety of Hα morphologies. The upper panel of Figure 2.16 shows how the specific star formation rates of galaxies depend on their local environment density and the relative extent of the current star formation. The scale radius ratios of galaxies with below average specific star formation rate (i.e. sSFR $< 10^{-10}\,\mathrm{yr}^{-1}$) in environments above and below $\log_{10}(\Sigma_5/\mathrm{Mpc}) = 0.5$ show a significant difference. Below this environment density the mean log scale-radius ratio in galaxies is -0.01 ± 0.01, but above this density, the mean log scale-radius ratio

is -0.07 ± 0.02. That is, galaxies in lower density environments that sit below the star formation main sequence exhibit a more diffuse and extended star formation morphology. Galaxies in higher density environments with star formation rates lower than the star formation main sequence have a more centrally concentrated star formation morphology. The dominant mechanism responsible for quenching the star formation in galaxies in low-density environments seems to differ qualitatively from the mechanisms reducing the star formation in higher density environments.

In the lower panel of Figure 2.16 we see the relationship between the scale-radius ratio, the stellar mass and the specific star formation rate for galaxies in our sample. There is no significant correlation between the stellar mass of a star-forming galaxy and the relative spatial extent of its star formation. Furthermore, galaxies with specific star formation rates below $10^{-10.8}\,yr^{-1}$ do not occupy any particular region of this parameter space and seem to have no tendency to have either their star-formation either spatially-extended or centrally-concentrated.

2.5 Discussion

We have used SAMI integral field spectroscopy to examine variations in the radial distribution of star formation in galaxies as a function of their local environment density. Our sample of 201 star-forming galaxies covers nearly three orders of magnitude in both stellar mass and local environment density. Using the dust-corrected Hα maps of the galaxies we have computed radial profiles of current star formation surface density.

Our analysis shows a change in the median radial distribution of current star formation between high and low-density environments for galaxies with $\log_{10}(M_*/M_\odot) > 9$. While this was not seen by Brough et al. (2013) this is unsurprising since the large variation in star formation morphologies in galaxies at a given mass and environment density makes environmental trends difficult to observe in small samples. The current sample is over an order of magnitude larger, allowing us to average over a wide range of galaxy morphologies that would dominate the conclusions drawn from small samples.

The radial profiles of star formation surface density in star-forming galaxies show a systematic change in normalisation with stellar mass. Higher mass galaxies have a larger star-formation rate surface density at all radii than do their low-mass counterparts. This is consistent with the known relationship between the total star-formation and stellar mass of a galaxy (Brinchmann et al., 2004). In Figure 2.8 we do not see a decline in the central star formation rate surface density with environment density for galaxies of a given mass. However, the global specific star-formation rates shown in Figure 2.9 do show a decline of 40% between the lowest and highest environment densities. The apparent disagreement between these two measurements is reconciled by the steeper star formation rate surface density gradients in higher density environments. This implies that the reduction in star-formation in galaxies in high density environments occurs primarily in their outskirts. This environmental effect may be responsible for the difference between the results of, for example, von der Linden et al. (2010) and Wijesinghe et al. (2012). As Wijesinghe et al. (2012) used Hα equivalent widths derived from single fibre spectroscopy at the centre of the galaxy as a proxy for specific star formation rate, and calculated

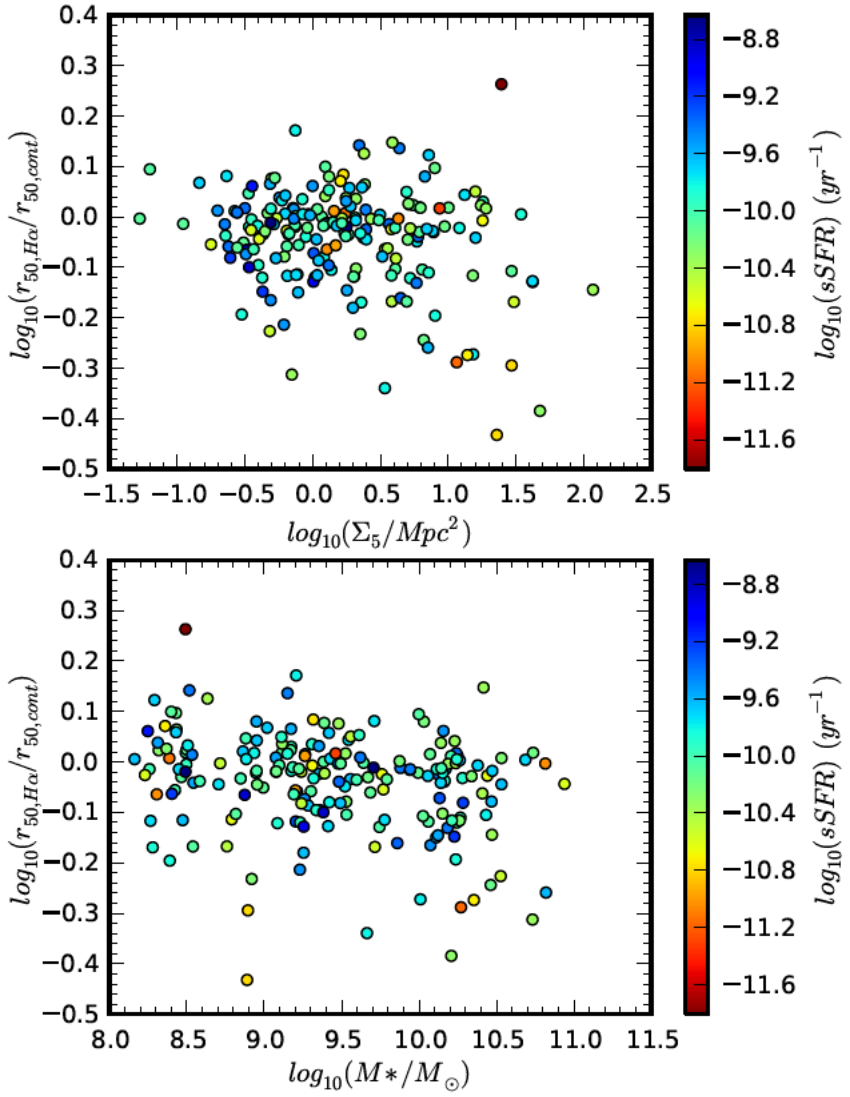

Figure 2.16: Scale radius ratio $r_{50,H\alpha}/r_{50,cont}$ as a function of $\log_{10}(\Sigma_5/Mpc^2)$ and $\log_{10}(M_*/M_\odot)$ for 201 star-forming galaxies across the full range of masses. Each point is coloured by the specific star formation rate in that galaxy. Galaxies in the densest environments with the lowest specific star formation tend to have the most centrally concentrated star formation. Conversely, galaxies in lower density environments with low specific star formation rates have a radially extended star formation morphology, implying that different quenching mechanisms may dominate in different density environments. The lower panel shows how the specific star formation rate varies with mass and the scale-radius ratio. There is no strong correlation between stellar mass and specific star formation rate for the star-forming galaxies, though more massive galaxies with centrally concentrated star formation do tend to have a lower specific star formation rate.

the star formation rate assuming that the emission line intensity as measured within the fibre was representative of the entire galaxy (Wijesinghe et al., 2011). If environmental effects primarily influence the outskirts of galaxies then the integrated star formation rates in dense environments may have been systematically overestimated (see Richards et al., 2016, for a discussion of these aperture effects). Thus, the scenario of short timescale quenching that was supported by the results of Wijesinghe et al. (2012) is not favoured by our data.

A simple parametrisation of the radial distributions of Hα luminosity is insufficient to diagnose the mechanisms for quenching. Variation in the structure of the galaxies, for example the presence of spiral arms, bars and other morphological features, as well as inhomogeneities in the galaxy angular size and observing conditions means that comparing star formation rate gradients directly is difficult. While the median profiles of Hα luminosity surface density roughly follow an exponential profile we lose information about the distribution of galaxy properties including the underlying stellar distribution with this type of comparison. Instead the spatial distribution of ongoing star formation can be quantified relative to that of previous star formation. The non-parametric scale radius ratio provides a differential test that is more robust to variation between galaxies as it is not reliant on an invalid parametrisation of a complicated structure. We find that the scale radius of Hα emission in galaxies in high-density environments is reduced relative to the scale radius of previous star formation by approximately 20% over the range of environment densities considered here. The reduction in the scale-radius ratio in increasingly dense environments is consistent with the environmental dependence of the median radial profiles seen in Figure 2.8 and the normalised profiles in Figure 2.11. The fraction of galaxies which show a centrally concentrated star formation morphology increases from $\sim 5\%$ below $\log_{10}(\Sigma_5/\mathrm{Mpc}^2) = 0.5$, the density above which the passive fraction of galaxies increases, to 29% above this density threshold.

Moreover, we have observed that in galaxies with a more centrally concentrated Hα distribution, the gradient of the D_n4000 spectral feature is shallower. This is indicative of an older stellar population in the outskirts relative to galaxies with ongoing star formation in their peripheries. In the most extreme cases, the D_n4000 spectral feature is strongest towards the edge of the galaxy, indicative that all significant star formation in their edges has ceased. Due to the degeneracy between age and metallicity in setting the strength of D_n4000, it is not possible to calculate the age gradient from this measurement alone. Even so, the timescale over which D_n4000 is likely to change is longer than the typical lifetimes of HII regions. The fact that the correlation between the D_n4000 gradient and $r_{50,H\alpha}/r_{50,cont}$ is so strong implies that the suppression of star formation in the outskirts of galaxies is maintained on timescales longer than the lifetimes of individual HII regions.

This observed outside-in mode of quenching is qualitatively different to the findings of Welikala et al. (2008), who found that local environment tended to reduce the star-formation rate in the central regions of galaxies. The disparity between these results and our own highlights the difficulties associated with spectral energy distribution fitting from broadband imaging given the degeneracies between dust-extinction, stellar age and metallicity in galaxy colours. The ability of integral field spectroscopy to obtain independent measurements of the dust extinction in galaxies will be invaluable to future studies

of environment quenching. Peng et al. (2010) observed a tendency for galaxies of larger mass to quench more readily than galaxies of lower mass, independent of their local environment. While there is some evidence for a correlation between galaxy stellar mass and $r_{50,H\alpha}/r_{50,cont}$ in Figure 2.12, this trend is very weak. Moreover, the measured steepening of the star-formation rate gradients in Figures 2.8 and 2.11 is greatest for the most massive galaxies in the sample. This does not necessarily indicate that galaxies of different masses experience different quenching mechanisms or that these processes are stronger for the most massive galaxies. Instead it is likely that the timescale over which quenching occurs is related to the galaxy mass. If lower mass galaxies are quenched rapidly by any means then observing these systems as quenching proceeds is less likely.

2.5.1 Environment-enhanced star formation

While we have only considered the quenching of star formation by environmental effects here, there is a growing body of evidence that suggests that star formation can be enhanced in group environments (e.g. Kannappan et al., 2013; Robotham et al., 2014). This enhancement can be from either gas-rich mergers, tidal torques from galaxy interactions or from the accretion of cold or hot gas from the intergalactic medium. Sancisi et al. (2008) argue that a large fraction of this gas must be accreted directly from the intergalactic medium, rather than through gas-rich mergers. Simulations by Kereš et al. (2005) showed that cold-mode accretion does not dominate in galaxy groups with space densities above $\sim 1\,\mathrm{Mpc}^{-3}$ (using a modified Σ_{10} density measure), implying that hot-mode accretion must re-supply the gas in galaxies in dense environments.

Observationally, the infall of cold gas onto a low mass ($\mathrm{M}_* < 10^9\,\mathrm{M}_\odot$) system will be manifest in localised, low metallicity and offset star-forming regions (e.g. Richards et al., 2014; Sánchez Almeida et al., 2015; Ceverino et al., 2016). Given that the unusual galaxy studied by Richards et al. (2014) is a part of our sample ($\mathrm{M}_* = 10^{8.5}\,\mathrm{M}_\odot$), this effect is certainly present in our data and helps explain the scatter in $r_{50,H\alpha}/r_{50,cont}$ at low stellar mass. At higher stellar masses the effects of gas accretion on star formation morphology are more difficult to diagnose as the specific morphological signatures can vary depending on the details of the accretion process. A better way of classifying the accretion of gas onto galaxies with $\mathrm{M}_* > 10^{10}\,\mathrm{M}_\odot$ would be to investigate their gas kinematics and metallicity, though this analysis is beyond the scope of this paper (but see Bryant et al. *in prep.*).

2.5.2 The Mechanism of Environmental Quenching

The suppression of star formation towards the edges of galaxies in dense environments is consistent with a number of proposed quenching mechanisms. Ram pressure stripping is commonly cited as a mechanism to remove gas from the edges of discs in group (Rasmussen et al., 2006) and cluster galaxies (Koopmann & Kenney, 2004b,a). The removal of cold gas from a galaxy by this method is possible only if the velocity of the galaxy through the intergalactic medium is such that the ram pressure force exerted on the interstellar medium is sufficient to overcome the gravitational potential of the galaxy. For the majority of more massive galaxies in our sample this is probably not the case, given that they are

drawn from field environments or groups with a velocity dispersion typically below 300 km s^{-1}. Nulsen (1982) points out that under these circumstances ram pressure is unlikely to be the dominant method of gas removal from galaxies, and instead suggests that turbulent or laminar viscous stripping may dominate. The removal of gas by viscous stripping in elliptical cluster galaxies has been modelled by Roediger et al. (2015), who show that this method acts in an outside-in way that is qualitatively consistent with what has been observed here, though the presence of a cool X-ray tail in the models cannot be verified for SAMI galaxies at present. The effect of viscous stripping is likely to be more efficient in galaxy clusters than in groups and the field. This will be the subject of future work on the SAMI Galaxy Survey cluster sample.

Tidal interactions are another mechanism that has been proposed to be responsible for a significant fraction of the passive population of galaxies in dense environments. Simulations (Hernquist, 1989; Moreno et al., 2015) have shown that tidal disturbances generated by a near miss with another galaxy will produce disc instabilities, which drive gas towards the galaxy's centre. The resulting enhancement of star-formation is predicted to persist on timescales of proximately 1 Gyr. Since this mechanism is most sensitive to the nearest neighbour distance, the correlation between tidal suppression of star formation and Σ_5 could potentially be weak.

It is likely that all of these quenching mechanisms act on galaxies in dense environments to some degree. Yozin & Bekki (2015) suggested that within galaxy groups the star formation distribution in a galaxy is influenced simultaneously by both tidal interactions causing central enhancement of star-formation and ram-pressure stripping reducing the star-formation rate at large galactic radius. Several profiles in the highest density environment bins in Figure 2.8 do seem to show evidence of both central enhancement of star-formation and its reduction at large radius, though examples of such systems are not numerous enough to alter the median profiles.

The SAMI observations are evidence for different modes of quenching occurring in different environments. In Section 2.4.3 we showed that for $\log_{10}(\Sigma_5/\mathrm{Mpc}^2) > 0.5$, galaxies with below average specific star formation rates tend to have their star formation concentrated towards their centres. In environments of lower density, systems with low specific star formation rates have more extended star formation. The spatial dependence for the quenching of star formation in galaxies varies across the range of environmental densities currently sampled by our survey.

Further insight into the nature of environmental effects on star formation in galaxies will be obtained by investigating how the spatial distribution of star formation is affected by the galaxy group properties. The separation of galaxies in dense environments into satellite and central systems has featured heavily in recent studies of environment processes (e.g. van den Bosch et al., 2008; Peng et al., 2012). This and the increased sample size that will be afforded by the full SAMI galaxy survey will enable us to investigate these aspects of environmental star formation quenching in much more detail. A study of the effects of galaxy group properties on star formation will be presented in a future paper.

2.5.3 How many galaxies do we need to observe?

While the number of systems that we have studied is a factor of 10 larger than that of Brough et al. (2013), the environmental quenching trends when separated into bins of mass, are too weak to quantify for the whole range of galaxy masses with the current sample. However, the results obtained from the present study set the scene for future investigations of this topic.

The SAMI Galaxy Survey sample is drawn from mass selected volumes derived from the GAMA survey. As a result our coverage of the whole range of environment densities is not uniform. The majority of galaxies in our sample exist in low and intermediate density environments where the intrinsic scatter in galaxy properties is dominant. We have circumvented this inhomogeneity in the environment density by splitting our sample and using metrics for comparison that are independent of the total number of galaxies in each bin, such as the fraction of galaxies with centrally concentrated star formation. These fractions still have an associated error, and in future studies of larger samples we will reduce the error bars and achieve a comparable statistical weight in a larger number of stellar mass and environment density bins.

If we assume that the observed trend between the fractions of galaxies with centrally concentrated star formation and Σ_5 holds, we can estimate the numbers of galaxies required to achieve 1σ errors of $\pm 5\%$ on the fractions. We do so by generating an ensemble of beta distributions defined by a variety of galaxy numbers in the same ratio as observed in our sample. For each beta distribution the 1σ error interval is define by the range between the 15.9^{th} and 84.1^{th} percentiles. In low-density environments where $\sim 95\%$ of star forming galaxies have extended star formation morphologies we need only ~ 25 galaxies per bin in stellar mass and environment density to achieve the 5% error bar. In high density environments, since the fraction of galaxies with centrally concentrated star formation is much higher, we need a larger number of galaxies in each bin. We estimate that approximately 75 galaxies are required in high density environments to constrain the fraction to better than 5%. Therefore, if we were to repeat the analysis from Figure 2.13, with three environment density bins showing low fractions of centrally concentrated star formation and two bins showing higher fractions of centrally concentrated star formation we would require 225 galaxies per mass bin, with a distribution that is highly weighted towards the high density environments[4].

The full SAMI survey will include ~ 3400 galaxies. This will allow us to separate galaxies into finer bins of stellar mass and local environment density. If we reject galaxies at the same rate as we have for this analysis (as detailed in Section 2.2.5; i.e. from an initial sample of 808 galaxies down to 201), we will have a total of 900 galaxies at our disposal for further analysis. Under the assumption that we will require 225 galaxies to detect an environmental trend with 5% errors, this implies that we will be able to study the environmental trends in roughly 4 bins of galaxy stellar mass. With the completion of SAMI and other large-scale IFU surveys we will have an unprecedented view of the environmental processes occurring in galaxies.

[4]A calculation is presented in Appendix A that, assuming the observed relationship between Σ_5 and $r_{50,H\alpha}/r_{50,cont}$ holds across a range of circumstances, suggests a total of 250 galaxies per stellar mass bin would be required to confidently detect the observed trends.

2.6 Conclusion

We have used SAMI integral-field spectroscopy to study the spatial distributions of ongoing star formation in a sample of 201 star-forming galaxies as a function of their local environment densities.

We have shown that the derived integrated Hα star formation rates from integral field spectroscopy will be underestimated by approximately 9% if a single average dust correction is applied to the galaxy. The non-linear nature of dust extinction demands that the attenuation must be accounted for locally within different regions of a galaxy. Failure to perform a local spaxel-by-spaxel dust extinction correction results in a systematic reduction of the total measured SFR of $\sim 8\%$ in the most star-forming galaxies.

Analysis of the star formation rate surface density radial profiles of 201 galaxies in our sample has shown a large variation in the radial distributions of star formation in our galaxies. For any given mass or environment density the normalisation of a galaxy's star formation rate radial profile can vary by more than a factor of 10. For our star-forming sample we note that the normalisation of the star formation increases almost linearly with stellar mass in accordance with the known star-formation rate versus stellar mass relation. There is no significant relationship between the central star formation rate surface density and the local environment density, but we note a 2σ significance steeping of the Hα radial profiles in high density environments in galaxies with masses in the range $9.92 < \log_{10}(M_*/M_\odot) < 10.94$. This is consistent with the relationship between the specific star formation rates and Σ_5 in Figure 2.9, and implies that the environmental suppression of star formation must occur first in the outskirts of galaxies

When the central star-formation rate surface density in a galaxy is controlled for, we see a significant steepening of the profiles in higher density environments. For galaxies in the highest mass bin ($9.92 < \log_{10}(M_*/M_\odot) < 10.94$) we observed the median normalised star formation rate profiles to steepen from $-0.54 \pm 0.18\,\mathrm{dex}\,r_e^{-1}$ to $-1.09 \pm 0.26\,\mathrm{dex}\,r_e^{-1}$.

We have also shown that $(30 \pm 15)\%$ of galaxies in high-density [$\log_{10}(\Sigma_5/\mathrm{Mpc}^2) > 0.5$)] environments exhibit a centrally concentrated star formation distribution. In low-density environments only $(5 \pm 4)\%$ show similar star formation morphologies. This is taken as evidence that the occurrence of outside-in quenching is more common in dense environments and is consistent with the findings of studies in clusters (e.g. Koopmann & Kenney, 2004a; Koopmann et al., 2006). This conclusion is supported by the observed radial gradients in the D_n4000 flux ratio. Galaxies which exhibit the most extremely centrally concentrated Hα also have stronger D_n4000 towards their edges, in contrast to systems which show extended Hα morphologies. As the D_n4000 spectral feature is sensitive to star formation quenching on timescales of up to ~ 1 Gyr, we estimate that this outside-in quenching must occur faster than this, though careful modelling and a more comprehensive study of the spectral features will be required to determine the timescales accurately.

The observed correlations between the star formation morphology of galaxies and the local environment density are significant but weak. These trends appear to be dominated by the intrinsic variation in galaxy properties across all environments. For this reasons sample sizes of over 225 galaxies per mass bin will be required to ensure the statistical

significance of the results of future studies.

In lower density environments ($\log_{10}(\Sigma_5/Mpc^2) < 0.5$), the smaller fraction of passive systems indicates that quenching must be occurring at a lower rate than in higher density regions. In these environments galaxies with the lowest specific star formation rates appear to have spatially extended Hα morphologies which we take to be the qualitative signature of different mechanisms (such as starvation) acting to suppress the star formation in galaxies.

Galaxies of higher stellar mass are more likely to show the signatures of outside-in quenching. Even when the effect of correlation between mass and environment density is controlled for, this relationship persists. We must therefore conclude one of several things: 1) that higher mass galaxies are more susceptible to environmental effects than low mass galaxies, 2) the environmental mechanisms that quench high mass and low mass galaxies are qualitatively different, or 3) that the outside-in quenching of star formation in massive galaxies proceeds at a lower rate in higher mass galaxies and occurs almost instantaneously in lower mass galaxies. We believe that the last two of these scenarios are most plausible.

A future study will utilise a larger sample size to investigate in more detail the role of galaxy mass on environmental quenching, and incorporate a more detailed analysis of the galaxy group properties that drive the various quenching processes.

2.7 Acknowledgements

We would like to thank the anonymous referee for their constructive comments and suggestions, which improved the clarity and presentation of our results.

The SAMI Galaxy Survey is based on observation made at the Anglo-Australian Telescope. The Sydney-AAO Multi-object Integral field spectrograph (SAMI) was developed jointly by the University of Sydney and the Australian Astronomical Observatory. The SAMI input catalogue is based on data taken from the Sloan Digital Sky Survey, the GAMA Survey and the VST ATLAS Survey. The SAMI Galaxy Survey is funded by the Australian Research Council Centre of Excellence for All-sky Astrophysics (CAASTRO), through project number CE110001020, and other participating institutions. The SAMI Galaxy Survey website is `http://sami-survey.org/`.

The ARC Centre of Excellence for All-sky Astrophysics (CAASTRO) is a collaboration between The University of Sydney, The Australian National University, The University of Melbourne, Swinburne University of Technology, The University of Queensland, The University of Western Australia and Curtin University, the latter two participating together as the International Centre for Radio Astronomy Research (ICRAR). CAASTRO is funded under the Australian Research Council (ARC) Centre of Excellence program, with additional funding from the seven participating universities and from the NSW State Government's Science Leveraging Fund.

GAMA is a joint European-Australasian project based around a spectroscopic campaign using the Anglo-Australian Telescope. The GAMA website is `http://www.gama-survey.org/`.

ALS acknowledges support from a European Research Council grant (DEGAS-259586).

SMC acknowledges the support of an Australian Research Council Future Fellowship (FT100100457). SB acknowledges funding support from the Australian Research Council through a Future Fellowship (FT140101166) JTA acknowledges the award of a SIEF John Stocker Fellowship. MLPG. acknowledges support from a European Research Council grant (DEGAS-259586) and the Science and Technology Facilities Council (ST/L00075X/1). MSO acknowledges the funding support from the Australian Research Council through a Future Fellowship Fellowship (FT140100255). MA is funded by an appointment to the NASA Postdoctoral Program at Ames Research Centre, administered by Universities Space Research Association through a contract with NASA. JvdS is funded under Bland-Hawthorn's ARC Laureate Fellowship (FL140100278). NS acknowledges support of a University of Sydney Postdoctoral Research Fellowship. This research made use of Astropy, a community-developed core Python package for Astronomy (Astropy Collaboration et al., 2013). We also used the Numpy and Scipy scientific python libraries.

Chapter 3

The SAMI Galaxy Survey: Observing the environmental quenching of star formation in GAMA groups

This chapter has been submitted to the Monthly Notices of the Royal Astronomical Society for publication. As such, it has had to be reformatted from the original MNRAS template style. The author list for the final publication will include A. L. Schaefer, S. M. Croom, N. Scott, S. Brough, J. T. Allen, K. Bekki, J. Bland-Hawthorn, J. V. Bloom, J. J. Bryant, L. Cortese, L. J. M. Davies, C. Federrath, L. M. R. Fogarty, A. W. Green, B. Groves, A. M. Hopkins, I. S. Konstantopoulos, A. R. López-Sánchez, J. S. Lawrence, R. E. McElroy, A. M. Medling, M. S. Owers, M. B. Pracy, S. N. Richards, A. S. G. Robotham, J. van de Sande, C. Tonini, and S. K. Yi.

A. L. Schaefer wrote the text and performed all analysis on the reduced SAMI data. A. L. Schaefer also calculated the tidal perturbation parameters presented in Sections 3.3.4 and 3.3.5, the galaxy velocities relative to the group that are used in Section 3.3.6, and R_{200} estimates from the GAMA data catalogues using the methods described in the text. All other environment measurements used were extracted from GAMA catalogues prepared by the authors cited in the text.

Abstract

We explore the radial distribution of star formation in galaxies in the SAMI Galaxy Survey as a function of their local group environment, and other measures of interaction associated with the suspected mechanisms for environmental quenching. We find that the dynamical mass of the parent halo of a galaxy is a good predictor for the signatures of environmental quenching. Groups with halo mass greater than $10^{12.5}\,\mathrm{M}_{\odot}$ marginally reduce the specific star formation rates of galaxies, but the spatially-resolved signature of this reduction appears to vary with the stellar mass of each galaxy. Galaxies more massive than $\mathrm{M}_{*} \sim 10^{10}\,\mathrm{M}_{\odot}$ have star formation quenched first in their outskirts, while galaxies less massive than this are quenched uniformly across their discs. The dominant star-forming galaxies in groups with mass less than $10^{12.5}\,\mathrm{M}_{\odot}$ appear to have their star formation enhanced by $\sim 0.2 \pm 0.09\,\mathrm{dex}$ over non-group galaxies of the same mass, with marginal evidence that this enhancement occurs in the centres of these galaxies.

3.1 Introduction

Much of the literature on the impact of galaxy environments on their star formation has been confined to studies of galaxy clusters. In these environments the evidence suggests that the removal of gas from galaxies and subsequent suppression of star formation is likely to be caused by one of two primary mechanisms: Ram pressure stripping or strangulation. Ram pressure stripping occurs when the kinetic interaction between the interstellar medium (ISM) of a galaxy in the intergalactic medium (IGM) forces the gas out of the galaxy (Gunn & Gott, 1972). Narrow-band imaging studies of the distribution of Hα emission in Virgo cluster galaxies (e.g. Koopmann & Kenney, 2004b,a; Koopmann et al., 2006) indicate that the ram pressure stripping of gas from galaxy discs is the main mechanism acting to suppress star formation. This conclusion is backed up by Cortese et al. (2012), who showed that the relative spatial extent of ultraviolet emission in Virgo galaxies was correlated with the amount of neutral gas present.

Strangulation occurs when the infall of gas onto the disc of a galaxy is halted, starving the galaxy of fuel for future star formation (Larson et al., 1980). This can occur when a galaxy falls into a cluster or group and its outer gaseous envelope is heated or removed. Strangulation has been proposed as one of the primary mechanisms for star formation quenching outside of clusters (Rasmussen et al., 2008b; Peng et al., 2015). Furthermore, other works that examined different star formation rate indicators as a function of environment density within clusters (e.g. von der Linden et al., 2010; Rodríguez del Pino et al., 2017) derived a slower quenching timescale than is expected from rapid ram pressure stripping. These authors suggested that quenching takes place over several Gyr, implying that ram pressure stripping can not be the primary physical mechanism that quenches galaxies that are situated in clusters.

Although clusters represent the most extreme environments, only approximately 5% of galaxies exist in rich clusters. There is evidence that less extreme environments such as galaxy groups play a role in quenching star formation in galaxies in the local universe. Since approximately $40 - 50\%$ of galaxies exist in groups at $z \sim 0$ (Eke et al., 2004;

Robotham et al., 2011), the majority of environment-driven galaxy evolution is likely to occur outside of clusters. Indeed, studies of the clustering of luminous passive galaxies show that they group together on larger spatial scales than galaxy clusters (Brown et al., 2008). Furthermore Eisenstein et al. (2005) showed that the redshift evolution of this clustering is the same for cluster and field populations, indicating that the build-up of the red sequence must be occurring both inside and outside of clusters.

For example, Wilman et al. (2005) showed a strong decline in the number of emission-line galaxies in groups between $z = 0.5$ and the present day. This work, and many other studies of large samples derived from spectroscopic and photometric surveys, have reached the conclusion that the environmental quenching of star formation must be a rapid process (Balogh et al., 2004; Wijesinghe et al., 2012). In these studies the scarcity of galaxies in transition between star-forming and passive was interpreted to signify a rapid quenching timescale. However, the measurement of the integrated star formation rates of galaxies from central spectra or integrated colours is not without its perils. Strongly dust-obscured star-forming galaxies can masquerade as part of the red sequence (eg. Wolf et al., 2005; Gallazzi et al., 2009) if an accurate obscuration correction is not applied. However, Schawinski et al. (2014) cautioned that the interpretation of the rarity of galaxies between the star-forming blue cloud and the passive red sequence as rapid quenching is erroneous if galaxy morphology is not taken into account. The majority of disc-like 'late type' galaxies inhabit the blue cloud and green valley on the colour-mass diagram, while 'early-types' form the majority of the red sequence. That is, when only disc-like galaxies are considered, the fraction of galaxies in transition is higher, and a longer quenching timescale is implied.

In a study that made a robust, multi-wavelength comparison of twelve different star formation rate metrics, Davies et al. (2016b) showed that the star formation rate calibrations can vary markedly between surveys. Differences between the star formation rates of populations of galaxies derived by different means can make direct comparisons of the quenching timescales found by different authors problematic. Discrepancies between the indicators discussed in this work result from differences in the timescales to which the observed emission is sensitive, as well as systematic differences between the calibration of these star formation rate indicators. Further, aperture biases are a concern for single-fibre spectroscopy (Hopkins et al., 2003b; Brinchmann et al., 2004; Richards et al., 2016) and thus the quenching timescales in dense environments have remained controversial.

Other authors, using data from single-fibre spectroscopic surveys, have argued that much of the environment-driven evolution of galaxies can be explained by interactions between close pairs. Robotham et al. (2014) showed that galaxies that are both dynamically and spatially close to their nearest neighbour are likely to have disturbed optical morphologies. This idea was expanded upon by Davies et al. (2015), who showed that star formation in galaxies separated by less than $\sim 30\,\mathrm{kpc}$ can also be affected. Their data showed that for galaxies in close pairs, the more massive galaxy tended to have its star formation enhanced, while the less massive galaxy had its star formation suppressed. They posited that the tidal disturbance of gas in the more massive galaxy would trigger star-formation. While the enhancement of star formation in close pairs was also reported in other studies (e.g. Patton et al., 2013), they did not study the suppression of star formation during these interactions. Davies et al. (2016a) showed that galaxies with stel-

lar masses below $\sim 10^{8.5}\,\mathrm{M}_\odot$ become quiescent only in the presence of a more massive companion and argued that the increasing timescales for interaction between a galaxy of this mass and a more massive companion are consistent with their star formation being suppressed by strangulation. It is unclear whether the environmental suppression of star formation in groups is due to galaxy-galaxy interactions or whether it can be attributed to the impact of the group environment at large.

Rasmussen et al. (2012) observed the star formation rates of star-forming galaxies in groups to be suppressed by 40 per cent relative to galaxies outside of groups and that this environmental quenching is visible out to $\sim 2R_{200}$. Their analysis of the distribution of star-forming galaxies in groups implied that star formation is quenched in galaxies on timescales of approximately 2 Gyr and is accomplished by a combination of ram pressure stripping and galaxy-galaxy interactions.

This conclusion is backed up by results from the narrow-band Hα Galaxy Group Imaging Survey (HAGGIS; Kulkarni, 2015)[1]. By examining the detailed distributions of Hα emission in galaxies in groups, they observed that galaxies below the star formation rate main sequence typically had compact star formation with a steep radial profile. They also noted that differences in the distribution of stellar light for galaxies that are apparently in the process of quenching compared to main-sequence systems implicate some kind of gravitational interaction in the evolution of these systems.

The evidence that ram pressure stripping plays a role in the suppression of star formation in galaxy groups is mounting. Brown et al. (2017) observed that the neutral gas in group galaxies is reduced relative to isolated galaxies, and that this was most strongly correlated with the group halo mass rather than the local galaxy density. At fixed stellar mass, in groups with halo masses above $10^{13}\,\mathrm{M}_\odot$, the neutral gas reservoirs of galaxies were observed to be reduced more rapidly than the specific star formation rate. A comparison of their results to semi-analytic models and hydrodynamic simulations showed that this is consistent with the gas being rapidly stripped from galaxies in these groups. This phenomenon was interpreted to mean that ram pressure stripping must be acting to some degree in galaxy groups. While these observations are analogous to other work done in studies of galaxy clusters (e.g. Cortese et al., 2012; Fossati et al., 2013; Rodríguez del Pino et al., 2017), this was the first time such data has been able to show that ram pressure stripping is a major factor in the evolution of galaxies in groups.

Schaefer et al. (2017) showed that as the local environment density increases around a galaxy, the specific star formation rates (sSFR; SFR/M_*) drop and this reduction in star formation occurs in the outer parts of the galaxy. The steepening of the radial profiles of star formation in the densest environments in the sample were not accompanied by a significant change in the central star formation rate surface density, and they concluded that quenching occurs from the outside-in in the environments they studied. In this paper we follow on from the results of Schaefer et al. (2017), studying how the spatial distribution of star formation changes in galaxies relative to physically motivated measures of local environment, in particular the properties of their local groups, their location within those groups and the estimated tidal force acting on each galaxy. Our current work assumes a flat ΛCDM cosmology with $H_0 = 70$ km s^{-1} Mpc^{-1}, $\Omega_M = 0.27$ and $\Omega_\Lambda = 0.73$. Unless

[1]Accessible at: `https://edoc.ub.uni-muenchen.de/18818/1/Kulkarni_Sandesh.pdf`

otherwise stated, we adopt a Chabrier (2003) stellar initial mass function for calculation of star formation rates.

3.2 Methods

3.2.1 SAMI Data

The data for this study have been taken from the Sydney-Australian Astronomical Observatory Multi-object Integral Field Spectrograph (SAMI; Croom et al., 2012) Galaxy Survey (Bryant et al., 2015) and the Galaxy and Mass Assembly (GAMA; Driver et al., 2011; Hopkins et al., 2013) survey. The SAMI Galaxy Survey is an ongoing resolved spectroscopic survey of approximately 3600 galaxies performed using SAMI, which is mounted on the 3.9 m Anglo-Australian Telescope (AAT) at Siding Spring Observatory in Australia. SAMI comprises 13 optical fibre hexabundles (Bland-Hawthorn et al., 2011; Bryant et al., 2014) plugged into a steel plate at the prime focus of the AAT, 12 of which are used to observe galaxies while the remaining hexabundle observes a standard star. These optical fibres feed into the AAOmega spectrograph, where the light is split into a red arm ($\lambda\lambda 6300 - 7400\,\text{Å}$) and dispersed at a resolution of $R = 4260$, and a blue arm ($\lambda\lambda 3700 - 5800\,\text{Å}$) where it is dispersed to a resolution of $R = 1810$ (van de Sande et al., 2017). The SAMI hexabundles are made of 61 optical fibres fused to cover an approximately circular field of view with a 15″ diameter on the sky. Within each hexabundle the optical fibres fill the aperture with an efficiency of $\sim 73\%$. As a result, observations of galaxies with SAMI must be dithered to uniformly cover the image. We used approximately 7 pointings of 1800 s integrations for a total 12600 s exposure. The raw data are reduced using the SAMI data reduction package, which has been written in the PYTHON language[2] and makes use of the 2dFDR pipeline (Croom et al., 2004). The circular fibre cores are resampled onto a regular grid of 50×50 0.″5 spaxels. For a full description of the data reduction, see Allen et al. (2015) and for a discussion of representing the fibre data in a regularly gridded data cube see Sharp et al. (2015).

The galaxies observed for the main SAMI Galaxy Survey sample have been drawn from the equatorial regions of the GAMA spectroscopic survey (see Section 3.2.2). The SAMI survey sample has a stepped selection function in stellar mass with redshift such that the final sample has a nearly uniform distribution of stellar masses. This sample selection covers a wide range of galaxy stellar masses ($10^7 < M_*/M_\odot < 10^{11.5}$) in the redshift range $0.004 < z < 0.11$ and includes galaxies in a wide variety of environments from non-group galaxies to galaxies in $10^{14}\,\text{M}_\odot$ group halos. The SAMI survey augments the main GAMA-selected sample with a targeted sample of ~ 800 cluster galaxies (Owers et al., 2017), chosen from the 2 Degree Field Galaxy Redshift Survey (Colless et al., 2001) and the Sloan Digital Sky Survey (York et al., 2000; Abazajian et al., 2009). The cluster galaxies have not been used for this work. A thorough discussion of the SAMI target selection is given in Bryant et al. (2015).

[2] Astrophysics Source Code Library, ascl:1407.006 `ascl.net/1407.006`

3.2.2 GAMA Data

GAMA, the parent survey for SAMI, is a deep, highly complete spectroscopic survey of galaxies made in three equatorial regions centred on 9, 12 and 15 hours Right Ascension, with two additional non-equatorial fields that were not used for the SAMI selection. The equatorial fields have 98.5% complete spectroscopy to $r = 19.8$ mag, two magnitudes deeper than the SDSS (Liske et al., 2015).

Sérsic photometry

The GAMA survey targeted regions that have been covered by SDSS imaging in the u, g, r, i and z photometric bands. These images were re-analysed by Kelvin et al. (2012), who extracted objects from the images and fit single component Sérsic profiles to galaxies. We have made use of these data products, in particular the measurements of the effective radii (R_e), ellipticities and position angles extracted from the Sérsic fits to the SDSS r-band images.

Stellar Masses

We have used the GAMA estimates of the stellar masses of the galaxies in our sample and their companions. Stellar masses were computed by Taylor et al. (2011) who used the *ugriz* photometry and local-flow-corrected spectroscopic redshifts (Tonry et al., 2000) to construct the rest-frame spectral energy distribution of each galaxy. These spectral energy distributions were used to model the stellar mass, star formation history, metallicity, and dust extinction in each galaxy assuming a Chabrier (2003) stellar IMF. These stellar mass estimates are accurate to approximately 0.1 dex for galaxies brighter than $r_{petro} = 19.8$ mag.

GAMA Galaxy Group Catalogue

The deep and spectroscopically complete nature of the GAMA survey has allowed the creation of one of the most robust catalogues of galaxy groups made to date. Robotham et al. (2011) used a friends-of-friends linking algorithm to assign galaxies to groups. This two-step process uses both the projected separations of the galaxies and their redshifts to recover the true grouping of galaxies in space. The nature of the algorithm used is such that even galaxies in pairs are assigned to groups. The grouping algorithm locates the central galaxy of a group and computes the group size, multiplicity (number of members above the detection limit), and velocity dispersion. From these measurements, it is possible to derive a number of properties of the group and its members including the total dynamical mass of the halo, the projected distance of each galaxy from the centre of the group, and the line-of-sight velocity of each galaxy with respect to the group centre. For an in-depth discussion of the group-finding algorithm used to derive the catalogue, see Robotham et al. (2011), though note that at the time the original paper was published, the GAMA survey was still ongoing and consequently the size of the group catalogue and the spectroscopic completeness have since increased. We use the GAMA Galaxy Group Catalogue version 9.

3.2.3 Sample Selection

We have selected galaxies from the SAMI Galaxy Survey in the GAMA regions. This does not include galaxies that form part of the SAMI targeted cluster sample. At the time of writing there were 1295 galaxies from the SAMI main survey that have been observed and for which the data had been reduced. These galaxies have been made available through the SAMI internal data release v0.9.1. Our study of the spatially-resolved star formation properties of galaxies requires the selection of a set of star-forming galaxies.

Our method for selecting our star-forming sample mimics that of Schaefer et al. (2017). To measure whether a galaxy has any ongoing star formation, we have integrated the data cubes across both spatial axes and from the resulting spectrum we measure the equivalent width (EW) of the Hα emission, correcting for the underlying stellar absorption. If the absolute value of this EW is less than 1 Å we say that the galaxy is not star-forming. This Hα equivalent width cutoff corresponds to a sSFR limit of approximately $10^{-12}\,\mathrm{yr}^{-1}$, and eliminates 253 galaxies from our sample. In addition to this constraint we classify galaxies based on their emission line ratios in the central 2″. Based on the ratios of [N II] λ6583 to Hα and [O III] λ5007 to Hβ in this inner spectrum, we classify galaxies as either star-forming, composite or AGN/LINER based on their location on the Baldwin et al. (1981) diagram. Galaxies with line ratios that place them above both the Kewley et al. (2001) and Kauffmann et al. (2003c) lines are classified as AGN/LINER, of which we find 333 in our sample. Between these two constraints are a total of 165 composite objects and below both lines are the star-forming objects.

Recent advances have been made in decomposing the emission lines in galaxies hosting AGN into star-forming and AGN-excited components. Davies et al. (2016c) proposed a technique whereby the lines are modeled as a linear combination of spectra from the uncontaminated AGN and HII regions within a given galaxy. Due to the redshift of the galaxies in our sample, this technique can not be applied in general. The physical resolution of SAMI is typically $\sim 1\,\mathrm{kpc}$, meaning that a pure AGN basis spectrum cannot reliably be extracted from the data.

To reduce the effect of having hexabundles with a finite aperture on measuring the spatial distribution of star formation we also limit the sizes of our galaxies that we include in our analysis. Twenty six galaxies with effective radii greater than 15″ are rejected, as are 149 galaxies for which the seeing of the observation is greater than R_e. We also excluded galaxies that have ellipticity values greater than 0.7 to eliminate 200 edge-on systems. Our final star-forming sample comprises 325 galaxies, including 158 galaxies not assigned to groups and 167 galaxies in groups. We show the distribution of halo masses for our star-forming sample in Figure 3.1, which covers a range of masses between 10^9 and $10^{14.5}\,\mathrm{M}_\odot$. These histograms do not include galaxies that have not been identified as belonging to a group in the GAMA Galaxy Group Catalogue.

The rejection of galaxies as a function of M_* and environment

These constraints on our sample of star-forming galaxies have eliminated approximately 75% of our parent sample of 1295 galaxies. We note that some galaxies have been rejected based on more than one constraint. For example, of the 333 galaxies identified

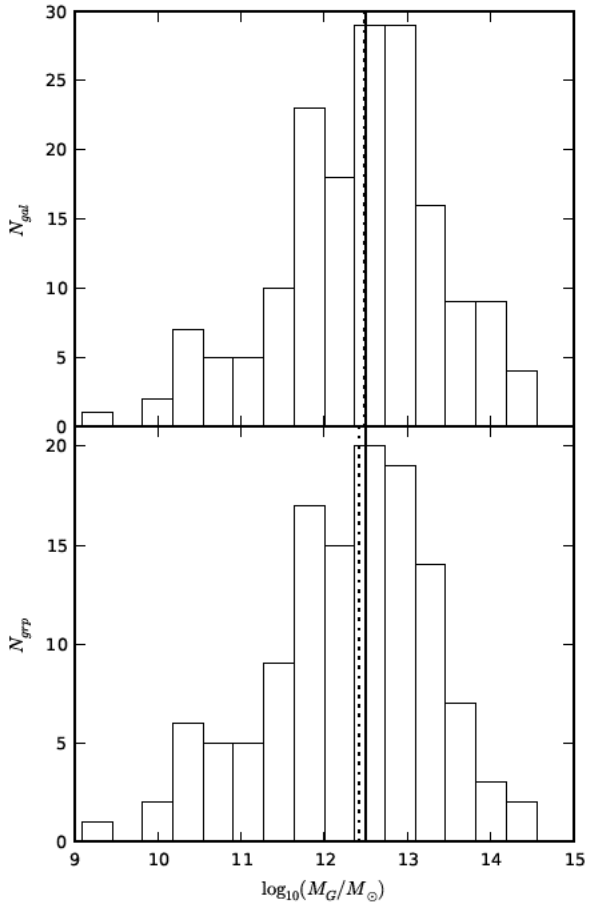

Figure 3.1: The distribution of halo masses for galaxies detected as being members of groups in our star-forming sample. In the upper histogram we show the number of galaxies in each interval of group mass, while in the lower histogram we show the number of individual groups in each interval of group mass. The vertical black solid line marks the $10^{12.5}\,\mathrm{M}_\odot$ division used throughout this work. The dotted line shows the median group mass, $M_G = 10^{12.46}\,\mathrm{M}_\odot$.

	(1) Coeff.	(2) Standard error	(3) z-value	(4) $P(z=0)$
Intercept	-36.4654	3.602	-10.124	4.31×10^{-24}
$\log(M_*/\mathrm{M}_\odot)$	3.5044	0.348	10.063	8.02×10^{-24}
$\log_{10}(\Sigma_5/\mathrm{Mpc}^2)$	0.2481	0.215	1.156	0.248

Table 3.1: The results of a logistic regression to determine the probability of rejecting a galaxy as a function of stellar mass and environment density. Column (1) shows the regression coefficients that represent the change in the log odds of a galaxy hosting a central AGN/LINER or composite spectrum. Column (2) is the standard error on the coefficients, column (3) is the ratio of the standard error to the coefficient, and column(4) is the p-value against the null hypothesis.

as AGN/LINER in their central regions, 203 were also rejected based on their low total level of Hα emission. The rejection of galaxies following the criteria outlined above was performed with the intention of selecting a clean sample within which our measurements of the distribution of ongoing star formation are robust. With such heavy losses to these criteria, it will be important to understand how the cuts affect the properties of galaxies in our sample.

Galaxies that have weak emission lines, and therefore fail our minimum 1 Å integrated Hα EW criterion, tend to have high stellar masses and preferentially inhabit the most dense environments. As noted above, of the 253 galaxies that have fail the Hα EW criterion, 203 have emission line ratios that are consistent with emission from a LINER. However, it could be possible that we are preferentially excluding galaxies based on their central emission line ratios that would otherwise have detectible star-formation in high-density environments. To test for this possibility, we perform a logistic regression (Cox, 1958; Walker & Duncan, 1967) that models the probability of having central AGN/LINER emission line ratios as a function of $\log_{10}(M_*/\mathrm{M}_\odot)$ and $\log_{10}(\Sigma_5/\mathrm{Mpc}^2)$. We use the Σ_5 metric to quantify environment in this test because it traces the environment density across the full range of galaxy environments present in our sample. Within our group sample we find that Σ_5 is highly correlated with the group mass or other environment density metrics. This implies that while the following test utilises Σ_5 to trace the environment density, the results should be applicable to most environment density metrics.

The logistic regression technique is used to understand the relationship between a dependent binary variable and one or more continuous explanatory variables, such as M_* or Σ_5. The logistic regression method models the log odds ratio of the dependent variable, y, being true as a function of the explanatory variables x_1 and x_2,

$$\ln\left(\frac{P(y=1)}{1-P(y=1)}\right) = \beta_0 + \beta_1 x_1 + \beta_2 x_2, \tag{3.1}$$

where β_0, β_1 and β_2 are the regression coefficients. These coefficients give the marginal increase in $\ln(P(y=1)/(1-P(y=1)))$ as the corresponding explanatory variable is increased, while the others are fixed.

Our test includes 477 galaxies that have integrated Hα EW larger than 1 Å, and satisfy all of the data quality constraints imposed upon our sample (PSF FWHM/R_e < 0.75, ellipticity < 0.7, $R_e < 15''$, and the environment density flag is 0 in the GAMA catalogues), though does contain galaxies with central AGN, LINER or composite spectra. The logistic regression shows that the probability of a galaxy hosting AGN/LINER or composite central emission line ratios is strongly correlated with its stellar mass, and that there is no significant relationship. The results of this regression are summarised in Table 3.1. This regression shows that the selection criteria that we have imposed on the central spectra of galaxies are strongly dependent on stellar mass, but not significantly dependent on Σ_5.

Although we are unable to reliably measure the distribution of star formation in galaxies with line ratios that are not consistent with excitation from young stars, we note that these galaxies are present across the full range of environments. The omission of these galaxies from our sample will not impact our conclusions on environment quenching.

Comparison of sample between different group environments

Interpreting any variation in the star-forming properties of galaxies between different subsamples requires that there be no major discrepancies in the galaxy properties between the different subsamples. In Section 3.3 we introduce three subsamples: i) galaxies that are not in groups, ii) galaxies that are in the Robotham et al. (2011) group catalogue with halo masses below $10^{12.5}\,M_\odot$, and iii) galaxies in groups with halo masses greater than $10^{12.5}\,M_\odot$. Fig. 3.1 shows the distribution of group halo masses. The mean halo masses for the samples above and below our $10^{12.5}\,M_\odot$ threshold are $10^{13.2}\,M_\odot$ and $10^{11.7}\,M_\odot$ respectively. It should be noted that there are only a handful of galaxies included that exist in haloes of mass greater than $10^{14}\,M_\odot$. Therefore our results reflect the role of group rather than cluster environments (where the nominal dividing line between the two is typically taken to be $10^{14}\,M_\odot$).

For the star-forming galaxies that satisfy the selection criteria outlined above, a K-S test indicates no statistically significant differences in the distributions of stellar mass, effective radius or redshift between the three environment samples (K-S< 0.2 and $p > 0.3$ between each variable in each group mass bin). However, given that errors in group mass can be large for low mass haloes we expect some overlap in halo mass between the ungrouped and low–mass group sample. We compare the environments in these two samples using the nth–nearest neighbour density (with the velocity limit of $1000\,\mathrm{km\,s^{-1}}$ and the same density defining sample as used by Schaefer et al. (2017)). These surface density measurements are described in full by Brough et al. (2013). Using a K-S test, the nth-nearest neighbour density is found to be significantly different between the ungrouped and low–mass group sample for all n values tested: $n = 5$ (Σ_5, K-S= 0.20, $p = 0.02$), $n = 3$ (Σ_3; K-S= 0.26, $p = 0.0005$) and $n = 1$ (Σ_1; K-S= 0.533, $p = 10^{-14}$). The increased significance for smaller n suggests that the low-mass group is dominated by groups of low multiplicity, including pairs.

Given that the mass, redshift and size distribution of our galaxies is the same for all samples, and that the GAMA spectroscopic completeness is over 98 per cent, it is clear that although there will be some overlap in halo mass between the ungrouped and

low-mass group sample, on average they correspond to different environments.

Our final star-forming sample is not mass complete. Galaxies with the highest stellar masses are preferentially removed from our sample, though as we have seen the loss of such galaxies occurs independent of environment. The sample of star-forming galaxies does not vary significantly with between different bins of group mass and we conclude that our analysis will focus on the same galaxies across all environments.

3.2.4 Analysis of SAMI data

The analysis of the SAMI data is as described in Schaefer et al. (2017), but for completeness we shall summarise the process here.

Annular Voronoi Binning

To facilitate a robust correction for dust attenuation along the line of sight, we applied annular Voronoi binning to the SAMI data cubes. Spaxels are added together in elliptical annuli to a signal-to-noise ratio of 10 per Å in the continuum at the wavelength of the Hβ line. An adaptive binning scheme has the advantage of providing sufficient signal to allow the subtraction of the Hβ absorption line and thus an accurate correction for dust extinction. This binning additionally ensures that the spatial scale over which a single dust correction is applied is minimised, while further ensuring that the radial structure in each galaxy is preserved. We have binned the SAMI data in 0.″5-wide elliptical annuli that are defined by the ellipticity and position angle obtained from the GAMA Sèrsic photometry.

Spectral fitting with lzifu

We fitted the spectrum within each annular Voronoi bin using LZIFU (Ho et al., 2016a). LZIFU is a spectral fitting pipeline written in the Interactive Data Language (IDL). It utilises the Penalised Pixel Fitting algorithm (pPXF; Cappellari & Emsellem, 2004) to model the stellar continuum light from each galaxy. For each spectrum we fitted a linear combination of simple stellar population (SSP) models from the MILES library (Vazdekis et al., 2010) with an 8th degree multiplicative polynomial to take into account any residual flux calibration errors and the reddening of the continuum from astrophysical sources. We used a 65 template subset of the full MILES library. This subset covers five metallicities from [Z/H] $= -1.71$ to 0.22 and thirteen ages spaced logarithmically in the range 0.063$-$14 Gyr. The continuum model derived by pPXF was subtracted from the data, and the emission lines, including Hα and Hβ, were fitted with single component Gaussians using the MPFIT routine (Markwardt, 2009).

3.2.5 Star-forming properties of galaxies

We use a number of metrics to determine the impact of the group environment on the star formation in the galaxies in our sample.

Integrated star formation rates

We calculated the total star formation rate within the SAMI aperture by adding the dust-corrected flux from each annular Voronoi bin. Dust extinction corrections are applied by measuring the departure of the Balmer decrement, the ratio of measured Hα flux to Hβ flux (BD; $f_{\mathrm{H}\alpha}/f_{\mathrm{H}\beta}$), from the canonical value of 2.86 predicted for Case B recombination under standard conditions. Under the assumption that the intervening dust forms a foreground screen to the HII regions in our target galaxies (Calzetti, 2001) and using the Cardelli et al. (1989) dust extinction curve, the obscuration-corrected Hα flux is

$$F_{\mathrm{H}\alpha} = f_{\mathrm{H}\alpha} \left(\frac{BD}{2.86} \right)^{2.36} \tag{3.2}$$

in each spectrum. In cases where the signal-to-noise ratio for the Hβ emission line is less than 3, or the measured Balmer decrement is less than 2.86, we assume no dust extinction and use the raw Hα flux. Integrating these dust-corrected fluxes over the SAMI aperture gives the integrated flux, which is converted to a luminosity using the redshift of each galaxy

$$L(\mathrm{H}\alpha) = \frac{F_{\mathrm{H}\alpha}}{4\pi d_L^2}, \tag{3.3}$$

where d_L is the luminosity distance to the galaxy. We calculate the star formation rates in our galaxies with the Kennicutt (1998) relation assuming a Chabrier (2003) IMF:

$$\mathrm{SFR} = \frac{L_{\mathrm{H}\alpha}\ (W)}{2.16 \times 10^{34}}\ \mathrm{M}_\odot\ \mathrm{yr}^{-1}. \tag{3.4}$$

In the case of galaxies that are quiescent, that is, with Hα equivalent width below 1 Å, we calculate a nominal star formation rate from the measured Hα emission. In these galaxies the Hα emission is highly contaminated by diffuse ionised gas, and emission caused by ionisation from sources other than a young stellar population (e.g. Cid Fernandes et al., 2011). The quoted star formation rates for quiescent galaxies therefore represent upper limits.

The spatial distribution of star formation

We quantify the radial extent of star formation in galaxies within our sample by making use of the ratio $r_{50,\mathrm{H}\alpha}/r_{50,cont}$, described at length in Schaefer et al. (2017). This measurement compares the radius within which half of the dust-corrected Hα emission emanates to the radius containing half of the continuum light from the part of the galaxy that lies within the view of the SAMI hexabundles. These radii are calculated by measuring the curve-of-growth for the emission or continuum light. In calculating the curves-of-growth we have made the assumption that galaxies in our sample are idealised thin discs and any ellipticity is due to their inclination to our line of sight. The ellipticity and position angle on the sky are taken from the GAMA Sèrsic photometric fits to SDSS r-band images. An in-depth discussion of the measurement, advantages of, and systematic effects that can arise by making this measurement on galaxies observed with 15″ integral field units can be found in Schaefer et al. (2017).

3.3 Results

3.3.1 Group mass and integrated star formation rates

There is a significant body of work in the literature that focusses on how the star formation rates of galaxies change with stellar mass and environment density (e.g. Peng et al., 2010; Wijesinghe et al., 2012; Peng et al., 2012; Alpaslan et al., 2015; Davies et al., 2016a). These results are generally based on large-scale single-fibre spectroscopic or photometric surveys. With a sample size of 325 star-forming galaxies, our primary aim is not to duplicate the results of these large surveys. Instead we measure integrated star formation rates with the intention of using these values as a diagnostic for the enhancement or suppression of star formation in galaxies. We shall restrict ourselves to a comparison of the values of star formation rates internally within SAMI galaxies, and not compare to the rates derived by other surveys. This restriction is due to the different treatment of aperture effects by us and by other surveys. See Richards et al. (2016) for a thorough discussion of this topic.

We quantify the effect of group environments on the star-forming properties of galaxies by comparing the sSFRs of galaxies in our sample to their stellar masses and the masses of their parent group haloes. In Figure 3.2 we split our entire sample into three intervals of halo mass. A non-grouped sample, which comprises galaxies that do not appear in the GAMA Galaxy Group Catalogue (Robotham et al., 2011), a low-mass group sample with groups that have multiple galaxies within halos of mass below $10^{12.5}\,\mathrm{M}_\odot$, and a high-mass group sample with galaxies in group halos more massive than $10^{12.5}\,\mathrm{M}_\odot$. This boundary was chosen to approximately evenly split the grouped galaxy sample in two. We note that group masses here are derived from the dynamics of galaxies within each halo. For galaxies in the ungrouped subsample, the method of Robotham et al. (2011) was unable to estimate the halo mass. Based on the tight correlation between total stellar mass within a group and its halo mass presented by Yang et al. (2007), we can estimate that the most massive halos in the ungrouped sample will be of order $10^{11} - 10^{12}\,\mathrm{M}_\odot$. We will not use this kind of estimate for the remainder of this paper.

In the upper row of panels of Figure 3.2, we show the sSFRs of star-forming galaxies using blue circles, and of passive galaxies with red triangles. Black points are the median values of the sSFRs for star-forming galaxies in bins of stellar mass. In all environments there is a sharp increase in the passive fraction of galaxies at approximately $10^{10.5}\,\mathrm{M}_\odot$, in agreement with numerous previous studies (e.g. Kauffmann et al., 2003b; Geha et al., 2012). In the two lowest density environments the fraction of passive galaxies below this stellar mass threshold is $5 \pm 2\%$ for ungrouped galaxies and $3 \pm 2\%$ for the groups below masses of $10^{12.5}\,\mathrm{M}_\odot$. In the highest halo mass bin, the fraction of passive galaxies below the $10^{10.5}\,\mathrm{M}_\odot$ stellar mass threshold is somewhat higher at $23 \pm 4\%$. This figure represents the fraction of passive galaxies over the entire mass range less than $10^{10.5}\mathrm{M}_\odot$.

In addition to the increasing passive fraction of galaxies in the most massive groups, the sSFRs of star-forming galaxies are reduced in dense environments. The mean sSFR of star-forming galaxies is reduced from $\log_{10}(\mathrm{sSFR/yr}^{-1}) = -10.19 \pm 0.03$ in ungrouped galaxies, to $\log_{10}(\mathrm{sSFR/yr}^{-1}) = -10.35 \pm 0.05$ in the high-mass group sample. The reduction in the star formation rates of galaxies in massive groups relative to the non-

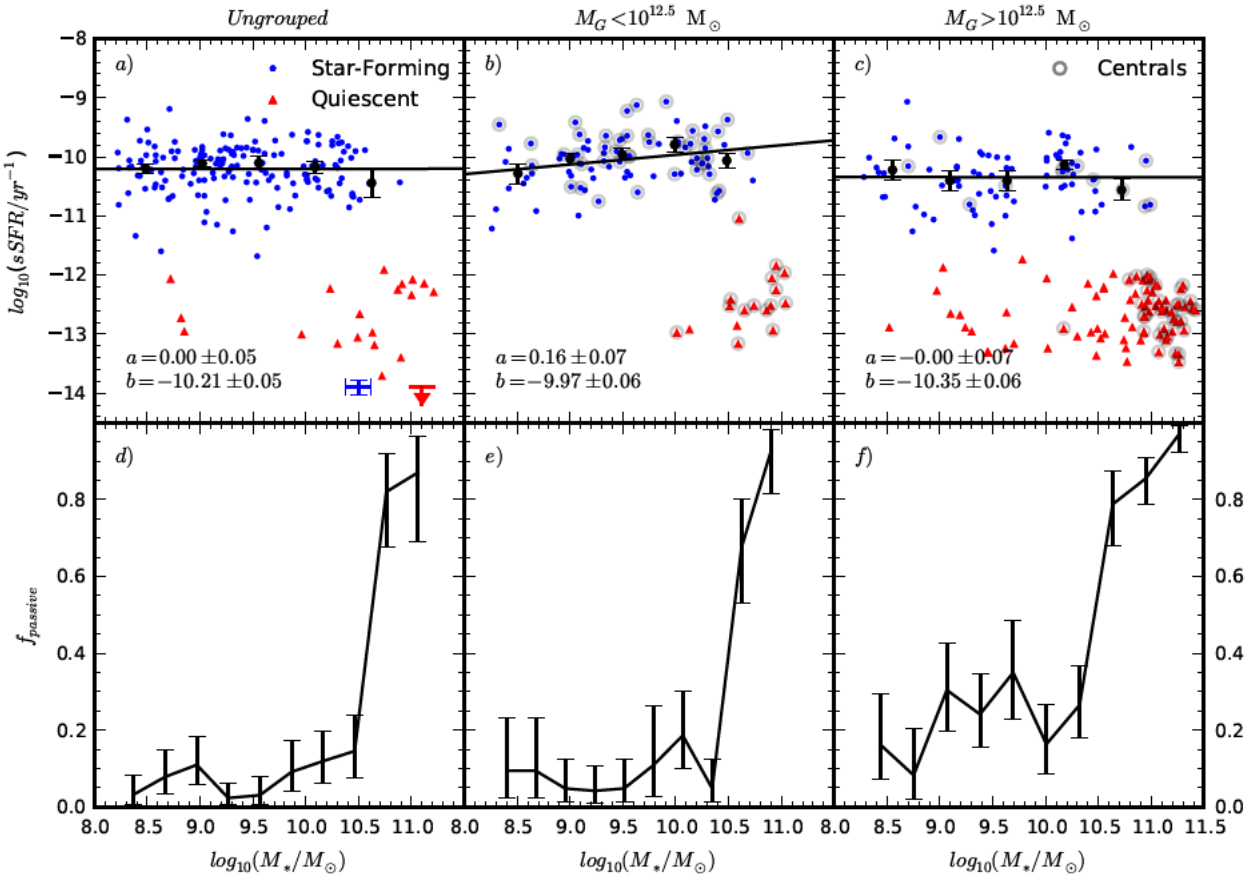

Figure 3.2: The top row shows the total sSFR of star-forming (blue points) and passive (red triangles) galaxies as a function of stellar mass, $\log_{10}(M_*/M_\odot)$, in different group environments. The indicated sSFRs of quiescent galaxies are upper limits. Markers surrounded by grey circles represent galaxies that are the centrals of their halo. The parameters for a straight-line fit to the sSFR-M* relation are displayed at the bottom left of each panel. The lower row shows the fraction of galaxies that were classified as passive in bins of stellar mass. For ungrouped galaxies and galaxies in low-mass groups, the passive fraction in galaxies with stellar masses below $10^{10.5}\,\mathrm{M}_\odot$ is $5\pm2\%$. In the higher mass groups the passive fraction of galaxies rises to $23\pm4\%$ for galaxies below the $\mathrm{M}_* = 10^{10.5}\,\mathrm{M}_\odot$ threshold.

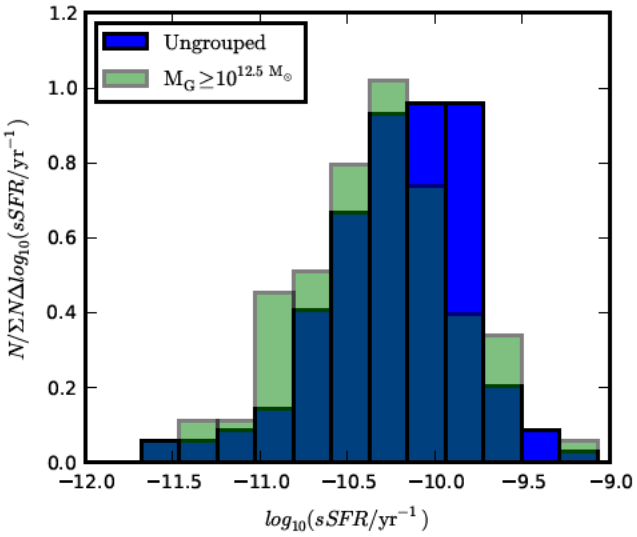

Figure 3.3: The normalised distribution of sSFRs for non-grouped galaxies (blue) and galaxies in groups with $M_G > 10^{12.5}\,M_\odot$ (green). The sSFRs of galaxies in massive groups are systematically lower than for ungrouped galaxies. A two-tailed Komogorov-Smirnov test indicates that the distributions differ with $\sim 2\sigma$ significance.

grouped sample is manifest in the changing of the distribution of sSFRs between the two environments. This change is demonstrated in Figure 3.3, which shows that the peak of the distribution in massive halos moves towards lower sSFRs with an asymmetry in the distribution imposed by a substantial tail towards lower values, and fewer galaxies with star formation rates above the non-grouped main sequence. The two-tailed Kolmogorov-Smirnov statistic for these two distributions is $D = 0.18$ with $p = 0.03$, which suggests a difference between the two distributions at the 2σ significance level. This difference requires investigation by a larger sample size.

While star formation appears to be suppressed in some galaxies in groups with masses above approximately $10^{12.5}\,M_\odot$, Figure 3.2 also shows the enhancement of star formation in galaxies in groups below this halo mass threshold. In the top row of panels we show the sSFRs of galaxies observed by SAMI as a function of their stellar mass in three bins of group halo mass. We have fitted a straight line of the form $\log_{10}(\mathrm{sSFR/yr}) = a \times \log_{10}(M_*/M_\odot - 10) + b$ to the star-forming galaxies in each bin of group environment and drawn this fit in solid black on the corresponding panel. The parameters of this fit show that the slope of the sSFR-stellar mass relation is steeper for galaxies in low mass groups compared to ungrouped systems by 0.16 ± 0.09. This change in slope represents an enhancement of star formation in higher mass galaxies in these low mass groups. Galaxy groups in this mass range typically have less than four members, with ~ 40 per cent of galaxies in this sample residing in groups with only two members at the depth of the GAMA survey spectroscopy. Galaxies at the higher mass end of this scale represent the most massive systems in these groups, and thus our observations agree with

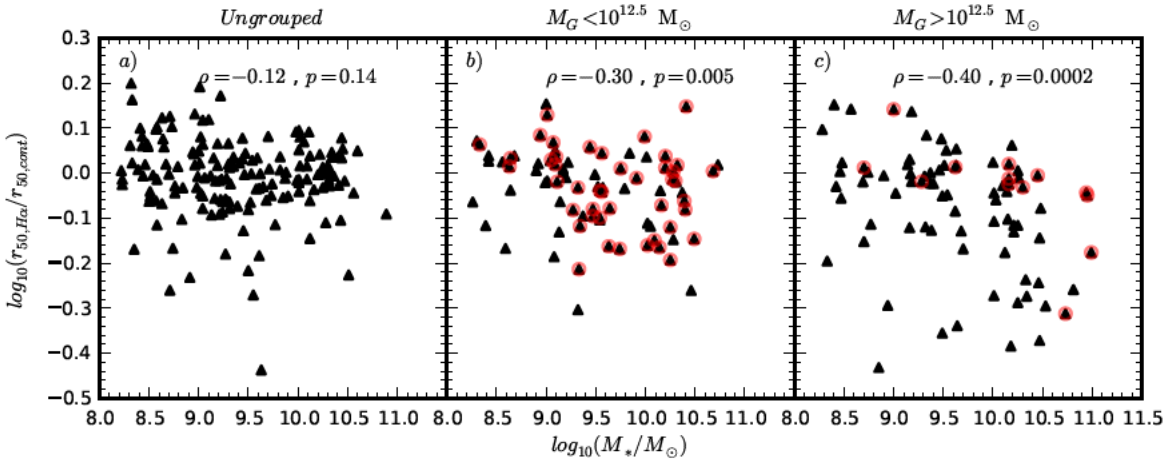

Figure 3.4: The scale-radius ratio as a function of stellar mass in different intervals of galaxy group halo mass. In the upper right of each panel we show the Spearman rank correlation coefficient and the associated p-value. For the ungrouped sample there is no statistically significant correlation, but in progressively more massive groups, more massive galaxies appear to have more centrally-concentrated star formation on average. Galaxies that have been identified as the centrals in their halos are marked with a red circle. In high-mass groups, the central galaxies have more spatially-extended star formation at a given stellar mass.

the enhancement of star formation in galaxy pairs reported by Davies et al. (2015) and Behroozi et al. (2015).

In all three bins of group environment, we note that he relationship between the sSFR of galaxies and their stellar mass is approximately flat, with the exception of the low-mass group bin, which has a mild positive slope. in all of these cases, the star formation rate main sequence, that is, the stellar mass vs star formation rate relation would have a split of 1.0 ± 0.07 or greater. This is somewhat steeper than the relations found by previous studies (e.g. Elbaz et al., 2007; Oliver et al., 2010; Zahid et al., 2012; Speagle et al., 2014; Davies et al., 2016b). Recently a number of authors have observed a turnover in the star formation rate main sequence at high stellar mass, with the slope diminishing above $\log_{10}(M_*/\mathrm{M}_\odot) \gtrsim 10.25$ (Whitaker et al., 2012; Gavazzi et al., 2015; Tomczak et al., 2016). The flattening of the main sequence has been linked to the varying mix of morphological types as a function of stellar mass, with systems containing larger bulges dominating at higher stellar mass (e.g. Weinzirl et al., 2009). Galaxies with larger bulge to total ratios are known to exhibit passive centres with the central emission lines exhibiting LINER-like line ratios (Belfiore et al., 2017). Our sample selection criteria has the effect of removing such galaxies, which will have the effect of masking the turnover in the star formation rate main sequence (e.g. Medling et al., 2018), and thus increasing the gradient. We note that galaxies with central LINER emission line ratios are rejected across all environments, meaning that our star-forming sample traces the same populations of galaxies in all bins of group mass.

		Ungrouped	$\log_{10}\left(\frac{M_G}{M_\odot}\right) < 12.5$	$\log_{10}\left(\frac{M_G}{M_\odot}\right) \geq 12.5$
$\log_{10}\left(\frac{M_*}{M_\odot}\right) < 10$	$\langle \log_{10}(r_{50,H\alpha}/r_{50,cont})\rangle$	-0.013 ± 0.009	-0.025 ± 0.012	-0.041 ± 0.018
	σ	0.093 ± 0.010	0.086 ± 0.009	0.126 ± 0.017
	f_{cen}	$0.04^{+0.02}_{-0.02}$	$0.05^{+0.03}_{-0.02}$	$0.10^{+0.05}_{-0.04}$
$\log_{10}\left(\frac{M_*}{M_\odot}\right) \geq 10$	$\langle \log_{10}(r_{50,H\alpha}/r_{50,cont})\rangle$	-0.005 ± 0.010	-0.063 ± 0.017	-0.124 ± 0.020
	σ	0.064 ± 0.010	0.089 ± 0.012	0.122 ± 0.011
	f_{cen}	$0.04^{+0.04}_{-0.03}$	$0.06^{+0.06}_{-0.04}$	$0.29^{+0.08}_{-0.07}$

Table 3.2: The scale-radius ratio of galaxies split into bins of stellar mass and group halo mass. $\langle \log_{10}(r_{50,H\alpha}/r_{50,cont})\rangle$ is the mean log scale-radius ratio, σ is the standard deviation of the log scale-radius ratio and f_{cen} is the fraction of galaxies with $\log_{10}(r_{50,H\alpha}/r_{50,cont}) < -0.2$.

3.3.2 The spatial extent of star formation in galaxy groups

We can estimate the spatial extent of ongoing star formation using the scale-radius ratio, $r_{50,\mathrm{H}\alpha}/r_{50,cont}$ for each galaxy in our star-forming sample. When this ratio is large, the star formation is spatially extended and occurs in the disc of the galaxy. When the ratio is small, the majority of star formation is occurring in the central parts of the galaxy.

We compare the scale-radius ratio to the galaxy stellar mass in the same three bins of group mass in Figure 3.4. The data show that galaxies in the most massive groups have more centrally-concentrated star formation on average. Across the three bins of group halo mass, the relationship between the stellar mass and the spatial extent of star formation changes. For ungrouped galaxies there is no correlation between the stellar mass and $r_{50,\mathrm{H}\alpha}/r_{50,cont}$. This is consistent with the findings of Schaefer et al. (2017), where we found no dependency of the scale-radius ratio on the stellar mass of galaxies in a smaller sample. Within groups, however, this is not the case. Galaxies in groups with $M_G < 10^{12.5}\,\mathrm{M}_\odot$ show a slight tendency to display smaller scale-radius ratios, particularly with increasing stellar mass. In these environments, the Spearman rank correlation coefficient between $\log_{10}(\mathrm{M}_*/\mathrm{M}_\odot)$ and $r_{50,\mathrm{H}\alpha}/r_{50,cont}$ is $\rho = -0.30$ with $p = 0.005$. In groups with $M_G > 10^{12.5}\,\mathrm{M}_\odot$ the strength of this correlation is increased to $\rho = -0.40$, $p = 0.0002$. In galaxy groups with halo masses above $10^{12.5}\,\mathrm{M}_\odot$, galaxies with stellar masses above $\sim 10^{10}\,\mathrm{M}_\odot$ will display star formation on a shorter radial scale than for similar ungrouped galaxies. For galaxies with stellar masses less than $\sim 10^{10}\,\mathrm{M}_\odot$, the spatial extent of star formation appears to be independent of the halo mass that the galaxy occupies. These results are summarised in Table 3.2.

We define galaxies as having 'centrally-concentrated' star formation if $\log_{10}(r_{50,H\alpha}/r_{50,cont}) < -0.2$ following Schaefer et al. (2017). This threshold was chosen to be 2 standard deviations below the mean for ungrouped galaxies. For galaxies with stellar masses greater than $10^{10}\,\mathrm{M}_\odot$, the fraction of galaxies that display centrally-concentrated star formation rises from $4^{+4}_{-3}\%$ in ungrouped galaxies, to $29^{+8}_{-7}\%$ in groups more massive than $10^{12.5}\mathrm{M}_\odot$. For galaxies below this stellar mass threshold, there is no statistically significant change in the fraction of centrally-concentrated star formers with group mass. In both ranges of galaxy stellar mass, the standard deviation from the mean of $r_{50,\mathrm{H}\alpha}/r_{50,cont}$ increases in

	Ungrouped, $M_G < 10^{12.5}$	$M_G > 10^{12.5}$	$P(\rho_1 = \rho_2)$
$8.2 < \log_{10}(M_*/M_\odot) < 9.1$	$\rho = 0.09$, $p = 0.42$	$\rho = 0.32$, $p = 0.18$	0.9σ, $p = 0.19$
$9.1 < \log_{10}(M_*/M_\odot) < 10.1$	$\rho = -0.20$, $p = 0.04$	$\rho = -0.17$, $p = 0.36$	0.17σ, $p = 0.63$
$10.1 < \log_{10}(M_*/M_\odot) < 11.0$	$\rho = -0.36$, $p = 0.007$	$\rho = 0.46$, $p = 0.009$	3.7σ, $p = 0.0001$

Table 3.3: Correlation coefficients for data displayed in Figure 3.5. ρ is the Spearman rank correlation coefficient between the sSFR and the scale-radius ratio in bins of stellar mass indicated in the first column, and in bins of group halo mass indicated in the top row.

groups with halo mass greater than $10^{12.5}\,M_\odot$. In low and high stellar mass samples, the standard deviation in the scale-radius ratio increases by 0.033 ± 0.020 and 0.058 ± 0.015 respectively. A summary of these figures is provided in Table 3.2.

Although Figure 3.4 shows that increased group mass tends to change the distribution of star formation in galaxies, it does not directly inform us whether group mass is associated with the quenching of star formation. Low values of $r_{50,\mathrm{H}\alpha}/r_{50,cont}$ can indicate either enhanced star formation in the centre of a galaxy or reduced star formation in the outskirts (or a combination of both). In Figure 3.5 we examine the relationship between the sSFRs of galaxies with the spatial extent of star formation as described by $r_{50,\mathrm{H}\alpha}/r_{50,cont}$ in different group environments. To highlight the qualitative differences in the quenching mechanisms at different stellar masses, we have divided our sample into three intervals of stellar mass. The various correlations for each stellar mass and environment interval are shown in Table 3.3.

For galaxies with $M_* > 10^{10.1}\,M_\odot$ that are either ungrouped or in group halos less massive than $10^{12.5}\,M_\odot$ (red points in Figure 3.5 c), there is a significant anti-correlation between the sSFR and $r_{50,\mathrm{H}\alpha}/r_{50,cont}$, with Spearman's $\rho = -0.36$ and $p = 0.007$. In these environments an increase in the sSFRs of galaxies is associated with a reduction in the scale radius ratio. A reduction in $r_{50,\mathrm{H}\alpha}/r_{50,cont}$ could correspond to either a suppression of star formation in the galaxy outskirts, or an increase in the star formation rate in the galaxy centre. In galaxies in that are either ungrouped or in halos less massive than $10^{12.5}M_\odot$, the corresponding increase in specific star formation implies an increase in the star formation rate in the galaxy centres. Conversely, the reduction of star formation occurs with star formation persisting on a relatively extended radial scale in low-mass groups.

For galaxies with $M_* > 10^{10.1}\,M_\odot$ in haloes more massive than $10^{12.5}\,M_\odot$ the distribution of star formation behaves differently as star formation is reduced (black crosses in Figure 3.5 c). For the massive group sample the sSFR correlates positively with $r_{50,\mathrm{H}\alpha}/r_{50,cont}$, with Spearman's $\rho = 0.46$, $p = 0.009$. Galaxies that have star formation rates that are below the average also have $r_{50,\mathrm{H}\alpha}/r_{50,cont}$ that indicates star formation is concentrated toward the centre of the galaxy. This implies that the onset of environmental quenching occurs in the outskirts of these galaxies. The outside-in quenching of star formation is the dominant form of environmental quenching in galaxies more massive than $10^{10}\,M_\odot$ in group haloes more massive than $10^{12.5}\,M_\odot$, while less massive galaxies have their star formation shut down more uniformly across their discs.

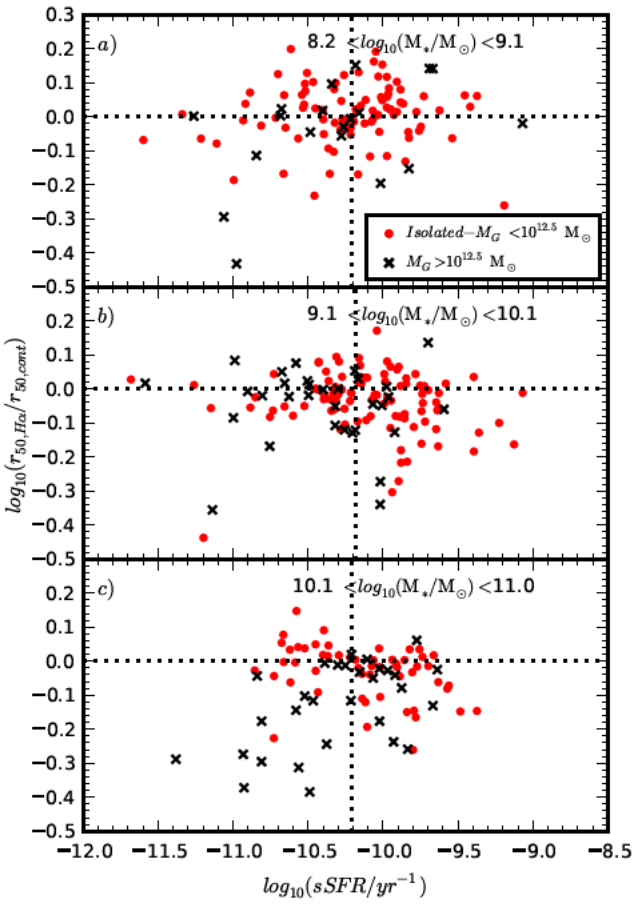

Figure 3.5: The scale-radius ratio as a function of the sSFRs of galaxies in the stellar mass intervals shown at the top of each panel.The vertical black dotted lines represent the mean $\log_{10}(\mathrm{sSFR/yr^{-1}})$ for ungrouped galaxies in each mass bin, and the horizontal dotted line represents equally extended star formation and stellar light. The distribution of star formation in galaxies as they move below the star formation rate main sequence depends on their stellar mass. In the two lowest stellar mass intervals, the star formation remains relatively extended across all environments. In the highest mass galaxies this is not the case. In massive groups, massive galaxies are quenched in their outskirts first.

Central enhancement of star formation in galaxies in massive groups?

We have calculated the central star formation rate surface density in a central 1″ aperture in each of the star-forming galaxies in our sample. With this aperture we are sampling the peak of the SAMI PSF, but are sensitive to enhancements on spatial scales smaller than the FWHM. The measured Σ_{sfr} all be lower than the true value, but differences within our sample will be meaningful in a relative sense. At the median redshift of galaxies in our sample of $z = 0.0295$, the typical seeing of 2.″2 corresponds to $\sim 1.7\,\mathrm{kpc}$. Based on the simulations of Moreno et al. (2015), the central enhancement of star formation following an interaction with a near neighbour should be visible on spatial scales smaller than $\sim 1\,\mathrm{kpc}$. We therefore expect that central enhancement from tidal interactions, if it exists in our sample, should be visible with this observation.

We have used the measured Σ_{sfr} values to test whether the central enhancement of star formation is able to explain the reduction in scale-radius ratio in high-mass groups. For galaxies with stellar masses in the range $10^{10} < M_*/\mathrm{M}_\odot < 10^{10.5}$, we compare the average central star formation rate surface density for normal galaxies and those with centrally-concentrated star formation. This limited range of stellar mass was chosen to minimise the influence of the relationship between central star-formation rate surface density and stellar mass. We find that in groups with halo mass greater than $10^{12.5}\,\mathrm{M}_\odot$ the mean central star formation rate surface density is $\log_{10}(\Sigma_{sfr}/\mathrm{M}_\odot\,\mathrm{yr}^{-1}\,\mathrm{kpc}^{-2}) = -1.41 \pm 0.11$ and $\log_{10}(\Sigma_{sfr}/\mathrm{M}_\odot\,\mathrm{yr}^{-1}\,\mathrm{kpc}^{-2}) = -1.20 \pm 0.19$ for normal and centrally-concentrated star-formers respectively. This yields a difference of 0.21 ± 0.31, which is below one sigma significance. The central star formation rate surface density in galaxies with centrally-concentrated star formation is not significantly different from other galaxies with similar stellar mass in the same environments.

Two possibilities exist for the reduction in $r_{50,\mathrm{H}\alpha}/r_{50,cont}$: either star formation is suppressed in the outskirts of these galaxies and the centre is unaffected, or the star formation profiles drop uniformly and the outer parts of the profile simply drop below our detection limit. The fact that the central star formation rate surface density in both normal and centrally-concentrated star-formers is similar discounts the second of these two scenarios.

The spatial extent of star formation and the colour-mass diagram

The position of a galaxy on the colour-mass diagram is commonly used diagnose its current evolutionary state. Galaxies in the blue cloud are often star-forming or have had a recent burst of star formation, while galaxies in the red sequence are often passive and have no evidence of star formation within the last several billion years. Galaxies in between the blue cloud and red sequence are often considered to be in the process of being quenched or having their star formation rejuvenated. We display the locations of the galaxies from our star-forming sample in this parameter space in Figure 3.6, dividing the sample into bins of group mass. We have used the dust-corrected $u-r$ colours as provided by Taylor et al. (2011). These have been corrected for foreground Milky Way extinction and internal extinction within the galaxy. In general, galaxies with $u-r$ colours placing them between the blue cloud and red sequence tend to have more centrally-concentrated Hα emission.

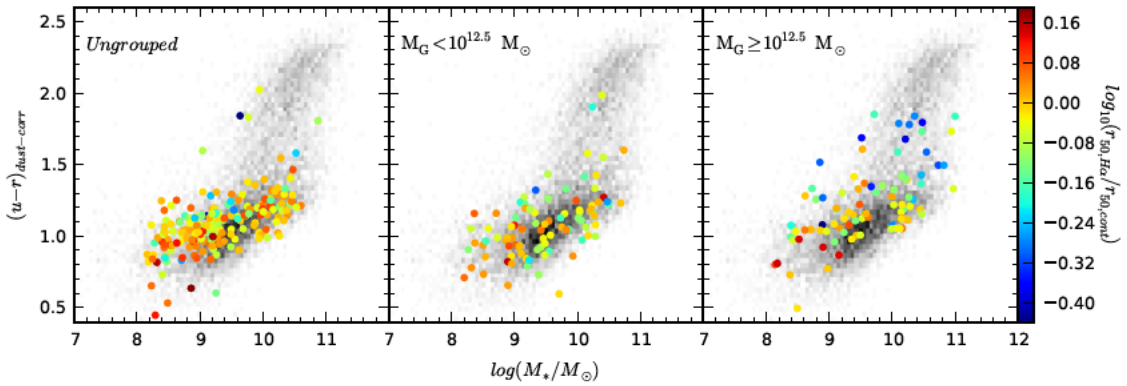

Figure 3.6: The position of galaxies in our star-forming sample on the $\log_{10}(M_*/\mathrm{M}_\odot)$ vs dust-corrected, rest-frame $u-r$ colour plane. Each panel shows an interval of group halo mass, The greyscale background represents the stellar mass and intrinsic $u-r$ colour of galaxies in the GAMA survey with $z < 0.1$, while the coloured points show the scale-radius ratio measured in SAMI galaxies. From left to right the panels include SAMI galaxies that are ungrouped, have measured group masses less than $10^{12.5}\,\mathrm{M}_\odot$ and have group masses above $10^{12.5}\,\mathrm{M}_\odot$. The colour scale is the same across all three group mass bins. Galaxies moving from the blue cloud to the red sequence in massive groups tend to have centrally-concentrated star formation.

This trend is especially visible in groups with mass greater than $10^{12.5}\,\mathrm{M}_\odot$. As galaxies in groups more massive than $10^{12.5}\,\mathrm{M}_\odot$ move away from the blue cloud, their star formation becomes more centrally-concentrated.

3.3.3 Satellite and central galaxies

Galaxies that are environmentally quenched may experience different processes that shut down their star formation depending on where they sit within their parent group halo. A galaxy that is at the centre of a group will be less likely to experience, for example, ram pressure stripping, than a galaxy that is its satellite. In galaxy groups that are dynamically relaxed, the most massive object will tend to sit at the centre of the halo, but this is not always the case (e.g. Skibba et al., 2011; Oliva-Altamirano et al., 2014). The group catalogue of Robotham et al. (2011) calculates an iterative group centre that is robust to the effects of massive galaxies in falling into groups. In this process, the galaxy that is most distant from the centre of light of the group is rejected and the centre of light is recalculated. This process is repeated until two galaxies remain, at which point the brightest of that pair is decided as the iterative centre. Robotham et al. (2011) reports that in 95 per cent of cases the iterative centre is the same as the brightest group galaxy. We term galaxies in our sample that are identified as the iterative centre of their group

as 'centrals' and all other group galaxies as 'satellites'.

In groups less massive than $10^{12.5}\,M_\odot$, the number of centrals in our sample is higher, representing a total of 48 of the 92 star-forming galaxies in this group mass bin. These galaxies preferentially occupy the higher end of the mass distribution and seem to drive the apparent enhancement of star formation seen in the low-mass group sample Figure 3.2 *b*).

Galaxies that are the centrals of massive groups are by definition rare and, having high stellar mass, are often passive. Of the 92 star-forming galaxies in groups more massive than $10^{12.5}\,M_\odot$, only 12 are centrals. This low number means that we are unable to make definitive statements about whether the spatial distribution of star formation in centrals differs in comparison to the star formation distribution in satellite galaxies in massive groups. In Figure 3.4 we have marked central galaxies with a grey circle. The reported correlation coefficient between $\log_{10}(M_*)$ and $\log_{10}(r_{50,\mathrm{H}\alpha}/r_{50,cont})$ goes from $\rho = 0.40$, $p = 0.0002$ with centrals included, to $\rho = 0.41$, $p = 0.0005$ for satellites only. We note that at all stellar masses, the star formation radial scale is higher for central galaxies in our sample than for satellite galaxies.

In Figure 3.5, we showed that the scale-radius ratio in galaxies with stellar masses greater than $10^{10.1}\,M_\odot$ in groups with halo mass greater than $10^{12.5}\,M_\odot$ correlated with their sSFRs. Galaxies that are environmentally quenched in these massive groups tend to have their star formation suppressed in their outskirts first. This trend is indicated by black crosses in the lower panel of Figure 3.5, and included both satellites and centrals. If we remove the central galaxies from this subsample we increase the strength of the correlation and its significance to $\rho = 0.53$ with $p = 0.006$, though the sample size is reduced to just 26 galaxies.

3.3.4 Galaxy-galaxy tidal interactions

A number of authors have suggested that dynamical disturbances driven by tidal interactions between galaxies in groups can cause gas to fall towards the centres of galaxies (e.g. Hernquist, 1989; Moreno et al., 2015). While this may cause the enhancement of star formation on short timescales, the consumption of gas by star formation induced by the interaction can ultimately cause the galaxy to become quenched earlier than in ungrouped galaxies. We can estimate the strength of the current tidal interaction using the perturbation parameter of Dahari (1984) and Byrd & Valtonen (1990),

$$P_{gc} = \left(\frac{M_c}{M_g}\right) \times \left(\frac{r_g}{d_{gc}}\right)^3, \tag{3.5}$$

where M_c is the mass of the companion, M_g is the mass of the galaxy being perturbed, r_g is the optical size of the galaxy and d_{gc} is the projected distance between the galaxy and its companion. Dahari (1984) and Byrd & Valtonen (1990) defined this r_g in terms of the optical sizes of galaxies as measured by hand from photographic plates, so we shall approximate this with the r-band r_{90}, the radius that contains 90% of the flux, as given by the GAMA Sérsic photometric fits. Byrd & Valtonen (1990) showed that gas infall is expected when the perturbation parameter is greater than $\sim 0.01 - 0.1$, depending on the

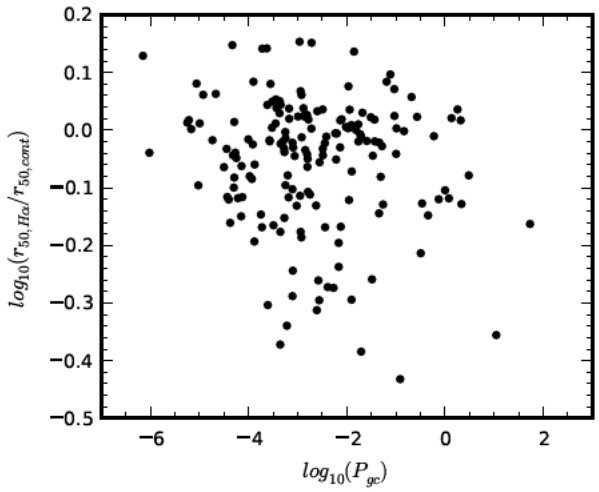

Figure 3.7: The scale-radius ratio as a function of the tidal perturbation parameter for galaxies in groups. With a Spearman rank correlation coefficient of $\rho = -0.06$ with $p = 0.41$, there is no evidence that the current tidal perturbation influences the radial distribution of star formation in these galaxies.

halo-to-disc mass ratio. We have calculated the perturbation parameter for all possible pairs of galaxies in the GAMA Galaxy Group Catalogue, and use the greatest perturbation within a group to estimate the tidal effects on a galaxy. Using this estimator of the strength of the tidal forces experienced by each galaxy in the group we find no evidence that tidal interactions change the radial extent of star formation in galaxy groups. This is shown in Figure 3.7. We must note that this does not necessarily imply that tidal interactions have no effect on the distribution of star formation in galaxies because there could be a considerable time delay between a tidal interaction and the movement of gas to the centres of the galaxies.

3.3.5 Tidal interactions with the group potential

The galaxy groups in this sample can be as massive as $10^{14}\,\mathrm{M}_{\odot}$. This means that tidal perturbations in individual galaxies can be caused by their gravitational interaction with the group potential as a whole. For a galaxy with mass M_g with radius r_g located at a distance d from the centre of a group halo of mass M_G, the tidal perturbation is given by

$$P_{Gg} = \left(\frac{M_G}{M_g}\right) \times \left(\frac{r_g}{d}\right)^3, \tag{3.6}$$

following Boselli et al. (2006). We calculate this value using the group mass and group-centric distances provided by the GAMA Galaxy Group Catalogue, and compare it to various properties of each galaxy. In Figure 3.8 we compare the group tidal perturbation

to the star formation rates and distributions in our sample. We find no correlation between the group tidal perturbation and the star-forming properties of the galaxies. The lack of correlation does not necessarily rule out that tidal interactions with the group potential could alter the properties of galaxies because the metric for tidal perturbation used has large systematic uncertainties. Each galaxy's distance d from the centre of the group is subject to projection effects, in addition to the group centre being poorly defined for groups with only a few members. The use of stellar masses for the mass of each galaxy is also systematically low; the amount of dark matter in each galaxy is unknown but likely higher than the stellar mass.

3.3.6 Projected phase space

Some recent works have made use of projected phase space diagrams as a means of diagnosing particular processes that may be acting on galaxies in clusters (e.g. Oman et al., 2013; Jaffé et al., 2015; Oman & Hudson, 2016; Weinzirl et al., 2017). In this scheme galaxies are placed in phase space with position and velocity measured relative to the host halo. Galaxies with velocities greater than the group velocity dispersion and within $0.5\,R_{200}$ are likely to undergo ram pressure stripping, low velocity galaxies far from the group centre are likely to be on their first passage through the group, and slow-moving galaxies close to the group centre are likely virialised within the group.

We calculate R_{200} for the groups in our sample using the prescription of Finn et al. (2005),

$$R_{200} = 1.73 \frac{\sigma_v}{1000\,\mathrm{km\,s^{-1}}} \frac{1}{\sqrt{\Omega_0 + \Omega_\Lambda (1+z)^3}} h_{100}^{-1}\,\mathrm{Mpc}, \tag{3.7}$$

where σ_v is the group velocity dispersion and z is the systemic redshift of the group.

In Figure 3.9 we display all galaxies in groups more massive than $10^{12.5}\,\mathrm{M}_\odot$ in projected phase space. Galaxies showing centrally-concentrated star formation ($\log_{10}(r_{50,H\alpha}/r_{50,cont}) < -0.2$) follow the same distribution in projected phase space as other star-forming galaxies. A two-sample Kolmogorov-Smirnov test comparing the centrally-concentrated star formers to the normal star-forming galaxies along each dimension of projected phase-space showed that the distributions are not significantly different. In group-centric radius the K-S statistic is $D = 0.21$ with p-value 0.62, and in relative velocity the K-S statistic is $D = 0.24$ with p-value 0.46.

All but one of the galaxies with centrally-concentrated star formation exist within R_{200} of their respective groups, and most have line-of-sight velocities relative to the group less than the group velocity dispersion. This projected phase space distribution may suggest that these galaxies have existed in their respective groups for several billion years.

3.3.7 Distribution of star formation vs group-centric radius

In Section 3.3.6 we saw that the distribution of centrally-concentrated star-forming galaxies in groups more massive than $10^{12.5}\,\mathrm{M}_\odot$ is not significantly different from other star-forming systems in projected phase space. We find no strong trend between $r_{50,H\alpha}/r_{50,cont}$ and group-centric radius for galaxies within groups. To highlight the difference between

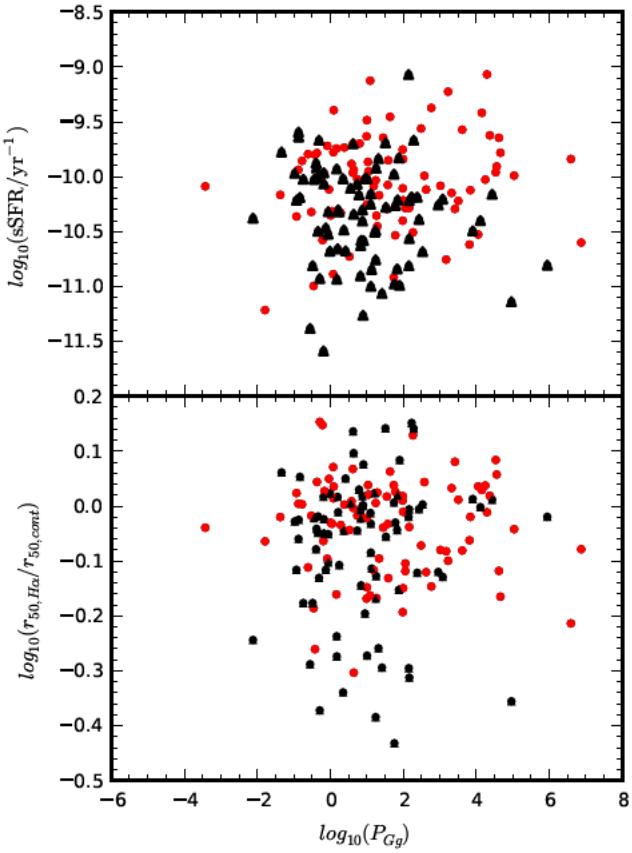

Figure 3.8: The star-forming properties of galaxies compared to the tidal influence of the group halo. In the upper and lower panels we compare respectively the sSFR and scale radius ratio to the group tidal perturbation parameter, P_{Gg}. Black points denote galaxies in groups more massive than $10^{12.5}\,\mathrm{M}_{\odot}$ and red points indicate galaxies in lower mass groups. There is no relationship with either measurement and P_{Gg}, though a systematic trend with the sSFR and $r_{50,\mathrm{H}\alpha}/r_{50,cont}$ does exist, both quantities being lower on average in more massive groups.

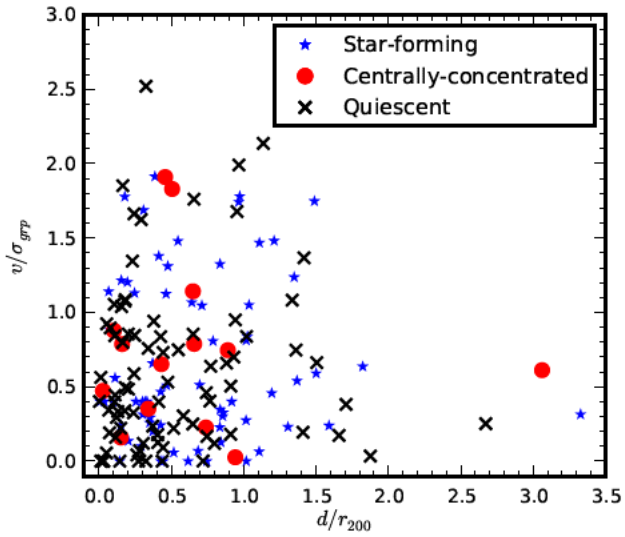

Figure 3.9: Projected phase space diagram for galaxies in groups with $M_G > 10^{12.5}\,\mathrm{M}_\odot$. The horizontal axis is the projected distance each galaxy is from the centre of the group, in units of R_{200}. The vertical axis is the velocity of each galaxy relative to the systemic velocity of the group compared to the velocity dispersion of the group. Blue stars and red circles are star-forming galaxies, and black crosses are passive galaxies. Red circles represent star-forming galaxies with centrally-concentrated star formation.

the galaxy populations within and outside of galaxy groups, we have matched galaxies from the ungrouped sample to the nearest group halo, within $\pm 1000\,\mathrm{km\,s^{-1}}$ from the matched group systemic velocity. Figure 3.10 shows the scale-radius ratio in galaxies in and around groups more massive than $10^{12.5}\,\mathrm{M}_\odot$. Within these groups, closer than R_{200} to the centre of the group, there is no correlation between d and $r_{50,H\alpha}/r_{50,cont}$. Within R_{200}, the fraction of star-forming galaxies with centrally-concentrated star formation is 35^{+9}_{-8} per cent. Outside of R_{200} this fraction drops to 7^{+7}_{-4} per cent[3]. There are relatively few galaxies with $M_* > 10^{10}\,\mathrm{M}_\odot$ outside of R_{200} that show the signatures of centrally confined star formation. Existing within R_{200} of a group with halo mass greater than $10^{12.5}\,\mathrm{M}_\odot$ appears to be the primary factor in determining the outside-in quenching of star formation for galaxies with $M_* > 10^{10}\,\mathrm{M}_\odot$.

3.3.8 Nearest neighbour interactions

Data from large-scale surveys has suggested that interactions between galaxies and their nearest neighbours may be able to either enhance or suppress star formation (e.g. Patton et al., 2013; Davies et al., 2015). To test this with SAMI, we use nearest-neighbour

[3]These fractions differ slightly, but not significantly from the fractions presented in subsection 3.3.2. This is because those fractions included galaxies that are associated with a group, but may have been further than R_{200} from the group centre.

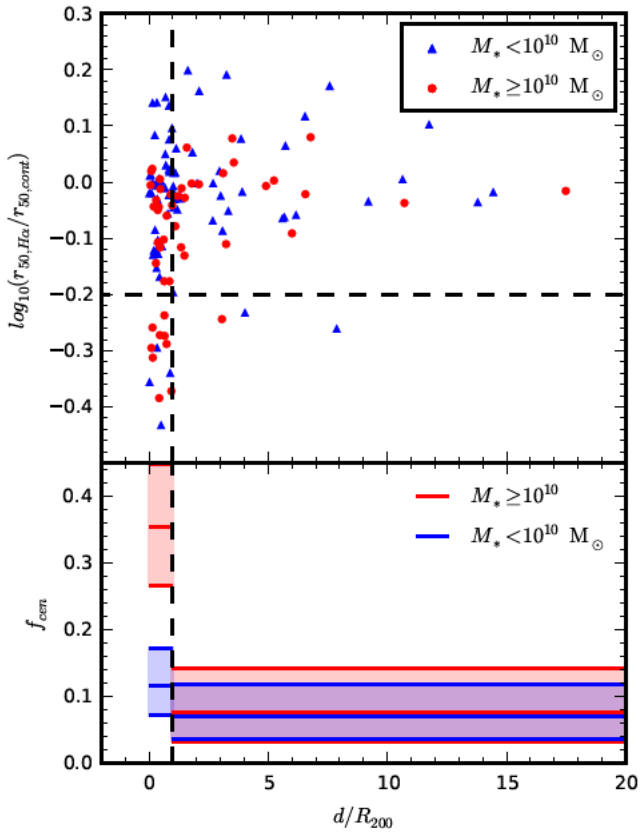

Figure 3.10: In the upper panel we show $r_{50,H\alpha}/r_{50,cont}$ for galaxies as a function of projected distance from the centre of the nearest group. This sample includes both galaxies that are in the GAMA Galaxy Group Catalogue and galaxies whose nearest group halo is more massive than $10^{12.5}\,\mathrm{M}_\odot$. The horizontal dashed line is the fiducial $\log_{10}(r_{50,H\alpha}/r_{50,cont}) = -0.2$ dividing line below which we say a galaxy has centrally-concentrated star formation. For $M_* > 10^{10}\,\mathrm{M}_\odot$, galaxies with centrally-concentrated star formation exist almost exclusively within R_{200}, though there is no correlation with projected group-centric distance within R_{200} in these groups. For galaxies less massive (blue) there is no radial trend at all, and the fraction of galaxies with $\log_{10}(r_{50,H\alpha}/r_{50,cont}) = -0.2$ is consistent with the scatter in the distribution. For massive galaxies the probability of having centrally-concentrated star formation increases significantly inside R_{200}. In the lower panel we show the fraction of galaxies with centrally-concentrated star formation inside and outside R_{200}. The fraction for low-mass galaxies is shown in blue and for high-mass galaxies it is shown in red. The shaded regions represent the range of fractions that cover the 68% confidence interval. There is no significant change in the fraction for low-mass galaxies within R_{200}.

		Ungrouped, $M_G < 10^{12.5}$	$P(\rho_{pairs} = \rho_{no\,pairs})$	$M_G > 10^{12.5}$	$P(\rho_{pairs} = \rho_{no\,pairs})$
$8.2 < \log_{10}(M_*/M_\odot) < 9.1$	pairs	$\rho = 0.09$, $p = 0.42$	0.28σ	$\rho = 0.32$, $p = 0.18$	-0.05σ
	no pairs	$\rho = 0.13$, $p = 0.26$	$P = 0.76$	$\rho = 0.30$, $p = 0.26$	$P = 0.96$
$9.1 < \log_{10}(M_*/M_\odot) < 10.1$	pairs	$\rho = -0.20$, $p = 0.04$	$6 \times 10^{-4}\sigma$	$\rho = -0.17$, $p = 0.36$	0.49σ
	no pairs	$\rho = -0.20$, $p = 0.06$	$P = 1.0$	$\rho = -0.02$, $p = 0.94$	$P = 0.62$
$10.1 < \log_{10}(M_*/M_\odot) < 11.0$	pairs	$\rho = -0.36$, $p = 0.007$	0.04σ	$\rho = 0.46$, $p = 0.009$	-0.53σ
	no pairs	$\rho = -0.35$, $p = 0.016$	$P = 0.96$	$\rho = 0.32$, $p = 0.19$	$P = 0.60$

Table 3.4: The strengths of the correlations between the sSFR and scale-radius ratio in galaxies in different bins of stellar mass and group halo mass. Also shown are the strengths of the correlations when close pairs (< 50 kpc separation) are removed. We have provided the significance of the difference in correlations, σ, and the probability P that they are the same. In our sample, galaxies in close pairs do not significantly affect our results.

projected distances from the GAMA spectroscopic catalogue, including galaxies that are not necessarily in the group catalogue, but are more luminous than $M_r = -18.5$ mag. For the sample as a whole, we find no dependence of the sSFRs of galaxies on the projected distance to the nearest neighbour, though we note that our sample size is several orders of magnitude smaller than the large samples acquired through single-fibre spectroscopy (e.g. Ellison et al., 2008). The ratio $r_{50,H\alpha}/r_{50,cont}$ appears to be reduced at small separations between galaxies, but the nearest-neighbour projected distance is strongly correlated with group mass, obscuring any strong conclusion. To resolve this issue we performed a partial Spearman rank correlation analysis between the group mass, nearest-neighbour projected distance, and $r_{50,H\alpha}/r_{50,cont}$ ratio for galaxies with group mass estimates. When the group mass is taken into account, the Spearman rank correlation coefficient between nearest neighbour projected distance and $r_{50,H\alpha}/r_{50,cont}$ is found to be small and not significant ($\rho = 0.09$, $p = 0.26$).

The effect of close pairs

As a further test for the effect of close pairs in galaxy groups, we remove the galaxies for which the nearest neighbour in the GAMA close pair catalogue of any luminosity is less than 50 kpc (projected distance) away. With the close-pairs removed from our sample we repeat the analysis of Figures 3.4 and 3.5. Removing the galaxies in close pairs has the greatest impact on the high-mass group sample, with the number of galaxies dropping from 82 to 53. In the massive groups and for galaxies more massive than $10^{10.1}\,M_\odot$ the Spearman rank correlation changes from $\rho = 0.46, p = 0.009$ to $\rho = 0.32, p = 0.19$. While the removal of the close pairs changes the value of the correlation coefficient and increases the p-value above the fiducial $p = 0.05$ significance level, the low numbers in the sample mean that the difference in the correlation coefficients is not significant. We find that the difference between the two correlation coefficients is significant at the level of 0.5σ. That is, within our sample removing the galaxy pairs is statistically no different from removing galaxies at random. We present the remainder of these results in Table 3.4, though no significant differences are found.

Davies et al. (2015) reported different environmental effects for galaxies depending on the relative mass of their nearest neighbour. Galaxies with a more massive companion are

more likely to be quenched, while those with a less massive companion are more likely to have their star formation enhanced. Our current sample size is not large enough to make any meaningful comment about this distinction.

3.4 Discussion

Taking advantage of the SAMI Galaxy Survey and the GAMA Galaxy Group Catalogue we have presented the relationships between the spatial extent of star formation and the total star formation rate with a number of metrics for local environment. The rationale behind this is that the signatures of particular quenching mechanisms will be most sensitive to the environment measures that best represent those processes. Based on the conclusions of previous authors we have identified tidal interactions, strangulation and ram pressure stripping as the primary candidates for quenching star formation in galaxy groups.

Our analysis has focussed on two measurements of the star formation that tell us about the nature of any quenching that is taking place. We study the sSFR, which tells us whether each type of environment is enhancing or suppressing star formation globally within a galaxy. In addition to the sSFR we include the scale-radius ratio, which provides information on the radial extent of star formation.

The SAMI data show that the mass of the group halo that a galaxy occupies is a good predictor of the signatures of star-formation quenching. Broadly, we find two intervals of group halo mass within which the star-forming properties of galaxies differ from each other and from an ungrouped sample. These are discussed below.

3.4.1 Massive groups, $M_G > 10^{12.5}\,\mathrm{M}_\odot$

Galaxies in more massive groups are more likely to be quenched, and star-forming galaxies in more massive groups have lower sSFRs than in ungrouped galaxies. Moreover, galaxies in groups with $M_G > 10^{12.5}\,\mathrm{M}_\odot$ with stellar masses greater than $\sim 10^{10}\,\mathrm{M}_\odot$ will have more centrally-concentrated star formation, while galaxies with stellar masses less than $10^{10}\,\mathrm{M}_\odot$ have more spatially-extended star formation. In both brackets of stellar mass, the sSFR is reduced in halos of greater mass. This trend, highlighted in Figure 3.4, indicates a qualitative difference in the way that star formation quenching proceeds for galaxies at different stellar masses. While this observation alone does not tell us what the mechanism is, it does have two implications for our understanding of the quenching process:

1. The environmental quenching of star formation is not an instantaneous process in group galaxies over the stellar mass range $8 < \log_{10}(\mathrm{M}_*/\mathrm{M}_\odot) < 11$ in halos up to $\mathrm{M}_G = 10^{14.5}\,\mathrm{M}_\odot$. If this quenching occurs on very short timescales, we would not see the lowering of the average sSFR by 0.15 ± 0.06 dex in the most massive groups. Instead we would only see an increase in the quenched fraction of galaxies.

2. Either low-mass galaxies and high-mass galaxies quench by a different mechanism, or a single mechanism causes the effects that we observe, but this mechanism affects the distribution of star formation in a way that depends on the stellar mass.

For example, if the timescale for the outside-in quenching of low-mass galaxies is substantially shorter than for high-mass galaxies, observing centrally-concentrated star-forming galaxies at low stellar mass will be less common.

In Table 3.2 we quantified the increased scatter of $r_{50,\mathrm{H}\alpha}/r_{50,cont}$ in the high-mass group sample. This increase in scatter is preferentially downward; that is, while some galaxies in more massive groups have radial star-formation distributions similar to those in ungrouped galaxies, a significant fraction have more centrally-concentrated star formation ($\log_{10}(r_{50,\mathrm{H}\alpha}/r_{50,cont}) < -0.2$), and very few have more extended star formation. In particular, 29^{+8}_{-7} per cent of galaxies more massive than $M_* = 10^{10}\,\mathrm{M}_\odot$ in the massive group sample have centrally-concentrated star formation, compared to 4^{+2}_{-2} per cent in ungrouped galaxies. The increase in the scatter in $r_{50,\mathrm{H}\alpha}/r_{50,cont}$ shows the mechanism that results in outside-in quenching in groups is not efficient. Simply being in a group does not guarantee the presence of a centrally-concentrated star formation morphology. It is not clear whether this process acts on all galaxies that fall into these groups, or whether the inclination of the galaxy disc to the direction of passage through the intergalactic medium influences the change in the star-formation distribution, as has been predicted by simulations of ram pressure stripping in galaxy groups and clusters (e.g. Bekki, 2014).

Alternatively, a small fraction of this scatter may be due to contamination of the group sample by foreground or background galaxies at approximately the same redshift. Such galaxies are likely to have star formation distributions that are similar to our ungrouped sample, that is with $\log_{10}(r_{50,\mathrm{H}\alpha}/r_{50,cont}) \sim 0$. These interlopers will certainly add to the scatter in our results, however we do not expect this kind of contamination to comprise a major fraction of our group sample. Applying their group finding algorithm to mock group catalogues, Robotham et al. (2011) found that the majority of interlopers are observed in the outskirts of groups, meaning that our results within R_{200} are unlikely to be dominated by interlopers.

We find that for galaxies that are identified as being the central object within their halo, at a given stellar mass the scale-radius ratio is higher than for satellite galaxies. For galaxies more massive than $10^{10.1}\,\mathrm{M}_\odot$, considering only the satellite galaxies increases the strength of the correlations between stellar mass and scale-radius ratio and sSFR and scale-radius ratio. The difference between the spatial distribution of star formation in satellites and centrals in massive groups is consistent with what previous authors (e.g. Peng et al., 2012) have concluded about the nature of environmental quenching. These authors have suggested that ram pressure stripping is a viable mechanism for the quenching of star formation in satellite galaxies.

3.4.2 Low-mass groups, $M_G < 10^{12.5}\,\mathrm{M}_\odot$

In contrast to the environmental suppression of star formation in galaxies in the high-mass group sample, we find that for galaxies in low-mass groups (that is, with halo mass $M_G < 10^{12.5}\,\mathrm{M}_\odot$), there is little evidence for environmental quenching in galaxies with stellar masses over $10^{10}\,\mathrm{M}_\odot$. We find that in these systems there is some evidence that star formation is slightly enhanced. Galaxies with stellar masses above $\sim 10^{10}\,\mathrm{M}_\odot$ appear to have their mean sSFRs boosted by 0.20 ± 0.09 dex above the mean for ungrouped galaxies

in the same stellar mass range. This enhancement is driven by the central galaxies in these low-mass groups, and based on the correlations presented in Figure 3.5, is accompanied by a small reduction in the scale radius of star formation.

A similar effect was noted by Davies et al. (2015) when studying the star formation rates of pairs of galaxies in the GAMA catalogue. They showed that the more massive galaxies in pairs have centrally-enhanced star formation, while the lower mass companion had its star formation suppressed. It is unclear whether we are observing the same trend as Davies et al. (2015), as they observed enhancement only late-stage mergers, and we have a substantially smaller sample and less coverage of small separation pair galaxies. The trends that we have reported here apply to galaxies separated by more than 30 kpc from their nearest neighbour.

In Figure 3.5 we investigated the radial extent of the star formation in galaxies as a function of their sSFR. Ungrouped galaxies and those situated in low-mass group environments tend to have more centrally-concentrated star formation as their sSFRs increase, while those with the lowest sSFRs tend to have extended Hα morphologies. This picture is broadly consistent with the simulations presented by Moreno et al. (2015), who showed that a close encounter between two galaxies will trigger the enhancement of star formation in a galaxy's centre.

Another possible explanation of our results comes from interpreting our data in the context of the discussion presented by Janowiecki et al. (2017). In this work, the authors observe that in galaxies in groups with only two members, the central tends to have higher a HI content than galaxies in isolation at the same stellar mass. These HI-rich systems were observed to have higher sSFRs as well. From these observations, the authors suggest that gas-rich minor mergers or direct feeding of gas from the intergalactic medium may be more common in such environments. The acquisition of HI gas mass measurements for our sample would allow us to comment further on this point.

3.4.3 Other metrics for interaction

Tidal Interactions

We do not find any significant correlation between the estimated strength of the tidal interaction between galaxies and their star-forming properties. The apparent strength of the tidal force acting on a galaxy, calculated from Equation 3.5, influences neither the total measured specific star formation or the scale radius of star formation relative to the scale radius of the stellar light. Superficially this might seem to contradict results from simulations (Hernquist, 1989; Moreno et al., 2015) that suggest a central burst of star formation can occur in a galaxy after a close encounter with a companion if gas is present. However, our measurement of P_{gc} is susceptible to systematic uncertainties imposed by projection effects when estimating the separation between two galaxies. The effect of projection will be to increase our estimate of the tidal interaction strength, and as such each measurement is at best an upper limit. A further shortcoming of this technique results from the fact that there is a delay between the time of closest approach for two systems and the time at which nuclear star formation will be triggered and is able to be measured. This delay, and the inability to distinguish between systems infalling towards

an interaction and those that are moving away after an interaction, makes identifying the signatures of tidal interactions difficult with this technique. Therefore, we cannot rule out the possibility that tidal interactions cause quenching in high-mass galaxy groups or enhancement in low-mass groups.

Projected phase-space

Within groups with halo mass greater than $10^{12.5}\,M_{\odot}$, we find no significant projected phase-space trends with $r_{50,\mathrm{H}\alpha}/r_{50,cont}$. Galaxies with the most centrally-concentrated star formation are predominantly found within R_{200}, with their projected group-centric distance distribution not differing significantly from other star-forming galaxies. With the exception of two systems their line-of-sight velocities relative to the group systemic velocity also lie mostly below the group velocity dispersion. Again, there is no significant difference between the distribution of line-of-sight velocities for galaxies with centrally-concentrated star-forming galaxies and other star-formers. If rapid ram pressure stripping was responsible for the cessation of star formation in these galaxies soon after their infall into these massive groups, we would expect a greater separation of these two types of galaxies in projected phase-space. Jaffé et al. (2015) observed the 21 cm neutral hydrogen emission line in galaxies outside the virialised region of galaxy clusters, and did not detect this line for galaxies inside the virialized region, where they have presumably resided in the clusters for several cluster dynamical times. A similar effect was seen by Weinzirl et al. (2017), who observed a deficiency of blue star-forming galaxies in the virialized centre of the Abel 901/2 cluster.

Given the difference in halo mass between the groups in our sample and the clusters studied by Jaffé et al. (2015) and Weinzirl et al. (2017), it is difficult to draw direct comparisons, but it seems probable that many of the galaxies with centrally-concentrated star formation are not on their first passage into their host groups. Indeed, comparing the distribution of these galaxies to the simulations of projected phase-space performed by Oman et al. (2013), we can conclude that the majority of centrally-concentrated star-forming galaxies have been in their groups for perhaps over three Gyr (see Oman et al., 2013, Figure 4). We interpret the distribution of these galaxies in projected phase space as a sign that the quenching of star formation by this outside-in mechanism is not instantaneous and persists over several group-crossing times.

Close pair interactions

Close-pair interactions have been reported to drive much of the environmental evolution of galaxies, including enhancing and suppressing their star formation (Robotham et al., 2014; Davies et al., 2015). We have found no statistically significant link between the nearest neighbour distance on either $r_{50,\mathrm{H}\alpha}/r_{50,cont}$ or the sSFRs of galaxies in our sample. However, we note that our sample contains low numbers of galaxies at separations small enough to adequately test the predictions of these previous studies. A more comprehensive study of the distribution of star formation in close pairs of galaxies will be possible once the full SAMI survey has been completed and a larger sample of close pairs can be constructed.

3.4.4 Comparison to other work

Our results have built on the work presented in Schaefer et al. (2017), and we find general agreement with the trends presented therein. While our previous work compared the spatial extent of star formation to the fifth-nearest neighbour surface density environment measure, the use of galaxy group properties has provided a framework for a more physical understanding of the processes at play. In contrast to Schaefer et al. (2017), we find an anti-correlation between the scale-radius ratio and the stellar mass of the galaxies, but this is only observed in more massive group haloes. The quenching of galaxies with stellar mass greater than $10^{10}\,\mathrm{M}_{\odot}$ from the outside-in in dense environments is consistent with our previous findings, with the lack of this signature at lower stellar masses made more significant by our expanded sample.

These results from SAMI echo the findings from Hα narrow-band imaging presented in Kulkarni (2015). Kulkarni observed that galaxies with small scale-radius ratios lie below the star formation main sequence. The centrally-confined distribution of star formation in these galaxies, along with an observed flattening in the stellar light profiles in the outskirts of the galaxies, led them to conclude that a combination of ram pressure stripping and gravitational interactions are the primary mechanisms influencing group galaxies today. While with SAMI we are unable to investigate the outer stellar discs of our sample, we do find agreement in the star formation morphologies. A future study that combines the radial coverage of narrow-band imaging with the spectroscopic advantages of integral field surveys will yield important clues as to the relative impact of these two processes on shaping the galaxy populations of today.

Bekki (2014) produced hydrodynamical simulations of the ram pressure stripping of gas from galaxies in groups and clusters. With these simulations they showed that the scale size of the star-forming discs of galaxies under ram pressure stripping can be reduced by a factor of two or more, depending on the halo mass of the group. In these simulations, galaxies under the influence of ram pressure stripping were capable of having their star formation either enhanced or suppressed. For high-mass satellite galaxies ($M_* > 10^{10}\,\mathrm{M}_{\odot}$) in our massive group sample, a reduction in the scale size of the star-forming disc is always accompanied by a reduction in the total specific star-formation rate. The galaxies for which we do see a reduced scale radius ratio accompanied by an enhancement of the integrated star formation rate are the centrals of low-mass group halos and are unlikely to be undergoing ram pressure stripping and perhaps more likely to have undergone recent minor mergers or experienced fuelling from extragalactic gas (Janowiecki et al., 2017).

In Figure 3.5 we showed that galaxies in massive groups ($M_G > 10^{12.5}\,\mathrm{M}_{\odot}$) with stellar mass greater than $10^{10.1}\,\mathrm{M}_{\odot}$ display a different star formation morphology as they become quenched than galaxies with lower stellar mass. Galaxies with lower stellar mass tend to quench with a more spatially extended star-formation morphology. The difference in the qualitative signatures of quenching at different stellar masses is difficult to reconcile with the idea of ram pressure stripping being the primary quenching mechanism for all galaxies. Bekki et al. (2002) showed that the removal of the halo gas surrounding a spiral galaxy resulting in the strangulation of the gas supply to the disc will result in the formation of an anaemic spiral. These simulations showed that as an anaemic spiral is formed, the star formation will fade uniformly across the galaxy disc. Combined with our

observation of radially extended star formation in low-mass galaxies as their star formation is reduced, these simulations may suggest that the quenching of star formation in galaxies with stellar mass less than $10^{10}\,M_\odot$ is caused by strangulation. This conclusion is reached independently by Davies et al. (2016a), who observed that the rate at which low-mass satellite galaxies become passive is consistent with the mechanism being strangulation.

3.5 Conclusion

We have used data from the SAMI Galaxy Survey to study the processes that suppress star formation in groups identified in the GAMA Galaxy Group Catalogue. The GAMA data provided several different metrics by which to quantify the environments of the galaxies in our sample. Our analysis shows that the dynamical mass of the group is a good predictor for the environmental quenching of star formation in galaxies of all stellar masses, with environmental quenching being strongest in groups more massive than $10^{12.5}\,M_\odot$. The tidal interaction parameter presented in Equation 3.5 does not correlate with any measurement of star formation suppression or enhancement, ruling out rapid quenching by tidal interactions. Indeed, the removal of galaxies for which the nearest neighbour is less than 50 kpc away did not influence the results, indicating that close-pair interactions are not responsible for the trends we have presented. We also showed that the positions of quenching galaxies in their group projected phase-space are inconsistent with rapid ram pressure stripping acting on their first passage through the group. This does not rule out ram-pressure as the mechanism responsible for the trends we observe, but it does indicate that the quenching of star formation in galaxy groups must take longer than the group dynamical time.

The spatial signature of this quenching depends on the stellar mass of the galaxies. We find that for satellite galaxies with stellar masses above approximately $10^{10}\,M_\odot$ in high-mass groups the scale radius of the star formation is reduced relative to that of the continuum for $29^{+8}_{-7}\%$ of galaxies, compared to $4^{+3}_{-4}\%$ for similar galaxies that are not in groups. This central confinement of the star formation is also associated with a reduction in the total star formation, with no strong evidence for central enhancement of star-formation. Star-forming centrals of massive groups do not appear to quench by this mechanism.

In the same massive groups, and in galaxies with stellar masses less than $10^{10}\,M_\odot$, the suppression of star formation does not show a tendency to accompany a central concentration of star formation. The qualitative variation in the spatial signature of quenching as a function of stellar mass suggests that different mechanisms are at play. Low-mass systems maintaining spatially-extended star formation while they become quiescent is consistent these galaxies quenching through strangulation, as was concluded by Davies et al. (2016a). In satellite galaxies in massive groups with stellar masses greater than $10^{10}\,M_\odot$, the central confinement of star formation during the transition from star-forming to quiescent is more consistent with ram-pressure stripping, tidal interactions, or a combination of both, taking place over several Gyr to quench star formation. This conclusion is in agreement with the simulations of Bekki (2014) and the estimated timescales are broadly consistent with the environmental quenching timescales outside of groups derived by other surveys

(Rasmussen et al., 2012; Fossati et al., 2017).

3.6 Acknowledgements

The SAMI Galaxy Survey is based on observation made at the Anglo-Australian Telescope. The Sydney-AAO Multi-object Integral field spectrograph (SAMI) was developed jointly by the University of Sydney and the Australian Astronomical Observatory. The SAMI input catalogue is based on data taken from the Sloan Digital Sky Survey, the GAMA Survey and the VST ATLAS Survey. The SAMI Galaxy Survey is funded by the Australian Research Council Centre of Excellence for All-sky Astrophysics (CAASTRO), through project number CE110001020, and other participating institutions. The SAMI Galaxy Survey website is `http://sami-survey.org/`.

The ARC Centre of Excellence for All-sky Astrophysics (CAASTRO) is a collaboration between The University of Sydney, The Australian National University, The University of Melbourne, Swinburne University of Technology, The University of Queensland, The University of Western Australia and Curtin University, the latter two participating together as the International Centre for Radio Astronomy Research (ICRAR). CAASTRO is funded under the Australian Research Council (ARC) Centre of Excellence program, with additional funding from the seven participating universities and from the NSW State Government's Science Leveraging Fund.

GAMA is a joint European-Australasian project based around a spectroscopic campaign using the Anglo-Australian Telescope. The GAMA website is `http://www.gama-survey.org/`.

MSO acknowledges the funding support from the Australian Research Council through a Future Fellowship (FT140100255). JTA acknowledges the award of a SIEF John Stocker Fellowship. JvdS is funded under Bland-Hawthorn's ARC Laureate Fellowship (FL140100278). SB acknowledges the funding support from the Australian Research Council through a Future Fellowship (FT140101166). S.K.Y. acknowledges support from the Korean National Research Foundation (2017R1A2A1A05001116) and by the Yonsei University Future Leading Research Initiative (2015-22-0064). This study was performed under the umbrella of the joint collaboration between Yonsei University Observatory and the Korean Astronomy and Space Science Institute. CF gratefully acknowledges funding provided by the Australian Research Council's Discovery Projects (grants DP150104329 and DP170100603). Support for AMM is provided by NASA through Hubble Fellowship grant #HST-HF2-51377 awarded by the Space Telescope Science Institute, which is operated by the Association of Universities for Research in Astronomy, Inc., for NASA, under contract NAS5-26555.

This research made use of Astropy, a community-developed core Python package for Astronomy (Astropy Collaboration et al., 2013). We also used the Numpy and Scipy scientific python libraries.

Chapter 4

Timing the quenching process using stellar populations

This chapter contains unpublished work by Adam Schaefer. In Section 4.2.2 we have made use of stellar population ages and metallicities based on the measurement and modelling of a set of Lick indices. These data were kindly provided by Dr. Nicholas Scott for this analysis. All other analysis was performed by Adam Schaefer.

4.1 Introduction

Having characterised the signatures of the environmental suppression of star formation in the previous chapters, we now turn our attention to characterising the timescale for this quenching. Understanding the timescale over which quenching occurs provides clues as to which mechanisms are causing the observed star formation suppression.

4.1.1 Timescales from ages

Integral field spectroscopy provides the opportunity to study the stellar populations of galaxies in great detail. Ongoing star formation in part of a galaxy provides a continued supply of young, massive stars that can contribute a large fraction of the light to the spectrum. When the star formation is shut down, these massive stars will quickly evolve and die, leaving behind the less-luminous and spectrally distinct lower mass stars. Thus, it is possible to determine the time since the last burst of star formation based on the spectral features observed across each galaxy.

The determination of the ages of the stellar populations in a galaxy can be achieved in a variety of ways. One can fit the entire spectrum with templates based on simple stellar population models using software such as the Penalised Pixel Fitting (pPXF; Cappellari & Emsellem, 2004). With pPXF a light-weighted, linear combination of templates with known ages and metallicities is returned, from which the mean stellar age and metallicity of the stars can be estimated. Alternatively, one can make use of the fact that the strengths of various spectral features depend on the mix of stars that contribute to the

local spectrum. Measuring a combination of defined absorption line features, and comparing these values to the predictions of stellar population models (e.g. González Delgado et al., 2005; Schiavon, 2007; Thomas et al., 2010) also allows us to estimate the stellar population properties. This technique has been in use for decades and was notably standardised with the Lick System of spectral index measurements (Faber et al., 1985; Worthey et al., 1994).

The strengths of each spectral feature may be sensitive to changes in the age and metallicity of a stellar population on different timescales. For example, molecular bands are weak in very young stellar populations, making them unsuitable for diagnosing quenching on short timescales, while changes in the Balmer absorption lines are not visible in stellar populations older than several billion years. Using a wide enough variety of spectral features allows us to probe changes in the stellar populations over a broad range of timescales, while controlling for differences in the strengths of spectral features that may result from changing abundance patterns.

4.1.2 Mechanisms from timescales

The environmental quenching of star formation can proceed in several different ways as introduced in Chapter 1. These include quenching by ram pressure stripping of the gas from the galaxy disc (Gunn & Gott, 1972), or strangulation as the resupply of gas to the galaxy is cut off (Larson et al., 1980). These processes can occur over very different timescales and as a result will leave a unique imprint on the stellar populations in galaxies.

Ram pressure stripping of the gas from galaxy discs is often observed in rich clusters. This can be diagnosed by a sharp truncation in the radial distribution of star formation (e.g. Boselli et al., 2006; Abramson et al., 2011), with evidence for young stellar populations beyond the truncation radius (Crowl & Kenney, 2006), though some of the strongest evidence comes from observations of the neutral gas in these galaxies. The ability of ram pressure to remove gas from a galaxy relies on it being strong enough to overcome the local gravitational field produced by the galaxy disc. If the ram-pressure does not exceed the restoring force of the galaxy potential then stripping can not occur. This was modelled analytically by Hester (2006), who showed that ram pressure stripping in a group environment is capable of removing gas only from the outer parts of a large spiral galaxy ($M_{disc} \sim 10^{11}\,\mathrm{M}_{\odot}$). The time over which the complete quenching of star formation may occur in a galaxy depends on the precise circumstances. The density, and temperature of the intergalactic medium, as well as the details of the galaxy orbit through its host cluster or group, and the inclination of the galaxy to its trajectory will have an impact on the quenching timescale. For a galaxy in a large cluster this quenching timescale can be as short as 100 Myr (Boselli & Gavazzi, 2006).

In contrast to ram pressure stripping, strangulation is thought to act over longer timescales, up to several Gyr (Larson et al., 1980; Peng et al., 2015). In the case of strangulation, young stellar populations are not expected to dominate the galaxy light, and strong gradients in the stellar populations will not be established. Furthermore, the sharp spatial truncation of star formation that is seen in ram-pressure stripped galaxies is unlikely to be seen. Strangulation is likely to produce the so-called anaemic disc galax-

ies, that maintain a similar spatial distribution of star formation to other star-forming galaxies, but at a lower level (van den Bergh, 1991; Elmegreen et al., 2002).

The mechanism by which a galaxy's star formation is suppressed will also influence the metal content of its gas and stars. Peng et al. (2015) argue that under the influence of strangulation the gas that remains in the galaxy disc will be enriched as the underlying stellar population evolves and recycles metals into the interstellar medium. As a result, the light-weighted metallicity in the galaxy will increase. In cases where the gas is removed from a galaxy rapidly, such as ram pressure stripping, very few new stars will form from gas that has been enriched by the by-products of subsequent stellar evolution, and the light-weighted stellar population will remain relatively metal-poor.

It is, in principle, possible to diagnose the quenching mechanism for star formation in a galaxy if sufficient information is known about the initial state of its stellar populations. However, this is not possible with a small sample of galaxies, and where measurements of the metallicity have considerable uncertainty. A large sample of stellar metallicity measurements across galaxies would be required to diagnose star formation quenching in this way.

4.1.3 Gas accretion and the distribution of star formation

In Chapter 3 we saw that galaxies in massive groups that are moving from the blue cloud to the red sequence often have centrally-concentrated star formation. On average, star-forming galaxies will have star formation distributions that are approximately exponentially declining with radius, and trace the distribution of light in the disc (recall that the scale-radius ratio in star forming galaxies is approximately 1 for galaxies on the main sequence). This distribution may be altered during the quenching process, and the mechanism by which this quenching occurs will have an impact on where the stars are currently forming. We have noted previously that processes such as ram pressure stripping, viscous stripping, as well as tidal interactions, will leave star formation restricted to the central parts of galaxies. Other processes exist that may produce a similar star formation distribution.

Recently Chen et al. (2016), using data from the MaNGA survey, reported a class of galaxy with centrally-concentrated star formation that could not be attributed to the environmental effects mentioned above. In these galaxies, which comprised $\sim 2\%$ of 489 star-forming galaxies in their sample, the mechanism that induced the star formation morphology was surmised to be the accretion of gas counter-rotating relative to the pre-existing gas. The collision between the in-falling and resident gas results in it losing angular momentum and falling towards the galaxy centre. Galaxies formed through this process exhibit gradients in their stellar populations, consistent with having quenched outer parts. Estimating the quenching timescale for this process is difficult. The time to use up the gas in each galaxy will depend on the amount of pre-existing gas, the amount of gas accreted, the resulting gas density and star formation rate, and whether or not further accretion of gas onto the galaxy continues. Nevertheless, the formation of galaxies with centrally-concentrated star formation by this mechanism can be tested by examining their gas and stellar kinematics. The presence of gas that is counter-rotating relative to the

CATAID (1)	z (2)	$\log_{10}(M_*/\mathrm{M}_\odot)$ (3)	n_r (4)	$\log_{10}(M_G/\mathrm{M}_\odot)$ (5)	SFR ($\mathrm{M}_\odot\,\mathrm{yr}^{-1}$) (6)	$r_{50,H\alpha}/r_{50,cont}$ (7)
517302	0.0287	10.18	3.11	13.08	0.49	0.41
543499	0.0535	10.25	1.80	14.06	0.07	0.52
594990	0.0435	10.34	2.55	13.47	0.26	0.53
492384	0.0554	10.46	1.54	13.15	1.21	0.57
346892	0.0585	10.28	2.09	ungrouped	1.38	0.78
297633	0.0550	10.43	1.40	ungrouped	2.58	0.79
485504	0.0561	10.20	1.94	ungrouped	0.41	0.99
575625	0.0547	10.24	1.51	ungrouped	0.38	0.99
619095	0.0527	10.47	1.13	ungrouped	3.67	0.96

Table 4.1: The properties of the quenching sample (above the central line) and the control sample (below the central line). Column (1): GAMA catalogue identification number; Column (2): spectroscopic redshift; Column (3): log stellar mass; Column (4): r-band Sérsic index; Column (5): Group halo dynamical mass; Column (6): star formation rate in the SAMI aperture; Column (7): The Hα-continuum scale radius ratio.

stars will be indicative of recent accretion being the cause of this particular mechanism.

4.2 Analysis of SAMI data

4.2.1 Sample Selection

In this chapter we perform a case study of four galaxies in massive groups that appear to be undergoing environment quenching, and and compare them to a control sample of five star-forming field galaxies. In Chapter 3 we saw that galaxies with stellar masses over $10^{10}\,\mathrm{M}_\odot$ appear to stop forming star first in their outskirts in groups more massive than $10^{12.5}\,\mathrm{M}_\odot$. For this reason our quenching sample has been chosen to occupy a narrow range of stellar masses ($10^{10.1} \leq M_*/\mathrm{M}_\odot \leq 10^{10.5}$), which minimises the impact of varying stellar mass on the types of quenching that may occur. The classification of a galaxy in a high-mass group as 'quenching' was performed on the basis of its star formation rate being below the average for galaxies of similar stellar mass (the mean SAMI star formation rate in this mass range is $1.8\,\mathrm{M}_\odot\,\mathrm{yr}^{-1}$), and having $\log_{10}(r_{50,H\alpha}/r_{50,cont}) < -0.2$. This definition is consistent with the definitions presented in Chapters 2 and 3, which is two standard deviations below the mean of -0.02. While other modes of star formation quenching may occur in massive galaxy groups, we will focus our attention on the outside-in mechanism that appears to occur in groups more massive than $10^{12.5}\,\mathrm{M}_\odot$. While four galaxies furnish only a relatively small sample, systems such as these are typical of quenching galaxies above $M_* = 10^{10}\,\mathrm{M}_\odot$ in massive groups. The techniques that we apply to these systems here can ultimately be applied to a larger sample to make a statistically robust measurement of the timescales of environment quenching and the effect of these processes on the galaxies.

In order to make a meaningful statement about the influence that environment quench-

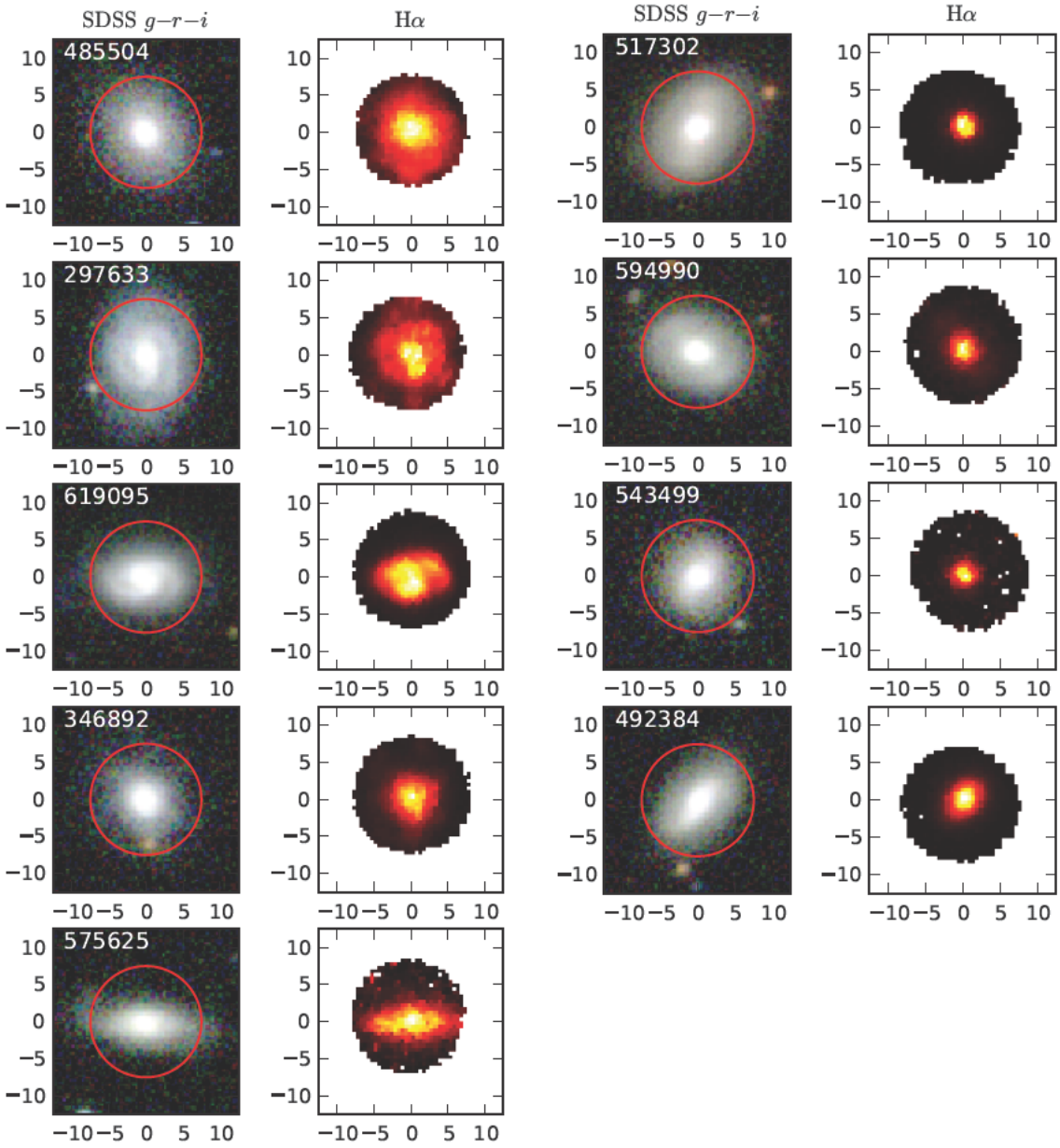

Figure 4.1: SDSS optical *gri* colour images of each galaxy in our two samples accompanied by their Hα linear flux map from SAMI. In each optical image we display the approximate SAMI field-of-view with a red circle. Galaxies in the control sample are on the left, while galaxies on the right-hand side are from our quenching sample. Galaxies in the quenching sample have Hα distributions that are more concentrated than the control sample. The units of each axis are in arc seconds offset from the centre of the field of view.

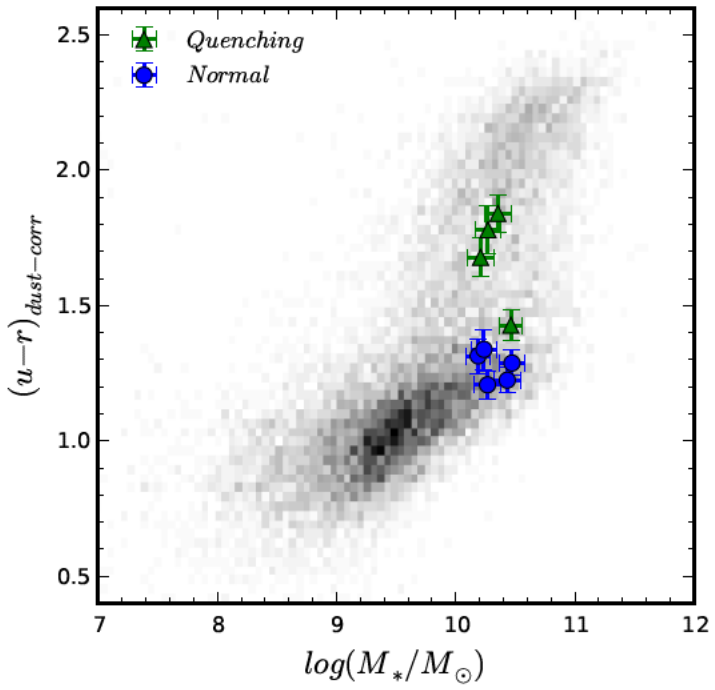

Figure 4.2: The positions of galaxies in the 'quenching' (green) and control (blue) samples in the $(u-r)$–$\log(M_*)$ plane. The greyscale background represents the density of galaxies in this parameter space for all galaxies below $z = 0.1$ as measured by the GAMA survey. The stellar colours have been corrected for dust attenuation and redshift effects by Taylor et al. (2011). At fixed stellar mass the quenching galaxies have redder colours than their mass-matched control-sample counterparts, indicating ageing stellar populations.

ing has on these galaxies, we have chosen a control sample of galaxies that match the properties of the quenching galaxies in high-mass groups as closely as possible. For each galaxy that is undergoing environment quenching we have chosen a control galaxy such that their stellar mass lies within ± 0.1 dex. Further, to ensure that morphological variation with environment does not influence the sample, we have selected the control sample to have r-band Sérsic indices (n_r) within ± 0.5 of the Sérsic index of each quenching galaxy, or as near as possible if no matching galaxy can be found. Optical images for each galaxy in the control and quenching samples are shown in Figure 4.1 and their properties are summarised in Table 4.1. The positions of the galaxies in the colour-mass diagram for the quenching and control samples are compared in Figure 4.2. The quenching galaxies are redder than those in the control sample at the same stellar mass.

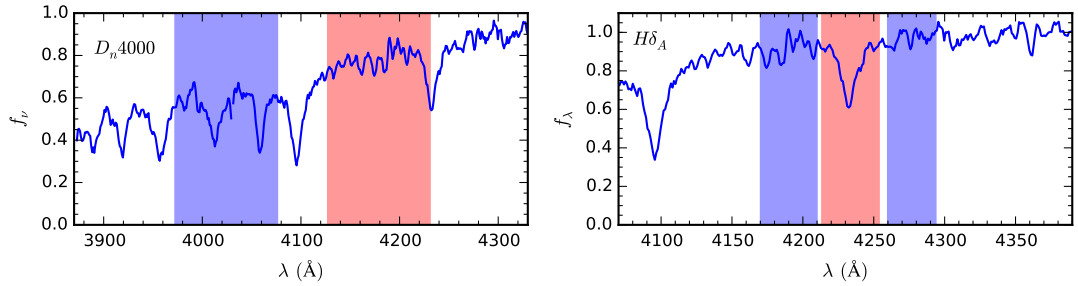

Figure 4.3: An illustration of the passbands used for the D_n4000 and Hδ_A calculation. The spectrum is a high signal-to-noise ratio example spectrum from a central square aperture over the galaxy GAMA 106549, which was chosen for its strong spectral features. This galaxy has a redshift of $z_{spec} = 0.03186$.

4.2.2 Measuring stellar populations

$\mathbf{D}_n4000$ and $\mathbf{H}\delta_A$

As a galaxy evolves passively, the age and metal content of its stellar populations will change in a predictable way. This evolution is determined by the star formation history, the lifetimes of the stars that form, and the amount of heavy elements returned to the interstellar medium by these stars as they age. In the integrated light, the evolution is manifested in the variation of the optical spectrum, in particular in the changing strength of a variety of atomic absorption lines and molecular bands. Two of the most prominent features for diagnosing these changes are the D_n4000 discontinuity and the Hδ_A absorption line index. Molecular absorption lines on the blue side of the Ca H line at 3968.5 Å cause a sharp discontinuity in the spectrum, that strengthens as the age and metallicity increase. The combination of D_n4000 and Hδ_A was shown by Kauffmann et al. (2003a) to be a good measure of the age of a stellar population if a starburst has occurred within the last $1-2$ Gyr, and over this timescale, metallicity plays a second-order role in determining the strengths of these features. In particular very strong Hδ_A is indicative of a large number of B and A-type stars being present, and suggests star formation within the last 100 Myr.

The strength of D$_n$4000 is calculated by taking the ratio of the continuum fluxes on each side of the step. This was originally defined by Bruzual (1983) as the ratio of fluxes integrated over frequency, F_ν, rather than wavelength,

$$D_n4000 = \frac{(\lambda_b^+ - \lambda_b^-)\int_{\lambda_r^-}^{\lambda_r^+} F_\nu d\nu}{(\lambda_r^+ - \lambda_r^-)\int_{\lambda_b^+}^{\lambda_b^-} F_\nu d\nu}. \tag{4.1}$$

We have chosen the limits of these integrations to correspond to spectral bands prescribed by Balogh et al. (1999). That is, $(\lambda_b^-, \lambda_b^+, \lambda_r^-, \lambda_r^+) = (3850.0, 3950.0, 4000.0, 4100.0)$ Å are the wavelength boundaries of the passbands in the galaxy rest-frame.

We calculate the Hδ_A absorption line equivalent width following Worthey & Ottaviani (1997). We first fit the galaxy continuum and absorption lines using LZIFU to estimate the Hδ emission. This emission is then subtracted from the spectrum to give a pure

absorption spectrum. This absorption spectrum is smoothed to the resolution of the Lick system (FWHM = 10 Å at the wavelength of Hδ) by convolution with a Gaussian kernel accounting for the velocity broadening. The equivalent width is then calculated using

$$\mathrm{H}\delta_A = (\lambda_2 - \lambda_1)\left(1 - \frac{F_I}{F_S}\right), \tag{4.2}$$

where $\lambda_1 = 4083.5$ Å and $\lambda_2 = 4122.25$ Å are the wavelengths denoting the boundaries of the feature passband, F_I is the integrated flux within the feature passband, and F_S is the continuum flux at the wavelength of Hδ estimated using a straight-line interpolation between the average flux levels of the sidebands passing through their central wavelengths. The continuum bands are in wavelength ranges $\lambda_{B,1} = 4041.6$ Å $- \lambda_{B,2} = 4079.75$ Å for the blue sideband and $\lambda_{R,1} = 4128.5$ Å $- \lambda_{R,2} = 4161.0$ Å for the red sideband. The measurement technique is illustrated in Figure 4.3.

Errors on both of these measurements have been estimated with a Monte Carlo method. The noise in the spectrum is estimated from the SAMI variance spectrum. These values are then used to generate artificial Gaussian noise, with dispersion that varies with wavelength. For each galaxy spectrum we add 1000 realisations of the noise spectrum to the best-fitting template returned by LZIFU and measure the strengths of the indices. The error on our measurement is taken as the standard deviation of the resulting distribution of indices.

To probe the radial structure in these features we apply a radial binning scheme. Spaxels were summed over elliptical annuli, with ellipticity and position angle determined by the GAMA r-band Sérsic photometry (Kelvin et al., 2012). These bins were constructed so as to be three spaxels ($1\farcs5$) in width.

Figure 4.4 shows the radial distribution of the strength of these features for the control sample of galaxies. In this Figure we compare our measured feature strengths to the model tracks of González Delgado et al. (2005). These models show the time evolution of D_n4000 and Hδ_A in a single stellar population after an instantaneous burst of star formation. D_n4000 is generally reduced towards the outskirts of galaxies in the control sample, with the average D_n4000 gradient being -0.1 ± 0.01 between the centre of the galaxy and R_e. Meanwhile the average Hδ_A equivalent width increases with radius, with an average gradient of 1.05 ± 0.29 Å, indicating stronger Balmer absorption towards the outer parts of their discs. We note that the D$_n$4000 and Hδ_A values for the galaxy 485504 do not fall within the model grid beyond R_e. This may be indicative of a flux calibration error. The results of this Chapter are not strongly affected by this.

In contrast to the control sample, the galaxies with centrally-concentrated star formation have gradients in D_n4000 that are positive for D_n4000 (0.05 ± 0.01) and negative for Hδ_A (-0.96 ± 0.25 Å), as shown in Figure 4.5. The strengths of these features in the galaxy centres, and their values at the r-band effective radius are given in Table 4.2. There is very little difference in these values in the centres of the galaxies between the control and quenching samples, but there is a difference at one effective radius. This difference in the average at R_e is significant at approximately 3σ for both D_n4000 and Hδ_A.

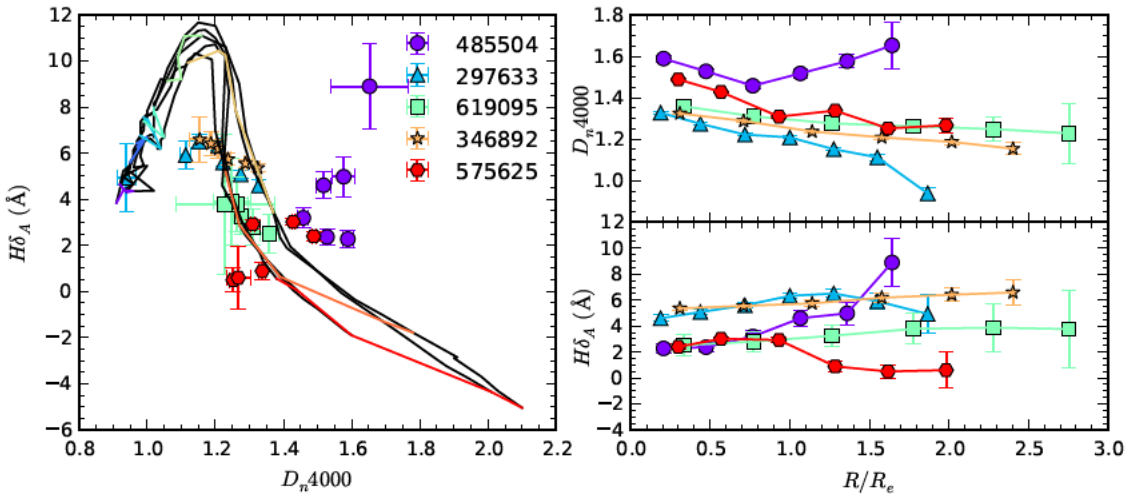

Figure 4.4: The radial distribution of the D_n4000 and Hδ_A spectral features for the galaxies in our control sample. The feature strengths are compared to model tracks that show how the strengths of these features will evolve after a single burst of star-formation (González Delgado et al., 2005). Lines of constant stellar metallicity are shown in black, while the coloured lines represent lines of constant stellar population age. Blue lines represent younger ages while red lines represent older ages.

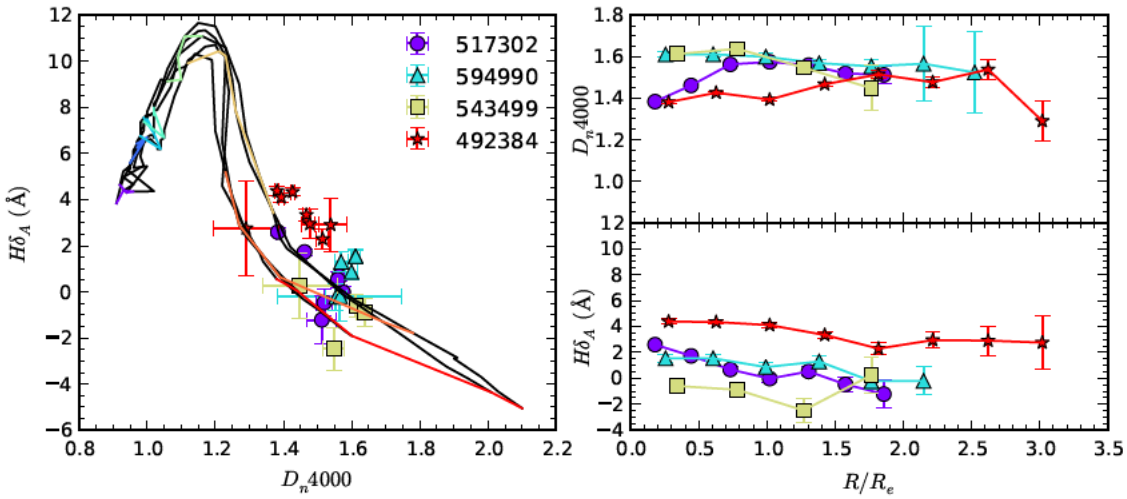

Figure 4.5: The radial distribution of the D_n4000 and Hδ_A spectral features for quenching galaxies in high-mass groups. The measurements are compared to the same model tracks as in Figure 4.4. The mean D_n4000 in these galaxies is lower in the centre than at R_e, while the Hδ_A equivalent width drops at larger radii.

	Centre				R_e				
Name	D_n4000	$H\delta_A$/Å	Age (Gyr)	$Z/Z_\odot$	D_n4000	$H\delta_A$/Å	Age (Gyr)	$Z/Z_\odot$	ΔAge
(1)	(2)	(3)	(4)	(5)	(6)	(7)	(8)	(9)	(10)
Control									
485504	1.59 ± 0.02	2.27 ± 0.4	1.92 ± 0.48	1.5 ± 0.36	1.52 ± 0.02	4.6 ± 0.59	1.5 ± 0.33	1.53 ± 0.31	-0.42 ± 0.59
297633	1.33 ± 0.01	4.6 ± 0.26	0.93 ± 0.12	1.32 ± 0.15	1.21 ± 0.01	6.32 ± 0.22	3.14 ± 0.71	0.14 ± 0.12	2.22 ± 0.72
619095	1.36 ± 0.03	2.52 ± 0.84	2.05 ± 0.15	0.72 ± 0.06	1.31 ± 0.02	2.8 ± 0.79	2.31 ± 0.19	0.54 ± 0.05	0.26 ± 0.24
346892	1.32 ± 0.01	5.36 ± 0.19	0.75 ± 0.04	1.82 ± 0.15	1.24 ± 0.01	5.74 ± 0.25	1.5 ± 0.07	0.47 ± 0.02	0.75 ± 0.08
575625	1.49 ± 0.01	2.4 ± 0.19	1.63 ± 0.16	1.58 ± 0.16	1.31 ± 0.01	2.92 ± 0.21	2.19 ± 0.10	0.58 ± 0.09	0.55 ± 0.19
Mean	1.42 ± 0.01	3.43 ± 0.20	1.45 ± 0.11	1.43 ± 0.13	1.31 ± 0.01	4.47 ± 0.21	2.12 ± 0.25	0.65 ± 0.07	0.67 ± 0.20
Quenching									
517302	1.38 ± 0.01	2.6 ± 0.17	0.9 ± 0.04	1.9 ± 0.06	1.57 ± 0.01	-0.02 ± 0.25	2.44 ± 0.46	1.48 ± 0.36	1.53 ± 0.46
594990	1.61 ± 0.01	1.54 ± 0.31	1.92 ± 0.46	1.53 ± 0.34	1.6 ± 0.02	0.87 ± 0.34	2.05 ± 0.47	1.5 ± 0.35	0.14 ± 0.66
543499	1.61 ± 0.02	-0.6 ± 0.5	3.51 ± 0.65	1.34 ± 0.43	1.64 ± 0.02	-0.88 ± 0.61	3.75 ± 0.75	1.36 ± 0.47	0.25 ± 0.99
492384	1.38 ± 0.01	4.38 ± 0.21	0.77 ± 0.19	1.76 ± 0.27	1.39 ± 0.01	4.1 ± 0.2	1.24 ± 0.24	1.73 ± 0.32	0.47 ± 0.3
Mean	1.50 ± 0.01	1.98 ± 0.16	1.77 ± 0.20	1.62 ± 0.16	1.55 ± 0.01	1.01 ± 0.19	2.37 ± 0.26	1.52 ± 0.19	0.60 ± 0.33

Table 4.2: The light-weighted stellar population ages and metallicities as calculated from D_n4000 and $H\delta_A$ using the González Delgado et al. (2005) model tracks and the method described in the text. Column (1): GAMA catalogue identification number. Columns (2)-(5) are for the central spectrum of each galaxy. Column (2): The value of D_n4000 in this spectrum; Column (3): The value of $H\delta_A$ in this spectrum; Column (4): Ages based on D_n4000, $H\delta_A$ in Gyr; Column (5): The measured metallicity; Columns (6)-(9): Same as (2)-(5) but calculated at R_e; Column (10): Age difference (outer−inner) in Gyr. The mean quantities for the quenching and control samples are given in the final row of each sample.

Estimating the stellar population ages from D_n4000 and $H\delta_A$

The use of D_n4000 and $H\delta_A$ as indicators of the stellar population properties is limited by the degeneracy between age and metallicity for some values of these features. For every age and metallicity for a stellar population there is a unique combination of D_n4000 and $H\delta_A$, but a given combination of these features may correspond to a range of stellar population properties. To explore the age-metallicity parameter space using these two stellar continuum features we sample between the model tracks of González Delgado et al. (2005) using a third-order spline interpolation. Comparing our measured feature strengths and uncertainties to the models, we obtain

$$\chi^2 = \frac{(D_n4000_{observed} - D_n4000_{model})^2}{\sigma^2_{D4000}} + \frac{(H\delta_{A,observed} - H\delta_{A,model})^2}{\sigma^2_{H\delta}}, \tag{4.3}$$

which forms a distribution in age and metallicity. The age and metallicity that minimises the χ^2 is the maximum-likelihood stellar population. This process is repeated 1000 times, changing the input D_n4000 and $H\delta_A$ by a Gaussian random number with standard deviation corresponding to the measurement error. This results in a distribution of possible ages and metallicities. We take the measured values as the best-fitting parameters and the standard deviation in the distributions of age and metallicity as their uncertainty. The process of estimating the stellar population parameters from D_n4000 and $H\delta_A$ is illustrated in Figure 4.6.

We have applied this method to spectra in the centres of the galaxies in our sample and at R_e. The ages and metallicities in our galaxies are displayed in Table 4.2. For the

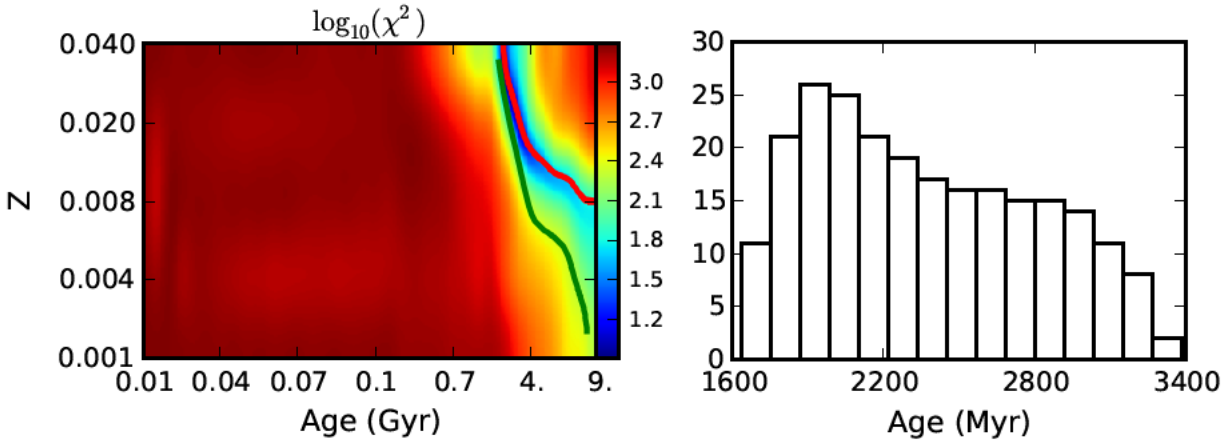

Figure 4.6: An illustration of the technique employed to estimate ages and metallicities from D_n4000 and $H\delta_A$ applied to the central spectrum of 594880. In the left-hand panel we have a map of $\log_{10}(\chi^2)$ for a range of stellar population ages and metallicities. Blue regions show an agreement between the observed spectral feature values and the model, while red regions show a large discrepancy. The red line traces the possible ages and metallicities implied by the measured D_n4000, while the green line shows the values implied by the $H\delta_A$ measurement. The models sample ages approximately logarithmically and the metallicity shows the mass fraction of elements heavier than He. $Z_\odot = 0.020$ in these models. The distribution of ages obtained with the Monte-Carlo resampling of the feature strengths is shown on the left. With the input values of D_n4000 and $H\delta_A$ we estimate the age of this spectrum to be 1.92 ± 0.46 Gyr and the metallicity to be $Z = 1.53 \pm 0.34\, Z_\odot$.

control sample of galaxies we find the mean difference between the age at R_e and the age at the centre to be 0.67 ± 0.20 Gyr, with the outer value being older. Taken at face-value, this implies the the reduction in D_n4000 with radius in the control sample of galaxies is largely driven by changes in the metallicity. The age gradients in the quenching galaxies are such that, on average, the galaxies are slightly older at R_e than in their centres. This is expected of a sample of galaxies that have no visible star formation in their outer regions. We find that the difference in stellar population ages for the quenching sample between the centre and R_e is 0.60 ± 0.33 Gyr. That is, there is no statistically significant difference between the stellar population age gradients between the two samples of galaxies.

The mean metallicity at the effective radius is estimated to be $0.65 \pm 0.07\, Z_\odot$ in the control sample, and 1.52 ± 0.19 in the quenching sample. This difference is significant at the level of 4σ, though it should be kept in mind that these uncertainties do not include any contribution that may arise from systematic errors in the calculation of D_n4000 or $H\delta$. Indeed, metallicities this high would place these galaxies above the stellar mass-metallicity

relation seen in large scale surveys (González Delgado et al., 2014; Peng et al., 2015; Scott et al., 2017; Lian et al., 2018). If the estimated metallicity is wrong this would imply that the derived age is incorrect as well. Furthermore, we note that the ages derived from the González Delgado et al. (2005) models assume a single burst of star formation followed by instantaneous quenching. Thus these values are illustrative only, and would be different to models that incorporate a more realistic star formation history.

We note that the measurements of D_n4000 and $H\delta_A$ in adjacent annular bins in each galaxy may be correlated by the PSF of the SAMI observations. The PSF FWHM is $\sim 2''$ for all galaxies, while the effective radii of all galaxies in this sample have been selected to be at least 1.25 times this size (recall that this is one of the selection criteria applied to our sample in Chapters 2 and 3). All gradient measurements made in this Chapter are made by comparing the strengths of spectral features at the galaxy centre and at R_e, and as such are minimally affected by any correlation imposed by the PSF.

Ages from Lick indices

Ages and metallicities can also be measured from other stellar indices. We use the values calculated by Scott et al. (*in prep.*) in elliptical annuli and based on the same methodology as presented in Scott et al. (2017). Ages, metallicities, and the abundances of alpha elements are estimated from the strengths of twenty stellar indices. These indices include the Balmer absorption lines ($H\delta_A$, $H\delta_F$, $H\gamma_A$, $H\gamma_F$, and $H\beta$), features associated with iron in stellar atmospheres (Fe4383, Fe4531, Fe5015, Fe5270, Fe5335, and Fe5406), molecular indices (CN1, CN2, Mg1, and Mg2), and five additional indices present in the SAMI spectra (Ca4227, G4300, Ca4455, C4668, and Mgb). The strengths of these features were measured in a fashion similar to the measurement of $H\delta_A$ as described above, using two continuum bands to define a pseudocontinuum level in the index passband. The wavelengths and widths of these bands conform with the definitions of Trager et al. (1998). Each index was measured at the spectral resolution of the Lick/IDS system (Worthey & Ottaviani, 1997).

The values of these spectral indices are converted to ages and metallicities by comparing them to the values predicted by single stellar population (SSP) models. This was done using the χ^2-minimisation method of Proctor et al. (2004). The light-weighted ages were calculated using the SSP models of Schiavon (2007) and metallicities from the models of Thomas et al. (2010). We utilised different SSP model grids to estimate the ages and metallicities to account for some known systematic effects in each model set. With the set of indices that we have used, the strengths of the Balmer lines have a large effect on the estimation of the stellar population ages. However, at low metallicity the Balmer line indices have been shown to lie outside the Thomas et al. (2010) model grids (Kuntschner et al., 2010; Scott et al., 2017). For this reason, the age estimates derived by the Thomas et al. (2010) models are not as reliable across the entire range of galaxy properties explored by the broader SAMI Galaxy Survey as those derived from the Schiavon (2007) models. However, the Thomas et al. (2010) grids do cover a larger range of metallicities than the Schiavon (2007) models, at lower metallicities in particular, and it is for this reason that we use the Thomas et al. (2010) models to derive this quantity. The estimated age and metallicity of a stellar population are naturally correlated when measurements

are made in this fashion. This is because the strengths of the spectral features that we are analysing depend on the temperatures of the stars that are producing the integrated spectrum. This in turn depends on both the stellar metallicity and the relative weighting of high-mass and low-mass stars in that region of the galaxy, which is a function of the local star formation history. Thus, the use of two different model grids to estimate ages and metallicities may introduce some systematic effects. Our current analysis will not make use of the Schiavon (2007) ages and the Thomas et al. (2010) metallicities simultaneously and is therefore insensitive to any systematic differences. The resulting properties are light-weighted age and metallicity measurements that assume a single stellar population without any consideration of the star formation history for each galaxy or any particular quirks of the chemical composition beyond the metallicity or alpha abundance.

Radial profiles of the age and metallicity of galaxies in our sample were derived by calculating these values in elliptical annuli. These annuli were $1''$ wide, with ellipticity and position angle defined by the light distribution in the SAMI data cubes. We show the radial profiles for the galaxies in our sample in Figure 4.7. For each galaxy we present the best-fitting age and metallicity in each radial bin where the continuum S/N $\geq$ 20. For the age profiles, the asymmetric error bars represent the span of ages that encompasses 68% of the probability. The errors on the metallicity are the symmetrical 1σ confidence intervals for each point. In all cases the χ^2 of the fit of the models to the data is small (< 1), indicating a good match between the measured indices and the models.

While the errors on each point are large, the age gradients in the control sample are, for the most part, flat out to R_e. The innermost measured ages in the control sample average to 2.5 ± 0.2 Gyr, and at R_e are 3.0 ± 0.5 Gyr, where the error bars here are based on the scatter in the best-fitting ages. For the quenching sample, the best-fitting age values are slightly younger than the control sample, with mean value 2.2 ± 0.2 Gyr in the galaxy centres, but the mean age increases to 3.7 ± 0.25 Gyr at R_e. This corresponds to a mean difference of 0.7 ± 0.6 Gyr at R_e between the quenching and control samples. We note that while this is not statistically significant it does suggest some tension with the conclusions drawn from the D_n4000 and Hδ_A measurements, where no difference in the age gradients was observed. Since the Lick index measurements incorporate a larger set of indices over a broader range in wavelengths, they are less susceptible to systematic errors.

4.2.3 The source of ionisation

The maps of Hα emission in our sample show that there is extended nebular emission in both the quenching and control samples. To understand how these galaxies are quenching, it may be important to know what the source of ionisation for this extended emission is. Should these galaxies be undergoing extreme ram-pressure stripping then shock ionisation of the gas in their outer discs may be present (Merluzzi et al., 2013). For strong shocks, the regions of higher ionisation will tend to have higher gas velocity dispersions. Alternatively, old stellar populations may lead to ionisation by stars in the post asymptotic giant branch (AGB) of the Herztsprung-Russell diagram (Sarzi et al., 2010). In parts of a galaxy where the gas surface density is low, ultraviolet light from these post-AGB stars

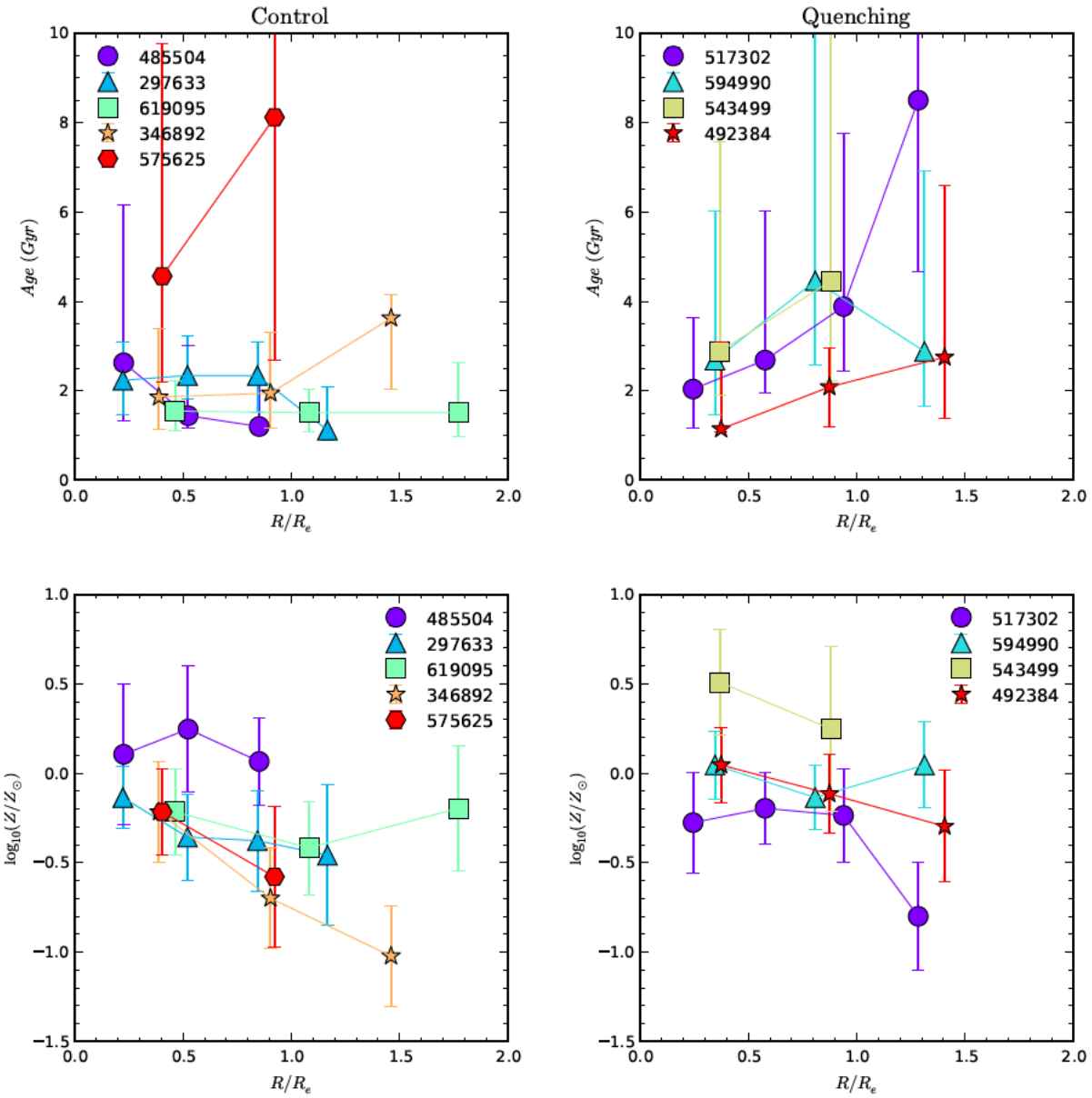

Figure 4.7: Top row: Light-weighted age radial profiles for control galaxies (left) and quenching galaxies (right). Bottom row: Metallicity profiles for control sample galaxies (left) and quenching galaxies (right). These profiles were calculated using the full set of Lick indices. While the errors on individual points are large, the age gradients tend to be flat in the control sample, and positive in the quenching sample.

can produce nebular emission with elevated levels of [N II] and narrow velocity dispersion. Such signatures were reported by Belfiore et al. (2017), in regions of galaxies where star formation has ceased. These possibilities can be explored by carefully examining the properties of the emission lines, their intensity ratios, velocity dispersion, and their correlation with the underlying stellar populations.

To estimate the stellar populations across the galaxies in our sample we have performed a standard Voronoi binning (Cappellari & Copin, 2003) to a S/N ratio of 20 in the continuum. We have opted to use a different binning scheme here so as to preserve as much azimuthal structure in the spatial distribution of the stellar populations as possible. In each bin we calculate D_n4000 and compare it to the emission line ratios in the unbinned data. We use the unbinned data so that spatial variation in the line ratios are not averaged over by the Voronoi binning. There are three galaxies (543499, 485504, 575625) where Voronoi binning is unable to achieve the desired S/N ratio, and for these systems we adopt the radial binning scheme used for the D_n4000 and $H\delta_A$ gradient measurements outlined in Section 4.2.2 above.

The results of our analysis are summarised in Figure 4.8. For each galaxy we present a resolved map of D_n4000 and the [OIII]λ5007/Hβ vs. [NII]λ6583/Hα BPT diagram, with points coloured by the local value of D_n4000. We investigate the possibility of shock excitation by looking for any correlation between the [NII]λ6583/Hα line ratio and the emission line velocity dispersion (see e.g. Rich et al., 2011; Ho et al., 2014; McElroy et al., 2015). We also provide spatially-resolved maps of [NII]λ6583/Hα to indicate regions within these galaxies of enhanced ionisation.

In the right-hand column of Figure 4.8 we show the spatial distribution of [N II]/Hα in our galaxies. The difference in the distribution of this line ratio between the quenching galaxies and the control sample is striking. Galaxies in the control sample have line ratio maps that are consistent with star formation all the way across the disc, with some regions of elevated line ratios that are not spatially coincident with regions of star formation.

In the third column of Figure 4.8 we note that for the control galaxies the [N II]/Hα is weakly correlated with the gas velocity dispersion. The partial Spearman rank correlation coefficient between [N II]/Hα, D_n4000 and σ is $\rho = 0.2$, with p-values less than 0.01 in all cases indicating statistical significance. These correlations are imposed by the fact that all of these quantities increase towards the centres of the galaxies due to the stellar population gradients discussed in Section 4.2.2. In fact, for the control sample, the gas velocity dispersion correlates best with the D_n4000, and for these galaxies, the stronger D_n4000 is located in their inner regions. This is an indication that the higher velocity dispersion seen in these galaxies is most likely an artefact of the steep rotation curves in the centres of galaxies being unresolved at the spatial resolution of the SAMI observations.

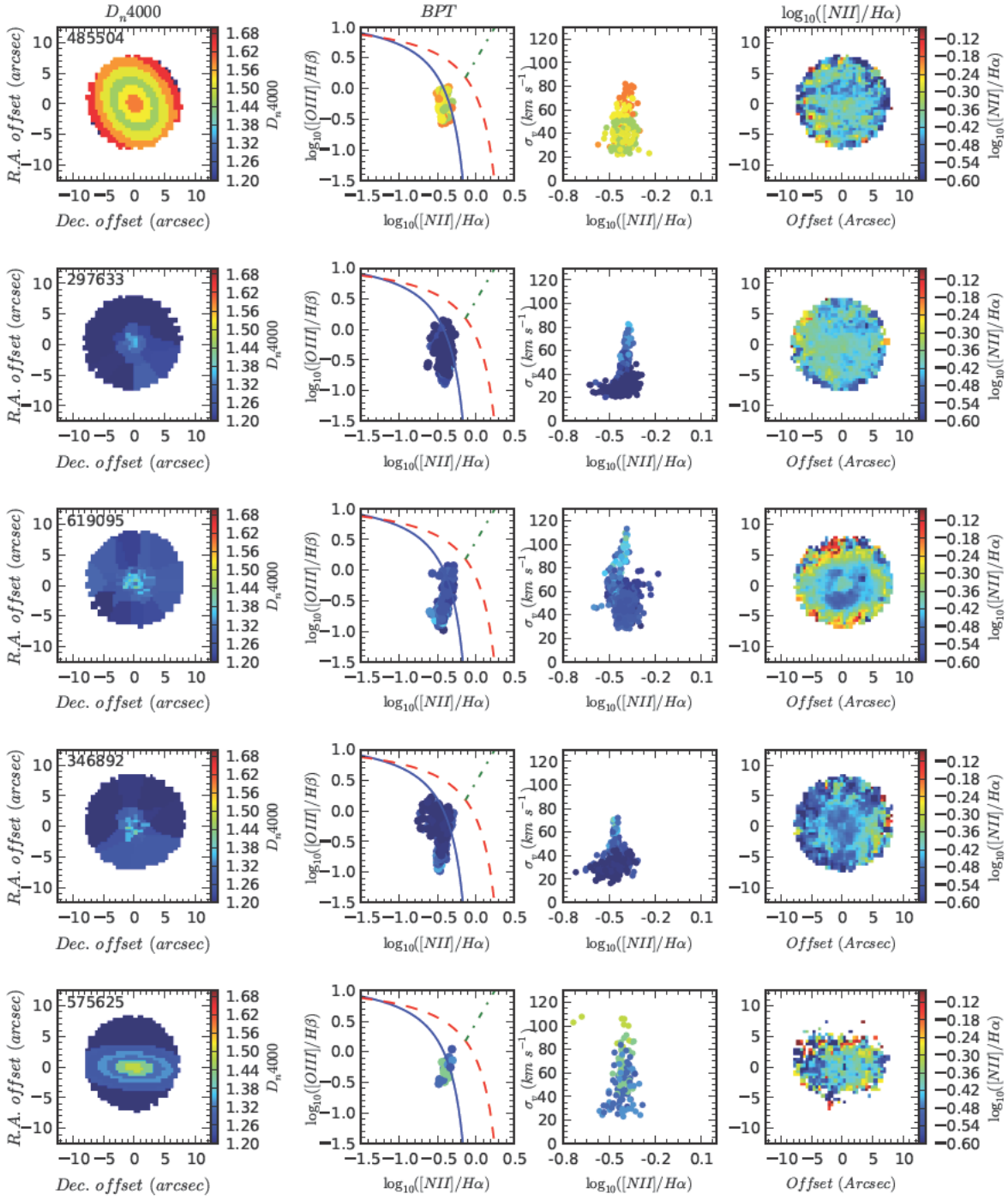

Figure 4.8: Various diagnostics for the ionisation of the gas in each galaxy in the control sample, correlated with the D_n4000 strength as a tracer of the stellar population. In the left column we show a map of D_n4000, calculated in Voronoi bins with continuum S/N of 20 where possible, and in elliptical annular bins otherwise. In column 2 we show the [O III]/Hβ vs. [N II]/Hα BPT diagram, with points coloured by the strength of D_n4000 in the corresponding region of the galaxy. Only spaxels where the S/N in all emission lines is larger than 3 are shown. The third column shows the gas velocity dispersion as a function of the [N II]/Hα ratio, again, points here are coloured by the D_n4000 strength. We have fixed the colour scale for D_n4000 between all images to allow for a fair comparison between galaxies. The final column shows the spatial distribution of [N II]/Hα in each galaxy. We only show spaxels where the S/N of both lines exceeds 3.

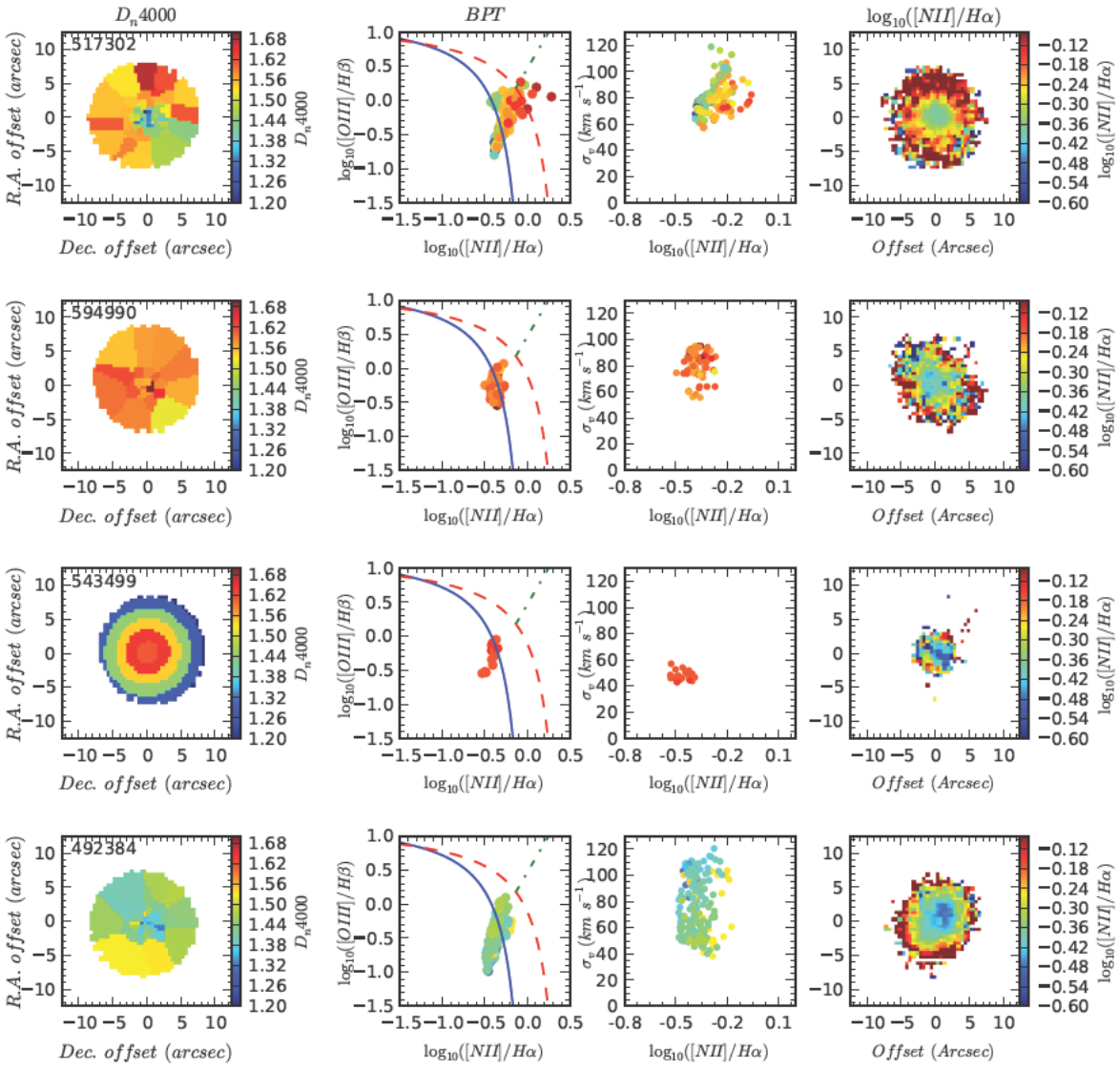

Figure 4.8: *continued.* Here we show the same maps as above but for the quenching sample. These galaxies have stronger D_n4000 and elevated [N II]/Hα in their outskirts, with the exception of 543499, where the lines have insufficient S/N.

Galaxies in the quenching sample show elevated [N II]/Hα across their discs, and outside the small, inner regions of centrally-concentrated star formation. That is, the outskirts of these galaxies show line ratios that are inconsistent with being ionised by a young stellar population. In three out of four cases, the average gas velocity dispersion is higher than for the control sample of galaxies. The exception is galaxy 543499, but this galaxy has very low S/N in the gas in the outer parts, making a measurement of the velocity dispersion here impossible. For galaxies 517302 and 492384 the elevation of [N II]/Hα correlates best with D_n4000. That is, the highest values for [N II]/Hα are in parts of the galaxy with the oldest light-weighted stellar populations. The lack of a correlation between the velocity dispersion in the gas and the emission line ratios, coupled with their relationship to the stellar spectral features, means that it is unlikely to be the

case that shock ionisation is the cause of the emission in the outer parts of the galaxies

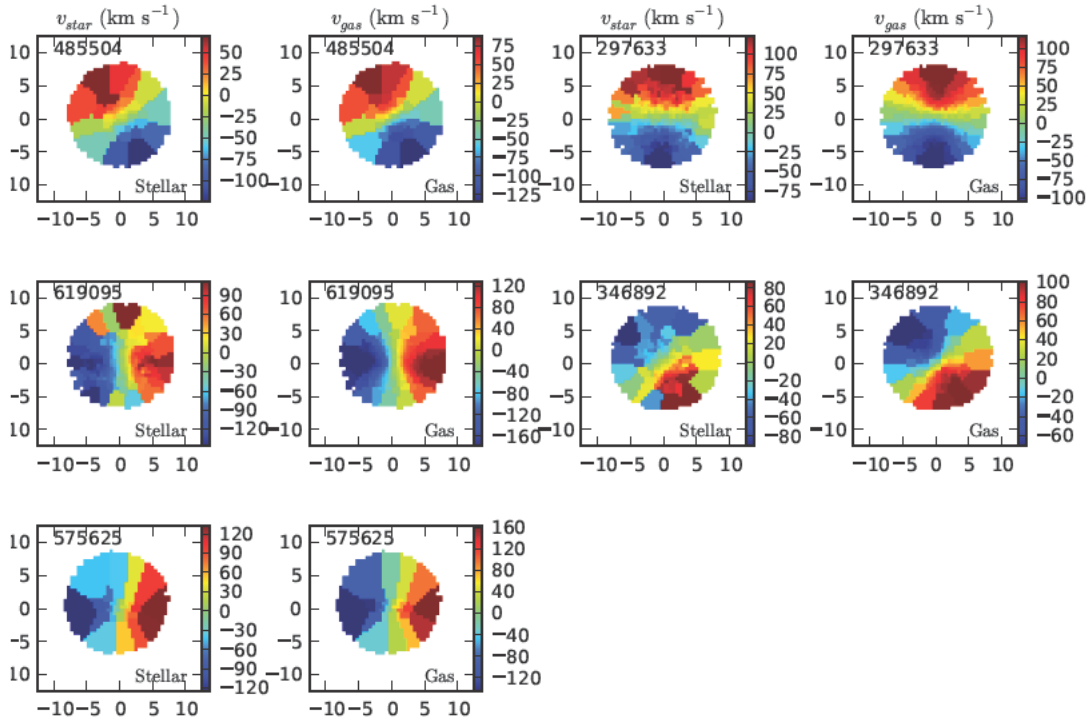

Figure 4.9: Stellar and gas kinematics for the control sample of galaxies. The data cubes were Voronoi binned to a continuum S/N of 10 around the wavelength of Hβ. Blue colours represent parts of each galaxy rotating towards us and red parts are rotating away. In all galaxies the gas and stars are co-rotating. Units along the x and y axes are in arc seconds.

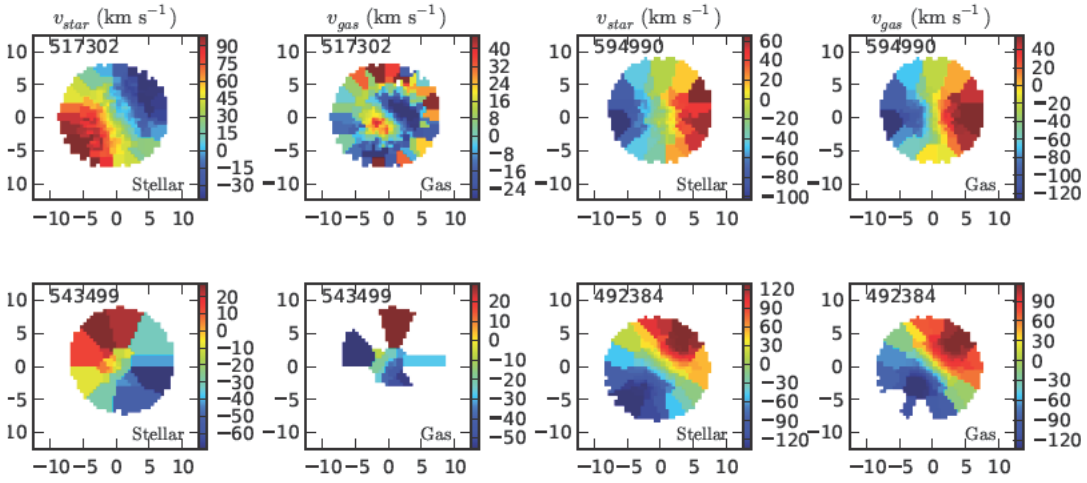

Figure 4.9: Stellar and gas kinematics for the quenching sample. Gas kinematics are not shown where the S/N of Hα is below 5. Note that in all cases the kinematics of the star-forming gas and the stars are aligned and rotating in the same direction.

4.2.4 Gas and stellar kinematics

LZIFU also returns the line-of-sight velocity of the gas in the galaxy, derived from the redshift of the emission lines. In addition to the gas kinematics, the code also calculates the stellar kinematics, which are derived and stored when the code calls pPXF. Mapping the stellar velocity from the galaxy continuum spectra requires a S/N ratio of at least 10. To facilitate this, we Voronoi bin the data to a S/N of 10 in the SAMI blue continuum. This S/N threshold has the advantage of giving good estimates of the stellar velocity, while also ensuring that the bin size is small enough to properly characterise the velocity maps. The kinematic maps are useful for describing the dynamical state of these galaxies, diagnosing recent mergers or tidal disturbance from encounters with massive galactic neighbours, and counter-rotating gas. We present the kinematic maps as derived by LZIFU in Figure 4.9.

For the control sample the gas and stellar kinematics are consistent with regular, unperturbed rotation. Regular gas and stellar kinematics are also present in the majority of the quenching sample. While our ability to accurately determine the gas rotation out to large radii is hampered by the reduced S/N of the emission lines in the outer parts of the galaxies, the inner parts of the galaxies are rotating regularly and in the same direction as the stars. One notable exception to this trend is the galaxy 517302. This galaxy exhibits regular rotation in its stars and in the inner star-forming component of the gas. However, at larger radii, there is a component of gas that is counter-rotating relative to the stars at this location. The line ratios from the same spatial region as the misaligned gas are not consistent with star formation.

4.3 Discussion

We have selected a sample of galaxies that appears to be undergoing environmental quenching. These galaxies were selected on the basis of their low specific star formation rate, having centrally-concentrated star formation and existing in galaxy groups with halo mass greater than $10^{12.5}\,\mathrm{M}_{\odot}$. We have submitted these systems to a comparison with a control sample of galaxies that are not in massive groups, but have the same stellar mass and similar r-band light profiles.

Using the strengths of D_n4000 and $\mathrm{H}\delta_A$ in radial bins across galaxies in both the control and quenching samples we found positive light-weighted age gradients. That is, regardless of the star-formation morphology of the galaxies, the stellar populations appear older at R_e than in the centre if we use D_n4000 and $\mathrm{H}\delta_A$ and the González Delgado et al. (2005) model tracks. A gradient in this sense was expected for the quenching sample, since star formation has ceased in the outer parts of the galaxies. However, it was surprising to observe older stellar populations in the outer parts of the control galaxies. An age gradient in this sense for normal star-forming galaxies of stellar mass $10^{10.5}\,\mathrm{M}_{\odot}$ would contradict the paradigm of the inside-out growth of galaxies (e.g. van de Sande et al., 2013; Pérez et al., 2013). The galaxy 279633 appears to be driving this trend, with an estimated stellar population age $2.22 \pm 0.72\,\mathrm{Gyr}$ older at R_e than in the centre. This galaxy also exhibits a factor of ~ 10 drop in metallicity with this measurement technique, which is inconsistent with the metallicity profile derived from the Lick indices in Figure 4.7.

Caution must be taken with the interpretation of these results. The models of González Delgado et al. (2005) predict the evolution of D_n4000 and $\mathrm{H}\delta_A$ after a single burst of star formation. In reality the galaxies that we have observed have more extended star formation histories. A significant fraction of the light, particularly from the central regions of the galaxies, will not be accounted for in the models. This can be seen in Figures 4.4 and 4.5, where the measured feature strengths for some galaxies do not coincide with the models at any age or metallicity. In these cases the χ^2 minimisation will find the nearest age and metallicity, but this will not necessarily correspond to the true values in these galaxies. As our work on this topic continues, stellar population models that incorporate more physical star formation histories will make a promising avenue of enquiry.

Further caution must be taken with these age estimates since there are many sources of systematic error in the measurements themselves. For example, both D_n4000 and $\mathrm{H}\delta_A$ require an emission line correction, which requires very accurate modelling of the stellar continuum. Indeed this is true of all the Balmer lines. Should any of these fits contain an unknown systematic, then the accuracy of the inferred ages and metallicities will in turn suffer.

Nevertheless, if we take the average strength of D_n4000 and $\mathrm{H}\delta_A$ at R_e in the control sample to represent the state of a galaxy before the onset of outside-in quenching, we can learn about the quenching timescale. Assuming that star formation is truncated promptly at a given location without any prior enhancement, then the stellar populations at R_e in the quenching sample can only get older. The assumption of no star formation enhancement prior to quenching may not be true in the case of strong ram-pressure stripping.

Bekki (2014) showed that compressive shocks may induce additional star formation in galaxies being stripped of gas by ram pressure. However, for simplicity we shall assume that there was no strong enhancement of star formation in these galaxies at the onset of the quenching process.

Since we find no discernible difference between the age gradients based on D_n4000 and $H\delta_A$ in the control and quenching samples, we might deduce that the star formation in the outskirts of these galaxies was shut down very recently. The measurements of stellar population ages based on the Lick indices that were introduced in Section 4.2.2 present us with a different story. These more robust measurements showed a difference of 0.7 ± 0.6 Gyr in the stellar population ages at R_e, with the outer parts of the quenching galaxies appearing to be older. This calls into question the values derived from D_n4000 and $H\delta_A$, though is not significant enough to rule them out entirely.

The age and metallicity gradients shown by the Lick index measurements in our quenching sample bear a striking resemblance to those seen in cluster S0 galaxies reported by Johnston et al. (2014). Their spectral bulge-disc decomposition technique showed that the star formation in the bulges of these galaxies was quenched later than in the disc. It is possible that the mechanism that is acting to produce S0 galaxies in clusters is effective in groups of mass $\sim 10^{13}\,M_\odot$.

The analysis of Johnston et al. (2014) suggests that investigating the abundance of α-elements across galaxies that are undergoing quenching in groups may be a way forward. By analysing the α-enhancement in the bulges of cluster S0 galaxies, they were able to successfully show that the most recent episode of star formation in their sample of fuelled by gas that had already been enriched by previous star formation in the galaxy discs. Measuring and modelling the α-abundances in the environmentally quenching galaxies in SAMI will provide a powerful tool to compliment the age and metallicity measurements in diagnosing the mechanisms that quench galaxies across all environments.

Whether the change in the spectra of these galaxies is due to variation in the age or the metallicity of the stellar populations, it has certainly been sufficient to move the galaxies well off the blue cloud and on the path to the red sequence as we saw in Figure 4.2.

4.3.1 Ionisation of gas

Galaxies undergoing strong ram pressure stripping have been observed to exhibit shock excitation of their gas at the boundary where the intergalactic medium impinges upon the interstellar medium (Fossati et al., 2016), though this is by no means always the case (Merluzzi et al., 2016). We see no relationship between the [N II]/Hα and the gas velocity dispersion in our galaxies that would be expected in the case of emission from shocked gas.

Given the low velocity dispersion, the emission line ratios of gas in our control sample galaxies are largely consistent with ionisation from a young stellar population in star-forming regions. There are locations in several of these galaxies where the ionisation parameter of the gas appears to be higher. Figure 4.8 shows that in the control sample of galaxies there is no correlation between the areas of enhanced line ratios and elevated

D_n4000. These regions may to correspond to diffuse interstellar gas or excitation from other internal sources of ionisation. This gas can potentially be ionised by ultraviolet radiation escaping from HII regions (e.g. Giammanco et al., 2005), but can also be explained by an underlying evolved stellar population (Zhang et al., 2017).

Conversely, in the quenching galaxy sample, the enhancement of the [N II]/Hα ratio does correlate spatially with areas of stronger D_n4000. This correlation was noted by Belfiore et al. (2017) in the context of diagnosing Low Ionisation Emission Region (LIER). Their findings are in agreement with the earlier work of Binette et al. (1994) on the source of photoionisation of the tenuous gas in elliptical galaxies, and generalised to non-star-forming galaxies by Stasińska et al. (2008). A plausible explanation for the properties of the emission lines in our galaxies is the presence of a considerable population of post-AGB stars in the outer discs of our quenching galaxies. The existence of older stellar populations and the reduction of the gas density associated with the outside-in mode of quenching. Importantly we see no correlation between the [N II]/Hα emission line ratio and the gas velocity dispersion. The presence of fast shocks driven by an interaction with the galaxy and its surroundings is not required to explain the elevated emission that we see in the quenched sample.

4.3.2 Kinematics

Our analysis of the gas and stellar kinematics for galaxies in both samples shows that co-rotation of the star-forming gas with the stars is the dominant mode of gas within our small sample. There is one galaxy (517302) that shows counter-rotating gas in its outer parts. It seems unlikely that this gas is related to the observed centrally concentrated star formation. The age profile for 517302 in Figure 4.7 suggests that that the quenching of the outer parts of the galaxy occurred over a Gyr ago. Gas accreted onto a galaxy at an angle to its stellar disc will experience a torque that forces it into alignment (or perfect misalignment) with the rotation of the stars. Lake & Norman (1983) showed that the time for this alignment to take place is $t_{torque} \approx t_{dyn}/\epsilon$, where t_{dyn} is the dynamical timescale for the galaxy and ϵ is the ellipticity of the potential. Davis & Bureau (2016) showed that this timescale could be $5t_{dyn}$ for the bulge of a lenticular galaxy. For A disc galaxy like 517302, the torque timescale would be shorter. Given the misalignment between the outer gas and stars seen in 517302 of $\sim 120°$, it is not likely that this gas has been present for longer than 1 Gyr. Of course this will need to be confirmed with more rigorous dynamical modelling.

The co-rotation of gas in the quenching sample is significant in the context of the recent findings of Chen et al. (2016). In their study of galaxies in the MaNGA integral field spectroscopic survey, these authors noted a class of blue, star-forming galaxies with centrally-concentrated Hα emission that were selected based on the fact that their gas was rotating in the opposite direction to the bulk of the stars. Their modelling suggested that as gas is accreted from outside that galaxy, it will lose angular-momentum through interactions with the interstellar medium, spiralling into the galactic centre. These galaxies showed the signatures of older stellar populations in their outskirts, but they tended to exist in lower-density environments. Based on the kinematics in our sample, and the fact

that our galaxies are in relatively massive groups, we are able to rule out the mechanism of Chen et al. (2016) as the instigator of the change observed in our galaxies.

4.3.3 Comparison to a simple strangulation model

Some recent results have implicated strangulation as the dominant mechanism for building the population of passive galaxies at $z = 0$. Modelling galaxies as 'closed boxes' with no gas accretion or expulsion after a quenching event, Peng et al. (2015) surmised that strangulation should account for approximately 50% of passive galaxies in the low-redshift Universe. This conclusion was based on galaxy age and metallicity measurements from single-fibre spectroscopy. In nearby galaxies this technique samples only the central parts, and for more distant targets is highly weighted by the light intensity peak towards the galaxy centres.

Despite the conjectured importance of strangulation in shaping galaxy demographics in the Universe today, there are very few simulations that model the detailed distribution of star formation as this process proceeds.

To test the possibility that strangulation is responsible for the centrally-concentrated distribution of star formation in our quenching sample we have developed a toy model for the strangulation. Our model for the evolution of star formation distribution is based on the Kennicutt-Schmidt star formation law (Schmidt, 1959; Kennicutt, 1998). This is an empirical law that relates the local star formation rate surface density to the local gas density and is expressed in the form

$$\Sigma_{SFR} = 2.5 \times 10^{-4} \times \left(\frac{\Sigma_{Gas}}{\mathrm{M}_\odot \, \mathrm{pc}^{-2}} \right)^{1.4} \mathrm{M}_\odot \, \mathrm{yr}^{-1} \, \mathrm{pc}^{-2}. \tag{4.4}$$

To investigate how the star formation rate distribution will evolve with time, we invert the Kennicutt-Schmidt law to calculate the gas density profile. We then subtract the amount of gas consumed over a small time step at the current star formation rate. This process is applied iteratively, with time steps of 0.5 Myr for a total of 5 Gyr. As an input to this model, we take the median star-formation rate radial profile from Chapter 2 for galaxies with stellar mass in the range $10^{10.01} < M_*/\mathrm{M}_* < 10^{10.94}$ and in intermediate environments. This profile is well fit by an exponential decline in star formation with radius with a central star formation rate surface density of $0.065 \, \mathrm{M}_\odot \, \mathrm{yr}^{-1} \, \mathrm{kpc}^{-2}$ and an exponential gradient of $-0.76 \, \mathrm{R_e^{-1}}$. To match the typical scale-radius ratio of $\log_{10}(r_{50,H\alpha}/r_{50,cont}) \sim -0.05$ we adopt a simple exponential profile for the stellar mass surface density, with central surface density of $10^{10.05} \, \mathrm{M}_\odot \, \mathrm{kpc}^{-2}$ and an exponential slope parameter of $-0.65 \mathrm{R_e^{-1}}$. Our toy-model shows that over the 5 Gyr that we ran the model for, the central star formation rate surface density declines fastest, leading to an increase in the scale-radius ratio, that is, more spatially extended star formation.

This toy-model must be treated with some suspicion. The structure of the galaxy is unphysical, we have left out any treatment of star formation or AGN feedback, we have assumed that the Kennicutt-Schmidt law applies at all times, and we have assumed that no gas is recycled by stars into the interstellar medium. Segers et al. (2016) estimates that approximately 40% of the mass of gas that forms star is recycled into the interstellar

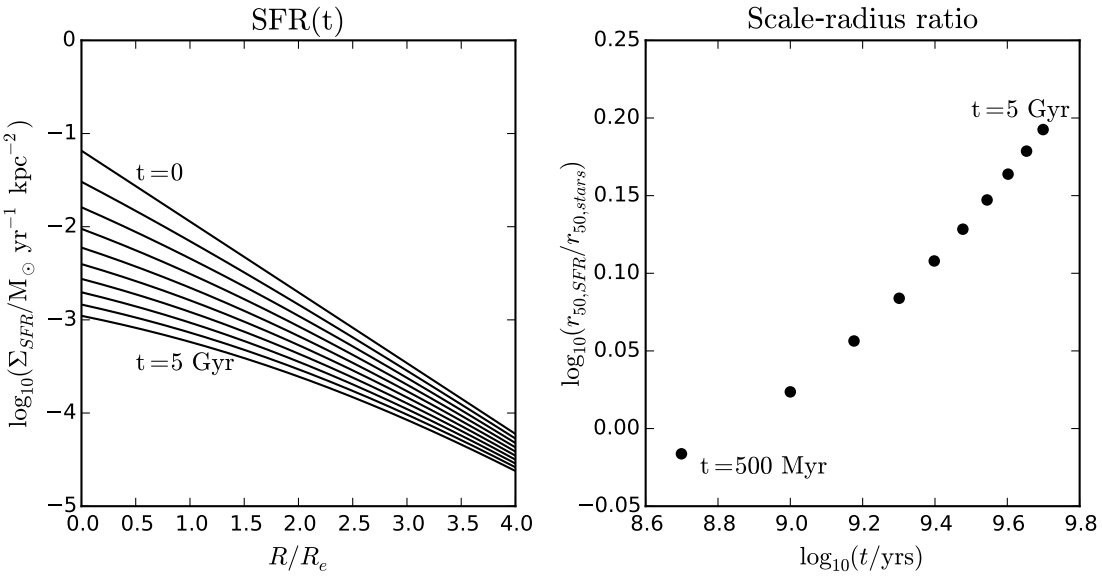

Figure 4.10: Left: The time evolution of the star formation rate surface density radial profile under the influence of strangulation. Right: How the scale-radius ratio will evolve. The calculation of the scale radius ratio uses the "half-light" radius of the star formation rate and stellar mass, rather than the half-light radius of Hα and the SAMI red-cube fluxes.

medium within 1 Gyr. These models can only be considered a very rough approximation to the evolution of a galaxy under strangulation. Nevertheless, the model demonstrates that without some external influence or the accretion of fresh gas, the star formation rate radial profiles will ultimately flatten. The centrally-concentrated star formation morphology seen in our environmentally quenching sample is not likely to be the result of strangulation alone.

4.4 Conclusion

We have looked in detail at the properties of galaxies in groups with dynamical masses between 10^{13} and $10^{14}\,\mathrm{M}_\odot$ that appear to be in the process of having their star formation quenched. We selected 4 such galaxies with stellar masses between $10^{10.2}$ and $10^{10.5}\,\mathrm{M}_\odot$ and a control sample of 5 galaxies of the same stellar mass and similar Sérsic index from outside massive groups. The Lick index measurements indicated an age difference of approximately 0.7 ± 0.6 Gyr or less at the effective radius between the quenching galaxies and the control sample. While this difference is only marginally significant, it is suggestive of an interesting trend that would benefit from investigation with a larger data set. This figure ignores the gradients derived using D_n4000 and Hδ, because we believe that further modelling is required to obtain accurate age gradients with these spectral features for our data.

4.4.1 The Mechanism for Quenching

Our measurements paint a complicated picture of the quenching process in groups of this mass. The comparison between the star formation distribution seen in our quenching sample and our toy model for strangulation suggests that strangulation cannot be responsible for the properties of these galaxies as we see them today.

The galaxies in our quenching sample show evidence for an event that stopped the star formation in their outer discs roughly 1 Gyr ago. This has left these galaxies with an ageing stellar population in their outer parts, and a waning star formation rate that has initiated their transition from the star-forming blue cloud on the colour-mass diagram in Figure 4.2.

The projected-phase-space positions of galaxies with centrally-concentrated star formation that we saw in Chapter 3, when compared to the simulations of Oman et al. (2013), suggested that these galaxies have existed in their parent groups for several Gyr and have likely experienced at least one pericentric passage past their group cores. The time that has elapsed since the quenching of the outer galaxy discs suggested by the stellar population age gradients is consistent with this possibility. If this is the case, it is possible that something like ram pressure stripping removed gas from the outer disc, while leaving gas in the centres of galaxies to continue forming stars.

The elevated emission line ratios beyond the radius of star formation can be accounted for by the presence of old stellar populations. Shock excitation from strong, ongoing ram pressure stripping is not required to explain these features.

An analysis of the gas and stellar kinematics of the sample showed that in all cases the gas and stars in the regions of star formation are co-rotating. This rules out the infall of gas as described by Chen et al. (2016) moving these galaxies from the quiescent red sequence towards the star forming blue cloud or otherwise explaining their centrally-concentrated star formation.

Whatever mechanism has quenched the outskirts of these galaxies, it seems to have been unable to completely extinguish star formation in the centres of these galaxies. It is likely that the remnants of star forming gas in these galaxies will be exhausted by star formation over the next few Gyr if no further episodes of gas removal take place. The quenching mechanism would be a hybrid of gas stripping, possibly by ram pressure, and strangulation.

The hybrid scenario of stripping and strangulation, if true, would have some interesting implications for the the conclusions of Peng et al. (2015). While the central regions of quenching galaxies in these massive groups do essentially undergo strangulation, their outer parts experience a more rapid suppression. Single fibre spectroscopic observations of the ages and metallicities of nearby galaxies would be unable to distinguish galaxies that were quenched by strangulation alone from those that have been partially quenched by some other mechanism. Integral field spectroscopy is required to understand the full picture of of how these galaxies go from star formation to quiescence.

Chapter 5

Conclusions

In this thesis our aim has been to investigate the processes that suppress star formation in galaxies in dense environments. We have been particularly interested in answering the following questions: how does the distribution of star formation in galaxies change as the total star formation rate declines? What sorts of environments cause this change? Over what timescale do these processes occur? Furthermore, it is important to know how the answers to these questions change with the stellar mass of a galaxy. Our study has made extensive use of the resolved spectroscopy from the SAMI Galaxy Survey combined with the accurate and diverse environment catalogues produced by the GAMA survey. With these datasets we have been able to explore the relationship between a galaxy's surroundings and its star formation morphology.

5.1 Environment quenching phenomenology

We have used the spatial distribution of dust-corrected Hα emission in the galaxies in our sample to trace their star formation and its variation with a number of metrics for environment. The data reveal some qualitative differences in the way that the environment quenches galaxies as a function of stellar mass. In galaxies with stellar masses lower than $\sim 10^{10}\,\mathrm{M}_{\odot}$, the reduction in specific star formation rate is not accompanied by the reduction in the spatial extent of star formation in the population as a whole, either in dense environments or in more isolated systems. Above stellar masses of $\sim 10^{10}\,\mathrm{M}_{\odot}$ the effect of environment on the radial extent of star formation becomes more apparent. Figure 3.5 panel *c* shows that these galaxies in massive groups ($M_G > 10^{12.5}\,\mathrm{M}_{\odot}$) have increasingly centrally-concentrated star formation as they fall below the main sequence. In less extreme environments, galaxies of similar mass show radially-extended star formation as they move towards a state of quiescence.

Our observations show that at any stellar mass, in any environment, there is a large degree of scatter in the star formation properties of galaxies. For example, in the star formation rate radial profiles shown in Figure 2.8, we see up to two orders of magnitude variation in the star formation rate surface density at all radii in a given bin of stellar mass and Σ_5. Some of this variation may be due to the size of each stellar mass bin. However, we see in Figure 2.11 that even when profiles are normalised to their central value, the

scatter persists. The fact that this scatter is present across the entire range of Σ_5 in our sample and in all bins of stellar mass implies that environment quenching must be an inefficient process. Not all galaxies that enter a dense environment will begin quenching immediately, and quenching may take a long time to complete. Another component of the scatter may be that Σ_5 does not trace the environment in a way that is relevant to the quenching process.

5.2 Where does environment quenching take place?

We have investigated the kinds of environment that correlate with he signatures of environment quenching. In Chapter 2 we compared the star formation distribution in galaxies to the Σ_5 surface density of galaxies in a density-defining population brighter than $M_r = -18.5$. In Chapter 3 we moved our focus to more physical measurements of environment, with the aim of understanding which types of environment are more likely to quench star formation. We found that at all stellar masses, increasing the group halo mass above $10^{12.5}\,\mathrm{M}_\odot$ increases the passive fraction of galaxies significantly above the fraction for non-grouped galaxies. For galaxies below $10^{10.5}\,\mathrm{M}_\odot$, the lower threshold for mass quenching, the passive fraction increases from $5 \pm 2\%$ in ungrouped sample, to $23 \pm 4\%$. Being in a massive group increases the likelihood of a galaxy no longer forming stars. Moreover, we saw that galaxies in these groups have lower specific star formation rates than their ungrouped counterparts. As was mentioned above, galaxies above $M_* = 10^{10}\,\mathrm{M}_\odot$ in these massive groups are quenched from the outside-in. Figure 3.6 shows this mechanism to be driving the progression of purely star-forming galaxies from the blue cloud to the red sequence in these environments.

Within groups, we tested the impact of nearest neighbour distance and the instantaneous projected tidal interaction strength on producing the observed trends. We found no evidence that either of these quantities correlate well with the reduction in star formation or the change in its spatial distribution. The star formation properties appear to be more dependent on the global group environment than on the immediate local environment. Galaxies with $M_* \gtrsim 10^{10}\,\mathrm{M}_\odot$ only show the signatures of outside-in quenching within R_{200} of the group centre, and inside their parent halo they are evenly distributed in projected phase space. Based on the simulations of Oman et al. (2013), it appears that these galaxies have existed in their group environment for longer than the group dynamical timescale.

5.3 How long does quenching take?

The above lines of reasoning do not give us a direct measure of the time it takes for a galaxy to move from the blue cloud to the red sequence in the colour-mass diagram. In Chapter 4 we attempted to estimate the outside-in quenching timescales more directly through the investigation of the stellar population gradients in a small sample of galaxies in massive groups. While the measurement errors on the stellar population ages are large, we find that star formation at the effective radius of these galaxies is approximately $0.7 \pm 0.6\,\mathrm{Gyr}$

older than in a sample of similar galaxies that are not in groups. The estimated error on this measurement is large in comparison to the measured difference, and this is due to the large uncertainties that come from modelling the stellar population parameters with spectral indices. However, we note that the sense of the age gradient is consistent with the truncated star formation in the outer parts of these galaxies. This is a lower bound on the timescale for this particular mode of quenching. The remaining star formation in the centre of these galaxies must still be extinguished before true quiescence is achieved. Barring the accretion of any additional gas or further rapid quenching of the remaining gas, this process is likely to take several Gyr.

Measuring the quenching timescales in galaxies with stellar masses below $10^{10}\,\mathrm{M}_{\odot}$ will be more challenging. The lower signal-to-nose ratio in the SAMI spectra, even with significant spatial binning, makes it difficult to perform the required spectral index measurements and derive the stellar population properties.

5.4 What processes quench star formation?

Inferring the mechanism by which star formation in galaxies is environmentally quenched remains difficult. For galaxies with $M_* < 10^{10}\,\mathrm{M}_{\odot}$ in high mass groups the quenching timescale may well be very short if the conditions in the intragroup medium are conducive to strong ram pressure stripping. Should these galaxies go through a phase of centrally-concentrated star formation while in a massive group, it is likely to be short-lived and will therefore be relatively rare in our dataset. In lower mass groups, it is likely that strangulation will cause these galaxies to become passive over several Gyr, as was described by Davies et al. (2016a). We showed in Chapter 4 that the slow strangulation of gas will not result in a large change in the star formation rate gradients in a galaxy while its integrated star formation rate declines. In either case, the observed spatial distribution of star formation is unlikely to show a significant trend. Following on from the work of Peng et al. (2015), some insights into this process will be gleaned by studying the metallicity of low-mass galaxies across different environments, though a large sample will be required to obtain statistically significant results.

For more massive galaxies, the environment quenching process is just as complicated. In groups with halo masses below $10^{12.5}\,\mathrm{M}_{\odot}$, our modelling in Section 4.3.3 suggested that strangulation is a probable mechanism for the ultimate suppression of star formation in these galaxies. At higher halo masses, as we have saw in Chapters 2 and 3, there may be several pathways between the blue cloud and the red sequence. A comparison between the outside-in quenching that we have presented and analytic modelling (Hester, 2006), or numerical simulations (e.g. Bekki, 2014) shows that episodes of rapid quenching by processes like ram pressure stripping may act on satellite galaxies. If these processes are not completely efficient then these galaxies may become passive by a combination of mechanisms.

5.5 Future work: can current-generation IFS surveys answer our questions?

Our work in this thesis helps to set the foundation for future studies of the environment quenching of star formation in integral field spectroscopic surveys. In the conclusions to Chapter 2 we estimated that, given the observed scatter in $r_{50,\mathrm{H}\alpha}/r_{50,cont}$, a total of 225 galaxies will be required to study environment quenching in a given stellar mass bin (A separate calculation is presented in Appendix A that puts the required sample size at ~ 250 per stellar mass bin). With the same stellar mass distribution as the SAMI Galaxy Survey, we would need 900 galaxies to study the trends in four mass intervals. We found that we were not able to measure the spatial distribution of star formation accurately in approximately 75% of galaxies, due to their inclination to our line of sight, the contamination of the emission lines by an AGN, or the lack of emission lines in passive galaxies. At this rate we will require approximately 3600 galaxies for this task, the full SAMI galaxy survey. If we wish to control for galaxy morphology as well, the required survey size would increase.

A further advantage of a larger sample size would be to reduce the errors in the age gradient measurements that we made in Chapter 4. Approximately $20 - 30$ suitable galaxies will be available in the full SAMI sample, which will decrease the errors on our age measurements by about a factor of two. The number of galaxies that are suitable for the control sample will increase in proportion, leading to a similar reduction in the measurement error there. Perhaps the most important future step for this aspect of the project will be to include more realistic stellar population models. The assumption of a single burst of star formation generating the spectra in our galaxies is inadequate. A more robust measurement of the stellar populations that incorporates the star formation history will be required to better understand the quenching timescales.

A natural avenue for further exploration with this work will be to compare our measurements of the spatial distribution of star formation in real galaxies to analytic models such as those presented by Hester (2006), and to the latest generations of large scale simulations such as EAGLE (Evolution and Assembly of GaLaxies and their Environments Schaye et al., 2015) and Illustris (Vogelsberger et al., 2014; Nelson et al., 2015). The cosmological nature of these simulations will mean that a more realistic interaction history between galaxies and their surroundings can be constructed. This will allow us to explore the extent to which various types of quenching mechanisms can act and over what timescales their signatures are expected to be seen.

The enormous volumes of both observational and simulated data that either are available now, or that will become available in the near future, foreshadow interesting times ahead for our understanding of the evolution of galaxies. What is clear is that integral field spectroscopic surveys such as the SAMI Galaxy Survey will play a major role in revealing the secrets of galaxy evolution.

Appendix A

More on the required sample size

In Chapter 2 we argued that an integral field spectroscopic survey such as SAMI would need to observe approximately 225 galaxies in each bin of stellar mass in order to detect the changing fraction of galaxies with centrally-concentrated star formation with environment. This argument was based on a simple prescription for scaling up of the sample size, assuming that the fraction of galaxies that we measured is close to the true fraction.

We can improve upon this estimate by modelling the distribution of scale-radius ratio by an empirical two dimensional distribution describing the relationship between $\log_{10}(\Sigma_5/\mathrm{Mpc}^2)$ and $\log_{10}(r_{50,\mathrm{H}\alpha}/r_{50,cont})$. To construct this two-dimensional distribution, we perform a Gaussian kernel-density estimate (KDE) based on the observed values of $\log_{10}(\Sigma_5/\mathrm{Mpc}^2)$ and $\log_{10}(r_{50,\mathrm{H}\alpha}/r_{50,cont})$ for the sample of 325 presented in Chapter 3. In constructing the empirical distribution in this way, we have made the assumption that the sample utilised in Chapter 3 is representative of the distribution of galaxies that might arise from a larger survey. This assumption would break down for very large samples that cover a broader range of environments, including galaxy clusters, where we have no knowledge about how $\log_{10}(r_{50,\mathrm{H}\alpha}/r_{50,cont})$ would behave in these environments. We note that this question can be explored using the SAMI cluster sample. Furthermore, the data used to generate the kernel-density estimate of the distribution of these parameters incorporates a range of stellar masses. If the observed relationship depends on stellar mass, then our calculations of the required sample size will change accordingly. Persisting, however, we construct the two dimensional distribution for the $\log_{10}(r_{50,\mathrm{H}\alpha}/r_{50,cont})$ and $\log_{10}(\Sigma_5/\mathrm{Mpc}^2)$ that is shown in Figure A.1.

We wish to understand how large a sample we need to observe in order to have a 90% chance of measuring a statistically significant ($p < 0.05$) correlation between $\log_{10}(\Sigma_5/\mathrm{Mpc}^2)$ and $\log_{10}(r_{50,\mathrm{H}\alpha}/r_{50,cont})$. To answer this question we extract a suite of artificial samples from the estimated empirical distribution. For a series of 20 numbers, N_{gal}, spaced roughly logarithmically between 10 and 1000, we draw 10000 random samples from the distribution and calculate the resulting Spearman rank correlation coefficient. We then compute the 90^{th} percentile of the p-values for each sample size, as shown in Figure A.2. For small sample sizes the p-value is close to 1 for the vast majority of the trials, and for samples of several hundred, the p-values are often well below the required $p = 0.05$. To estimate the number of galaxies required to achieve $p = 0.05$ or less in 90%

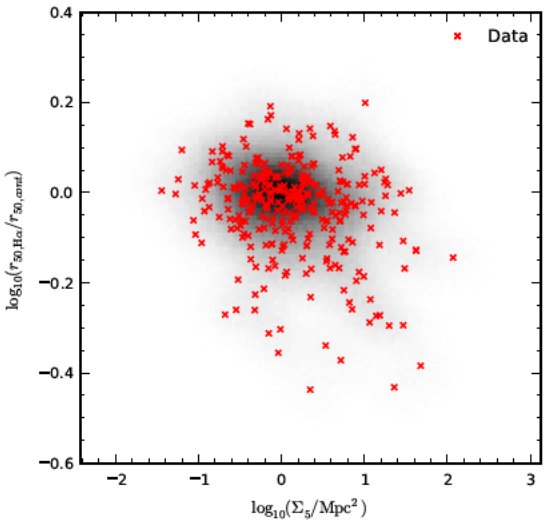

Figure A.1: The Gaussian kernel density estimate of the distribution of $\log_{10}(\Sigma_5/\mathrm{Mpc}^2)$ and $\log_{10}(r_{50,\mathrm{H}\alpha}/r_{50,cont})$ in our sample is shown in grey. Darker shades represent areas of this parameter space that are more likely to contain a galaxy. On the same axes we display the measured values of these variables for 325 galaxies presented in Chapter 3.

of cases, we interpolate between the points in the right-hand panel of Figure A.2. We find that in order to achieve a statistically significant result in 90% of samples, the sample size must be $N_{gal} = 247$. This is consistent with the estimate provided in Chapter 2.

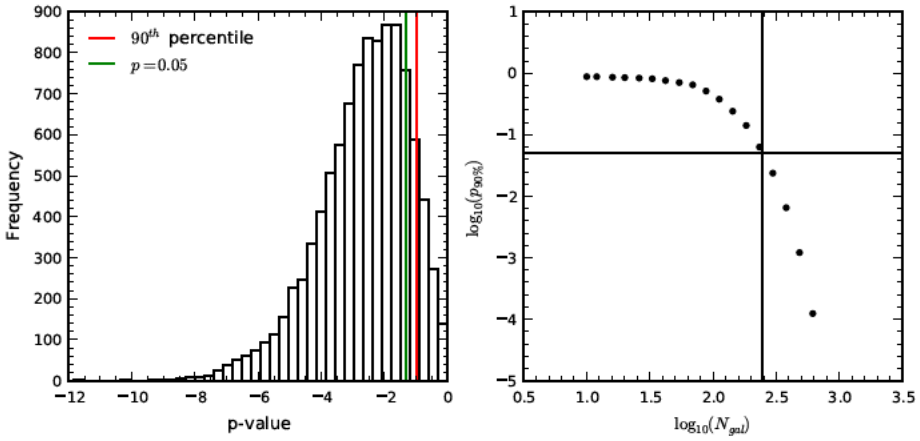

Figure A.2: (*left*) The distribution of p-values derived by calculating the Spearman rank correlation coefficient for 10000 random samples of size $N_{gal} = 200$ from the estimated distribution of $\log_{10}(\Sigma_5/\mathrm{Mpc}^2)$ and $\log_{10}(r_{50,\mathrm{H}\alpha}/r_{50,cont})$. The vertical red line shows the 90^{th} percentile of the distribution, and the vertical green line shows the $p = 0.05$ level. (*right*) The 90^{th} percentile of p-values as a function of N_{gal}. The horizontal line is the $p = 0.05$ level, and the vertical line shows where the p-value is estimated to be 0.05 exactly.

Bibliography

Abadi, M. G., Moore, B., & Bower, R. G. 1999, MNRAS, 308, 947

Abazajian, K. N., Adelman-McCarthy, J. K., Agüeros, M. A., et al. 2009, ApJS, 182, 543

Abd al-Rahman al-Sufi. 964, Book of Fixed Stars

Abell, G. O. 1965, ARA&A, 3, 1

Abramson, A., Kenney, J. D. P., Crowl, H. H., et al. 2011, AJ, 141, 164

Adams, S. M., Zaritsky, D., Sand, D. J., et al. 2012, AJ, 144, 128

Allen, J. T., Croom, S. M., Konstantopoulos, I. S., et al. 2015, MNRAS, 446, 1567

Alpaslan, M., Robotham, A. S. G., Driver, S., et al. 2014, MNRAS, 438, 177

Alpaslan, M., Driver, S., Robotham, A. S. G., et al. 2015, MNRAS, 451, 3249

Aragon-Calvo, M. A., Neyrinck, M. C., & Silk, J. 2016, ArXiv e-prints, arXiv:1607.07881

Astropy Collaboration, Robitaille, T. P., Tollerud, E. J., et al. 2013, A&A, 558, A33

Bacon, R., Copin, Y., Monnet, G., et al. 2001, MNRAS, 326, 23

Bai, L., Rasmussen, J., Mulchaey, J. S., et al. 2010, ApJ, 713, 637

Baldry, I. K., Balogh, M. L., Bower, R. G., et al. 2006, MNRAS, 373, 469

Baldry, I. K., Glazebrook, K., Brinkmann, J., et al. 2004, ApJ, 600, 681

Baldwin, J. A., Phillips, M. M., & Terlevich, R. 1981, PASP, 93, 5

Balogh, M. L., Baldry, I. K., Nichol, R., et al. 2004, ApJ, 615, L101

Balogh, M. L., Morris, S. L., Yee, H. K. C., Carlberg, R. G., & Ellingson, E. 1999, ApJ, 527, 54

Balsara, D., Livio, M., & O'Dea, C. P. 1994, ApJ, 437, 83

Barnes, D. G., Staveley-Smith, L., de Blok, W. J. G., et al. 2001, MNRAS, 322, 486

Becker, R. H., White, R. L., & Helfand, D. J. 1995, ApJ, 450, 559

Behroozi, P. S., Zhu, G., Ferguson, H. C., et al. 2015, MNRAS, 450, 1546

Bekki, K. 2009, MNRAS, 399, 2221

—. 2014, MNRAS, 438, 444

Bekki, K., Couch, W. J., & Shioya, Y. 2002, ApJ, 577, 651

Belfiore, F., Maiolino, R., Maraston, C., et al. 2016, MNRAS, 461, 3111

—. 2017, MNRAS, 466, 2570

Bianconi, M., Smith, G. P., Haines, C. P., et al. 2018, MNRAS, 473, L79

Binette, L., Magris, C. G., Stasińska, G., & Bruzual, A. G. 1994, A&A, 292, 13

Bland-Hawthorn, J., Bryant, J., Robertson, G., et al. 2011, Optics Express, 19, 2649

Blanton, M. R. 2006, ApJ, 648, 268

Bluck, A. F. L., Mendel, J. T., Ellison, S. L., et al. 2014, MNRAS, 441, 599

Boselli, A., Boissier, S., Cortese, L., & Gavazzi, G. 2008, ApJ, 674, 742

Boselli, A., Boissier, S., Cortese, L., et al. 2006, ApJ, 651, 811

Boselli, A., & Gavazzi, G. 2006, PASP, 118, 517

Bowen, I. S. 1938, ApJ, 88, 113

Bower, R. G., Benson, A. J., Malbon, R., et al. 2006, MNRAS, 370, 645

Boylan-Kolchin, M., Ma, C.-P., & Quataert, E. 2008, MNRAS, 383, 93

Bretherton, C. F., Moss, C., & James, P. A. 2013, A&A, 553, A67

Brinchmann, J., Charlot, S., White, S. D. M., et al. 2004, MNRAS, 351, 1151

Brough, S., Croom, S., Sharp, R., et al. 2013, MNRAS, 435, 2903

Brown, M. J. I., Zheng, Z., White, M., et al. 2008, ApJ, 682, 937

Brown, T., Catinella, B., Cortese, L., et al. 2017, MNRAS, 466, 1275

Bruzual, A. G. 1983, ApJ, 273, 105

Bryant, J. J., Bland-Hawthorn, J., Fogarty, L. M. R., Lawrence, J. S., & Croom, S. M. 2014, MNRAS, 438, 869

Bryant, J. J., Owers, M. S., Robotham, A. S. G., et al. 2015, MNRAS, 447, 2857

Buat, V., Boissier, S., Burgarella, D., et al. 2008, A&A, 483, 107

Buitrago, F., Trujillo, I., Conselice, C. J., et al. 2008, ApJ, 687, L61

Bundy, K., Bershady, M. A., Law, D. R., et al. 2015, ApJ, 798, 7

Byrd, G., & Valtonen, M. 1990, ApJ, 350, 89

Calzetti, D. 2001, PASP, 113, 1449

Cameron, E. 2011, PASA, 28, 128

Cappellari, M., & Copin, Y. 2003, MNRAS, 342, 345

Cappellari, M., & Emsellem, E. 2004, PASP, 116, 138

Cardelli, J. A., Clayton, G. C., & Mathis, J. S. 1989, ApJ, 345, 245

Cattaneo, A., Dekel, A., Devriendt, J., Guiderdoni, B., & Blaizot, J. 2006, MNRAS, 370, 1651

Ceverino, D., Sánchez Almeida, J., Muñoz Tuñón, C., et al. 2016, MNRAS, 457, 2605

Chabrier, G. 2003, PASP, 115, 763

Chen, Y.-M., Shi, Y., Tremonti, C. A., et al. 2016, Nature Communications, 7, 13269

Churchwell, E., & Walmsley, C. M. 1975, A&A, 38, 451

Cid Fernandes, R., Stasińska, G., Mateus, A., & Vale Asari, N. 2011, MNRAS, 413, 1687

Colless, M., Dalton, G., Maddox, S., et al. 2001, MNRAS, 328, 1039

Condon, J. J., Cotton, W. D., Greisen, E. W., et al. 1998, AJ, 115, 1693

Conroy, C., van Dokkum, P. G., & Kravtsov, A. 2015, ApJ, 803, 77

Conselice, C. J. 2014, ARA&A, 52, 291

Conselice, C. J., Rajgor, S., & Myers, R. 2008, MNRAS, 386, 909

Conselice, C. J., Wilkinson, A., Duncan, K., & Mortlock, A. 2016, ApJ, 830, 83

Content, R. 2006, in Proc. SPIE, Vol. 6269, Society of Photo-Optical Instrumentation Engineers (SPIE) Conference Series, 62693S

Cortese, L., Catinella, B., Boissier, S., Boselli, A., & Heinis, S. 2011, MNRAS, 415, 1797

Cortese, L., Gavazzi, G., Boselli, A., et al. 2006, A&A, 453, 847

Cortese, L., Boissier, S., Boselli, A., et al. 2012, A&A, 544, A101

Cox, D. R. 1958, Journal of the Royal Statistical Society. Series B (Methodological), 20, 215

Coziol, R., & Plauchu-Frayn, I. 2007, AJ, 133, 2630

Croom, S., Saunders, W., & Heald, R. 2004, Anglo-Australian Observatory Epping Newsletter, 106, 12

Croom, S. M., Lawrence, J. S., Bland-Hawthorn, J., et al. 2012, MNRAS, 421, 872

Crowl, H. H., & Kenney, J. D. P. 2006, ApJ, 649, L75

Dahari, O. 1984, AJ, 89, 966

Darvish, B., Mobasher, B., Sobral, D., et al. 2016, ApJ, 825, 113

Davies, L. J. M., Robotham, A. S. G., Driver, S. P., et al. 2015, MNRAS, 452, 616

—. 2016a, MNRAS, 455, 4013

Davies, L. J. M., Driver, S. P., Robotham, A. S. G., et al. 2016b, MNRAS, 461, 458

Davies, R. L., Groves, B., Kewley, L. J., et al. 2016c, MNRAS, 462, 1616

Davis, T. A., & Bureau, M. 2016, MNRAS, 457, 272

Davis, T. A., Young, L. M., Crocker, A. F., et al. 2014, MNRAS, 444, 3427

de Vaucouleurs, G. 1961, ApJS, 5, 233

Dekel, A., & Birnboim, Y. 2006, MNRAS, 368, 2

Di Matteo, T., Springel, V., & Hernquist, L. 2005, Nature, 433, 604

Dopita, M., Hart, J., McGregor, P., et al. 2007, Ap&SS, 310, 255

Dopita, M. A., & Sutherland, R. S. 2003, Astrophysics of the diffuse universe

Dressler, A. 1980, ApJ, 236, 351

Dressler, A., & Gunn, J. E. 1992, ApJS, 78, 1

Driver, S. P., Norberg, P., Baldry, I. K., et al. 2009, Astronomy and Geophysics, 50, 5.12

Driver, S. P., Hill, D. T., Kelvin, L. S., et al. 2011, MNRAS, 413, 971

Eales, S., de Vis, P., Smith, M. W. L., et al. 2017, MNRAS, 465, 3125

Eardley, E., Peacock, J. A., McNaught-Roberts, T., et al. 2015, MNRAS, 448, 3665

Eisenhauer, F., Abuter, R., Bickert, K., et al. 2003, in Proc. SPIE, Vol. 4841, Instrument Design and Performance for Optical/Infrared Ground-based Telescopes, ed. M. Iye & A. F. M. Moorwood, 1548–1561

Eisenstein, D. J., Blanton, M., Zehavi, I., et al. 2005, ApJ, 619, 178

Eke, V. R., Baugh, C. M., Cole, S., et al. 2004, MNRAS, 348, 866

Elbaz, D., Daddi, E., Le Borgne, D., et al. 2007, A&A, 468, 33

Ellison, S. L., Patton, D. R., Simard, L., & McConnachie, A. W. 2008, AJ, 135, 1877

Elmegreen, B. G., Bournaud, F., & Elmegreen, D. M. 2008, ApJ, 688, 67

Elmegreen, D. M., Elmegreen, B. G., Frogel, J. A., et al. 2002, AJ, 124, 777

Faber, S. M., Friel, E. D., Burstein, D., & Gaskell, C. M. 1985, ApJS, 57, 711

Faber, S. M., Willmer, C. N. A., Wolf, C., et al. 2007, ApJ, 665, 265

Fang, J. J., Faber, S. M., Salim, S., Graves, G. J., & Rich, R. M. 2012, ApJ, 761, 23

Finn, R. A., Zaritsky, D., McCarthy, Jr., D. W., et al. 2005, ApJ, 630, 206

Font, A. S., Bower, R. G., McCarthy, I. G., et al. 2008, MNRAS, 389, 1619

Fossati, M., Fumagalli, M., Boselli, A., et al. 2016, MNRAS, 455, 2028

Fossati, M., Gavazzi, G., Savorgnan, G., et al. 2013, A&A, 553, A91

Fossati, M., Wilman, D. J., Mendel, J. T., et al. 2017, ApJ, 835, 153

Franx, M., van Dokkum, P. G., Förster Schreiber, N. M., et al. 2008, ApJ, 688, 770

Frenk, C. S., & White, S. D. M. 2012, Annalen der Physik, 524, 507

Fujita, Y., & Goto, T. 2004, PASJ, 56, 621

Fumagalli, M., Fossati, M., Hau, G. K. T., et al. 2014, MNRAS, 445, 4335

Gallazzi, A., Bell, E. F., Wolf, C., et al. 2009, ApJ, 690, 1883

Gavazzi, G., Boselli, A., Cortese, L., et al. 2006, A&A, 446, 839

Gavazzi, G., Consolandi, G., Dotti, M., et al. 2015, A&A, 580, A116

Geha, M., Blanton, M. R., Yan, R., & Tinker, J. L. 2012, A Stellar Mass Threshold for Quenching of Field Galaxies, arXiv:1206.3573

Giammanco, C., Beckman, J. E., & Cedrés, B. 2005, A&A, 438, 599

Giovanelli, R., & Haynes, M. P. 1983, AJ, 88, 881

—. 1985, ApJ, 292, 404

Gómez, P. L., Nichol, R. C., Miller, C. J., et al. 2003, ApJ, 584, 210

González Delgado, R. M., Cerviño, M., Martins, L. P., Leitherer, C., & Hauschildt, P. H. 2005, MNRAS, 357, 945

González Delgado, R. M., Cid Fernandes, R., García-Benito, R., et al. 2014, ApJ, 791, L16

Grootes, M. W., Tuffs, R. J., Popescu, C. C., et al. 2017, AJ, 153, 111

Gunn, J. E., & Gott, III, J. R. 1972, ApJ, 176, 1

Haines, C. P., Pereira, M. J., Smith, G. P., et al. 2015, ApJ, 806, 101

Hambly, N. C., MacGillivray, H. T., Read, M. A., et al. 2001, MNRAS, 326, 1279

Heavens, A., Panter, B., Jimenez, R., & Dunlop, J. 2004, Nature, 428, 625

Heckman, T. M. 1990, in NASA Conference Publication, Vol. 3098, NASA Conference Publication, ed. J. W. Sulentic, W. C. Keel, & C. M. Telesco

Hernquist, L. 1989, Nature, 340, 687

Herschel, W. 1786, Philosophical Transactions of the Royal Society of London Series I, 76, 457

—. 1789, Philosophical Transactions of the Royal Society of London Series I, 79, 212

—. 1802, Philosophical Transactions of the Royal Society of London Series I, 92, 477

Hester, J. A. 2006, ApJ, 647, 910

Ho, I.-T., Kewley, L. J., Dopita, M. A., et al. 2014, MNRAS, 444, 3894

Ho, I.-T., Medling, A. M., Groves, B., et al. 2016a, Ap&SS, 361, 280

Ho, I.-T., Medling, A. M., Bland-Hawthorn, J., et al. 2016b, MNRAS, 457, 1257

Hopkins, A. M., & Beacom, J. F. 2006, ApJ, 651, 142

Hopkins, A. M., McClure-Griffiths, N. M., & Gaensler, B. M. 2008, ApJ, 682, L13

Hopkins, A. M., Miller, C. J., Nichol, R. C., et al. 2003a, ApJ, 599, 971

—. 2003b, ApJ, 599, 971

Hopkins, A. M., Driver, S. P., Brough, S., et al. 2013, Galaxy And Mass Assembly (GAMA): spectroscopic analysis, arXiv:1301.7127

Hubble, E., & Humason, M. L. 1931, ApJ, 74, 43

Hubble, E. P. 1925, The Observatory, 48, 139

—. 1926, ApJ, 64, doi:10.1086/143018

—. 1936, Realm of the Nebulae

Irwin, J. A. 1994, ApJ, 429, 618

Jaffé, Y. L., Smith, R., Candlish, G. N., et al. 2015, MNRAS, 448, 1715

Janowiecki, S., Catinella, B., Cortese, L., et al. 2017, MNRAS, 466, 4795

Jeans, J. H. 1902, Philosophical Transactions of the Royal Society of London Series A, 199, 1

Johnston, E. J., Aragón-Salamanca, A., & Merrifield, M. R. 2014, MNRAS, 441, 333

Kannappan, S. J., Stark, D. V., Eckert, K. D., et al. 2013, ApJ, 777, 42

Kauffmann, G., Heckman, T. M., White, S. D. M., et al. 2003a, MNRAS, 341, 33

—. 2003b, MNRAS, 341, 54

Kauffmann, G., Heckman, T. M., Tremonti, C., et al. 2003c, MNRAS, 346, 1055

Kawata, D., & Mulchaey, J. S. 2008, ApJ, 672, L103

Kelvin, L. S., Driver, S. P., Robotham, A. S. G., et al. 2012, MNRAS, 421, 1007

Kelz, A., Verheijen, M. A. W., Roth, M. M., et al. 2006, PASP, 118, 129

Kenney, J. D. P., van Gorkom, J. H., & Vollmer, B. 2004, AJ, 127, 3361

Kennicutt, Jr., R. C. 1998, ApJ, 498, 541

Kereš, D., Katz, N., Weinberg, D. H., & Davé, R. 2005, MNRAS, 363, 2

Kewley, L. J., Dopita, M. A., Sutherland, R. S., Heisler, C. A., & Trevena, J. 2001, ApJ, 556, 121

Koopmann, R. A., Haynes, M. P., & Catinella, B. 2006, AJ, 131, 716

Koopmann, R. A., & Kenney, J. D. P. 2004a, ApJ, 613, 866

—. 2004b, ApJ, 613, 851

Kulkarni, S. K. 2015, PhD thesis, Max-Planck-Institut für extraterrestrische Physik

Kuntschner, H., Emsellem, E., Bacon, R., et al. 2010, MNRAS, 408, 97

Lake, G., & Norman, C. 1983, ApJ, 270, 51

Larson, R. B. 1972, Nature, 236, 21

Larson, R. B., Tinsley, B. M., & Caldwell, C. N. 1980, ApJ, 237, 692

Lawrence, A., Warren, S. J., Almaini, O., et al. 2007, MNRAS, 379, 1599

Lewis, I., Balogh, M., De Propris, R., et al. 2002, MNRAS, 334, 673

Lian, J., Thomas, D., Maraston, C., et al. 2018, MNRAS, 474, 1143

Lilly, S. J., Carollo, C. M., Pipino, A., Renzini, A., & Peng, Y. 2013, ApJ, 772, 119

Lilly, S. J., Le Fevre, O., Hammer, F., & Crampton, D. 1996, ApJ, 460, L1

Liske, J., Baldry, I. K., Driver, S. P., et al. 2015, MNRAS, 452, 2087

Loveday, J., Norberg, P., Baldry, I. K., et al. 2015, MNRAS, 451, 1540

Lundmark, K. 1926, Arkiv for Matematik, Astronomi och Fysik, 19, 1

Madau, P., & Dickinson, M. 2014, ARA&A, 52, 415

Madau, P., Ferguson, H. C., Dickinson, M. E., et al. 1996, MNRAS, 283, 1388

Madau, P., Pozzetti, L., & Dickinson, M. 1998, ApJ, 498, 106

Markwardt, C. B. 2009, in Astronomical Society of the Pacific Conference Series, Vol. 411, Astronomical Data Analysis Software and Systems XVIII, ed. D. A. Bohlender, D. Durand, & P. Dowler, 251

Martig, M., Crocker, A. F., Bournaud, F., et al. 2013, MNRAS, 432, 1914

Martin, D. C., Wyder, T. K., Schiminovich, D., et al. 2007, ApJS, 173, 342

McCarthy, I. G., Frenk, C. S., Font, A. S., et al. 2008, MNRAS, 383, 593

McElroy, R., Croom, S. M., Pracy, M., et al. 2015, MNRAS, 446, 2186

Medling, A. M., Cortese, L., Croom, S. M., et al. 2018, MNRAS, arXiv:1801.04283

Merluzzi, P., Busarello, G., Dopita, M. A., et al. 2016, MNRAS, 460, 3345

—. 2013, MNRAS, 429, 1747

Miller, G. E., & Scalo, J. M. 1979, ApJS, 41, 513

Moreno, J., Torrey, P., Ellison, S. L., et al. 2015, MNRAS, 448, 1107

Morgan, W. W. 1961, Proceedings of the National Academy of Science, 47, 905

Moss, C., & Whittle, M. 2000, MNRAS, 317, 667

Moss, C., Whittle, M., & Pesce, J. E. 1998, MNRAS, 300, 205

Muldrew, S. I., Croton, D. J., Skibba, R. A., et al. 2012, MNRAS, 419, 2670

Naab, T., Johansson, P. H., & Ostriker, J. P. 2009, ApJ, 699, L178

Nandra, K., Georgakakis, A., Willmer, C. N. A., et al. 2007, ApJ, 660, L11

Nelson, D., Pillepich, A., Genel, S., et al. 2015, Astronomy and Computing, 13, 12

Nelson, E. J., van Dokkum, P. G., Momcheva, I., et al. 2013, ApJ, 763, L16

Newman, J. A., Cooper, M. C., Davis, M., et al. 2013, ApJS, 208, 5

Nichols, M., & Bland-Hawthorn, J. 2011, ApJ, 732, 17

Noeske, K. G., Weiner, B. J., Faber, S. M., et al. 2007, ApJ, 660, L43

Nulsen, P. E. J. 1982, MNRAS, 198, 1007

Oemler, Jr., A. 1974, ApJ, 194, 1

Oliva-Altamirano, P., Brough, S., Lidman, C., et al. 2014, MNRAS, 440, 762

Oliver, S., Frost, M., Farrah, D., et al. 2010, MNRAS, 405, 2279

Oman, K. A., & Hudson, M. J. 2016, MNRAS, 463, 3083

Oman, K. A., Hudson, M. J., & Behroozi, P. S. 2013, MNRAS, 431, 2307

Owers, M. S., Couch, W. J., Nulsen, P. E. J., & Randall, S. W. 2012, ApJ, 750, L23

Owers, M. S., Allen, J. T., Baldry, I., et al. 2017, MNRAS, 468, 1824

Pan, Z., Zheng, X., Lin, W., et al. 2016, ApJ, 819, 91

Patton, D. R., Carlberg, R. G., Marzke, R. O., et al. 2000, ApJ, 536, 153

Patton, D. R., Torrey, P., Ellison, S. L., Mendel, J. T., & Scudder, J. M. 2013, MNRAS, 433, L59

Peng, Y., Maiolino, R., & Cochrane, R. 2015, Nature, 521, 192

Peng, Y.-j., Lilly, S. J., Renzini, A., & Carollo, M. 2012, ApJ, 757, 4

Peng, Y.-j., Lilly, S. J., Kovač, K., et al. 2010, ApJ, 721, 193

Pérez, E., Cid Fernandes, R., González Delgado, R. M., et al. 2013, ApJ, 764, L1

Pierce, A. K. 1965, PASP, 77, 216

Poggianti, B. M., Fasano, G., Omizzolo, A., et al. 2016, AJ, 151, 78

Postman, M., & Geller, M. J. 1984, ApJ, 281, 95

Proctor, R. N., Forbes, D. A., & Beasley, M. A. 2004, MNRAS, 355, 1327

Quilis, V., Moore, B., & Bower, R. 2000, Science, 288, 1617

Quireza, C., Rood, R. T., Bania, T. M., Balser, D. S., & Maciel, W. J. 2006, ApJ, 653, 1226

Rasmussen, J., Mulchaey, J. S., Bai, L., et al. 2012, ApJ, 757, 122

Rasmussen, J., Ponman, T. J., & Mulchaey, J. S. 2006, MNRAS, 370, 453

Rasmussen, J., Ponman, T. J., Verdes-Montenegro, L., Yun, M. S., & Borthakur, S. 2008a, MNRAS, 388, 1245

—. 2008b, MNRAS, 388, 1245

Reeves, S. N., Sadler, E. M., Allison, J. R., et al. 2015, MNRAS, 450, 926

Rich, J. A., Kewley, L. J., & Dopita, M. A. 2011, ApJ, 734, 87

Richards, S. N., Schaefer, A. L., López-Sánchez, Á. R., et al. 2014, MNRAS, 445, 1104

Richards, S. N., Bryant, J. J., Croom, S. M., et al. 2016, MNRAS, 455, 2826

Robotham, A. S. G., Norberg, P., Driver, S. P., et al. 2011, MNRAS, 416, 2640

Robotham, A. S. G., Driver, S. P., Davies, L. J. M., et al. 2014, MNRAS, 444, 3986

Rodríguez del Pino, B., Aragón-Salamanca, A., Chies-Santos, A. L., et al. 2017, MNRAS, 467, 4200

Roediger, E., & Hensler, G. 2004, Astronomische Nachrichten Supplement, 325, 54

Roediger, E., Kraft, R. P., Nulsen, P., et al. 2013, MNRAS, 436, 1721

Roediger, E., Kraft, R. P., Nulsen, P. E. J., et al. 2015, ApJ, 806, 104

Rosse, T. E. O. 1850, Philosophical Transactions of the Royal Society of London Series I, 140, 499

Roth, M. M., Kelz, A., Fechner, T., et al. 2005, PASP, 117, 620

Safronov, V. S. 1960, Annales d'Astrophysique, 23, 979

Salim, S., Fang, J. J., Rich, R. M., Faber, S. M., & Thilker, D. A. 2012, ApJ, 755, 105

Samet, H. 1984, ACM Comput. Surv., 16, 187

Sánchez, S. F., Kennicutt, R. C., Gil de Paz, A., et al. 2012, A&A, 538, A8

Sánchez Almeida, J., Elmegreen, B. G., Muñoz-Tuñón, C., et al. 2015, ApJ, 810, L15

Sancisi, R., Fraternali, F., Oosterloo, T., & van der Hulst, T. 2008, A&A Rev., 15, 189

Sandage, A. 1961, The Hubble Atlas of Galaxies

Sandage, A., Sandage, M., & Kristian, J. 1975, Galaxies and the Universe

Sarzi, M., Shields, J. C., Schawinski, K., et al. 2010, MNRAS, 402, 2187

Schaefer, A. L., Croom, S. M., Allen, J. T., et al. 2017, MNRAS, 464, 121

Schawinski, K., Kaviraj, S., Khochfar, S., et al. 2007, ApJS, 173, 512

Schawinski, K., Urry, C. M., Simmons, B. D., et al. 2014, MNRAS, 440, 889

Schaye, J., Crain, R. A., Bower, R. G., et al. 2015, MNRAS, 446, 521

Schiavon, R. P. 2007, ApJS, 171, 146

Schmidt, M. 1959, ApJ, 129, 243

Scott, N., Brough, S., Croom, S. M., et al. 2017, MNRAS, 472, 2833

Scoville, N., Aussel, H., Brusa, M., et al. 2007, ApJS, 172, 1

Scoville, N., Lee, N., Vanden Bout, P., et al. 2017, ApJ, 837, 150

Segers, M. C., Crain, R. A., Schaye, J., et al. 2016, MNRAS, 456, 1235

Sharp, R., Saunders, W., Smith, G., et al. 2006, in Proc. SPIE, Vol. 6269, Society of Photo-Optical Instrumentation Engineers (SPIE) Conference Series, 62690G

Sharp, R., Allen, J. T., Fogarty, L. M. R., et al. 2015, MNRAS, 446, 1551

Skibba, R. A., van den Bosch, F. C., Yang, X., et al. 2011, MNRAS, 410, 417

Smethurst, R. J., Lintott, C. J., Bamford, S. P., et al. 2017, MNRAS, 469, 3670

Solanes, J. M., Manrique, A., García-Gómez, C., et al. 2001, ApJ, 548, 97

Speagle, J. S., Steinhardt, C. L., Capak, P. L., & Silverman, J. D. 2014, ApJS, 214, 15

Stasińska, G., Vale Asari, N., Cid Fernandes, R., et al. 2008, MNRAS, 391, L29

Strateva, I., Ivezić, Ž., Knapp, G. R., et al. 2001, AJ, 122, 1861

Sugai, H., Hattori, T., Kawai, A., et al. 2010, PASP, 122, 103

Sullivan, III, W. T., Bates, B., Bothun, G. D., & Schommer, R. A. 1981, AJ, 86, 919

Tabor, G., & Binney, J. 1993, MNRAS, 263, 323

Tal, T., van Dokkum, P. G., Nelan, J., & Bezanson, R. 2009, AJ, 138, 1417

Taylor, E. N., Hopkins, A. M., Baldry, I. K., et al. 2011, MNRAS, 418, 1587

—. 2015, MNRAS, 446, 2144

Thomas, D., Maraston, C., Schawinski, K., Sarzi, M., & Silk, J. 2010, MNRAS, 404, 1775

Tinsley, B. M. 1968, ApJ, 151, 547

Tinsley, B. M., & Danly, L. 1980, ApJ, 242, 435

Tomczak, A. R., Quadri, R. F., Tran, K.-V. H., et al. 2016, ApJ, 817, 118

Tonry, J. L., Blakeslee, J. P., Ajhar, E. A., & Dressler, A. 2000, ApJ, 530, 625

Toomre, A. 1964, ApJ, 139, 1217

Toomre, A., & Toomre, J. 1972, ApJ, 178, 623

Trager, S. C., Worthey, G., Faber, S. M., Burstein, D., & González, J. J. 1998, ApJS, 116, 1

Trujillo, I., Conselice, C. J., Bundy, K., et al. 2007, MNRAS, 382, 109

van de Sande, J., Kriek, M., Franx, M., et al. 2013, ApJ, 771, 85

van de Sande, J., Bland-Hawthorn, J., Fogarty, L. M. R., et al. 2017, ApJ, 835, 104

van de Voort, F., Schaye, J., Booth, C. M., & Dalla Vecchia, C. 2011, MNRAS, 415, 2782

van den Bergh, S. 1991, PASP, 103, 390

van den Bosch, F. C., Aquino, D., Yang, X., et al. 2008, MNRAS, 387, 79

Vazdekis, A., Sánchez-Blázquez, P., Falcón-Barroso, J., et al. 2010, MNRAS, 404, 1639

Vila-Costas, M. B., & Edmunds, M. G. 1992, MNRAS, 259, 121

Vogelsberger, M., Genel, S., Springel, V., et al. 2014, Nature, 509, 177

von der Linden, A., Wild, V., Kauffmann, G., White, S. D. M., & Weinmann, S. 2010, MNRAS, 404, 1231

Walker, S. H., & Duncan, D. B. 1967, Biometrika, 54, 167

Weinzirl, T., Jogee, S., Khochfar, S., Burkert, A., & Kormendy, J. 2009, ApJ, 696, 411

Weinzirl, T., Aragón-Salamanca, A., Gray, M. E., et al. 2017, MNRAS, 471, 182

Welikala, N., Connolly, A. J., Hopkins, A. M., & Scranton, R. 2009, ApJ, 701, 994

Welikala, N., Connolly, A. J., Hopkins, A. M., Scranton, R., & Conti, A. 2008, ApJ, 677, 970

Wetzel, A. R., Tinker, J. L., Conroy, C., & van den Bosch, F. C. 2013, MNRAS, 432, 336

Whitaker, K. E., van Dokkum, P. G., Brammer, G., & Franx, M. 2012, ApJ, 754, L29

Wijesinghe, D. B., Hopkins, A. M., Sharp, R., et al. 2011, MNRAS, 410, 2291

Wijesinghe, D. B., Hopkins, A. M., Brough, S., et al. 2012, MNRAS, 423, 3679

Wilman, D. J., Balogh, M. L., Bower, R. G., et al. 2005, MNRAS, 358, 88

Wisnioski, E., Glazebrook, K., Blake, C., et al. 2012, MNRAS, 422, 3339

Wolf, C., Gray, M. E., & Meisenheimer, K. 2005, A&A, 443, 435

Wolf, M. 1908, Publikationen des Astrophysikalischen Instituts Koenigstuhl-Heidelberg, 3, 109

Worthey, G., Faber, S. M., Gonzalez, J. J., & Burstein, D. 1994, ApJS, 94, 687

Worthey, G., & Ottaviani, D. L. 1997, ApJS, 111, 377

Wuyts, S., Förster Schreiber, N. M., Genzel, R., et al. 2012, ApJ, 753, 114

Yan, R., Newman, J. A., Faber, S. M., et al. 2006, ApJ, 648, 281

Yang, X., Mo, H. J., van den Bosch, F. C., et al. 2007, ApJ, 671, 153

York, D. G., Adelman, J., Anderson, Jr., J. E., et al. 2000, AJ, 120, 1579

Yozin, C., & Bekki, K. 2015, MNRAS, 453, 14

Zabludoff, A. I., Zaritsky, D., Lin, H., et al. 1996, ApJ, 466, 104

Zahid, H. J., Dima, G. I., Kewley, L. J., Erb, D. K., & Davé, R. 2012, ApJ, 757, 54

Zaritsky, D., Kennicutt, Jr., R. C., & Huchra, J. P. 1994, ApJ, 420, 87

Zhang, K., Yan, R., Bundy, K., et al. 2017, MNRAS, 466, 3217